## *Remote sensing of energy and water fluxes over Volta Savannah catchments in West Africa*

Opoku-Duah, Stephen

# Remote Sensing of Energy and Water Fluxes over Volta Savannah Catchments in West Africa

**Thesis submitted for the Degree of Doctor of Philosophy**
**Department of Geography**
**Durham University**



**Stephen Opoku-Duah, B.Sc., M.Sc.**

**November, 2007**

# Remote sensing of energy and water fluxes over Volta savannah catchments in West Africa

Stephen OPOKU-DUAH

## Abstract

The deterioration of the West African savannah in the last three decades is believed to be closely linked with about $0.5^0$C rise in temperature leading to evaporation losses and declining levels of the Volta Lake in Ghana. Although hydrological models can be used to predict climate change impacts on the regional hydrology, spatially-observed ground data needed for this purpose are largely unavailable. This thesis seeks to address this problem by developing improved methods for estimating energy and water fluxes (e.g. latent heat [*ET*]) from remotely sensed data and to demonstrate how these may be used to parameterize hydrological models. The first part of the thesis examines the potential of the Penman-Monteith method to estimate local-scale *ET* using ground-based hydrometeorological observations, vegetation coefficients and environmental data. The model results were compared with pan observations, scintillometer (eddy correlation) measurements and the Thornthwaite empirical method. The Penman-Monteith model produced better evaporation estimates (~3.90 mm day$^{-1}$ for the Tamale district) than its counterpart methods. The Thornthwaite, for example, overestimated predictions by 5.0-11.0 mm day$^{-1}$. Up-scaling on a monthly time scale and parameterization of the Grindley soil moisture balance model with the Thornthwaite and Penman-Monteith data, however, produced similar estimates of actual evaporation and soil moisture, which correlated strongly ($R^2$ = 0.95) with water balance estimates. To improve *ET* estimation at the regional-scale, the second part of the thesis develops spatial models through energy balance modelling and data up-scaling methods, driven by radiometric measurements from recent satellite sensors such as the Landsat ETM+, MODIS and ENVISAT-AATSR. The results were validated using estimates from the Penman-Monteith method, field observations, detailed satellite measurements and published data. It was realised that the MODIS sensor is a more useful source of energy and water balance parameters than AATSR. For example, stronger correlations were found between MODIS estimates of *ET* and other energy balance variables such as NDVI, surface temperature and net radiation ($R^2$ = 0.67-0.73) compared with AATSR estimates ($R^2$ = 0.31-0.40). There was also a good spatial correlation between MODIS and Landsat ETM+ results ($R^2$ = 0.71), but poor correlations were found between AATSR and Landsat data ($R^2$ = 0.0-0.13), which may be explained by differences in instrument calibration. The results further showed that *ET* may be underestimated with deviations of ~2.0 mm day$^{-1}$ when MODIS/AATSR measurements are validated against point observations because of spatial mismatch. The final part of the thesis demonstrates the application of the *ET* model for predicting runoff (*Q*) using a simplified version of the regional water balance equation. This is followed by analysis of flow sensitivity to declining scenarios of biomass volume. The results showed the absence of *Q* for >90% of the study area during the dry season due largely to crude model approximation and lack of rainfall data, which makes model testing during the wet season important. Runoff prediction may be improved if spatial estimates of rainfall, *ET* and geographical data (e.g. land-use/cover maps, soil & geology maps and DEM) could be routinely derived from satellite imagery.

**TABLE OF CONTENTS**

**LIST OF APPENDICES**



**LIST OF FIGURES**

## LIST OF TABLES



## LIST OF EQUATIONS

Symbols & Constants, their Units and Definitions

| Symbol | Unit | Definition |
|---|---|---|
| $h_c$ | J $s^{-1}$ | Planck's constant ($6.620*10^{-34}$) |
| $\sigma$ | $Wm^{-2}$ $K^{-4}$ | Stefan-Boltzmann constant ($5.67*10^{-8}$) |
| $c_p$ | $JKg^{-1}$ $K^{-1}$ | Air specific heat capacity (1004) |
| $k_b$ | $JK^{-1}$ | Boltzmann's gas constant ($1.381*10^{-23}$) |
| $c$ | m $s^{-1}$ | Speed of light ($3.0*10^{8}$) |
| $k$ | - | von Karman constant (0.41) |
| $G_{SC}$ | 1367 W $m^{-2}$ | Global solar constant |
| $d_s$ | AU | Astronomical Units |
| $K^{\uparrow}_{toa}$ | $Wm^{-2}$ $sr^{-1}$ $\mu m^{-1}$ | Extra-terrestrial solar radiation |
| $K^{\downarrow}$ | $Wm^{-2}$ | Incoming shortwave solar radiation |
| $K^{\uparrow}$ | $Wm^{-2}$ | Outgoing shortwave solar radiation |
| $r_p$ | - | Planetary reflectance |
| $r_a$ | - | Atmospheric reflectance |
| $L^{\downarrow}$ | $Wm^{-2}$ | Incoming long wave radiation |
| $L^{\uparrow}$ | $Wm^{-2}$ $sr^{-1}$ $\mu m^{-1}$ | Outgoing long wave radiation |
| $\alpha$ | - | Albedo |
| $R_n$ | $Wm^{-2}$ | Net radiation |
| $G_0$ | $Wm^{-2}$ | Soil heat flux |
| $H$ | $Wm^{-2}$ | Sensible heat flux |
| $LE$ | $Wm^{-2}$ | Latent heat flux |
| $d_s$ | m | Earth-sun distance |
| $d_r$ | m | Inverse Earth-sun distance |
| $L$ | W $m^{-2}$ | Radiance |
| $\lambda$ | $\mu m$ | Band wavelength |
| $VIS$ | $\mu m$ | Visible band |
| $NIR$ | $\mu m$ | Near-infrared band |
| $MIR$ | $\mu m$ | Mid-infrared band |
| $TIR$ | $\mu m$ | Thermal infrared band |
| ø | Rad | Sun zenith angle |
| $JD$ | days | Julian day (Day of the year) |
| $r_a$ | - | Atmospheric reflectance |
| $\varepsilon_0$ | - | Surface emissivity |
| $\varepsilon_a$ | - | Atmospheric emissivity |
| $T$ | $K/^0C$ | Temperature |
| $T_a$ | K | Air temperature |
| $T_s$ | K | Surface temperature |
| $LST$ | K | Land surface temperature |
| $T_g$ | K | Soil temperature |
| $K$ | Kelvin | Degree Kelvin |
| $\Delta T$ | K | Temperature difference |
| $T_B$ | K | Brightness temperature |
| $t$ | s (hrs) | Local time (GMT) |
| $\delta$ | Rad | Solar declination |
| $\omega_{(x)}$ | Rad | Solar hour angle |
| $t_{(x)}$ | Rad | Decimal hours |
| $\theta$ | Rad | Solar zenith angle |
| $E_0$ | - | Eccentricity factor |

| | | |
|---|---|---|
| Lat/lon | Degrees | Latitude/longitude |
| $\tau$ | - | Transmissivity |
| $\tau^2$ | - | Two-way transmittance |
| $\theta_s$ | mm | Soil moisture |
| *SMD* | mm | Soil moisture deficit |
| $\Delta S$ | mm | Soil moisture storage |
| *P* | mm | Precipitation |
| *Q* | mm | Runoff/discharge |
| *E* | mm | Reference evaporation |
| *PE* | mm | Potential evaporation |
| *ET* | mm | Evapotranspiration |
| *PET* | mm | Potential evapotranspiration |
| *AE* | mm | Actual evapotranspiration |
| $E_{pan}$ | mm | Pan evaporation |
| $\Lambda$ | - | Evaporative fraction |
| *%H* | % | Relative humidity |
| $e_s$ | kPa | Saturated vapour pressure |
| $e_a$ | kPa | Actual vapour pressure |
| $e_d$ | kPa | Vapour pressure deficit |
| $\Delta$ | kPa | Slope of vapour pressure curve |
| *z* | m | Vertical height |
| $z_{oh}$ | m | Roughness length of momentum transfer |
| $z_{om}$ | m | Roughness length of heat transfer |
| *q* | kg $kg^{-1}$ | Specific humidity |
| *w* | m $s^{-1}$ | Vertical wind velocity |
| *d* | m | Zeroplane displacement |
| $r_a$ | m $s^{-1}$ | Aerodynamic resistance |
| $r_s$ | m $s^{-1}$ | Bulk resistance |
| $\gamma$ | kPa $^0C$ | Psychometric constant |
| *NDVI* | - | Normalized difference vegetation index |
| *LAI* | $m^2$ $m^{-2}$ | Leaf area index |
| $K_p$ | - | Pan coefficient |
| $K_c$ | - | Crop coefficient |
| *r* | - | Pearson product-moment correlation coefficient |
| $R^2$ | - | Pearson coefficient of determination |

## Declaration

The material contained in this thesis has not been previously submitted by the candidate for a degree in this or any other University.

## Statement of Copyright

## Acknowledgements

A great number of individuals and institutions have assisted with the research and production of this thesis, for which I am extremely grateful. My foremost thanks go to Jehovah God, whose able hand sustained my health, energy and ability in many times of great difficulties. In this context, I greatly appreciate the support of my young family, especially my beloved wife, Evelyn, whose love, prayers and encouragement have been extraordinary. Also, my gratitude goes to the Elders and members of the Washington Church of Christ (England), particularly Dr. Rodney Thomas and family, for their spiritual support.

I wish to sincerely thank my Ph.D. supervisors, Prof. Tim P. Burt and Dr. Daniel N.M. Donoghue for their invaluable technical advice, research guidance and friendship. My gratitude also goes to many other academic friends and colleagues in Durham University, who are so numerous to mention. But I wish to make special mention of Drs. Charles Owiredu of Ghana, K.M.S. Huda and S.T. Islam of Bangladesh, Nikolaos Galiatsatos of Greece, and Richard Hardy and David Milledge both of England; these men have greatly influenced my research life in Durham.

I also wish to thank: (1) all the staff and students of the Department of Geography (Durham University), especially Mr. Terry Harrison and his IT staff, for their immense technical support; (2) Dr. Stuart Marsh, Head of Geological Remote Sensing of the British Geological Survey and Chair of the UNESCO/IGOS GARS Theme for his personal interest in my research work; and (3) Ms. Theresa McKinven, Senior Tutor of Ustinov College for her generosity towards my family.

Finally, I wish to express sincere gratitude to the following institutions: (1) the CSIR-Water Research Institute and the Ghana Scholarships Secretariat (GOG) for providing my Ph.D. study fellowship; (2) the European Space Agency (ESA) for providing free ENVISAT AATSR research data through the ESA/UNESCO Volta TIGER Project #2992; (3) UNESCO's Groundwater Applications in Remote Sensing (GARS) project for conference funds and knowledge capacity building; (4) NASA for free MODIS data; (5) Ghana Meteorological Services Department (MSD) and the Ghana Hydrology Department of the Ministry of Water, Works and Housing for free hydrometeorological data; (6) the GLOWA-Volta Project for access to their detailed climate data for 2002 and 2004; and (7) Durham Geography for extensive use of their state-of-the-art Remote Sensing/GIS facilities.

# Chapter 1

# Background, Aims and Objectives

## 1.1 Regional Context

This study uses satellite remote sensing to estimate evapotranspiration (*ET*) across the Volta River basin, one of the most drought-prone regions of the world (Figure 1). The study is motivated by several factors, of which the need for spatial data for climate change and hydrological modelling is of utmost importance; hydrological modelling is often constrained by the scarcity of ground observations. This is particularly important in terms of estimating the water balance of the Volta Lake, which is currently under stress because of drought. In Africa, water scarcity is a critical issue and is closely linked with the continent's level of poverty and underdevelopment (World Bank, 2005; Washington *et al.*, 2006). For example, the declining levels of the Volta Lake continue to affect a number of important economic activities, including water supply, energy (hydropower generation), irrigation and lake transport. Because droughts, water scarcity and climate change are hugely interlinked, research on climate change and its impact on the regional hydrology will probably remain an important priority for a long time (Andreini & van de Giesen, 2001; Jung, 2006).

The Volta basin is well known for its savannah grassland ecosystems which are used mainly for subsistence agriculture. Primary production in the region is strongly influenced by a highly variable precipitation regime which, coupled with high temperatures, controls the frequency of droughts. Instrumental records and proxy data for the last two centuries indicate significant fluctuations of precipitation and river discharge

at the decadal time scale (Irizarry-Ortiz *et al.*, 2003), the most recent example being the severe persistent drought in the Sahelian region during the last three decades. This has motivated two important regional studies, the [1]HAPEX-Sahel (Prince *et al.*, 1995; Goutorbe *et al.*, 1997) and GLOWA-Volta (ZEF, 1999; Andreini & van de Giesen, 2001), as well as several other desktop studies (e.g. Irizarry-Ortiz *et al.*, 2003; Wang *et al.*, 2003; Zheng & Eltahir, 1998). These have collectively documented the high sensitivity of West African monsoon rainfall to both large-scale oceanic forcing and local land cover changes.

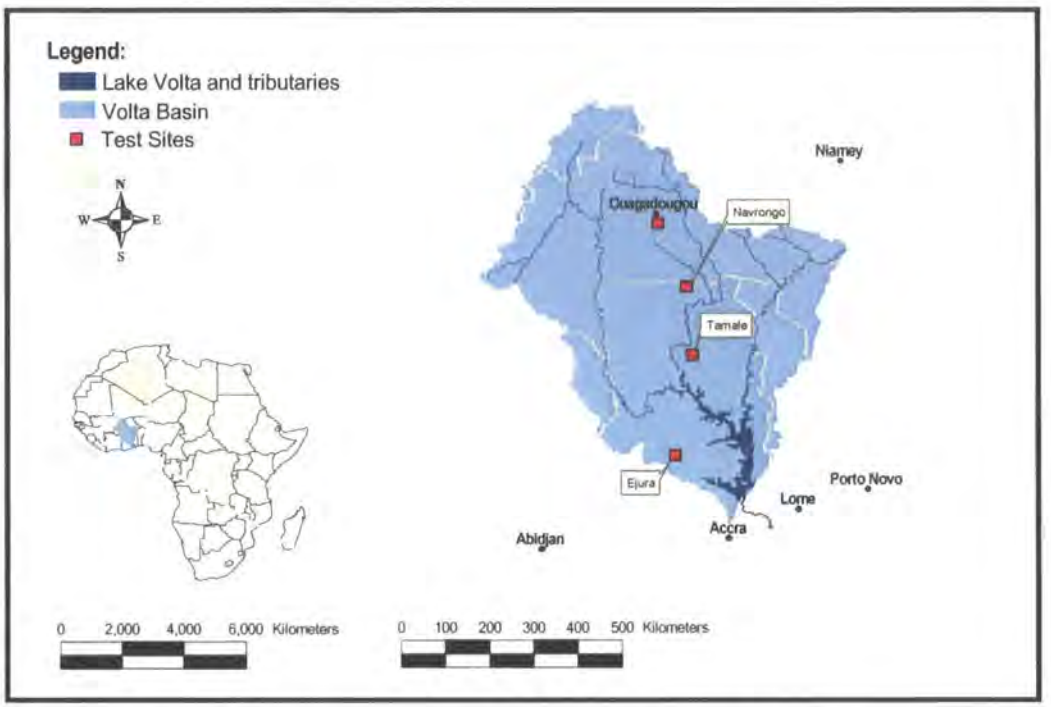


Figure 1.1 Location of the regional Volta River Basin. (Source: [ZEF, 1999])

Wang & Irizarry-Ortiz (2003) demonstrated that vegetation dynamics in West Africa reinforces the effect of drought-inducing forcing, whether it is the large-scale ocean forcing or local land cover degradation. This enhances both the severity and persistence of

[1] HAPEX-Sahel = Hydrological-Atmospheric Pilot Experiment; GLOWA-Volta = Global Change in the Hydrological Cycle

a dry anomaly. In addition to the historical drought occurrence, vegetation dynamics are believed to have contributed to the contrast between the present-day dry climate and the mid-Holocene wet climate in West Africa, enhancing the response of the monsoon circulation to the Earth's orbital forcing (Wang *et al.*, 2003).

Several studies relating land surface processes to water stress in West Africa have modelled the impacts of large-scale land cover changes from arboreal to grassland and then from grassland to desert-type landscapes in the past (Xue & Shukla, 1993, Zheng & Eltahir, 1997). The common conclusion is that vegetation degradation in savannah landscapes causes a significant decrease of precipitation, which suggests that human activities may have contributed to Sahelian droughts of the last half-century. Although these studies are often criticized as being unrealistic for the large magnitude and area of vegetation change modelled, they do suggest that the regional climate is highly sensitive to vegetation change, setting the stage for a new type of studies that emphasizes the role of natural vegetation dynamics (Zeng *et al.*, 1999; Wang & Eltahir, 2000; Wang *et al.*, 2003).

Studies based on the vegetation-change approach consider the two-way feedback between land cover and hydro-climatic responses using models that simulate not only the impact of vegetation changes on climate, but also the response of vegetation to hydro-climatic conditions. One key example is the research by Zeng *et al.* (1999) who used a quasi-equilibrium tropical circulation model coupled with a simple land model to demonstrate interactively the enhancement of vegetation on decadal variability of savannah rainfall. When driven with SST forcing from the 1950 onwards, the model-simulated water stress is comparable with observations, but only if the impact of interactive vegetation is accounted for. Also, using a zonally symmetric atmospheric

model coupled with a dynamic biosphere model driven with SST forcing from 1898 to 1997, Wang and Eltahir (2000) found that vegetation dynamics enhances the low-frequency variability of the Sahel rainfall while, in part, suppressing the high-frequency variability. It was also found that vegetation dynamics reinforce the impact of human activities, which can potentially lead to a transition of the regional climate system from a wet/green metastable equilibrium to a dry/barren one. Such a climate transition takes place in the form of a persistent and severe savannah drought similar to what has been observed. The studies by Wang and Eltahir (2000) further concluded that vegetation is able to provide a long-term memory that carries information about water stress from one year to the next. Even though studies by Zeng *et al.* (1999) and Wang and Eltahir (2000) are useful for their reduced-form climate models and computational efficiency, they can be criticized for being less accurate representations of reality compared with comprehensive general circulation models (GCM).

The uncertainties associated with vegetation-driven GCMs, which were aimed at understanding water stress conditions in West Africa over relatively long periods (e.g. 10-20 years), have been reported by Wang and Eltahir (2000). As a follow up study, Wang *et al.* (2003) investigated the impact of vegetation dynamics on rainfall variability in the area using the coupled atmosphere-biosphere model GENESIS-IBIS, which consists of the GENESIS (Global ENvironmental and Ecological Simulation of Interactive Systems) GCM and the dynamic global vegetation model IBIS. They drew similar conclusions that hydro-climatic anomalies in West Africa depend on mid-latitude disturbances and long-term vegetation deterioration. It was also found that global ocean forcing in the last three decades was favourable for drier-than-normal conditions in West Africa, and the effect of

this drought-inducing forcing is significantly enhanced by vegetation dynamics. Without the impact of vegetation dynamics, water stress would have been much less severe (Wang *et al.*, 2003).

Vegetation dynamics in West Africa is, however, not limited to climatic variability and land use changes at the historical time scale; the Earth's orbital changes are of fundamental importance to both climate variability and its effects on land cover. Soil moisture feedback is also a critical factor; the spatial association between vegetation and soil moisture cannot be easily disconnected (Wang & Irizarry-Ortiz, 2003). Thus, sustained research on the complex interactions between soil, vegetation and atmosphere (SVAT) at various temporal and spatial scales and their relationship with the regional water balance in West Africa remains an issue of great scientific importance. In this regard, key regional experiments such as the HAPEX-Sahel and GLOWA-Volta Project are of particular significance.

### *1.1.1 HAPEX-Sahel*

The HAPEX-Sahel was an international experiment designed to provide field data needed to model the climate of the Sahel (14-20$^0$ N) and its dependence on land surface conditions (Goutorbe *et al.*, 1997; 1994). The HAPEX-Sahel experiment was guided by theoretical knowledge that interaction between the land surface and the atmosphere involves multiple processes and feedbacks, all of which may vary simultaneously (Anderson & Burt, 1985). The value of GCM and mesoscale models to reproduce these interactions, being the main tools for investigating the sensitivity of the climate to changes in surface conditions, has already been stated. The main purpose of the HAPEX-Sahel was

therefore to improve the realism and accuracy of predictions by improving model representation of the Sahelian environment (Goutorbe *et al.*, 1997). This was achieved by a combination of experimental and modelling work with the highest priority being collection of the necessary land surface, atmospheric and remotely sensed data. The data were then used for the development of models and algorithms at scales ranging from one to several hundred kilometres, the grid length at which meteorological models often operate. The project provided greater understanding at a regional scale of the interactive processes of land surface, atmospheric, oceanic forcing and their feedback mechanisms with global processes.

The HAPEX-Sahel was, in fact, part of a twin project – the Global Energy and Water Cycle Experiment (GEWEX) and the International Geosphere-Biosphere Programme (IGBP). It constituted one of a series of large-scale land-surface-atmosphere experiments which took place within the framework of international programmes, among which were: (1) [2]HAPEX-MOBILHY in South-West France (André *et al.*, 1988); (2) FIFE in Kansas, USA (Sellers *et al.*, 1992); and (3) EFEDA in La Mancha, Spain (Bolle *et al.*, 1993). The research structure, content and key findings of the HAPEX-Sahel are well documented as a special edition of *Journal of Hydrology* edited by Goutorbe *et al.* (1997).

[2] HAPEX-MOBILHY = Hydrological-Atmospheric Pilot Experiment, Modélisation du Bilan Hydrique; FIFE = First (International Satellite Land-Surface Climatology Project) Field Experiment; EFEDA = European Field Experiment in Desertification threatened Area

### *1.1.2 GLOWA-Volta*

The GLOWA-Volta project was initiated in 2000 by European scientists and their African counterparts. The principal aim was greater understanding of the physical and socio-economic determinants of the hydrological cycle in the Volta Basin (8-13$^0$N and 2$^0$W-2$^0$E) in the face of global change (van de Giesen *et al.*, 2002; Andreini & van de Giesen, 2001; ZEF, 1999; http://www.glowa-volta.de). The project was designed with the objective of establishing a scientifically sound Decision Support System (DSS) for water resources management. The 9-year project is still underway. It is being implemented and co-ordinated by the Centre for Development Research (ZEF), University of Bonn, Germany. GLOWA-Volta is part of a larger Global Change in the Hydrological Cycle (GLOWA) Program financed by the German Federal Ministry for Education and Research, with additional funding from the Ministry of Science and Research of North Rhine-Westphalia.

The GLOWA-Volta research continues to focus on the modelling of the major processes that affect water supply and demand. Its strength lies in the integrated nature of the model, in which social and environmental processes are directly coupled. Eventually, the model expects to drive the DSS, which through policy analysis will provide decision makers with quantified information on the impact of different water management strategies (van de Giesen *et al.*, 2002). The current research achievements of the GLOWA-Volta Project are sufficiently documented as part of ZEF's technical publications - "Ecology and Development Series" which are edited by Vlek *et al.* (2004). A large publication list is also available on their website – http://www.glowa-volta.de

## 1.2 Local Context

The variability of Sahelian climate has notable consequences for savannah landscapes, such as the Volta basin (8-13$^0$ N), as noted in the preceding section. Numerous studies (e.g. Section 1.1.1) have reported important effects of land surface change in this area: e.g. vegetation effects on soil wetness (Kumar *et al.*, 2002); rainfall-runoff modelling using local climate data (Gyau-Boakye & Timbulto, 2000); rainfall-runoff variability (Opoku-Ankomah & Amisigo, 1998); and climate variability in sub-humid West Africa (Paturel *et al.* 1997). An important factor underlying these findings is related to the complex interrelationships between land use and land cover changes (e.g. increased regional population translating into competition in land use) and climatic change impacts.

Most of the above studies have shown that rainfall in savannah West Africa has declined since 1970; however, the magnitude of decline may not be as large as the reduction in river discharge (Figure 1.2). Whereas annual rainfall is believed to have declined by about 16% in the last half-century (Opoku-Ankomah & Amisigo, 1998), discharges from two major catchments in the Volta basin in Ghana (Saboba and Nawuni) have reduced by about 32.5% and 23.1%, respectively (Gyau-Boakye & Timbulto, 2000). Paturel *et al.* (1997) have also demonstrated that land surface deterioration (i.e. soil and vegetation) has significantly contributed to approximately 0.5$^0$C rise in temperature between 1945 and 1993 (48 years). This has consequently increased the potential of surrounding air to hold water vapour by approximately 5-6%, thus increasing regional evapotranspiration losses (Gyau-Boakye & Timbulto, 2000; Rosenberg *et al.*, 1990). The

overall effect is, for instance, a decline in lake levels at the Akosombo dam site (downstream in Ghana) leading to periodic countrywide (hydroelectric) power rationing.

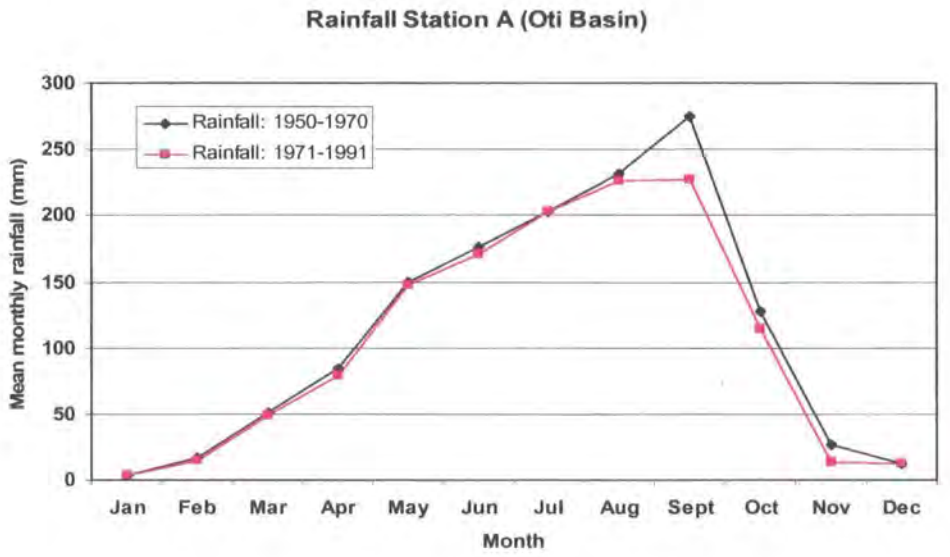


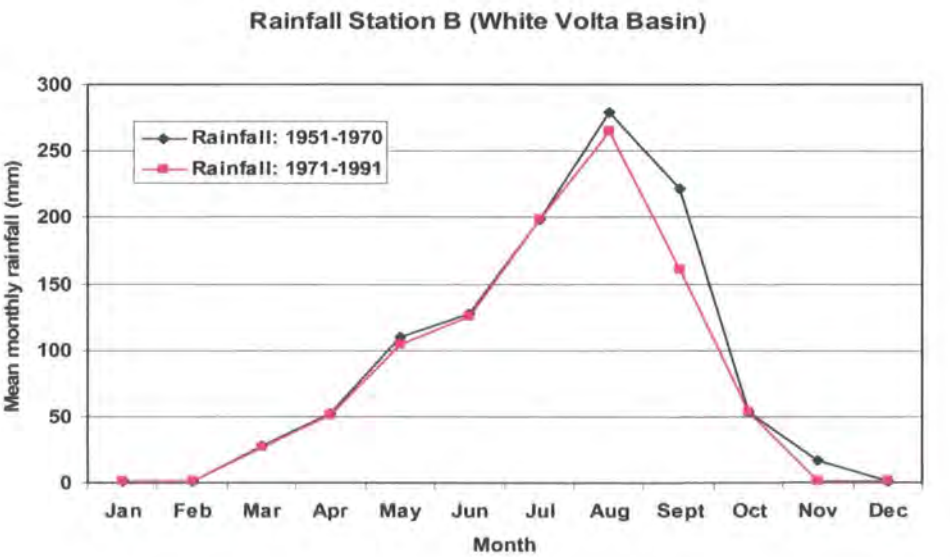


Figure 1.2a

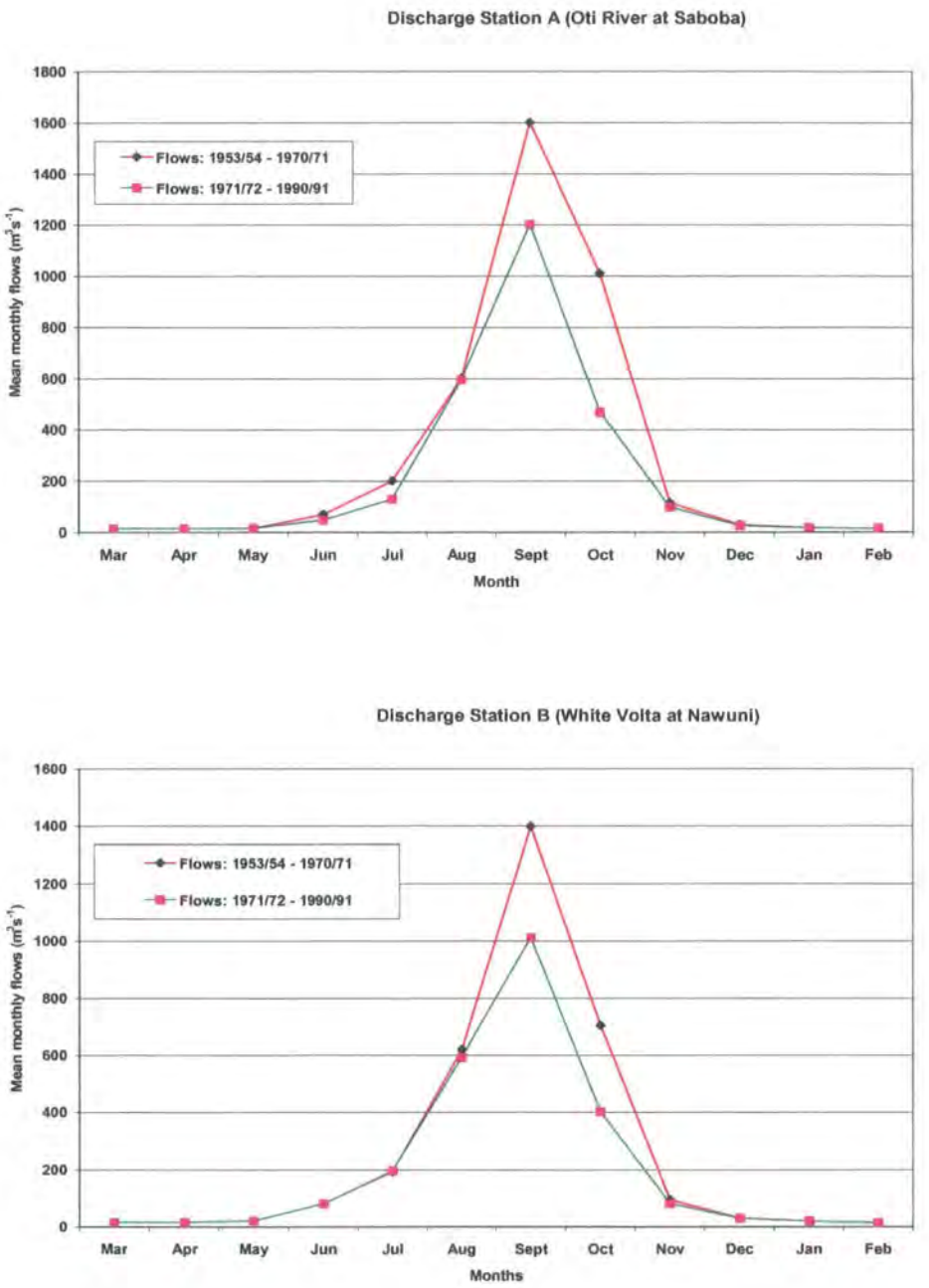


Figure 1.2b

Figure 1.2a Rainfall variation in the Oti (Station A) and White Volta (Station B) basins. Figure 1.2b Streamflow variation from similar catchments in the above basins. On an annual basis, rainfall has declined by about 16% for the most recent period, but discharges have reduced by about 32% and 23% for the Oti and White Volta basins respectively. Sources: Opoku-Ankomah & Amisigo (1998); Gyau-Boakye & Timbulto (2000).

Most studies concerning the Volta landscape have not been very successful in modelling key factors that control water availability in the Volta basin for a number of important reasons. First of all, there is lack of understanding about the spatial distribution of thermal energy and water fluxes, which are key factors in the water balance. The estimation of the energy balance variables such as surface temperature ($T_s$) directly affects the prediction of evapotranspiration (*ET*), which is a critical determinant of water availability in tropical catchments. *ET* is often considered as the residual term of the water balance equation (Anderson & Burt, 1985). To date, accurate measurement or prediction of *ET* at the regional scale remains a huge challenge mainly because a large number of intermediate parameters (climate, vegetation, etc.) need to be derived first, which is a particular problem where spatially-derived ground data are unavailable. In the savannah region, detailed characterisation of vegetation cover and how this controls *ET* processes is a critical issue because the region covers a very large area and the vegetation cover is extremely heterogeneous. Apart from this, there is poor understanding of *ET* dynamics and other ground conditions including soil moisture status, groundwater recharge, plant moisture-uptake and their overall feedback with seasonal and inter-annual rainfall fluctuation. This deficiency is understandable given that previous research has either focussed attention on the local scale (mainly using highly spatially variable hydro-meteorological measurement records) or applied statistical interpolation and linear regression methods mainly because of lack of sufficient and accurate ground data.

Given the huge increase in computer power, advances in spatial hydrological modelling and development of comprehensive analytical tools e.g. GIS-based geo-statistical tools, current hydrological research need not be limited to records from sparsely

distributed point measurements. In particular, recent advances in Earth observation based on satellite technology makes it unnecessary for hydrological research to be constrained by scarcity of spatially distributed land surface and atmospheric data (Cruise & Miller, 2003).

This is the area where this research has sought to make a contribution by retrieving land surface variables from remotely sensed data and to use such data for predicting *ET* at the regional scale in order to help our understanding of water losses in the Volta basin. The approach seeks to improve the previous "traditional" methods in three ways. Firstly, spatially-derived parameters are generated without needing to rely on scarce ground observations. Secondly, vegetation cover is classified over very wide areas, which would be impossible to achieve via field measurement programmes. Thirdly, the current approach helps to overcome the burden of extensive fieldwork, cost, and heavy deployment of field instruments.

## 1.3 Research Questions, Aim & Objectives

### 1.3.1 Research Questions

Figure 1.1 shows that rainfall and river discharge have both declined in the savannah Volta basin. However, the reduction in discharge cannot be fully explained by the reduction in rainfall, which means that research into *ET* within the region must be a priority. To this end, the review of previous research in the Volta basin has generated the research questions below.

1. To what extent can a spatial knowledge of *ET* help to predict the availability of water in the Volta basin?

2. Given the scarcity of ground data, are there suitable satellite sensors which can provide reasonable estimates of *ET* and related energy and water balance parameters at the regional-scale?
3. Can the spatial estimates of *ET* derived from one be validated using independent data (including different satellite-based predictions)?
4. Can the spatial estimates of *ET* be used as inputs for new-generation hydrological models needed for the prediction of un-gauged catchments upstream the Volta Lake?

### 1.3.2 Aim of the Research

The aim of the research is to use remote sensing methods as a means of providing some of the key data inputs (e.g. DEM, *ET*, land cover, etc.) for hydrological models. Existing hydrological models are used as a platform for predicting the water balance of the Volta River basin.

### 1.3.3 Objectives

In order to address the research aim, the following objectives are proposed:

1. To investigate whether the spatial dynamics of *ET* are a major limitation to water availability in the savannah Volta basin and to assess the advantages of satellite-based methods (e.g. [3]SEBAL algorithm) for spatial *ET* modelling.
2. To assess whether the coarse-scale (1 km) MODIS and AATSR sensors are useful sources of spatial data for *ET* modelling in this context.

[3] SEBAL = Surface Energy BAlance for Land algorithm

3. To apply the NASA's SRTM DEM for the delineation of savannah catchments needed as "substrate" for *ET* and hydrological modelling.
4. To apply ASTER and Landsat ETM+ data as sources of detailed information for: (1) guiding fieldwork and image classification; and (2) land cover mapping and validation of spatial estimates of energy and water balance parameters.
5. To validate the spatial estimates of *ET* using a variety of data sources: (1) published data; (2) scintillometer (eddy correlation) observations; (3) Landsat ETM+ data; and (4) local-scale Penman-Monteith estimates.
6. To demonstrate how spatially derived *ET* data may first be verified using sensitivity experiments and subsequently used as inputs to new-generation hydrological models (e.g. the modified Pitman model) for predicting ungauged catchments upstream the Volta Lake.

## 1.4 Plan of the Research Methodology

Chapter 2 of the thesis provides a detailed description of the Volta as a study area including its regional geography, hydro-climatology and socio-economic conditions. Chapter 3 presents a detailed description of remote sensing data which may be used to address the scarcity of ground observations. The 1 km MODIS and AATSR sensors are used to provide regional estimates of albedo ($\alpha$), vegetation density (NDVI) and surface temperature ($T_s$) as key input parameters for *ET* models. Compared to previous sensors such as the AVHRR, the well-defined bands of the above sensors are capable of mapping vegetation properties and $T_s$ with much greater precision. With respect to MODIS, the data can also be provided at a much higher temporal frequency of 1 to 2 days (Brata et al.,

2006; Parks *et al.*, 2005; Sòria & Sobrino, 2005). For regional studies, the MODIS and AATSR sensors are particularly suitable given their capabilities to cover the entire Volta basin from a single image. Also, most of MODIS raw data are freely available and a variety of hydrology-based products can be easily derived from its 36 multi-spectral channels. Additionally, the SRTM DEM (see Section 3.3.1) has been selected to help delineate catchment boundaries, which solves two fundamental problems: (1) it overcomes the scarcity of digital topographic information in the study area; and (2) the new DEM may not only be used as "substrate" for *ET* modelling, but also in relevant hydrological models. Similarly, the ASTER and Landsat ETM+ imagery have chosen, respectively, to derive: (1) ground truth information to guide fieldwork and image classification; and (2) land cover and *ET* maps as sources of validation for the coarse-scale MODIS and AATSR data.

Chapter 4 describes methods for local-scale *ET* modelling using a variety of approaches for example, the Penman-Monteith, Thornthwaite and Grindley methods and parameterized by limited ground data. The chapter highlights the limitations of extrapolating results from the Tamale district to the entire basin, emphasising the need for remote sensing methods. In Chapter 5, the application of satellite data to parameterize the Surface Energy Balance Algorithm for Land (SEBAL) is described. The adoption of the SEBAL algorithm is motivated by its record as one of the most accurate methods for spatial *ET* modelling over heterogeneous landscapes (Mekonnen, 2005; Bastiannssen *et al.*, 1998). Although SEBAL is a public-domain algorithm, there are problems associated with its application; in particular, it is hard to find clearly written codes in peer-reviewed literature. Nor is it clear how the SEBAL algorithm can be used for extracting information from time series data. To overcome this, Chapter 6 describes operational methods for

running the SEBAL algorithm using an integrated MATLAB-GIS approach. This provides a useful link between the physics of the algorithm (Chapter 5) and the derivation of spatial *ET* models in Chapter 7. Chapter 8 concludes the research methodology; it describes a conceptual approach in the application of derived *ET* estimates as an input for hydrological models. Chapter 9 ends the thesis with an evaluation of the research objectives, a discussion on the limitations of the energy and water balance modelling approach and recommendations for further research.

# Chapter 2

# Study Area

## 2.1 The Savannah Volta Basin

### 2.1.1 Geographical Location

The Volta basin is located between latitudes 5-14$^0$ 30$'$ N and longitudes 5$^0$ 30$'$ W and 2$^0$ E (see Figure 1.1). The northern half (~ lat. 12-14$^0$ N) is semi-circular with an approximate diameter of 400 km which covers the Sahelian zone in Burkina Faso. The middle part (lat. 8–12$^0$N) forms a trapezium in Ghana. The base is triangular in shape and tapers narrowly into the Gulf of Guinea.

The term "Volta" comes from a Portuguese word which means "*meander*". This aptly describes the long (~1,850 km) curvy sinuous nature of the Volta River system. The basin covers an approximate surface area of 398,390 km$^2$ encompassing six West African countries (i.e. Benin, Burkina Faso, Côte d'Ivoire, Ghana, Mali and Togo; Table 2.1).

Table 2.1 Partition of the Volta basin among the riparian countries

| Country | Main River System | Estimated Area of Basin (km$^2$) | Upstream Riparian Countries | Average Annual Rainfall (mm) | Average Annual Evaporation (mm) |
|---|---|---|---|---|---|
| Mali | Sourou | 12,430 | Nil | 685 | 3,015 |
| Burkina Faso | White Volta | 171,105 | Mali | 950 | 2,130 |
| Côte d'Ivoire | Black Volta | 9,890 | Burkina Faso, Mali | 1,358 | 1,486 |
| Togo | Oti | 25,545 | Burkina Faso, Mali | 1,305 | 1,697 |
| Benin | Oti | 13,500 | Burkina Faso, Togo | 1,294 | 1,400 |
| Ghana | Volta (Proper) | 165,830 | Burkina Faso, Mali, Togo, Côte d'Ivoire, Benin | 1,320 | 1,415 |

Source: ORSTOM (1977); AGRHYMET (1998)

As noted in Chapter 1, the above countries depend on the Volta basin for sustenance including housing, water, food and energy (hydropower) supply, and lake transport. Table 2.2 describes important physical characteristics of the basin.

Table 2.2 General hydro-physical characteristics of the Volta basin

| Characteristic | Black Volta | White Volta | Oti | Lower Volta |
|---|---|---|---|---|
| Minimum altitude at MSL (m) | 60 | 60 | 40 | 1 |
| Maximum altitude at MSL (m) | 762 | 530 | 920 | 972 |
| Mean Sea Level (MSL) | 284 | 285 | 218 | 256 |
| Surface Area ($km^2$) | 145,750 | 111,270 | 80,070 | 398,390 |
| Average length of river (km) | 1,851 | 1,624 | 1,240 | 200 |

Source: ORSTOM (1977); AGRHYMET (1998)

The Kalarakun catchment (shown as Landsat ETM+ image in Figure 2.1) was selected as the study area. The choice of this catchment is important for scientific and practical reasons. As a major catchment of the White Volta basin, hydrology and micro-climatic parameters in the area such as stream flow and rainfall is believed to be declining over the last 50 years (Gyau-Boakye & Timbulto [2000]; see Figure 1.2). At the same time, temperature seems to be increasing as illustrated later in Figure 2.9. Since the area has not been previously researched, yet very well represents the Guinea savannah landscapes of the Volta, it readily presents a good scientific test site.


Figure 2.1 Location of the Kalarakun catchment area (5,311 km$^2$). The bottom inset is a false colour composite Landsat ETM+ image of 05/01/2004. Red-Green-Blue colours represent ETM bands 4, 3, 2. The study area encompasses parts of the Tamale, Yendi and Salaga districts.

The Kalarakun catchment encompasses Tamale, the largest town in northern Ghana with a population of about 220,000 (GSS, 2002). As capital of the Northern Region, Tamale houses the major public and private land surface data generation and archiving institutions, e.g. Meteorological and Hydrological Services Departments, Survey Department and the Environmental Protection Agency. Additionally, several other institutions have regional offices in Tamale whose activities relate to generation and storage of land and water data (e.g. Ghana Water Company, Community Water and Sanitation Agency, NGOs, UNICEF, WHO and USAID).

These institutions are vital sources for research data. Furthermore, the study area is reasonably accessible via tarred and paved feeder road networks leading to and from Tamale (e.g. Tolon-Kumbungu, Yendi and Salaga districts). Finally, the fieldwork was facilitated by taking advantage of the technical, laboratory and equipment support from the Tamale-based University of Development Studies and two research institutions of the Council for Scientific and Industrial Research (CSIR) – the Savannah Agricultural Research Institute and the Water Research Institute.

### 2.1.2 Climate

The movement of the Inter-Tropical Convergence Zone (ITCZ) influences the climate of West Africa. This zone is an area of low pressure that forms where the Northeast Trade Winds meet the Southeast Trade Winds near the Earth's equator. As these winds converge, moist air is forced upward. This causes water vapour to condense, as the air cools and rises, resulting in a band of heavy precipitation around the globe. This band moves seasonally, always being drawn towards the area of most intense solar heating, or warmest surface temperatures. It moves towards the Southern Hemisphere from September through February and reverses direction in preparation for Northern Hemisphere Summer that occurs in the middle of the calendar year (http://www.climate-zone.com).

As a result, West Africa is characterised by hot, dry and dusty *"Harmattan"* winds from high-pressure cells (anticyclones) of the Azores that meet cold moist *"Monsoon"* winds from the south Atlantic anticyclones. The timing, intensity and duration of the ITCZ over an area determine the amount and duration of rainfall (Nicholson & Grist, 2001; Hastenrath, 2000). Rainfall is heaviest (~2500mm) in the

forested humid south, decreasing generally northwards along the latitudinal gradient. Table 2.3 describes the general climatic conditions of West Africa.

Table 2.3 Climatic conditions of West Africa

| Rainfall station | Geographical location | | Country | Ecological zone | Mean annual rainfall (mm) | Mean annual evapotranspiration (mm) | Mean annual temp. ($^0$C) | Period of climate records |
|---|---|---|---|---|---|---|---|---|
| | Lat. | Lon. | | | | | | |
| Niamey | 13$^0$ 48'N | 2$^0$ 16'W | Niger | Sahel savannah | 560 | 2000 | 36.0 | 1905-1989 |
| Koro | 12$^0$ 46'N | 7$^0$ 49'W | Mali | Sahel savannah | 522 | 2041 | 36.8 | 1971-1990 |
| Bobo Dioulasso | 11$^0$ 16'N | 4$^0$ 31'W | Burkina Faso | Sudan savannah | 759 | 1958 | 31.5 | 1971-2000 |
| Tamale | 9$^0$ 25'N | 0$^0$ 50'W | Ghana | Guinea savannah | 1087 | 1650 | 28.2 | 1961-2000 |
| Axim | 5$^0$ 9'N | 2$^0$ 57'W | Ghana | Forest | 2148 | 1315 | 25.8 | 1961-2000 |

Source: Modified after Prince *et al.* (1995); http://www.climate-zone.com/

Table 2.3 also illustrates the trend of regional evapotranspiration (*ET*). ET increases from lower to higher latitudes, varying directly with temperature and inversely with vegetation biomass. Gyau-Boakye & Timbulto (2000) have shown, for instance, that progression from Guinea to Sudan savannah landscapes increases surface temperature by about 1-3$^0$C, elevating evapotranspiration as a result. The hydrology and land surface change dynamics in response to microclimatic conditions of the study area has been detailed in Chapter 4.

### 2.1.3 Geomorphology, Relief and Drainage

The relief of West Africa is generally low with the exception of few high altitudes such as the Jos plateau in Central Nigeria (~1580m). In Ghana, the Akwapim-Togo mountain ranges constitute the highest relief (920m). The Kwahu plateau (450m) located in the mid-western section of the country separates the lower

Volta basin from the rest of the country. This forms an extensive gorge, which now accommodates the Volta Lake. Most of the well-developed alluvial flood plains and terraces of the Volta River are currently under the lake. The plains are normally 8-13m high and the terraces are about 20-25m above the riverbed (Adu, 1995). The northern savannah landscapes are characterised by low-lying plains (~150m) with broad valleys (see Figure 2.2). The plains are however, often interspersed with undulating hills and a few inselbergs (Adu, 1995).

West Africa is drained by three main transboundary river systems - the Niger, Senegal and Volta. The preponderance of the plateau relief has marked effects on regional drainage. Thus, unlike East African river systems, those in West African flow from fairly low plateaux and sluggishly pass over long distances, forming swamps and wide flood plains along their paths from where they discharge into the Gulf of Guinea (Ayibotele, 1993). Along the Volta channel several small swamps result, serving as important regulating reservoirs. Lake Volta (~8,500 $km^2$) developed from the Volta River (see Figure 1.1), forms a massive inland drainage and flow regulating system, whose detailed hydrological conditions is central to this research and constitutes the main objective of Chapter 4.

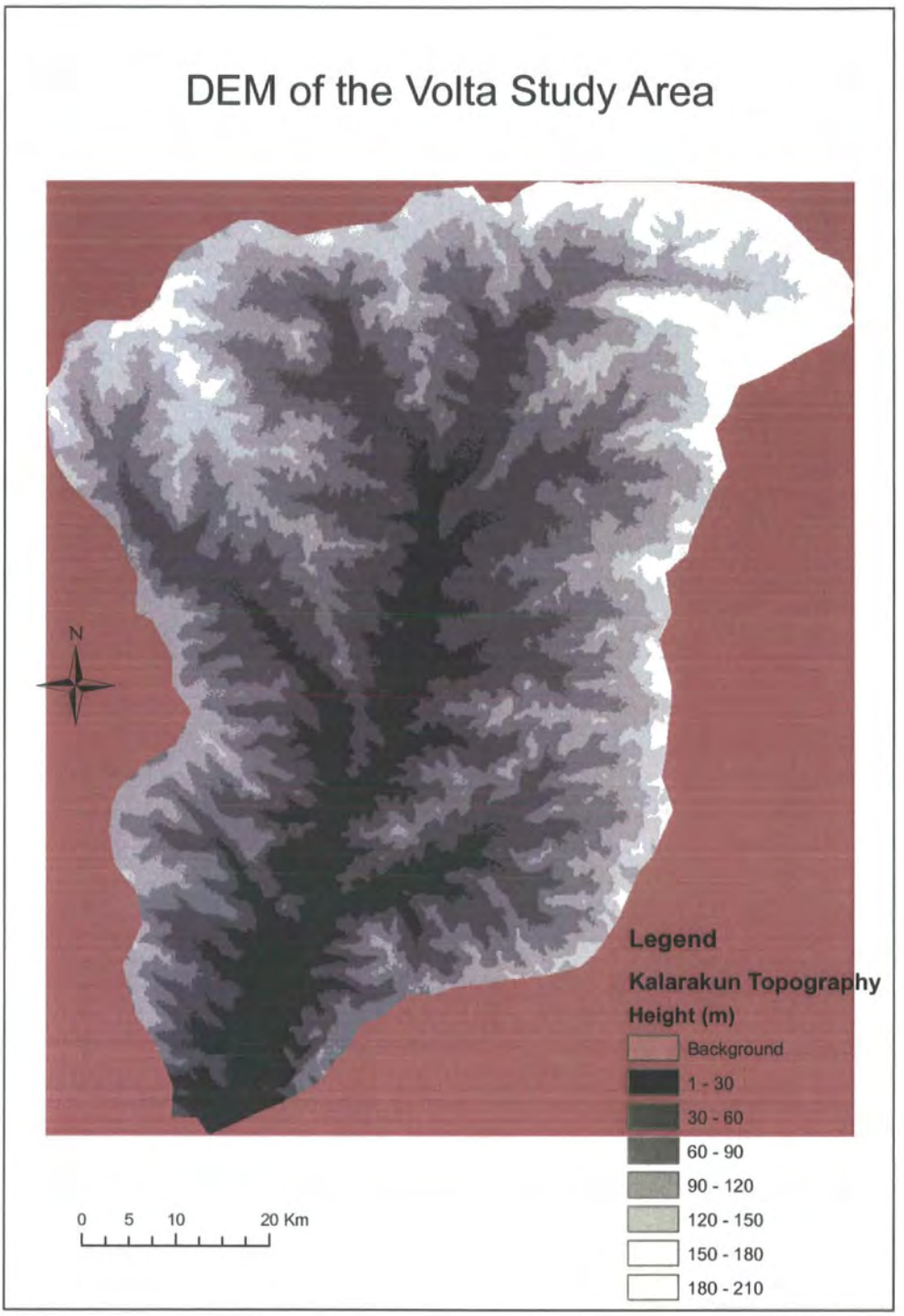


Figure 2.2 Digital elevation model (DEM) of the Kalarakun catchment. This represents the topography of Guinea savannah catchments of the White Volta basin. Most of the areas are below 200m except the north-eastern hills of the Gamgaba scarp (not shown here).

### 2.1.4 Geology

The African pedestal with its granites and all the cortege of metamorphic rocks is of the Precambrian age over $3.0x10^9$ years old (Kesse, 1985). The rocks can be grouped under lower, middle and upper Precambrian rocks.

The primary materials that underlie the Volta basin are mainly Cambrian, Silurian and Ordovician. Local geologists describe the above in terms of predominant rock chains, chiefly the Voltaian, Dahomeyan, Tarkwaian, Atacorian and Birimian. The Dahomeyan best describes the granite-gneissic bands of the south-eastern zone of Ghana (Figure 2.3) stretching as far as Togo. The Atacorian chain stretches over 1000 km from Accra (Ghana) to Western Nigeria. The Atacorian and Birimian (middle Precambrian) are also well-defined in western Côte d'Ivoire. The term "Atacorian" is mostly used in Benin but also makes reference to the "Akwapim ranges" in Ghana and "Togo series" in Togo. The lower Birimian, with its schists and quartizes occupy an immense portion of the Volta basin underlying over approximately 17% of Ghana. The study area (see inset of Figure 2.3) is covered by the Voltaian sedimentary sandstone, covering nearly 43% of Ghana (Kesse, 1985). According to this report, the rocks are essentially flat-bedded and are un-deformed by orogenic movements, except the eastern and southern margins of the Volta gorge. Unlike the Birimian chain, they lack mineral deposits of economic value.

The Volta geology is mainly valued in terms of its shallow aquifers. The contribution of groundwater recharge (which remains a research gap) is of great interest for understanding the hydrology of the Volta basin. Bates (1962) has suggested that water supply in the White Volta basin is very well related to the underlying rock, vegetation and land management. This report further suggests that

the ground cover and soil texture are more important recharge factors than rainfall amount, as these tend to influence the amount of water that can percolate into the underlying rock. The central Voltaian formation (e.g. Atebubu, Salaga, Nasia and Tamale) are underlain by shale with few sandstone patches in the Tamale district (Kesse, 1985). However, there is also widespread occurrence of shallow soils underlain by ≥30cm of lateritic hardpan, beneath which water percolation is practically zero (Agyare, 2004).

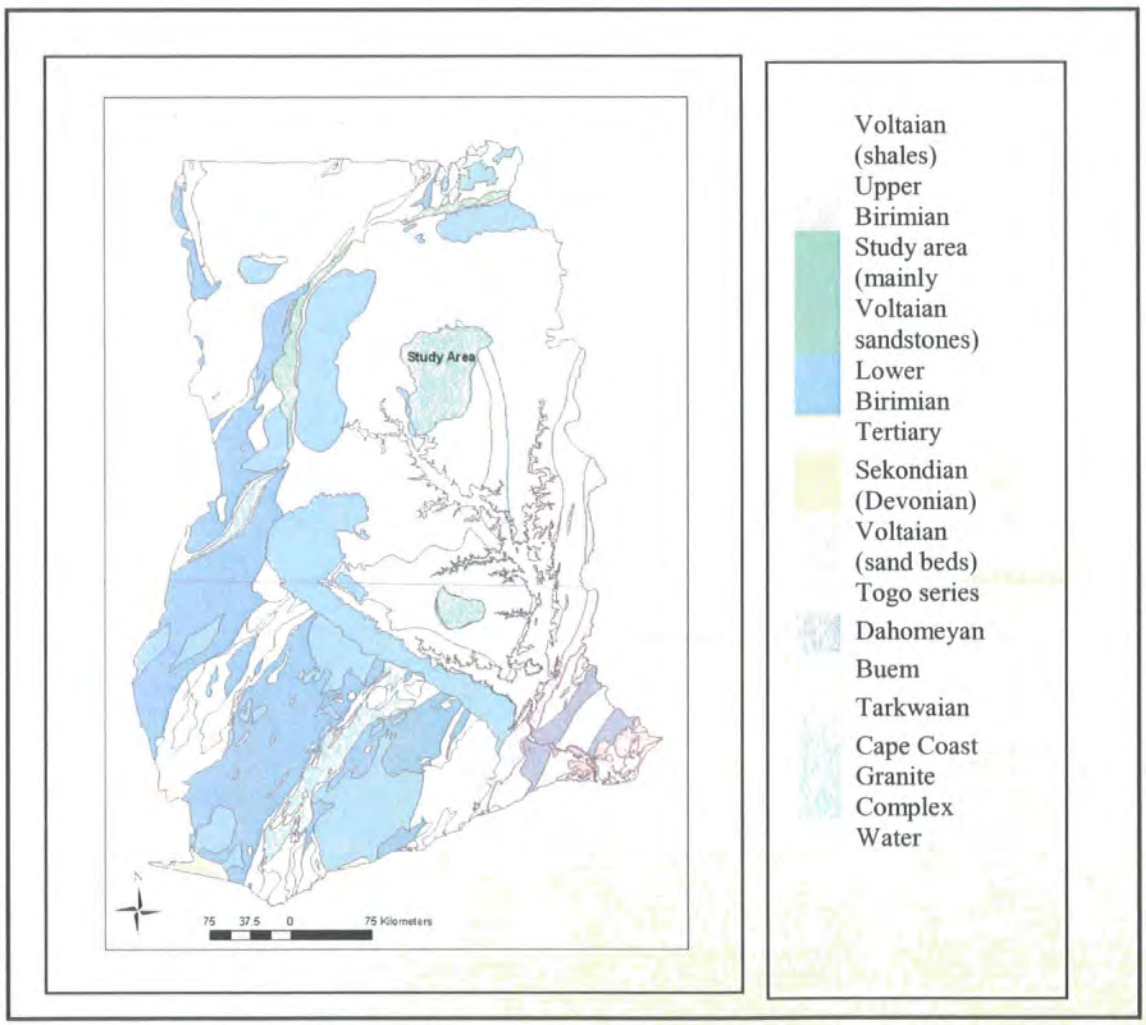


Figure 2.3 Geology map of Ghana. (Source: Modified after Geological Survey Department, Ghana)

### 2.1.5 Soils

The soils of West Africa are marked by extensive areas of deep weathering on old, geologically stable shields and by smaller occurrences of younger residual materials. These are often exposed because of erosion and deposition processes, and mixtures with colluvial, alluvial and other rejuvenated deposits from volcanic action (Kesse, 1985).

In the Volta basin, the characteristic soils of the wetter areas are red and yellow in colour, old and strongly leached. The most dominant soil groupings are Lixosols, Leptosols, Plinthosols, Acrisols and Luvisols (Figure 2.4). These are largely formed from the Voltaian sediments and vary widely in terms of soil texture and productivity. Their fertility is generally low in comparison with granite-derived soils (Adu, 1995). Different hydrological conditions along the slopes have led to the development of different soils from upland to lowland, resulting in various associations (e.g. Kpelesawgu-Changnalili-Lima series located in northern Ghana) (Adu, 1995).

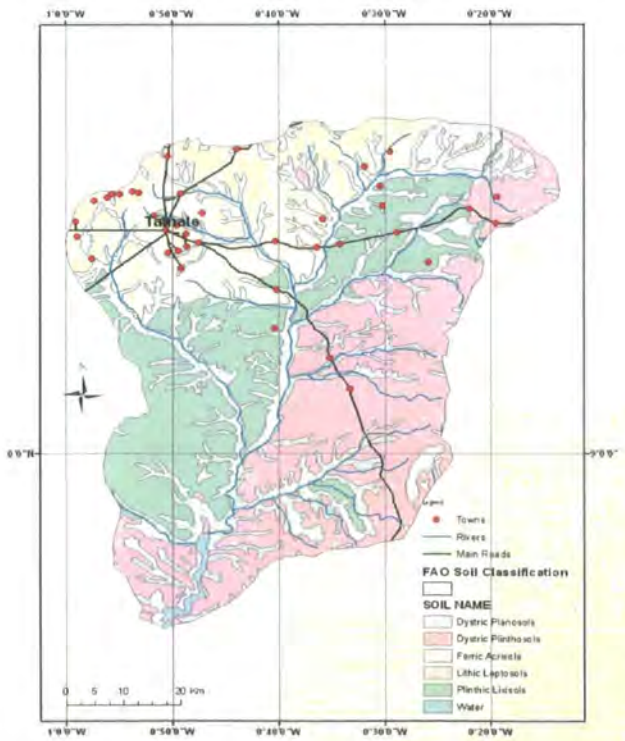


Figure 2.4 Soil map of the Kalarakun catchment area (Modified after: Soil Research Institute (2004))

In the Volta basin, concretionary and shallow iron-pans occur widely making the soils quite unsuitable for cultivation and vulnerable to erosion (Asiamah, 2002). These are especially widespread in the upper slopes in the Tamale district (Agyare, 2004). The soils' low aggregate stability status is a notable geophysical property (e.g. Hauffe, 1989; Adu, 1995; Agyare, 2004). The soils are limited by unfavourable pore size distribution, low infiltration rate and high susceptibility to surface sealing by rain water. Table 2.4 presents summary statistics of soil physical properties of the area.

Table 2.4 Soil physical characteristics of Tamale (Volta basin)

| Parameter | Soil level | Minimum | Maximum | Mean | Standard deviation | Coeffici ent of variation (%) | Skew-ness | Kurtosis |
|---|---|---|---|---|---|---|---|---|
| Sand (%) | Topsoil | 23.0 | 83.6 | 55.8 | 12.9 | 23.1 | 0.03 | -0.73 |
| | Subsoil | 17.9 | 79.6 | 43.8 | 13.6 | 31.1 | 0.18 | -0.55 |
| Clay (%) | Topsoil | 0.36 | 37.6 | 7.05 | 5.50 | 78.0 | 2.16 | 6.78 |
| | Subsoil | 3.12 | 53.1 | 22.9 | 12.2 | 53.3 | 0.69 | -0.26 |
| Silt (%) | Topsoil | 7.76 | 60.4 | 37.1 | 10.8 | 29.1 | -0.17 | -0.66 |
| | Subsoil | 13.6 | 60.3 | 33.3 | 8.08 | 24.2 | 0.29 | 0.45 |
| Carbon | Topsoil | 0.04 | 1.37 | 0.46 | 0.26 | 55.5 | 0.91 | 0.59 |
| (%) | Subsoil | 0.05 | 1.09 | 0.38 | 0.19 | 50.4 | 1.01 | 1.10 |
| CEC | Topsoil | 0.54 | 6.24 | 2.17 | 1.21 | 55.8 | 1.18 | 0.77 |
| (cmol (+)$kg^{-1}$) | Subsoil | 0.40 | 6.39 | 2.55 | 1.40 | 55.1 | 0.81 | -0.25 |
| pH | Topsoil | 3./73 | 7.34 | 4.87 | 0.51 | 10.5 | 0.88 | 2.22 |
| | Subsoil | 3.71 | 7.22 | 4.60 | 0.57 | 12.3 | 1.69 | 4.32 |
| $K_s$ | Topsoil | 0.02 | 17.3 | 2.20 | 2.81 | 128 | 2.65 | 8.49 |
| ($cmh^{-1}$) | Subsoil | 0.01 | 13.9 | 1.41 | 2.16 | 153 | 2.93 | 10.6 |
| Bulk | Topsoil | 1.15 | 1.86 | 1.49 | 0.13 | 8.8 | 0.46 | 0.62 |
| density | Subsoil | 1.10 | 1.93 | 1.50 | 0.11 | 7.3 | 0.03 | 2.25 |

Source: Agyare (2004)

## 2.1.6 Vegetation & Land Use

West Africa encompasses six main ecological landscapes, namely coastal savannah, forest belt, derived savannah, Guinea savannah, Sudan savannah and Sahel savannah (north-eastern tip of Burkina Faso and Mali). The contribution of

tropical savannah to global carbon circulation and its feedback relationships with climate and hydrology have been described in Chapter 1. Indeed, vegetation dynamics in the region are a function of climate seasonality, land use, soil moisture and socio-economic conditions. The functional relationship between rainfall and biomass volume and how that reduces along latitudinal gradient from south to north has been noted in Chapter 1. Sudan and Sahel vegetation, for instance, is scantier than Guinea savannah, which also has much lesser biomass in comparison with forests closer to the Gulf coast.

Sudano-sahelian vegetation is characteristically short grass species. The areas are intensively exploited for agriculture and livestock grazing leading to massive land degradation. Drought-resistant grain crops (e.g. millet, sorghum, etc.) are cultivated to meet subsistent needs. The Sourou (White and Red Volta) basin in northern Burkina Faso and southern Mali is a typical example. The northern part of the coastal countries (Ghana, Togo, Benin and Côte d'Ivoire) fall within the Sudan and Guinea savannah zones. Here, dense bushes with scattered trees exist across most of the area. Agriculture is the mainstay of the rural population often leading to land degradation and soil erosion. As a result, fire resistant medium-to-tall grasses (e.g. *Panicum maximum, Imperata cylindrica, etc.*) proliferate in areas of minimum soil moisture.

Vegetation cover in the lower Volta basin is considerably denser with natural woodlands interspersed with various tropical grass species. In the more protected areas (e.g. forest reserves), tall broad-leaved tree species exist and contribute substantially to biodiversity and catchment hydrology. Figure 2.5 reveals the evolution of vegetation cover in response to rainfall, soil moisture and land use in the area.


Figure 2.5 Evolution of vegetation cover in response to rainfall, soil moisture and land use in the Volta basin (Dates of photographs (a-d) are shown above. October ends the wet season. Drought commences in November reaching a peak in January, when natural and artificial burning for game and fresh grazing pastures is severe).

The rainfall season ends in October at which time soil moisture supports a dense vegetative cover. Figure 2.5 illustrates how this rapidly changes in 4-8 weeks. The occurrence of drought is severe from November-February, usually reaching a peak in January when land surface temperature can reach 40-45$^0$C. This fuels natural and artificial burning leading to increased soil evaporation and vegetation water stress. The reasons for artificial burning are variable and numerous. The most important ones are: (1) easy extraction of fuel wood; (2) game hunting; (3) regeneration of fresh pasture grasses; (4) easy soil tillage (for the next growing

season); (5) establishment of new farm villages; and (6) vandalism arising from tribal and ethnic tensions.

### 2.1.7 Socio-economic Conditions

West Africa is well endowed with human and natural resources, yet it remains one of the poorest regions of the world. There are several reasons for this, the most important being extremely slow economic growth rate as direct consequence of ethnic and political instability, and debilitating climatic conditions. These are strongly related to other extraneous issues such as high population growth rate and illiteracy, poor industrial and production technology, and widespread corruption at various social, political and administrative levels. Table 2.5 describes the economic conditions of the Volta riparian countries.

Table 2.5 Socio-economic indicators of Volta riparian countries as at 1995

| Country | Area ($km^2$) | Population ($10^{-6}$) | Annual growth rate (%) | Life expect-ancy | Annual per capita GDP (US$) | Sector share in total GDP (%) | | | | | Adult literacy rate (%) |
|---|---|---|---|---|---|---|---|---|---|---|---|
| | | | | | | I | Mg | Mn | A | S | |
| Benin | 112,622 | 5.6 | 3.1 | 47.6 | 354 | 14 | 4 | - | 46 | 39 | 37.0 |
| Burkina Faso | 274,200 | 10.2 | 3.6 | 47.4 | 258 | 25 | 15 | 3 | 38 | 38 | 19.2 |
| Côte d'Ivoire | 322,462 | 14.2 | 2.7 | 51.0 | 740 | 25 | 16 | - | 36 | 39 | 40.1 |
| Ghana | 238,537 | 16.4 | 2.6 | 56.0 | 407 | 16 | 8 | 2 | 51 | 33 | 65.0 |
| Mali | 1,240,192 | 10.8 | 3.3 | 46.0 | 235 | 12 | 6 | - | 54 | 35 | 31.0 |
| Togo | 56,785 | 3.9 | 3.2 | 55.0 | 322 | 18 | 7 | 7 | 29 | 54 | 51.7 |

Source: World Bank (1997) Sub-Saharan Africa: From Crisis to Sustainable Growth, p.224-5
I = Industry, Mg = Manufacturing, Mn = Mining, A = Agriculture and S = Services

Increasing population, undefined land tenure policy, ineffective farming systems and land use remain key socio-economic issues in terms of vegetation dynamics in West Africa. Northern Ghana, for example, has approximately 0.4%

higher population growth rate in comparison with the national average of 2.6% (GSS, 2002). At the same time, agriculture accounts for 67.2% of all economic activity in the area compared to 54.6% in southern Ghana (GSS, 2002). The consequence is uncontrolled conversion of natural vegetation into arable lands. Asiamah (2002) has reported that soil fertility problems (nutrient mining), overgrazing, bush burning and soil erosion appear to be the most compelling factors for accelerated vegetation degradation in the savannah zones of Ghana.

Accurate and timely measurement of vegetation dynamics is therefore, essential for understanding the regional water and energy balance of the Volta basin. The next chapter (Chapter 3) gives a detailed description of the measurement methods which have been utilised towards the accomplishment of this goal.

## 2.2 Hydro-climatology of Savannah Volta

This section provides a detailed description of hydro-climatology of the Guinea savannah Volta. Daily measurement of water and energy flux determinants such as air temperature, rainfall, evaporation and discharge commenced in Ghana through a network of ground stations established by the British Colonial Government in the early 1920s (MSD, 2004). However, since the early 1960s, only 21 key stations have remained functional in terms of data collection. In the savannah region, only five meteorological stations (see Figure 2.6) continue to provide considerably reliable ground data. Even so, attention is only given to the most critical parameters such as rainfall, temperature and discharge. Several reasons account for the poor network, data unreliability and obsolete archival system. These include historical political instability, economic recession, obsolete equipment, technical incompetence and drought/fire devastation of field equipment. The best

historical data record is probably the last 40 years and therefore forms the basis of the current analysis.


Figure 2.6 Location of the key hydro-meteorological stations in the Savannah Volta basin in Ghana

## 2.2.1 Air Temperature

Air temperature ($T_a$) is one of the easiest and most accurately measured energy balance parameters whose importance is seen as a key driver for the soil-vegetation-atmosphere (SVAT) system. Appendix 2.1 presents the summary

(monthly) statistics of long-term air temperature of the Volta basin. Similarly, Figure 2.8 illustrates the annual dynamics of air temperature on a regional scale.

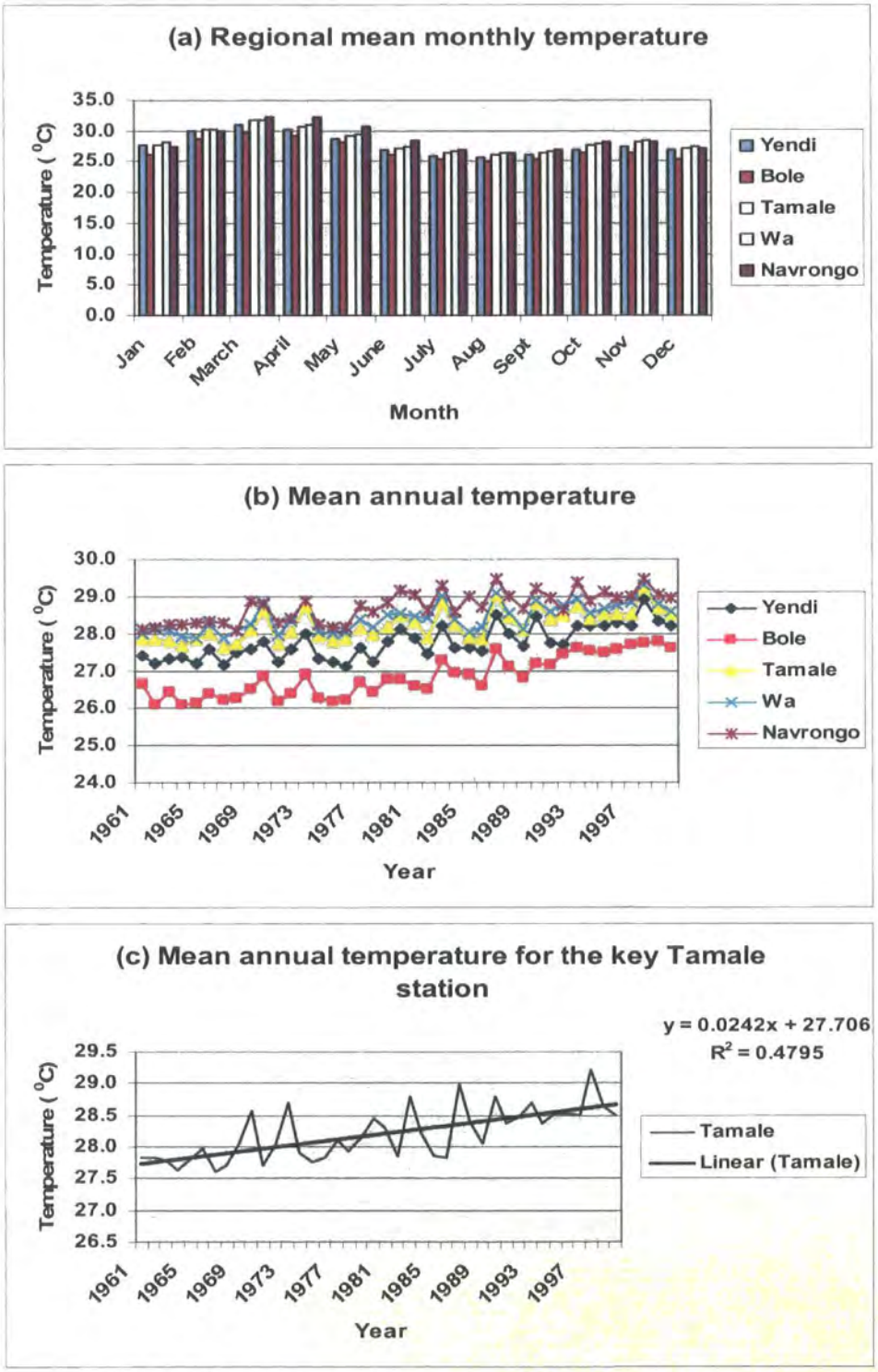


Figure 2.7 Temperature dynamics in the Volta basin

Figure 2.7(b) and (c) particularly exemplify warming conditions in the savannah regions of the Volta with obvious consequences on bio-chemical and physical conditions, such as carbon circulation and regional hydrology. This compels further examination of the nature and magnitude of warming in the area. Variation in annual temperature over the last 20-years (1981-2000) has therefore been statistically tested against the preceding 20-year period. The results have graphically been shown in Figures 2.8 and 2.9.

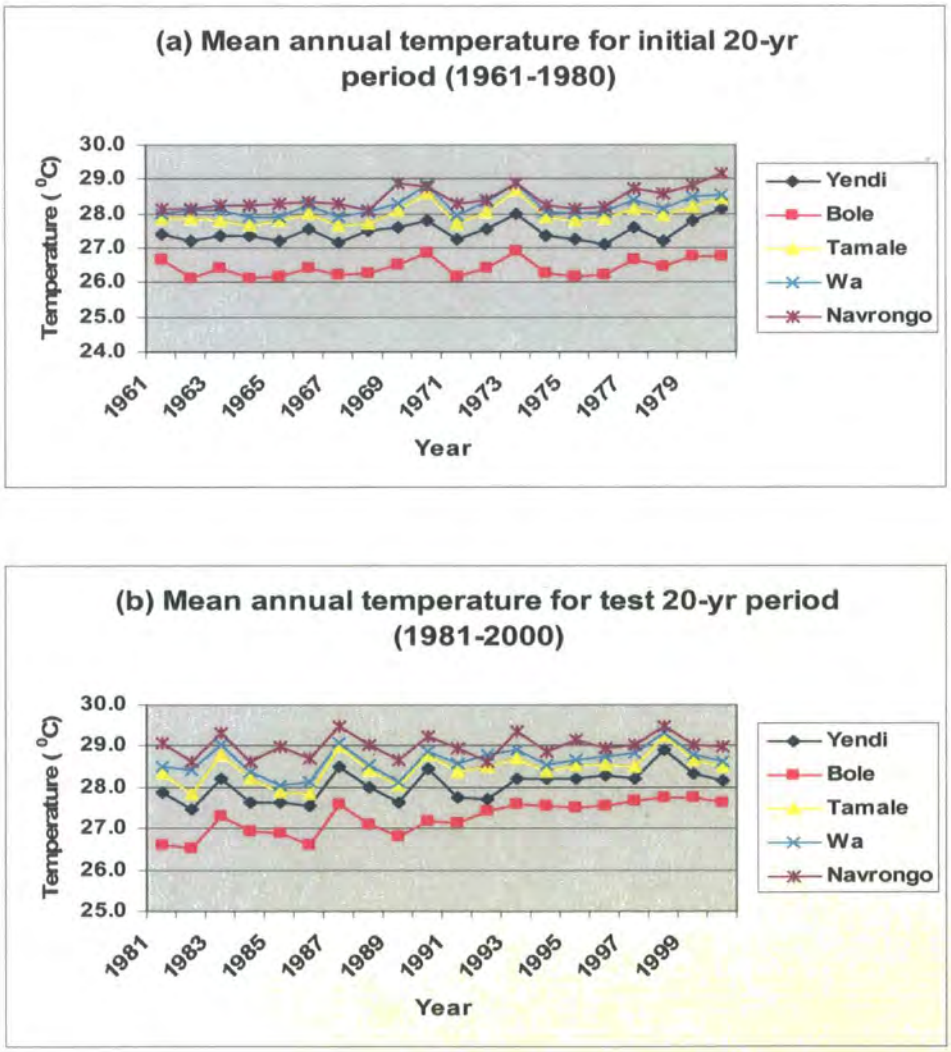


Figure 2.8 Mean annual regional temperature variation over 40 years

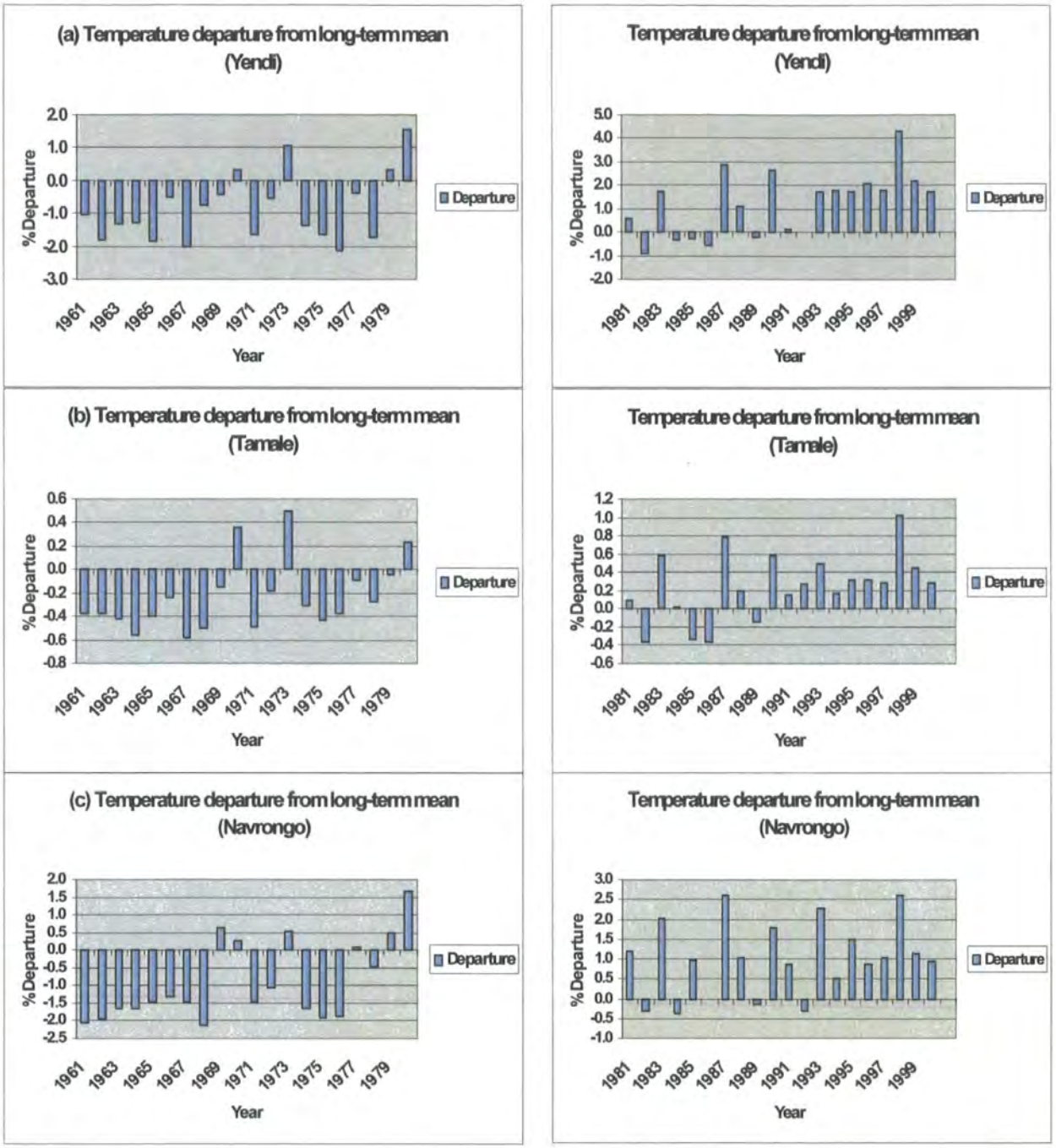


Figure 2.9 Regional warming exemplified by temperature elevation in Guinea savannah stations over the last 20 years (a) Yendi ground station is located in the transitional forest-savannah woodland zone; (b) Tamale station is located in the Guinea savannah woodland zone and (c) Navrongo station is located in the Sudan savannah woodland area. % rainfall departure (% Departure) is calculated as $d_r = \frac{t_i - t_r}{t_r} * 100$ where $t_i$ and $t_r$ are mean annual station and regional temperature, respectively.

The above probably confirms previous research, e.g. Rosenberg (1990); Paturel, *et al.* (1997); Gyau-Boakye & Timbulto (2000); Hulme et al. (2001) that indeed, West Africa is warming up. But what is the magnitude of temperature rise in the Volta savannah region? This is a question whose answer requires examination by climatologists and thus, is beyond the scope of this thesis. However, from Figures 2.8 and 2.9, elevation in regional temperature may range from 1-5%, representing about 0.28-0.56$^0$C, with a mean value of 0.45$^0$C and a standard deviation of 0.07$^0$C. Over two decades, this is a significant temperature rise, necessary to raise concerns about water stress problems, particularly downstream the Volta Lake at Akosombo.

### 2.2.2 Rainfall

Daily rainfall ($R$) in the Volta basin is measured using a network of rain gauges. In hydrology, the key value of long-term rainfall records lies in the possibility to use that as a predictive quantity for other components of the water balance equation, i.e. runoff, evapotranspiration, soil moisture and groundwater discharge. Appendix 2.2 presents summary rainfall statistics of the Volta basin. Figure 2.10 also accentuates the temporal regional rainfall pattern of West Africa. Figure 2.10(a) particularly typifies the mono-modal peak (monthly) rainfall distribution of higher latitudes in sharp contrast with the bi-modal distribution in lower latitudes (Figure 2.10[b]). Also, note the characteristic attenuation of annual rainfall totals, mainly in response to the complex interplay of latitudinal and ecological (vegetation) changes of the area (Figure 2.10[c] and [d]) (see also Chapter 1, Section 1.2).

However, contrary to popular opinion that rainfall in Ghana's savannah has declined over the last 2-3 decades (see Opoku-Ankomah & Amisigo, 1998), analysis of Table 2.7; Figure 2.10 and Figure 2.11 do not appear to fully support this view. Although rainfall variability is characteristic for most tropical regions, the case of the Volta savannah depicts a reasonably stable feature, especially in the last two decades. Compared to regional temperature, this is not completely unexpected. This is because detection of regional warming (temperature elevation) is often easier over the short-medium time steps (e.g. half-century) whereas rainfall decline is not easily detectable unless time-series data over a century or more have been well investigated (Shaw, 1994). Another important reason is that temperature measurement has a much higher temporal frequency (hourly to daily) whereas tropical rainfall is often seasonal, where daily events over an annual cycle is not possible. Also, rainfall measurement is more expensive over the regional scale than temperature.

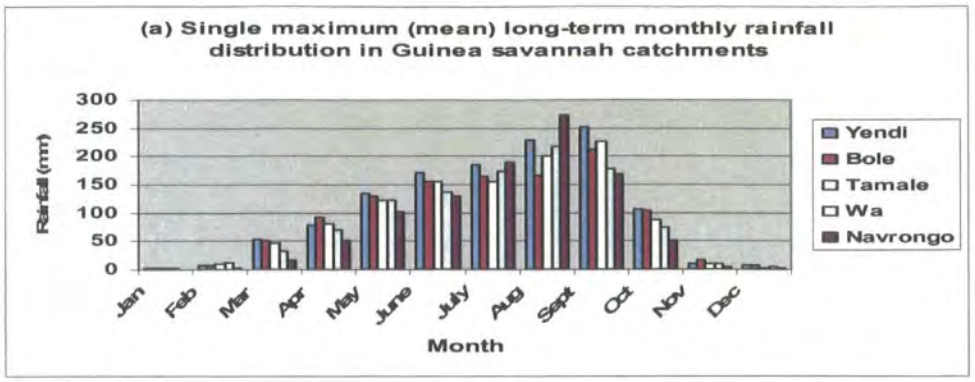


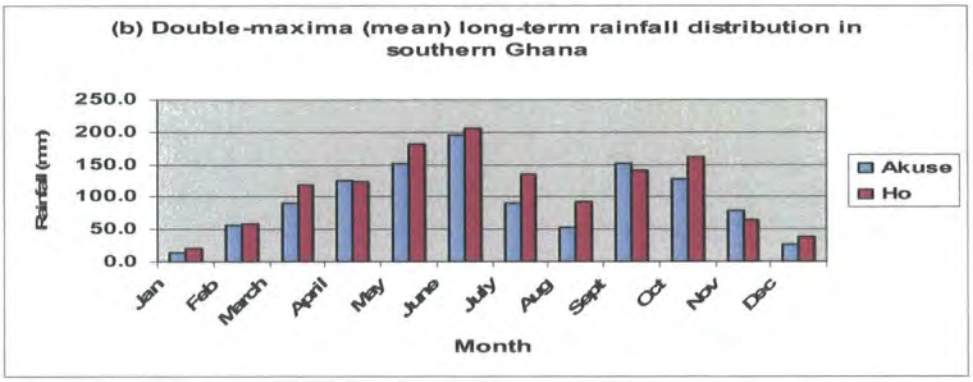


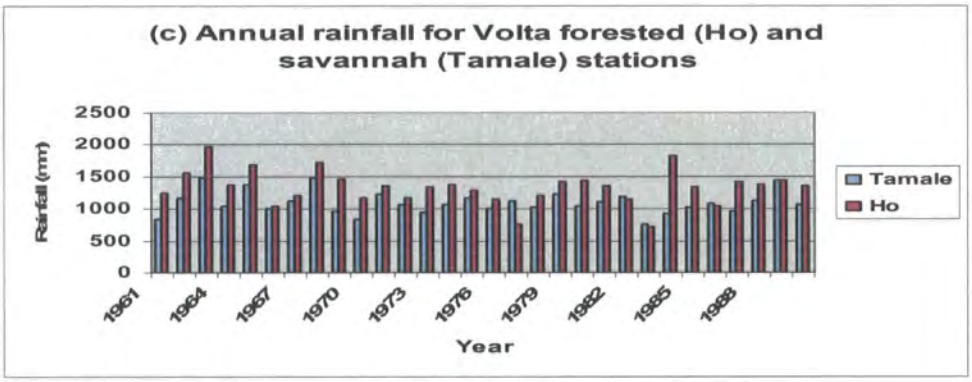


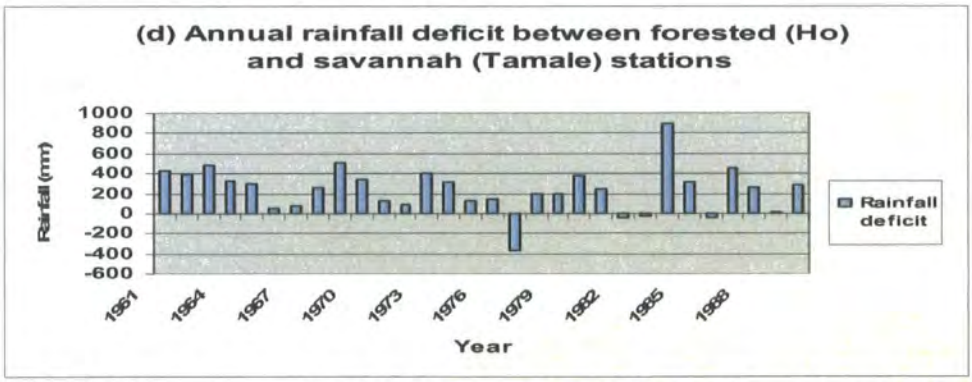


Figure 2.10 Guinea savannah rainfall compared with that of forested southern Volta. Graphs (a)-(b) and (c)–(d) compare monthly and annual distribution, respectively. Note the remarkable influence of latitude and land cover change on the distribution of regional rainfall. Rainfall deficit is calculated as the difference between the Ho station totals and that of Tamale.

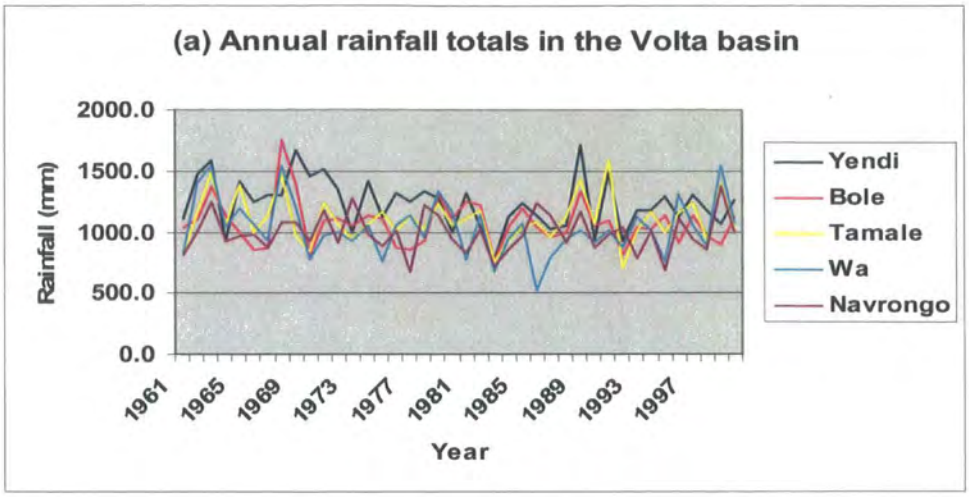


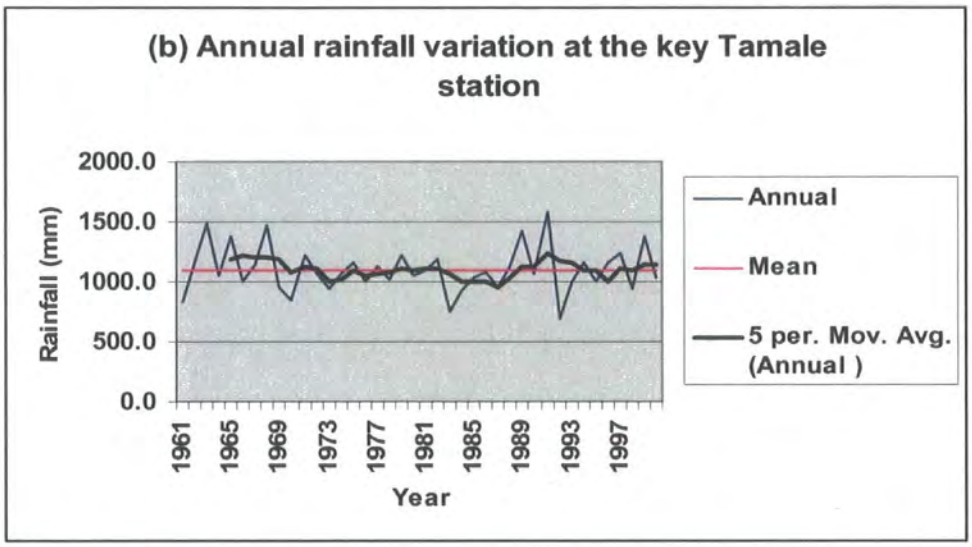


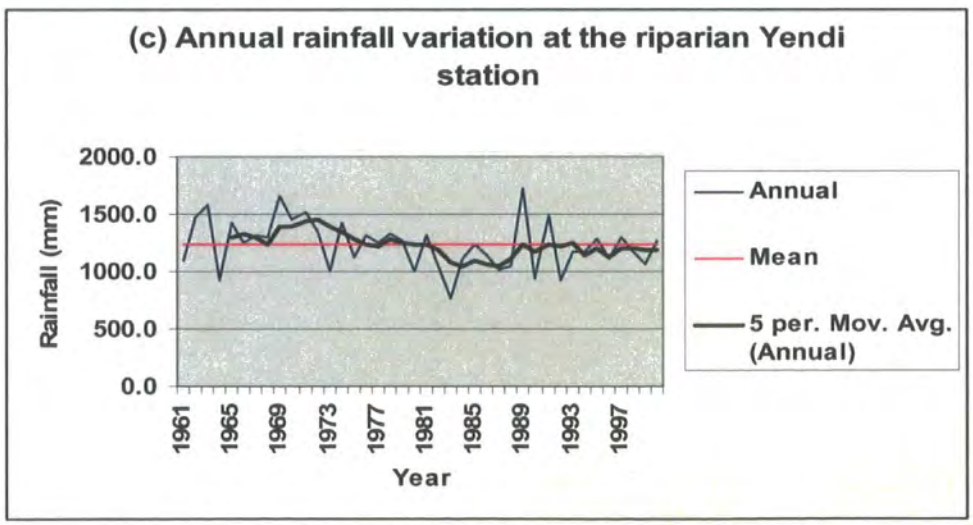


Figure 2.11 Regional rainfall variation in the Volta region

### 2.2.3 Pan evaporation

Evaporation ($E$) is an important quantitative estimate of several hydrological processes including water loss from evaporating surfaces, vapour pressure, soil and stream water storage, circulation and precipitation (Oke, 1977). Evaporation is generally measured in Ghana through the use of the Class-A pan. Accurate gap-free long-term evaporation records are however, hard to find in respect of the study area; Figure 2.12 illustrates the region's evaporation regime.

In the absence of very accurate measurement methods, Figure 2.12(b) demonstrates the usefulness the Class-A pan for estimating evapotranspiration in the area. In this case, the pan method quite accurately measures surface evaporation for the wet (summer) months but as expected, poorly estimates dry (winter) evaporation during temperature extremes (Figure 2.12[b] & [d]). From Figure 2.12(c), approximately 1200mm of moisture per year may be required to overcome the stresses of evapotranspiration. How these stresses are spatially organised in the area is a central concern in this research.

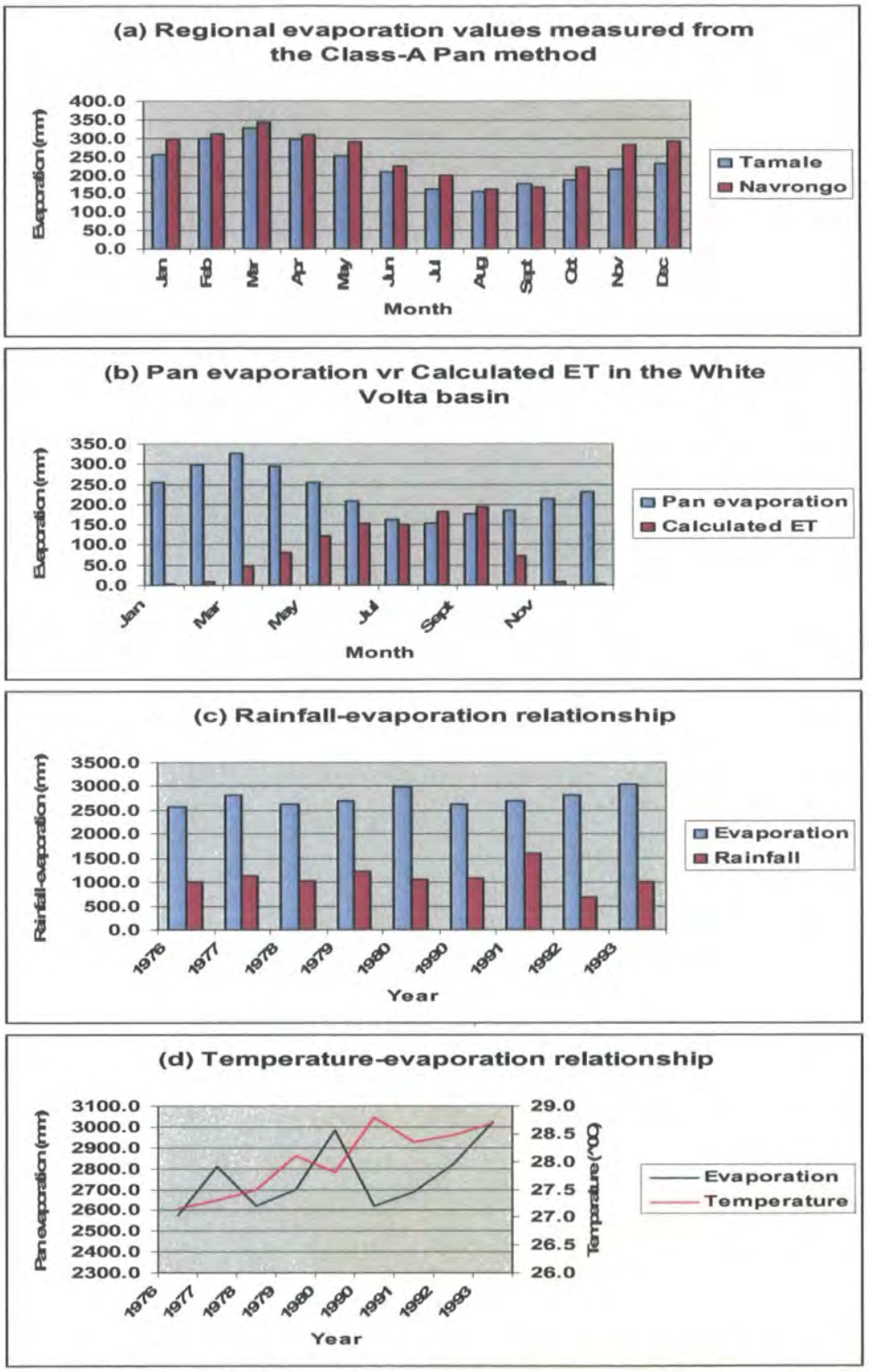


Figure 2.12(a) Regional evaporation is measured from the Class-A Pan – only 9 years of gap-free evaporation record exists (1976-1993). (b) Pan evaporation is crudely compared with calculated ET based on the regional water balance equation. Relationships between evaporation and rainfall (c) and evaporation and temperature (d) are also investigated.

### 2.2.4 Discharge

River discharge ($Q$) defines water flux through stream channels over time. The most important value of discharge measurements in the Volta basin is the quantification of surface runoff into the Volta Lake; which also determines the availability of reservoir water for hydropower generation. As in the case of meteorological stations, most of the river gauging stations in Ghana deteriorated over a decade (1980-1990); thus, discharge records have extensive missing data as shown in Figure 2.13.

Careful examination of Figure 2.13(a) and (b) shows that discharge in the savannah area quite closely reflects high autumn rainfall; in contrast to summer wet months, characteristic of southern Ghana. Here, it is important to make reference to Figure 2.12(a) & (b) and Figure 2.14(d). In this case, long-term elevation of air temperature does not only drive evapotranspiration processes but also seasonal water stress as shown by the rainfall-runoff curve in Figure 2.14(c).

It is necessary to emphasize that the current hydro-climatic trends provide a strong basis for exploring new investigative tools to help understand some of the key drivers involved in the environmental feedback processes, e.g. the spatial organisation of evapotranspiration over short temporal scales. One important such tool is remote sensing technology. As a first step, a detailed description of a range and value of satellite data sources is provided in the next chapter (Chapter 3). The relevant technical details required for the extraction of key evapotranspiration modelling parameters have also been explained.

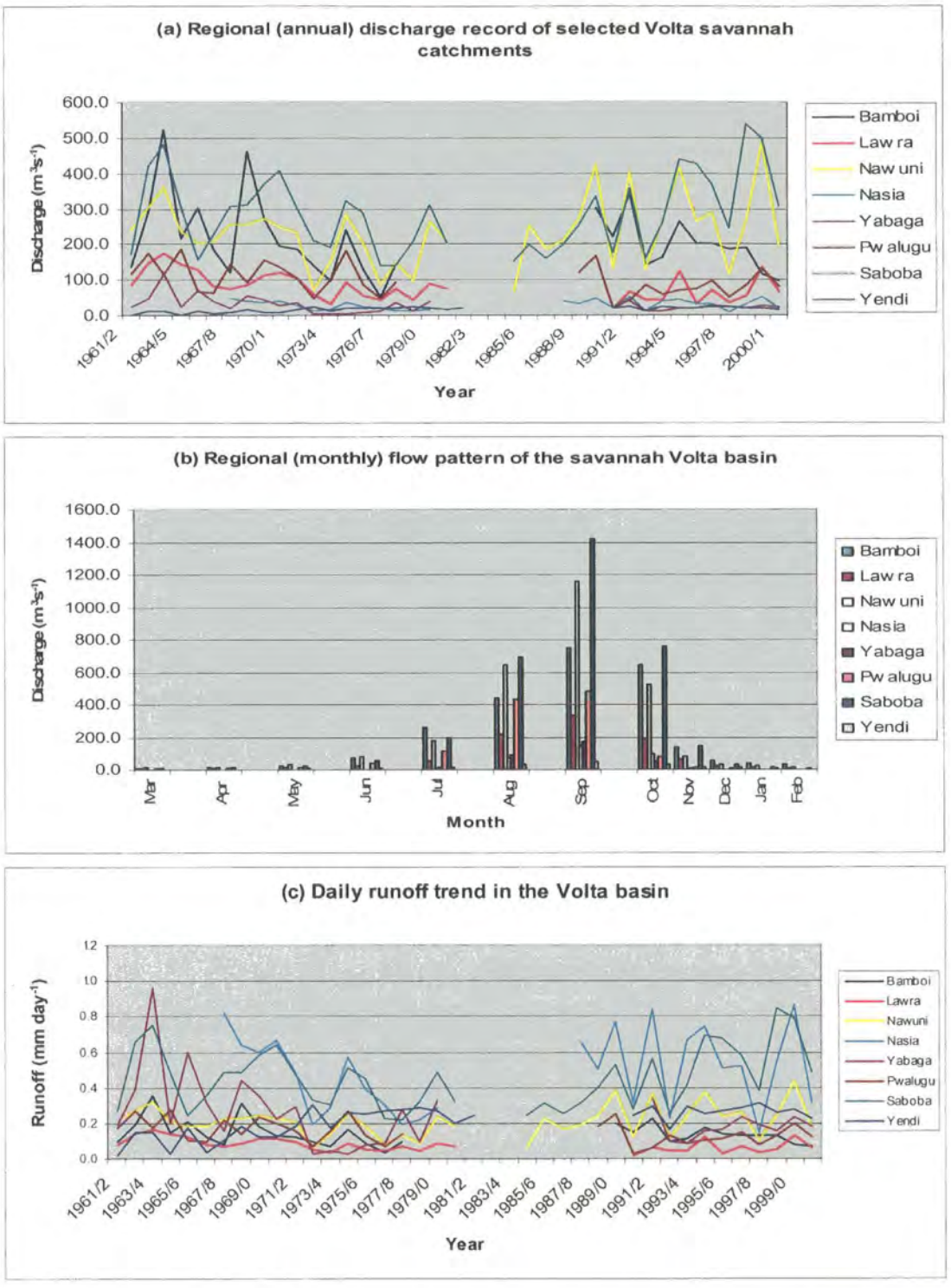


Figure 2.13 Regional discharges (a) Annual (b) monthly and (c) daily flow patterns in the Volta basin. The first and last two discharge stations represent the Black and Oti Volta sub-basins (see Figure 1.1 & Table 2.1). The remaining stations cover the White Volta where the Nawuni station encompasses the key Tamale study area. The gaps shown illustrate lack of data records due partly to the West African droughts of the 1970s and 1980s and deterioration of recording stations as a result of economic recession.

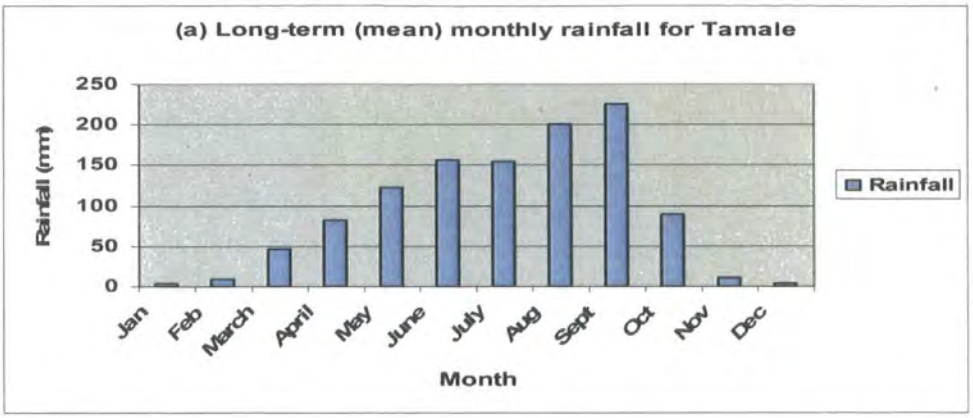


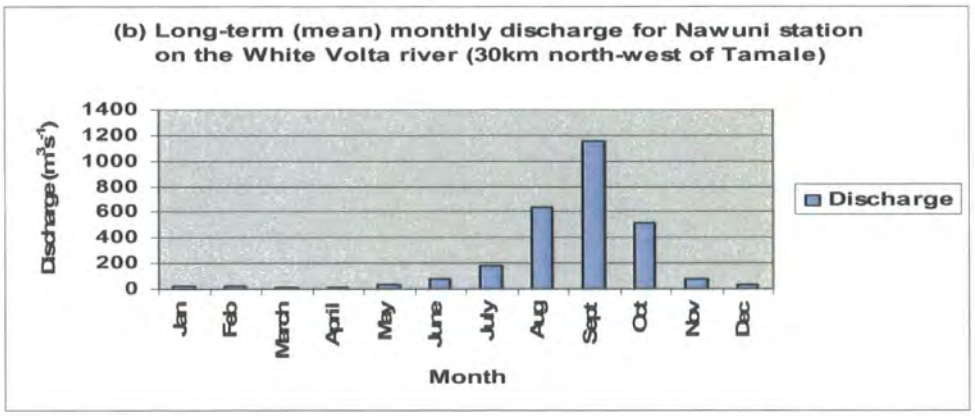


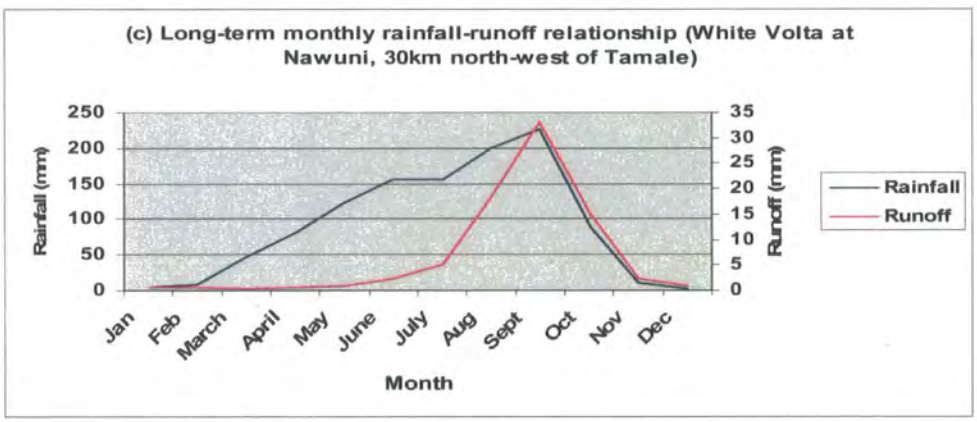


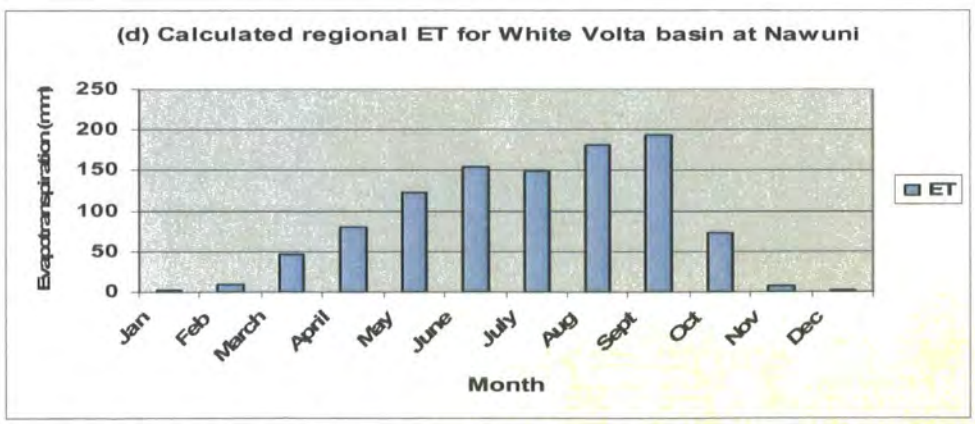


Figure 2.14 Regional water balance of the White Volta sub-basin at Nawuni - located ~30km north-west of Tamale. Monthly runoff ($R$) was calculated as: $R$=Q*3600*24*30/(A*$10^3$); where $Q$=discharge ($m^3$ $s^{-1}$) and A=basin area (90,658$km^2$). Based on the regional water balance equation, $ET$ was calculated as difference between monthly rainfall and runoff assuming negligible soil moisture and groundwater discharge at a basin scale.

## 2.3 Summary

First of all, the chapter provided a detailed description of the regional Volta basin and then focused more on the Kalarakun study site. Apart from detailed information about the geography of the savannah Volta basin, analysis of long-term (40 years) hydro-climatic conditions of the Volta basin accentuates the principal assumption (see Section 1.1.3 of Chapter 1) that *ET* is probably the most critical issue concerning water availability in this region. Increasing *ET* may be explained by regional climate.

One of the most important contributions from this chapter is therefore, provision of general information about the Volta's regional hydrology, a discussion on data scarcity, which is a major limitation to hydrological modelling and the issue of regional warming. These are further justification why remote sensing is needed as a source of spatial data for energy and water balance studies.

# Chapter 3

# Volta Satellite Imagery & Field Data

## 3.1 Introduction

This chapter is designed to build up on the previous chapters, which emphasised remote sensing as a vital source of spatial data for the parameterisation of energy and water balance models, given the scarcity of spatially-observed ground data in the Volta basin (see Sections 1.1.2 & 1.3). The focus of the chapter is to provide a detailed description of satellite sensors e.g. MODIS, AATSR, Landsat ETM+, etc. from which data may be derived to parameterize the Surface Energy Balance for Land (SEBAL) algorithm (Bastiannssen *et al.*, 1998a & b). In terms of energy balance modelling, the SEBAL is considered as one of the simplest but most accurate land surface schemes (LSS) (Mekonnen, 2005), further details of which are given in Chapters 5 - 7.

Anderson & Bates (2001) have reported the importance of remote sensing data for a wide range of today's LSS – from the classic "bucket" models (e.g. Manabe, 1969) to detailed soil-vegetation-atmosphere transfer schemes (SVAT) (e.g. Dickinson *et al.*, 1993, Sellers *et al.*, 1996). At the basin scale, Lyon *et al.* (2003) have provided a range of compelling examples which further illustrate the importance of remote sensing data to parameterize semi-distributed hydrological models. For most tropical catchments where economic and operational constraints fail to support a wide network of climate and hydrology ground stations, remote sensing probably remains the most feasible way to provide spatial data (Beven, 2001). Integrated solution of the regional water and energy balance equations using satellite measurements complemented by minimum ground data has been widely recognised by various authors (e.g. Bastiannssen *et al.*, 1998; Su *et al.*, 1999; Bastiannssen, 2000; Lyon *et al.*, 2003; etc).

Another important aspect of this chapter is a demonstration of the necessity of field data as complementary sources of information for the evaluation, integration and/or validation of remotely sensed data in the parameterisation scheme.

## 3.2 Satellite Data Sets

West Africa is well covered by several old and new sensors e.g. [1]NOAA/AVHRR, Landsat TM and ETM+, MODIS, ASTER and ENVISAT-MERIS/AATSR. But the question is: what is the potential of relatively new sensors as parameterisation inputs for large-scale land surface schemes? For very large surface areas, how can we ensure, for instance, accuracy of measurements? Here, emphasis can be placed on new data such as SRTM, ASTER, Landsat ETM+, MERIS, AATSR and MODIS. What is important about these sensors is that they provide incredibly high quality spectral image data regardless of their differential spatial resolutions. They also provide operationally useful inputs to land surface schemes in so far as robust data assimilation algorithms can be developed for such schemes (Donoghue, 2000). Importantly, their products are radiometrically and geometrically calibrated and often of high quality, most of which are applicable for use in GIS-based hydrological models. Table 3.1 displays the general characteristics of some of the applicable datasets in this research. Data from the ASTER and SRTM sensors are particularly useful for topographic modelling, including production of digital elevation models (DEM) relevant for terrain and channel mapping, and drainage delineation in hydrological models. Further details are provided in the subsequent section.

[1] NOAA/AVHRR = National Oceanic Atmospheric Administration-Advanced Very High Resolution Radiometer

Table 3.1 General characteristics of satellite data sets

| Data source | Spatial resolution (m) | Spectral range (μm) | | | |
|---|---|---|---|---|---|
| | | Visible | NIR | MIR | TIR |
| ASTER Level 1B | 15, 30 & 90 for VIS, IR & TIR spectral ranges, respectively | Band1 (0.52-0.60) Band2 (0.63-0.69) | Band3 (0.78-0.86) | Band4 (1.60-1.70) Band5 (2.14-2.18) Band6 (2.18-2.22) Band7 (2.23-2.28) Band8 (2.29-2.36) Band9 (2.36-2.4.3) | Band10 (8.12-8.47) Band11 (8.47-8.82) Band12 (8.92-9.27) Band13 (10.2-10.8) Band14 (10.95-11.65) |
| Landsat ETM+ | 30 (15m for panchromatic and 60m for thermal band) | Band1 (0.45-0.52) Band2 (0.52-0.60) Band3 (0.63-0.69) Pan (0.5-0.90) | Band4 (0.76-0.90) | Band5 (1.55-1.75) Band7 (2.08-2.35) | Band6 (10.4-12.50) |
| ENVISAT AATSR Level 1B | 1km | Band1 (0.545-0.565) Band2 (0.649-0.669) | Band3 (0.855-0.875) | Band4 (1.580-1.640) | Band5 (3.505-3.895) Band6 (10.40-11.30) Band7 (11.50-12.50) |
| MODIS Level 1B | 250 (500m for bands 3-7) and 1000m for bands 8-36) | Band1 (0.620-0.670) Band3 (0.459-0.479) Band4 (0.545-0.565) Band8 (0.405-0.420) Band9 (0.438-0.448) Band10 (0.438-0.493) Band11 (0.526-0.536) Band12 (0.546-0.556) Band13(0.662-0.672) Band14 (0.673-0.683) | Band2 (0.841-0.876) Band5 (1.230-1.250) Band15 (0.743-0.753) Band16 (0.862-0.877) Band17 (0.890-0.920) Band18 (0.931-0.941) Band19 (0.915-0.965) | Band6 (1.628-1.652) Band7 (2.105-2.155) Band26 (1.36-1.39) | Band20 (3.66-3.84) Band21 (3.92-3.98) Band22 (3.92-3.98) Band23 (4.02-4.08) Band24 (4.43-4.49) Band25 (4.48-4.54) Band31 (10.78-11.28) Band32 (11.77-12.27) |

Source: Modified after Lillesand & Kiefer (2000) and various NASA and ESA websites (e.g. http://daac.gsfc.nasa.gov; http://www.msct.ssai.biz; http://envisat.esa.int/instruments/; etc. (VIS=Visible, NIR=Near Infrared, MIR=Middle Infrared & TIR=Thermal Infrared band)

## 3.3 SRTM data

The Shuttle Radar Topography Mission (SRTM) is a joint project between NASA and NGA (National Geospatial-Intelligence Agency) to map the world in three dimensions. The SRTM utilizes dual Spaceborne Imaging Radar (SIR-C) and dual X-band Synthetic Aperture Radar (X-SAR) configured as a baseline interferometer, thus acquiring two images at the same time (see Figure 3.1). These images, when combined,

can produce a single 3-D image. Flown aboard the NASA Space Shuttle Endeavour in February 2000, SRTM successfully collected data over 80% of the Earth's land surface, for most of the area between $60^0$ N and $56^0$S latitude (http://srtm.usgs.gov). The SRTM data is now being used to generate a digital topographic map of the Earth's land surface with data points spaced every 3 arc seconds for global coverage of latitude and longitude (approximately 90 metres). The absolute horizontal and vertical accuracy is 20 metres (circular error at 90% confidence) and 16 metres (linear error at 90% confidence), respectively. High spatial resolution SRTM data (1 and 2 arc seconds – approximately 30 and 60m exist for North America and most parts of Europe).

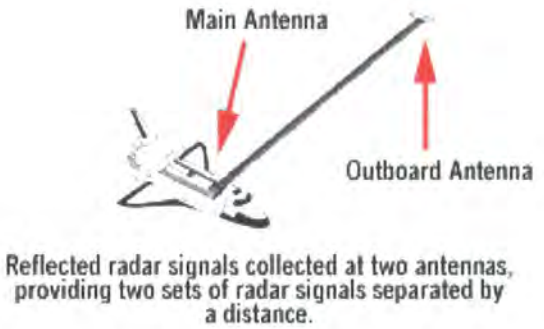


Figure 3.1 SRTM radar interferometric signals. To get two images from different vantage points, a main antenna was installed in Space Shuttle Endeavour's cargo bay. The main antenna both transmitted and received radar signals. Once the shuttle was in space, a mast was deployed from a canister that was attached to the main antenna truss. The mast extended out 60 metres. At the end of the mast, an outboard antenna acted as the second vantage point and received radar signals.
Source: http://www2.jpl.nasa.gov/srtm/index.html

## 3.3.1 SRTM Processing & DEM Generation

### *3.3.1.1 Raster Geo-referencing*

The raw $1^0$ SRTM tiles (image files) are freely available from the USGS server: ftp://edcsgs9.cr.usgs.gov/pub/data.srtm/. In this case, 95 tiles were selected based on the Volta coordinates and spatial extent. The 16-bit SRTM unique tiles (*.hgt files) are readable using special application software (e.g. USGS 3-D Visualization Toolbox

(Appendix 3.1). The 3-D Visualization Toolbox is helpful in three ways: reading raw images; filling raster data gaps; and geo-referencing. New-generation remote sensing software such as ERDAS Imagine and ENVI are powerful tools for mosaicing SRTM tiles using algorithms that register adjacent tiles until the study area is completely covered. This process was optimized using 30 randomly distributed ground control points (GCP) selected from an analogue 1:250,000 map with a root mean square error (RSME) of <0.5 pixel size in X and Y directions. The result was re-projected unto UTM (WGS84) projection and saved as Geo-TIFF file.

### *3.3.1.2 DEM Generation*

The ESRI Arc-Hydro Software is a powerful tool for digital elevation model (DEM) generation and spatial modelling. Its *Terrain Pre-processing* wizard for instance, is well suited for automatic delineation of river basins (Maidment, 2002). In this case, the program was used to define the Volta tributaries, their flow direction, drainage points and flow accumulation. Figure 3.2 shows the key processing steps. This is the first time a more accurate high-resolution DEM has been produced for the Volta basin. Hitherto, 100m resolution analogue copies have often been produced from manually digitized topographic maps.

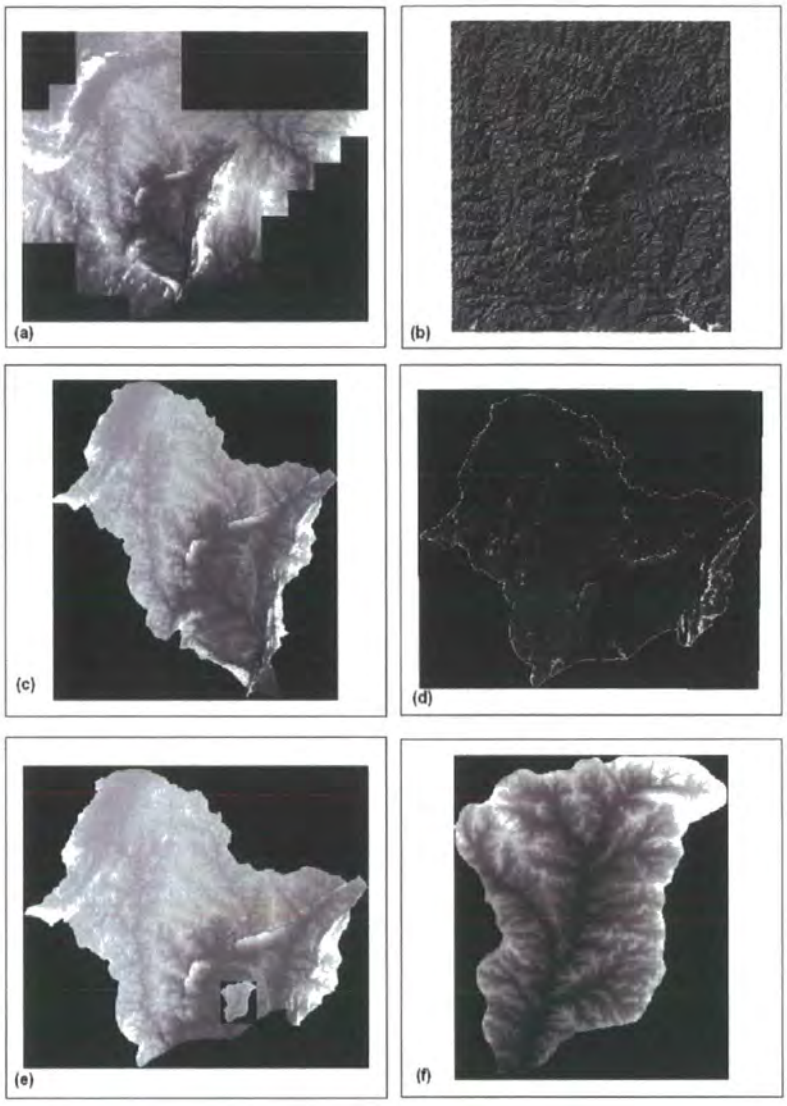


Figure 3.2 Stepwise DEM processing from SRTM data (a) Mosaic of 95 SRTM granules; (b) sinks and voids are filled; (c) entire Volta basin is extracted from the large mosaic output; (d) a slope map is generated; (e) the Volta savannah region is extracted; and (f) the study area is clipped out.

Even though its accuracy is not fully determined in this thesis, Figure 3.2 is important for a variety of reasons: (1) definition of a catchment boundary for the present study; (2) "substrate" for future topographic hydrological modelling; and (3) reproducible method for areas of similar topography.

### *3.3.1.3 Use of SRTM DEM*

Developments in computers, broadening of visualization applications and the availability of geospatial data have now made the use of DEMs an indispensable quantitative environmental variable in many research applications. The landscape change and process-based studies in digital Earth sciences, for instance, require the excessive use of DEM for landslide susceptibility/hazard assessment (Süzen & Doyuran, 2004); erosion susceptibility (Kääb, 2002); glacier monitoring (Bolch, 2003); geomorphological mapping (Baily *et al.*, 2003), etc., in order to quantitatively represent or to analyse the morphology of the landscape. The conventional methods used to produce DEMs need large field campaigns that result in land surveying teams using analogue or analytical techniques. In recent decades, satellite stereo image-based topographical map production has turned into an operational process from its previously experimental state. Now, many local-scale landscape or topographical monitoring requirements are maintained by high-resolution satellite images. However, for high temporal resolution and for very large regional coverage, neither the conventional methods nor the high resolution images are feasible. SRTM data are therefore a very promising solution.

### *3.3.1.4 New SRTM Products*

What is the future of SRTM products? In January 2006, a new product was released which is of even greater interest to the hydrology community. This is the SRTM Water Body Data (http://edc.usgs.gov/products/elevation/swbd.html). This is a by-product of data editing performed by the National Geospatial-Intelligence Agency (NGA) to produce the finished SRTM Digital Terrain Elevation Data (DTED) Level 2. In accordance with the DTED-L2 specification, the terrain elevation data have been

edited to portray water bodies that meet minimum capture criteria. Ocean, lake and river shorelines have been identified and delineated, orthorectified and saved in ESRI 3-D shapefile format. Though this is not yet globally available (being unavailable for parts of the northern and southern hemispheres), the source is invaluable for technical and operational reasons. First, void pixels no longer present processing and application problems. Secondly, availability of mosaics for large areas and their availability as ESRI-shapefiles make them directly applicable for standard GIS software.

## 3.4 ASTER Data

The Advanced Spaceborne Thermal Emission and Reflection Radiometer (ASTER) sensor is a large digital camera fixed to NASA's Terra satellite which was launched in 1999. The Terra bus has four other instruments, including Terra and Aqua MODIS. The satellite circles the Earth at a distance of 705 km, from pole to pole, about every 100 minutes, crossing the equator at about 10:30 am local time with a repeat frequency of 16 days. The ASTER (Table 3.2) itself takes about 600 pictures ("scenes") a day, each covering an area of 60 x 60 km. Like most satellite sensors, ASTER is much more complex than a hand-held digital camera. First and most importantly, a separate image is created for each colour (or more precisely, each wavelength range, or "band").

Table 3.2 ASTER spectral bands

| Parameter | Comment |
|---|---|
| Product ID | AST_L1B product ID-003:2003867300 |
| Date of image acquisition | 27/12/2000 |
| % Cloud cover | 2.0 |
| Path | 194 |
| Row | 53 |
| Central coordinates | Lat $9.1^0$N; Lon $-0.6^0$W |

The multiple ASTER bands have uses for a variety of land applications. For example, different surface materials are better modelled by band spectral variety. Also, the high spatial resolution of ASTER (15m for visible bands) complemented by a relatively high temporal frequency, makes ASTER relevant for a wide range of land applications including hydrology, agronomy, mineral exploration and landscape modelling. The ASTER instrument and its operation is a joint project between the US and Japan. Japan designed and built the instrument, the Level 1 processing system and the operations system. Japan experts also perform the day-to-day mission planning and the Level 1 data processing. The US designed, built and continues to operate the Terra spacecraft and the associated ground system (http://asterweb.jpl.nasa.gov/).

### 3.4.1 Processing ASTER Data

ASTER Level 1B scenes are archived at a data centre in South Dakota, USA (as well as at the equivalent centre in Tokyo). Access to the data in the US archive is by an online ordering toolbox (http://edcimswww.cr.usgs.gov/pub/imswelcome); which is fairly simple to use. The following order process was followed: (1) familiarisation with the Java-scripted ordering toolbox based on the USGS quick-start tutorial; (2) completion of user registration details; (3) selection of product type and choosing

user's search area using the "Gazetteer" tool; (4) evaluation of online quick-looks; (5) populating the add-selection tool, and (6) completion of the ordering process. ASTER products (also called granules) are often delivered to users in Geo-Tiff format. Through an *ftp-pull* option, large image files can be directly pulled from the NASA/USGS server. A single ASTER image (2.1GB) acquired on 27$^{th}$ December 2000 was pulled from the NASA server mainly as a source of validation data for its low-resolution counterparts such as MODIS. Raw ASTER images are viewable and easily processed using a suite of new generation application software (e.g. PC-ERDAS Imagine, ENVI, ER-Mapper, PCI-Geomatica, ARC-GIS, etc.). The main processing steps are described below.

#### *3.4.1.1 Geo-referencing*

ASTER user products are largely radiometrically and geometrically corrected in UTM (WGS84) projection. However, image Geo-referencing to local map coordinates is necessary, especially if co-registration of multi-temporal images is required.

#### *3.4.1.2 Radiometric Enhancement*

Simple radiometric enhancement (Figure 3.3) of ASTER data may produce profound improvements in pixel contrast and target discrimination (Mah, 2004). The benefit of this method, histogram equalisation (Figure 3.4), has been employed here.

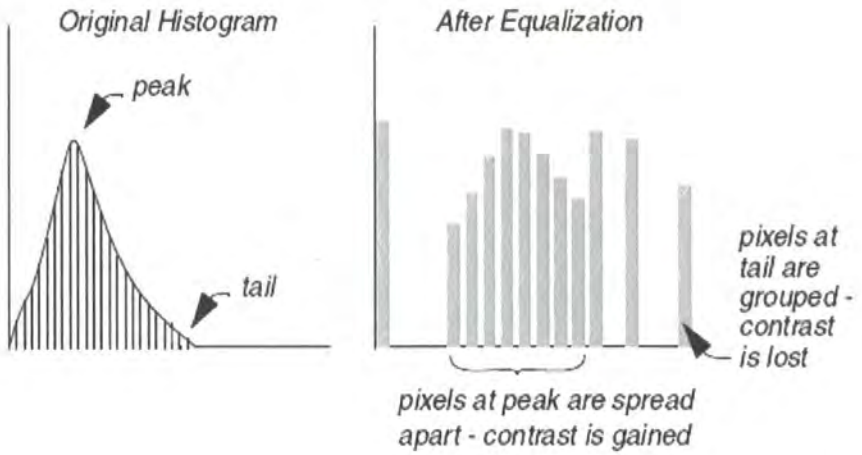


Figure 3.3 Histogram equalisation: In this method the pixel values of an image (either data file or brightness values) are reassigned to a certain number of bins (numbered sets of pixels). The pixels are then given new values based on the bins to which they are assigned. Source: [Leica Geosystems (ERDAS Field Guide, 2003; p. 153)]

The ASTER image in Figure 3.4 exemplifies the radiometric enhancement concept. Here, nonlinear stretching redistributes pixel values so that there are approximately, the same number of pixels with each value within a range; the result approximates a flat histogram. Therefore, contrast is increased at the peaks and lessened at the tails. The result is a qualitative improvement of the right-hand image of Figure 3.4.

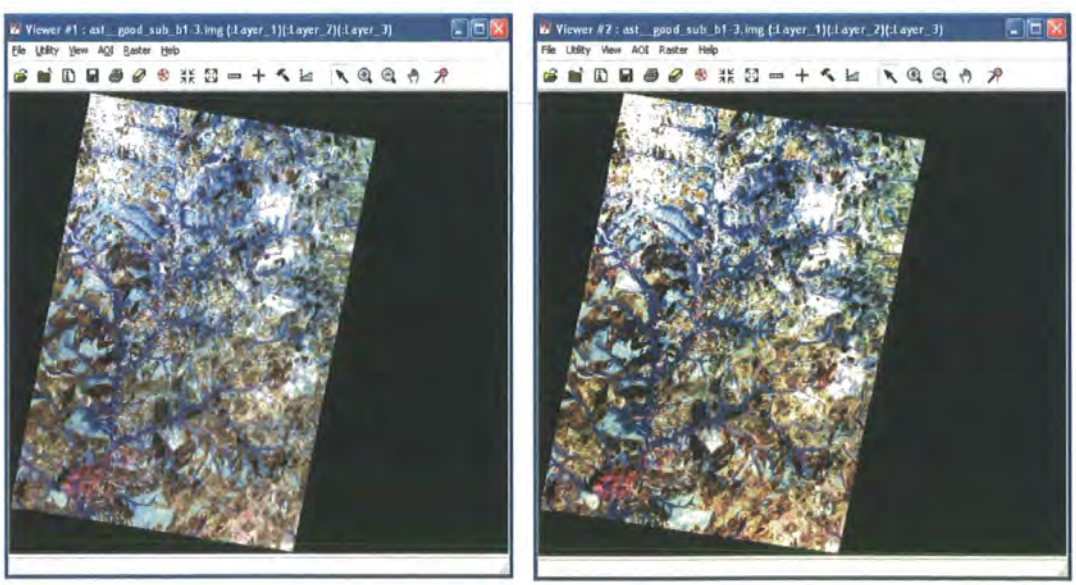

Figure 3.4 Histogram equalisation of ASTER image of the Volta. Note the improvement of enhancement of surface targets in the right-hand image. This is important for image classification and extraction of geophysical variables.

## 3.5 Landsat-7 ETM+

Landsat is one of the commonest satellite data sources used in Earth surface biophysical modelling (Hudak *et al.* 2001). This is in large part due to its widespread availability and unrivalled length of record (since 1972) but also because the spatial resolution and multispectral features make Landsat series suitable for a variety of environmental applications at landscape to regional scales. Landsat spectral data are typically related to vegetation structural attributes via spectral vegetation indices (SVIs); the potential of SVIs has been extensively examined for various land surface modelling schemes (e.g. Chen & Cihlar, 1996; Cohen *et al.* 2003). The ETM+ instrument currently flying on Landsat-7 is similar to the earlier TM but adds an extra 15-metre resolution panchromatic band and improved resolution for the thermal-infrared band (60-metres) (Table 3.1). This new instrument also features enhanced radiometric resolution over its TM predecessor which is a hopeful aid to empirical models relevant for retrieving geophysical variables.

### 3.5.1 Processing Landsat ETM+ Data

The USGS Global Visualization Viewer (http://glovis.usgs.gov/) (Appendix 3.2) managed by the Centre for Earth Resources Observation and Science (EROS), constitutes the main browser for ordering Landsat ETM+ data. In this case, a single cloud-free Landsat ETM+ scene was used. Table 3.3 describes the Landsat ETM+ scene selected for this research.

Table 3.3 Landsat ETM+ image used for the Volta research

| Parameter | Comment |
|---|---|
| Product ID | Landsat ETM+ Side Looking Complex – gap filled product ID-7194054000235150 |
| Date of image acquisition | 05/01/2004 |
| % Cloud cover | 0.0 |
| Path | 194 |
| Row | 53 |
| Central coordinates | Lat $10.1^0$N; Lon $-0.6^0$W |

Landsat ETM+ products are orthorectified using existing corrected TM data as horizontal control (http://edc.usgs.gov/about/landsat/) using the pixel cross-correlation control method. A patented Landsat large block triangulation procedure is used to perform a photogrammetric adjustment of each individual Landsat ETM+ scene; the data are then placed into a UTM (WGS84) map projection. All bands are individually re-sampled, using a nearest neighbour algorithm. The result is a final image map product with RMSE better than 50 metres in positional accuracy. The Landsat ETM+ scenes were pan-sharpened by the data providers using a resolution merging process allowing the high-resolution panchromatic and lower-resolution multispectral imagery to fuse together to create a single high-resolution colour image. This process allows the image to retain the greatest value of the spectral information as much as possible from the multiband raster image. The resulting high-resolution colour image preserves the original colour fidelity, which allowed better visualization, interpretation and clarity in this research, thus, easing image processing significantly. The main processing steps described in Section 3.4.1 were also used for ETM+ data.

#### *3.5.1.1 Landsat ETM+ Geophysical Products*

The literature shows increasing use of ETM+ data for various environmental applications at various temporal and spatial scales. It has recently been used for applications such as glacial mapping (Jenssen & Glosser, 2005), groundwater exploration (Tcherepanov *et al.*, 2005), agronomy (Peterson, 2005), mineral exploration (Ranjibar *et al.*, 2004), urban planning (Lo & Choi, 2004) and monitoring of volcanoes (Nama, 2003). Its capability to provide direct biophysical inputs to soil-vegetation-atmospheric transfer (SVAT models) has previously been considered by Nouvellon *et al.* (2000). These authors have shown, for example, how ETM+-derived surface variables in combination with meteorological data can be used to parameterize and update empirical models to help understand evaporation dynamics of the San Pedro River Basin in USA. This is an approach of great relevance to this research.

## 3.6 ENVISAT AATSR Data

The Environmental Satellite (ENVISAT) Advanced Along-Track Scanning Radiometer (AATSR) instrument is unique in its use of along-track scanning to provide two views of the surface and thus improve atmospheric correction. The surface is first viewed along the direction of the orbit track, at an angle of 55°, as the spacecraft flies towards the scene. Then, 150 seconds later, or when the satellite has moved approximately 1000km forward along the ground track, a second observation is made of the same scene at the sub-satellite point, as shown in Figure 3.5.

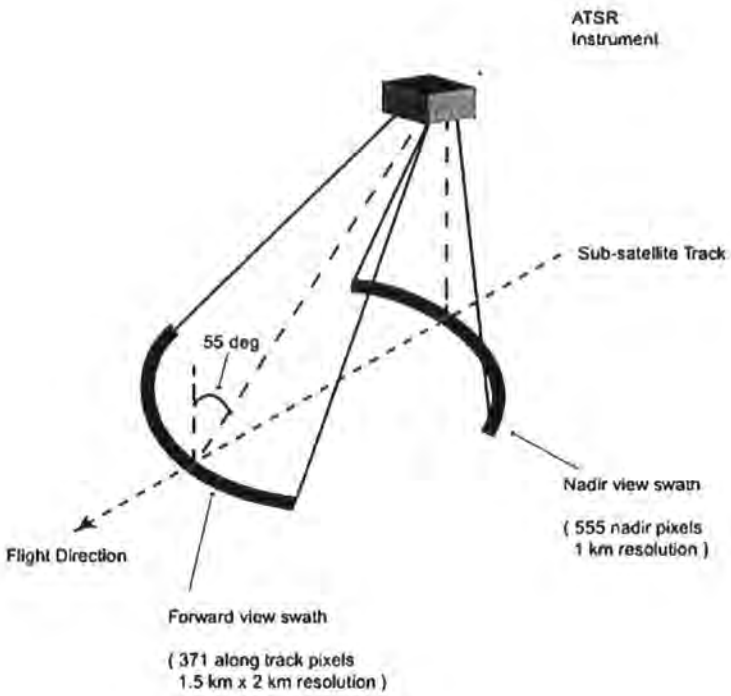


Figure 3.5 AATSR viewing geometry Source: ESA (2005)

The primary mission objective of the AATSR instrument is to extend the long-term consistency of global sea surface temperature (SST) measurements started with ATSR-1 and continued with ATSR-2. Thus, the sensor has thermal infrared channels measuring upwelling radiance from land and ocean surface and atmosphere at 3.7, 11 and 12 μm. SST is calculated from the 11 and 12μm channels during the day and the 11, 12 and 3.7μm channels at night based on their calibrated top-of-atmosphere brightness temperatures (*BT*) values. Very high levels of accuracy and precision are required to support global climate monitoring and change detection. Therefore, the AATSR instrument and ground-processing system are required to produce SST retrievals routinely from the corresponding *BTs* with an absolute accuracy better than 0.3K; globally, both for a single sample and when averaged over areas of 0.5° longitude

by 0.5° latitude, under certain cloud free conditions (i.e. >20% cloud free samples within each area http://envisat.esa.int/dataproducts.aastsr/CNTR1-1.htm).

But of what benefit is AATSR to land remote sensing? The thermal bands used for SST retrieval are also available over land and are used to retrieve land surface temperature (LST) in the AATSR gridded (1 km) product. Algorithms for deriving LST using split-window radiances are sufficiently advanced that accuracies of 1-3 K are possible. Better accuracies (~ 1 K) are obtained at night when differential surface heating is absent. Measurements of radiance over exceptionally hot targets such as deserts, burning vegetation and volcanic eruptions are also possible using AATSR's "low-gain" mode. This prevents saturation of the thermal channels and applies to targets with an upper limit of 500°C.

The AATSR sensor also includes three visible/near-infrared channels centred at 0.55, 0.67 and 0.87μm. These were first introduced on ATSR-2 and have extended the instrument's capabilities over land, particularly for the study of vegetation. Much of the time, the basic calibrated top-of-atmosphere (TOA) reflectance measurements from the AATSR visible and near infrared channels are used for studies of vegetation quantity and quality. In order to cope with all possible normal variations in brightness over the Earth's surface without saturation whilst maximising the accuracy of the measurements, the gain and offset of the visible channels is selectable in flight. These channels have a signal to noise ratio of 20:1 at 0.5% spectral albedo and measure top of the atmosphere radiances to an absolute accuracy of 5% over its entire range.

### 3.6.1 Processing AATSR Data

Interactive catalogues are available for browsing the European Space Agency (ESA) earth observation data (http://www.envisat.esa.int/services/). Table 3.4 displays specific characteristics of AATSR data used in this research.

Table 3.4 Characteristics of AATSR data used for the study

| Date of image acquisition | Satellite overpass (UTC) | Orbit | Track | Frame | Central coordinates Lat | Lon |
|---|---|---|---|---|---|---|
| 281102 | 10:07:24 - 10:09:00 | 3897 | 337 | 3500 | $9^0$ 49'N | $0^0$ 32'W |
| 171202 | 10:10:11 - 10:11:47 | 4169 | 108 | 3500 | $9^0$ 54'N | $1^0$ 14'W |
| 050103 | 10:13:07 - 10:14:43 | 4441 | 380 | 3500 | $9^0$ 51'N | $1^0$ 58'W |
| 090203 | 10:13:04 - 10:14:40 | 4942 | 380 | 3500 | $9^0$ 57'N | $1^0$ 57'W |
| 131104 | 10:04:47 - 10:06:23 | 14146 | 65 | 3500 | $9^0$ 18'N | $0^0$ 04E |
| 021204 | 10:07:35 - 10:09:11 | 14418 | 337 | 3500 | $9^0$ 36'N | $0^0$ 35'W |
| 181204 | 10:04:44 - 10:06:20 | 14647 | 65 | 3500 | $9^0$ 19'N | $0^0$ 04'E |
| 250105 | 10:10:25 - 10:12:01 | 15191 | 108 | 3500 | $9^0$ 37'N | $1^0$ 18'W |

AATSR nadir-view gridded brightness temperature and reflectance data covering the Volta area

The above datasets were selected for two principal reasons: day-time images for temperature extraction and coincidental MODIS dates for sensor inter-comparison. ENVISAT imagery such as AATSR has unique data formats (*.N1) whose processing requires dedicated tools. The ESA Basic ERS & Envisat AATSR and [2]MERIS Toolbox (BEAM) (Appendix 3.3) is one such tool. The BEAM is a collection of executable tools and an application programming interface which have been developed to facilitate the utilisation, viewing and processing of ESA's MERIS, AATSR and ASAR data. BEAM is particularly useful for: (1) data importing; (2) visual interpretation; (3) image geo-referencing; and (4) band arithmetic and image statistical analysis.

[2] MERIS = Medium Resolution Imaging Spectrometer; ASAR = Advanced Synthetic Aperture Radar

### *3.6.1.1 Geo-referencing*

The *Tools* menu encapsulates key processing algorithms such as map projection, band arithmetic, orthorectification, image subsetting, mosaicing and atmospheric correction. Its map projection functions were used to re-project images to UTM-Automatic (WGS84) using the *nearest neighbour* resampling method. This assured co-registration of multi-temporal datasets.

### *3.6.1.2 Atmospheric Correction*

The BEAM-SMAC Processor v.1.4 implements the Simplified Method for Atmospheric Correction (SMAC) as described by Rahman and Dedieu (1994). The SMAC is a semi-empirical approximation of the radiative transfer in the atmosphere; with the satellite signal written as the sum of the following components: (1) 2-way gaseous transmission; (2) atmospheric spherical albedo; (3) total atmospheric transmission; (4) Rayleigh scattering; and (5) aerosol scattering. The well established 6S code was used in developing the SMAC algorithm. Applying top-of-atmosphere (TOA) radiances, empirical surface pressure values, ozone content, water vapour and continental aerosol depth as inputs, the SMAC algorithm was used to correct atmospheric defects and to convert top-of-atmosphere temperature to surface values, expressed as degrees Kelvin (K). The BEAM fully supports the widely readable Geo-TIFF form using its image exporting functions.

### *3.6.1.3 AATSR Geophysical Products*

Previous studies by Prata (2000, 2002) have developed the theoretical basis for extracting AATSR-based land surface temperature (LST). Several application examples following Prata's work are now recorded in the research by Coll *et al.* (2004),

(2005) and Sória & Sobrino (2005). ESA has also provided a comprehensive review of AATSR capabilities at http://envisat.esa.int/workshops/meris_aatsr2005/; however, most of the articles focus on LST. Only a few articles derive vegetation products from AATSR reflectance bands. This is one of the products that is considered in Chapter 7.

## 3.7 MODIS Data

The Moderate Resolution Imaging Spectroradiometer (MODIS) is a key instrument aboard the Terra (EOS AM) and Aqua (EOS PM) satellites. The Terra space craft was launched in December 1999. Its orbit around the Earth is timed so that it passes from north to south across the equator in the morning, while Aqua passes south to north over the equator in the afternoon. Terra MODIS and Aqua MODIS are viewing the entire Earth's surface every 1 to 2 days, acquiring data in 36 spectral bands, or groups of wavelengths (see Table 3.1). Data from the MODIS instrument is now helping to improve our understanding of global dynamics and processes occurring on the land, in the oceans and in the lower atmosphere. NASA and the USGS has provided elaborate information (e.g. http://daac.gsfc.nasa.gov/MODIS/products.shtml) about MODIS products and the role the sensor can play in the development of validated, global, interactive Earth system models to help predict global change accurately and to assist policy makers in making sound decisions concerning the protection of our environment. Table 3.5 displays selected MODIS imagery for this research.

Table 3.5 Characteristics of TERRA-MODIS data used for this study

| Date of image acquisition | Satellite overpass (UTC) | Orbit | Central coordinates Lat | Lon |
|---|---|---|---|---|
| 291102 | 10:50:00 - 10:55:00 | 15685 | $09^0$ 49'N | $00^0$ 32'W |
| 191202 | 10:35:00 - 10:40:00 | 15976 | $09^0$ 54'N | $01^0$ 14'W |
| 040103 | 10:25:00 - 10:30:00 | 16209 | $09^0$ 51'N | $01^0$ 58'W |
| 090203 | 10:10:00 - 10:05:00 | 16733 | $09^0$ 57'N | $01^0$ 57'W |
| 131104 | 10:30:00 - 10:35:00 | 26097 | $03^0$ 54'N | $00^0$ 53$^0$E |
| 021204 | 11:00:00 - 11:05:00 | 26374 | $06^0$ 83'N | $07^0$ 51$^0$E |
| 181204 | 11:00:00 - 11:00:00 | 26607 | $07^0$ 91'N | $07^0$ 32$^0$E |
| 250105 | 10:25:00 - 10:30:00 | 27160 | $09^0$ 37'N | $01^0$ 18'W |

### 3.7.1 Processing MODIS Data

A range of MODIS products exists. The Level 1B product remains one of the most freely available satellite datasets and of immense value to Earth systems research. Individual daily MODIS scenes can be obtained for any part of the Earth. The files are already geocorrected and have a spatial resolution of 1 km. The 36-band image data are interspersed through 85 total bands in each file and the data are stored as digital numbers in 16 bit unsigned integer format. These need to be converted to radiance values and then to surface reflectance and/or brightness temperature values. The Terra file names begin with MOD021KM with a generic ordering reference as Calibrated Radiances 5-Min L1B Swath 1km (http://edcimswww.cr.usgs.gov/pub/imswelcome).

The hierarchical data format (HDF) is a used for MODIS data, given their incredibly large files. Only very few image processing software (e.g. ERDAS Imagine v.8.7) have capacity to import such data files. Even then, reading MODIS 85 layers for each dataset, regenerating their statistical information and re-projecting them to UTM can take a prohibitively long time. One of the easiest processing options is using NASA's Earth Observing System (EOS) HDF-EOS to GeoTIFF (HEG) Tool (Appendix 3.4).

### *3.7.1.1 Geo-referencing*

The HEG Tool helped to geo-reference (nearest neighbour interpolation method), re-project and convert images to Geo-TIFF format for subsequent qualitative and quantitative analysis.

### *3.7.1.2 Calibration of MODIS L1B Data*

**(a) Reflective Solar Bands (Bands 1 & 2)**

The MODIS Level 1B generates two calibrated data products for the Reflective Solar bands (RSB) - the reflectance and the Earth-exiting radiance (MODIS User Guide, 2003). Writing these two products in floating-point format to the Level 1B Earth view product files would make the file sizes excessively large. Instead, the Level 1B writes a 16-bit scaled integer representation of the calibrated digital signals measured by the MODIS, from which the reflectances and radiances can be calculated from two pairs of scale and offset terms written as attributes to the reflective band datasets. These two pairs are derived from the calibration parameters that are input to Level 1B as look up tables. Level 1B corrects the raw digital signals measured at the Reflective Band detectors, *DN,* for all known instrumental effects, to produce corrected digital signals, *dn**. Level 1B then adjusts the values of *dn** for the effects of variations in calibration parameters from detector to detector within each band so that one pair of calibration terms applies to every detector in each band. The values of *dn** adjusted in this way, called *dn***, are scaled to the 16-bit representation in the RSB science datasets.

The values of *dn*** over the dynamic range of $[D_{min}, D_{max}]$ are scaled to a range of [0, 32767] and placed into an integer variable. The values of $D_{max}$ and $D_{min}$ are input

to Level 1B through look up tables, and are indexed by band only. Figure 3.6 shows the relationship between *dn*** and the scaled integer values, *SI*.

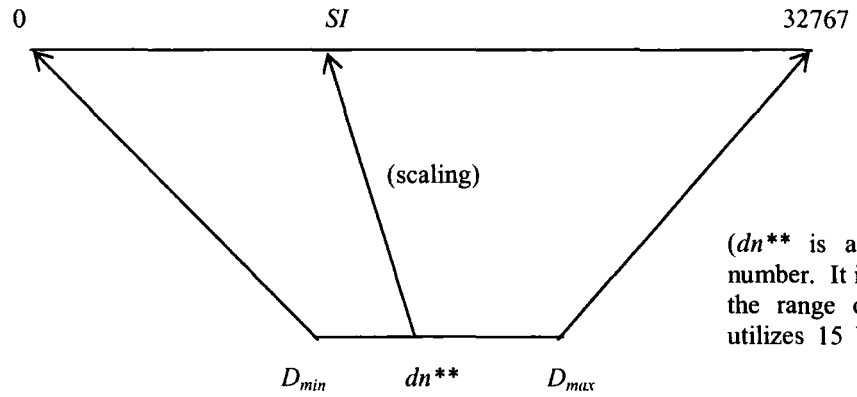


(*dn*** is a 32-bit floating point number. It is scaled to an integer in the range of 0 to 32767, which utilizes 15 bits of a 16-bit integer

Figure 3.6 Relationship MODIS between *dn*** and scaled integers (SI)
Source: NASA's MODIS L1B Product User's Guide

The relationship between *dn*** and *SI* is given by the equation:

$$dn^{**} = corrected\_counts\_scale\ (SI - corrected\_counts\_offset) \qquad 3.1$$

where, $corrected\_counts\_scale = (D_{max} - D_{min}) / 32767$, and 3.1a

$$corrected\_counts\_offset = -(32767\ D_{min})/(D_{max} - D_{min}) \qquad 3.1b$$

The values of *corrected_counts_scale* and *corrected_counts_offset* are computed inside Level 1B and are written as attributes to the science datasets. Thus, *dn*** is easily recovered from *SI* values by reading the attributes and applying Equation 3.1.

**(b) Thermal Emissive Bands (Bands 31 & 32)**

The Level 1B data also generate radiances in 32-bit floating-point format for each thermal emissive band measurement. It scales these radiances to an integer representation to the Earth View 1km Emissive science datasets. The values of

radiance, $L$, over the dynamic range of $[L_{min}, L_{max}]$ are scaled to a range of [0, 32767] and placed into an integer variable. The values of $L_{max}$ and $L_{min}$ are input to Level 1B through look up tables and are indexed by band only. Figure 3.7 shows the relationship between $L$ and the scaled integer values, $SI$. Values of radiance that lie outside the range of $[L_{min}, L_{max}]$ are set to $L_{min}$ or $L_{max}$ as appropriate.

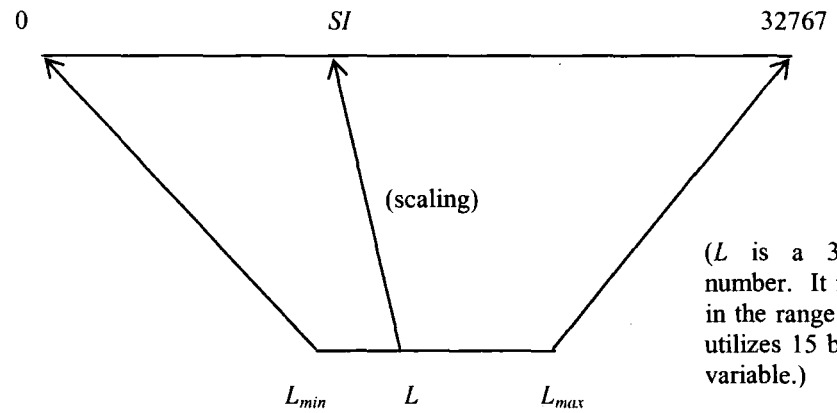


Figure 3.7 Relationship between Thermal Emissive Band Radiance ($L$) and its scaled integer representation. Source: NASA's MODIS L1B Product User's Guide

In the Level 1B product scaled integer SDS (which is a 16-bit unsigned integer data type), the least significant 15 bits are used for the valid range of the scaled value of $\boldsymbol{L}$. The most significant bit of the 16-bit integer is reserved to indicate invalid data. Thus, the dynamic range of valid data in integer representation is [0, 32767] and any value greater than 32767 represents invalid (or unusable) data. The relation between $\boldsymbol{L}$ and $\boldsymbol{SI}$ is given by an equation of the form:

$$L = radiance\_scales\ (SI - radiance\_offsets) \qquad 3.2$$

where, $radiance\_scales = (L_{max} - L_{min}) / 32767$ 3.2a

and, $radiance\_offsets = -(32767\ L_{min})/(L_{max} - L_{min})$ 3.2b

The values of radiance_scales and radiance_offsets are computed inside Level 1B and written as attributes to the Science data sets. Thus, radiance may be simply recovered from *SI* by reading these two attributes and applying Equation 3.2.

In this case, the *scale and offset* coefficients for reflectance (Band 1 & 2) and emissive bands (Band 31 & 32) were extracted using NASA's specialised HDF Explorer Toolbox. The coefficients for each MODIS scene used in this research are given in Appendices 3.5 & 3.6.

### *3.7.1.3 Atmospheric Correction*

Several algorithms are applied to remove the effects of cirrus clouds, water vapour, aerosols and atmospheric gases from MODIS bands. The well-known split-window algorithm (Becker & Li, 1990) originally developed for NOAA-AVHRR Bands 4 & 5 was applied. Cai *et al.* (2005) have recently described similar split window methods which use MODIS Band 31 (10.78 – 11.28μm) and Band 32 (11.78 – 12.27μm), firstly to correct for atmospheric defects and secondly to derive land surface temperature ($T_s$). This procedure was followed here.

Table 3.6 Land surface parameters and their key data sources

| Parameter | Variable | Data source (s) | Application |
|---|---|---|---|
| 1. Precipitation (mm) | $P$ | Ground-climate and radar data | Partitioning into runoff and evapotranspiration (regional water balance equation) |
| 2. Air temperature ($^0$C) | $T_a$ | Ground-climate data | Cross validation for remotely sensed TIR data. Calculation of radiative fluxes. |
| 3. Surface temperature (K) | $T_s$ | Remote sensing thermal infrared *TIR* data | Sub-input for regional evapo-transpiration modelling |
| 4. Air humidity (%) | $h$ | Ground-climate data | Same as above |
| 5. Wind speed (m s$^{-1}$) | $u$ | Ground-climate data | Same as above |
| 6. Net radiation (W m$^{-2}$) | $R_n$ | Remote sensing *VIS* data, but also determinable from daily sunshine (ground) data | Main input for regional evapo-transpiration modelling |
| 7. Surface albedo (-) | $\alpha$ | Remote sensing *VIS* spectral data | Sub-input for *ET* |
| 8. Emissivity (-) | $\varepsilon$ | Same as above | Same as above |
| 9. Vegetation index (-) | *NDVI* | Calculable from ratio between VIS & NIR data | Same as above |
| 10. Residual soil moisture (m m$^{-3}$) | $\theta_s$ | Calculated as rest term from $P$ less *ET* and $Q$ | Main input for water balance |
| 11. Soil temperature (K) | $T_g$ | Empirical sources (See Zu *et al., 1999*; Bastiaanssen, 2000) | Input for calculating ground heat flux $G$ |
| 12. Sensible heat flux (W m$^{-2}$) | $H$ | Same as above | Main input for regional energy balance |
| 13. Runoff (mm) | $Q$ | Ground-hydrology data (measurement at catchment outlet) | Main input for water balance<br>*NB:* May not be immediately needed in the modelling scheme, but can be useful manipulative information for validating runoff data |
| 14. Digital elevation model (m) | *DEM* | USGS generated online data (coarse spatial resolution (250m) USGS GTOPO data) | |

## 3.8 Field Research

The quality, accuracy and relevance of Earth science research employing remotely sensed datasets depends hugely on ground data generated from fieldwork.

This motivated an 8-week campaign in the Volta basin from 10th November 2004 – 7th January 2005.

## 3.8.1 Materials and Methods

The fieldwork strategy focussed mainly on minimum ground measurements and compilation of historical data from relevant institutions. The intention of the fieldwork was to build an environmental database, first, to complement satellite imagery and secondly, to provide validation inputs to such imagery (Table 3.5). Thus, time series climatic data (e.g. rainfall, air temperature, humidity and wind speed) were compiled from a large database established at the GLOWA-Volta Project and the Ghana Met Office in Accra. Field mobility was promoted using geo-positional systems (GPS) survey. Technical, logistics and manpower support was also received from Tamale's University of Development Studies and the CSIR Water Research Institute.

### *3.8.1.1 Materials*

Table 3.7 displays an assembly of equipment deployed for the fieldwork. Notably, Table 3.7 does not to fully represent *in situ* measurements needed to support satellite image interpretation and/or validation. Bastiansseen (2000) has suggested a wide range of land, vegetation and atmospheric parameters which may be measured to support energy and water balance studies, e.g. surface albedo, leaf area index, net radiation, soil moisture, etc. In this case, practical constraints such as inadequate research budget, academic time frame, overseas travel difficulties and lack of relevant equipment, made minimum fieldwork the only practicable option.

3.7 Field equipment and their uses

| Type of equipment | Specification | Field Uses | Activity Record |
|---|---|---|---|
| Pocket-sized iPod loaded with ArcPad (GIS) software | HP iPAQ hx 2795 Pocket PC | Provision of digital maps of the study for navigation purposes | Weather and software constraints did not fully support direct upload of surface measurements |
| Hand-held GPS | Garmin GPS-60 Waterproof System | Recording and storage of ground control points in geographic coordinates as well as elevation data | About 178 points were randomly compiled over a total area of about 264 $km^2$ |
| River flow meter | AUT-E30 meter with low flow propeller | Measurement of river flow | Spot flow measurements were carried out the Kalarakun river outlet |
| Laser beam distance meter with metal tape | Makita Ultrasonic UML-15 rubber housing set | Sample measurement of vegetation heights | Different vegetation types and their heights were measured. The average values were recorded. |
| Double-ring infiltrometer | Eijkelkamp standard "steel" double ring infiltrometer set | Measurement of infiltration rates | Nine sites were randomly sampled based on diversity of their vegetation and land cover types |
| Rain gauge | Copper-type conical rain gauge | Measurement of daily rainfall | No rainfall was recorded throughout the period of fieldwork |
| Thermal loggers | ONSET Computer HOBO® 4-Channel Outdoor Data Logger. | Measurement of air temperature | Air temperature was measured at five main sites at 10minutes intervals and the daily average recorded. |
| Soil auger & digger | The Ghana Soil Research Institute Auger & Digger Set | Collection of soil samples | Two samples at average depths of 0-10 and 20-40cm were collected for laboratory analysis |
| Digital camera | Samsung 4.0 Mega Pixels, $12^x$ Zoom Digimax V4 | Digital photographic copies of land cover and field activities | Photographs of land cover and other features were used to classify satellite images. |
| Laptop computer loaded with standard software | Toshiba: Celeron 2.20 GHz CPU; 192 MB Ram with 40GB hard disk | Storage and analysis of field data | Data stored on the HOBO instrument was transferred and analysed. |

### *3.8.1.2 Methods*

#### (a) Instrumentation

Using a true-colour composite Landsat ETM+ image (Figure 3.8a) and GPS as survey guide, five parcels with relatively homogeneous land cover types were identified for instrumentation (Figure 3.8b). Rain gauges and thermal loggers were installed at these sites. Local volunteers were trained to monitor the equipment and

take rainfall readings appropriately (Figure 3.8b). Infiltration measurements were done *in situ.*

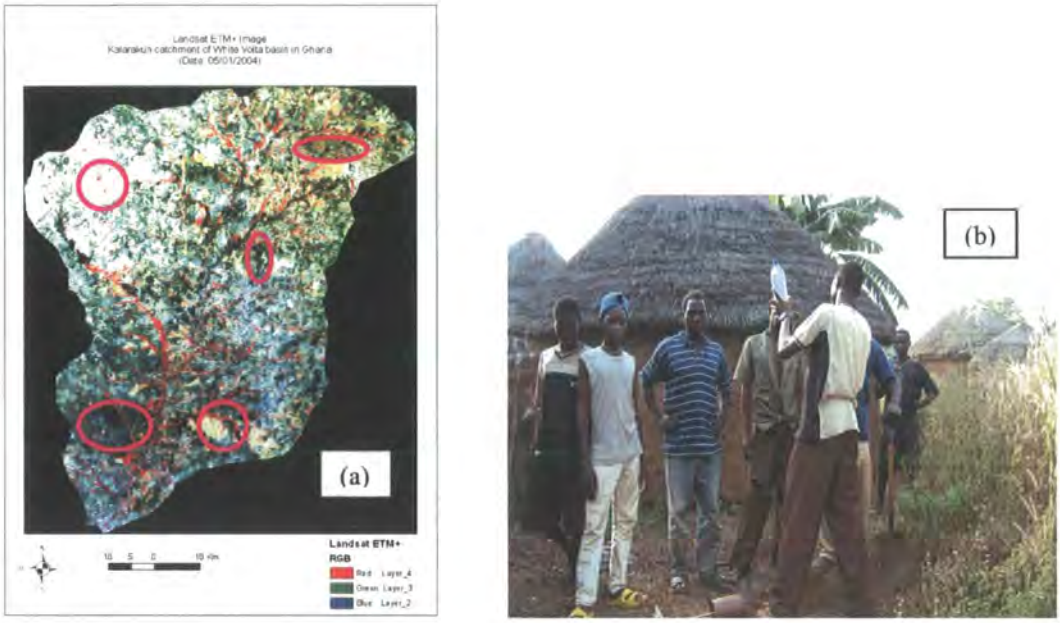


Figure 3.8 Field instrumentation (a) Relatively homogeneous land cover types selected for detailed study are shown in pink borders. (b) A training session to install, monitor and read rain gauges at the topmost right site in (a).

A total of 178 geographic co-ordinates and ground elevation (ground control) points were recorded with GPS. These were later used as aid to geo-reference, interpret and classify satellite imagery.

### (b) Soil & Vegetation Characterisation

Extensive soil and vegetation characterisation has been carried out in the Volta basin by the GLOWA-Volta experimental team (e.g. Agyare, 2004; Duadze, 2004). Thus, emphasis here was limited to local soil hydraulic properties and vegetation cover. The purpose of this was two-fold: (1) elucidation of soil moisture dynamics; and (2)

acquisition of improved ground knowledge to support accurate classification of satellite imagery.

Random soil samples taken from nine stations (five test sites [Figure 3.8] inclusive) were analysed at Tamale's Savannah Agricultural Research Institute (SARI). The soil textural properties were examined using both local and FAO classification systems. Soil infiltration rates were also measured using the *Eijkelkamp* double-ring infiltrometer method (Appendix 3.7). Vegetation was characterised employing a local tree-counting method [number of woody trees per hectare (ha)] originally developed by Agyepong *et al.*, (1999) and now modified by Duadze (2004) as follows: (1) closed savannah woodland of tree density >150 trees $ha^{-1}$; (2) open savannah woodland, 75-150 trees $ha^{-1}$; (3) riparian (riverine) vegetation, <50 trees $ha^{-1}$; and (4) mixture of grasses, shrubs and trees, <20 trees $ha^{-1}$ (Figure 3.9).

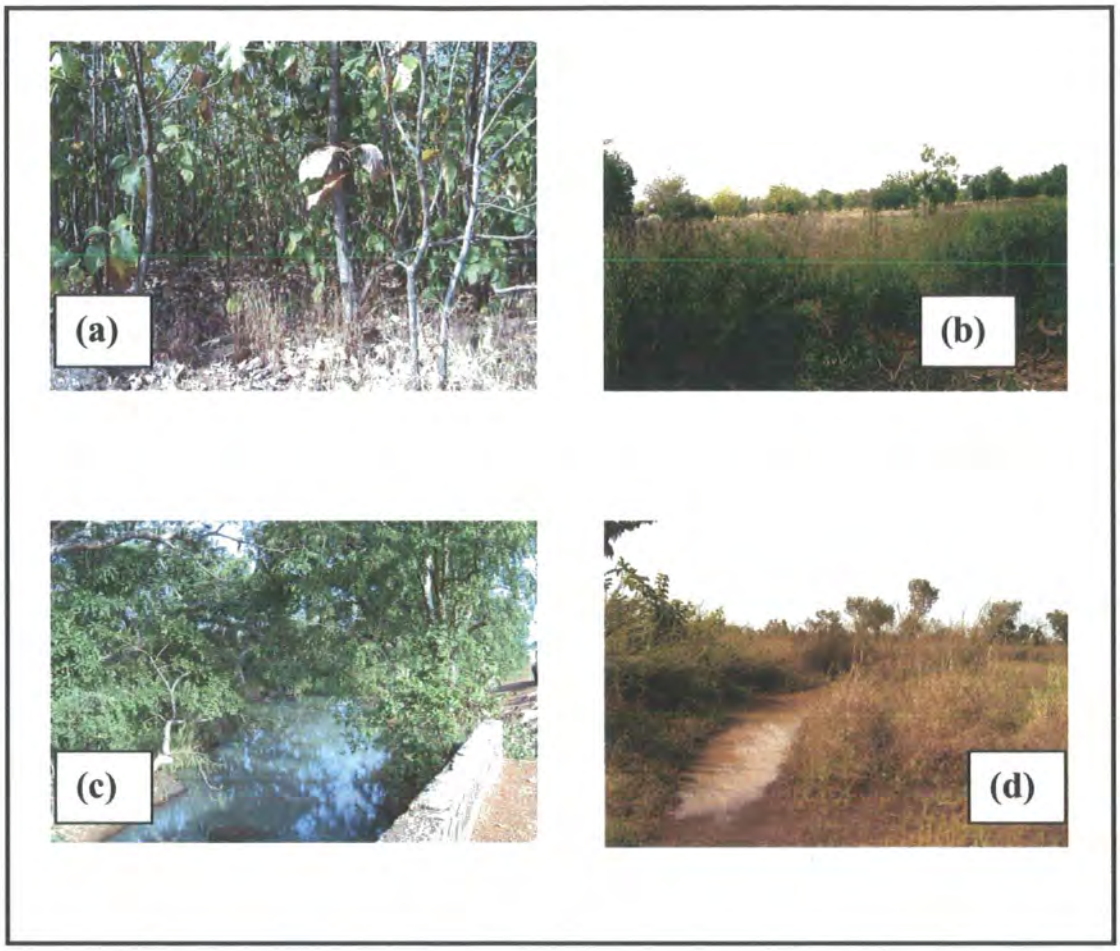


Figure 3.9 Main vegetation classes of the Volta basin. (a) Close savannah woodland of tree density >150 trees $ha^{-1}$, (b) Open savannah woodland, 75-150 trees $ha^{-1}$, (c) Riparian (riverine) vegetation, <50 trees $ha^{-1}$ and (d) Mixed grass, shrub & tree vegetation, <20 trees $ha^{-1}$ ha.

Based on surveying principles and guided by the Landsat ETM+ image shown above, the average tree count of two random transects (30 x 30 m) per site was taken. The aggregation of this result eventually provided a useful validation source for medium-resolution satellite imagery (e.g. MODIS). Agyepong *et al.* (1999) have recognised this as an extremely helpful approach for estimating fractional vegetation-cover using empirically developed coefficients.

**Land Cover Classification Using Landsat ETM+ Data**

Although existing land cover maps (e.g. Agyepong *et al.*, 1999) provided useful information for fieldwork, they were not entirely suitable for the current research. First of all, the maps were outdated and required extensive updating. Secondly, they provided country-wide (Ghana) land cover classes without specific details of hydrological interest. Thirdly, the maps were mainly available in analogue form which required extra effort to reproduce them into digital formats. Therefore, a new land cover map of specific interest to the study was derived from a Landsat ETM+ scene acquired on 5$^{th}$ January 2004. The image classification procedure is described in a step-wise order as follows:

**Step 1: Selection of Training Samples**

Using ERDAS Imagine image processing tools, training sites were first selected and validated based on site GPS surveys, analysis of aerial photographs (1:20,000) and existing land cover/use maps. This process was guided using covariance matrix based on histogram and signature statistics and a set of parametric decision rules (Leica Geosystems, 2003).

**Step 2: Discrimination of Training Samples**

In the second step, the training samples were evaluated using a variety of spectral separation methods such as querying elliptical boundaries on scatter plots, feature class separation based on statistics, contingency matrices and the Jeffries-Matusita divergence algorithm (Leica Geosystems, 2003). "Divergence" is a measure of statistical separability between two groups or classes (Jensen, 1983) and serves as an indirect measurement of classification accuracy.

**Step 3: Image Classification**

The third step involved scene classification using the widely used maximum likelihood classification (MLC) algorithm (e.g. Colby & Keating, 1998; Jensen, 1983). Apart of its wide application, several papers (e.g. Colby & Keating, 1998) have examined the spatial interpolation techniques of the MLC method and have documented its relative accuracy in assigning pixel objects of similar spectral response to specific land cover classes.

**Step 4: Accuracy Assessment of the Classified Image**

The final step involved land cover classification accuracy assessment, results of which are shown later in Chapter 7. Here, two complementary error measurement methods were applied: (1) the accuracy assessment CellArray (AACA), and (2) the Kappa coefficient methods (Leica Geosystems, 2003). The AACA was used to compare the classified image with the reference data.

The CellArray is simply a list of class values for the pixels in the classified image file and the class values for the corresponding reference pixels. In this case, the reference pixels were supplied using ground truth data (field samples) whereas the CellArray data were retrieved from the image file. The Kappa coefficient was used to express the proportionate reduction in error generated by the classification process compared with the error from a completely random classification. For example, a Kappa coefficient of 0.70 implies that the classification process avoided 70% of the errors generated from a completely random classification.

### (c) Temperature monitoring

In this research context, savannah temperature monitoring is important for three main reasons: (1) energy balance modelling, (2) source of evaluation data for thermal imagery, and (3) extrapolation of instantaneous measurements to cover the diurnal cycle. Thermal probes, connected to a Tempcon® HOBO-H8 data logger (Appendix 3.8) were installed at the five key stations. For consistency, the data logger was connected as follows: Channel 1 - air temperature; Channel 2 – 0 cm soil depth; Channel 3 - 5 cm depth and Channel 4 - 30 cm depth. The soil probes were inserted with minimal disturbance in order to preserve the structural integrity of the soil profile. Temperatures were monitored at 10-minute intervals for 15 days. The records were downloaded using BoxCar Pro® 3.1v software. This was then aggregated into hours and daily values using standard database and spreadsheet.

### (d) GLOWA-Volta Data Archive

The GLOWA-Volta Office in Accra has a large store of climate and environmental research data on the Volta basin. A considerable amount of time was dedicated to exploring this database and retrieving relevant ground data. Chapter 4 importantly depends on this effort to estimate local-scale evapotranspiration at the Tamale district.

### (e) Field Constraints

The risks and hazards associated with field work in remote tropical catchments such as the Volta are a well-known problem (Agyapong *et al.* 1999). Apart from health and safety issues, vehicle, equipment and software breakdown can present great difficulties. Wild fires, for example, destroyed one of our temperature probes.

Assembling a full complement of the required field equipment can also be highly problematic. This notwithstanding, a considerable amount of data was generated to support this research.

## 3.9 Summary

This chapter has provided a detailed description of the range of satellite imagery deployed for the current research. A detailed account of their processing methods has also been given. The value of satellite imagery as parameterisation inputs for regional land surface schemes and their key application areas have also been described. This is followed by description of field research aimed at generating ground data as complementary and/or validation information for remote sensing measurements. The relevance and limitations of such ground data has also been highlighted. It is worth mentioning that this chapter was not designed to provide full a description of algorithms for retrieving land surface parameters from satellite imagery; this is the central objective of Chapter 5.

# Chapter 4

# Local-Scale Evapotranspiration Modelling

## 4.1 Introduction

This chapter has two main parts - the first part describes the local-scale evapotranspiration (*ET*) modelling approach, which is an important part of the entire research methodology (see Section 1.3 of Chapter 1), while the second part discusses the model results. Detailed meteorological measurements (10-minute observations from data loggers) are now available for estimating actual evapotranspiration (*AE*) in selected Guinea savannah catchments in West Africa (by courtesy of the GLOWA-Volta Project). In this study, the data has been used to calculate potential evapotranspiration (*PE*) in the Tamale district based on the widely used Penman-Monteith equation. The potential of data-efficient empirical models such as the Thornthwaite method has also been examined to see whether they can provide an alternative solution to the more data-intensive Penman-Monteith method. On the basis of the above methods, *AE* has been calculated using the Grindley (1970) soil moisture accounting method. The validation strategy includes: (1) evaluation of potential evapotranspiration (*PE*) based on adjusted local evaporation records using the Class-A pan method; and (2) evaluation of calculated *AE* based on [1]scintillometer eddy correlation measurements by the GLOWA-Volta research team.

[1] The Dutch-made scintillometer instrument is used to measure turbulent intensity fluctuations of the refractive index of air. The device consists of a transmitter and a receiver which emits infrared light (0.94μ) parallel to the Earth's surface towards the receiver. The receiver which can be placed up to a distance of 5km analyses the intensity fluctuations (turbulent eddies) expressed as $C_n^2$, the structure of the

Evapotranspiration (*ET*) refers to the combination of several processes by which water is lost from the Earth's surface by evaporation. In a catchment, evaporation includes water loss from open water sources, soil and vegetated surfaces (Shaw, 1994). Evaporation and transpiration occur simultaneously and there is no easy way of distinguishing the processes. For evaporation to proceed, energy is required to change the state of water molecules from liquid to vapour. Direct solar radiation and to a lesser extent, the ambient temperature of the air provides this energy. The controlling mechanism for removing water vapour from evaporating surfaces is the difference between the water vapour pressure at a surface and that of the surrounding atmosphere. As evaporation proceeds, the surrounding air becomes gradually saturated and the process slows down and might even stop if the humid air is not transferred to the atmosphere. The replacement of the saturated air with drier air depends greatly on wind speed. Hence, solar radiation, air temperature, air humidity and wind speed are climatological parameters to consider when assessing the evaporation process (FAO, 1998).

Transpiration, on the other hand, consists of the vaporization of liquid water contained in plant tissues and the vapour removal to the atmosphere. Plants predominantly lose water through their stomata – small openings on the leaf through which gaseous and hydraulic exchanges take place. Transpiration, like direct evaporation, depends on the energy supply, vapour pressure gradient and wind conditions. The soil water content and the ability of the soil to conduct water to the

---

refractive index of the air. The device allows measurements of heat transfer between the Earth's surface and the air above it referred to as sensible heat flux.

roots also determine the transpiration rate. Other factors include vegetation characteristics, soil and environmental conditions.

As indicated above, the central concern of this chapter is numerical modelling of *AE* based on local-scale climatic variables measured in the Tamale savannah district. For such complex landscapes, accurate estimation of *AE* is not easy. Nevertheless, the FAO (1998) has proposed estimation of reference or potential evapotranspiration (*PE*); a quantity which makes reference to a hypothetical well-watered grass after which a correction factor is applied to obtain *AE*. In the literature (e.g. Allen *et al.*, 1994; Shaw, 1994; Doorenbos & Pruitt, 1977), three general approaches are used to calculate *PE* from evaporating surfaces. The first one is the mass transfer or vapour flux method:

$$PE = f(u)\ (e_s - e_d) \qquad (4.1)$$

where $PE$ = evaporation rate, $f(u)$ = function of wind speed and $(e_s - e_d)$ = saturated vapour deficit. This formula shows that evaporation is related to wind speed and is proportional to the vapour pressure deficit (i.e. difference between the saturation vapour pressure at the temperature of the evaporating surface and the actual vapour pressure of the surrounding air). This formula attributable to Dalton in the 19$^{th}$ century has been widely used to explain the governing physics of evaporation, see Figure 4.1 (reproduced from Shaw [1994]).

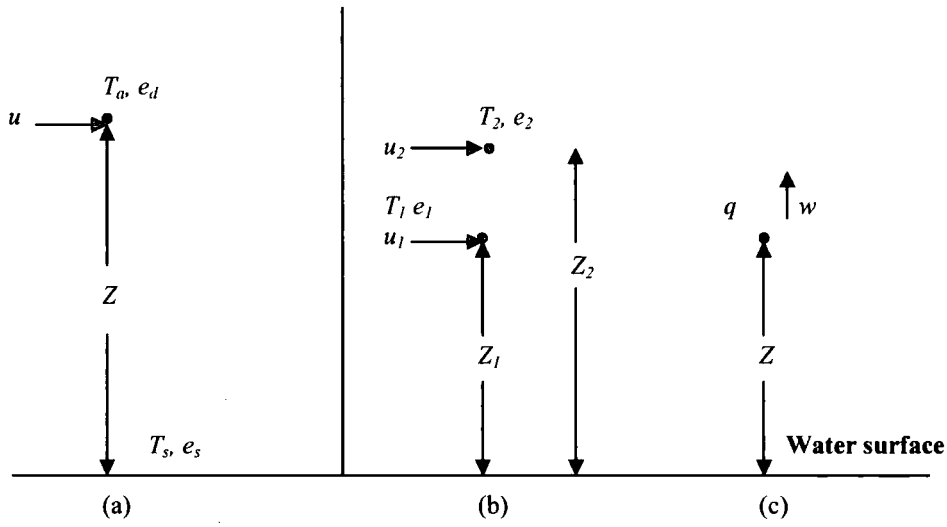


Figure 4.1 Measurements for mass transfer (a) and (b) $T_s$ = temperature of the water surface, $T_a$ = air temperature at height $z$ ($T_1$ and $T_2$ at two heights $z_1$ and $z_2$), $e_s$ = saturated vapour pressure of air at water surface, $e_d$ = vapour pressure of air ($e_1$ and $e_2$) at the two heights, and $u$ = horizontal wind velocity at height $z$. (c) $w$ = vertical wind velocity at height $z$, $q$ = specific humidity at height $z$. (Source: Shaw, 1994)

Research has shown that $f$(u) in Equation 4.1 depends on the height at which wind and temperature measurements are made; the bulk aerodynamic function may also take two forms as follows: $a(b + u)$ and $Nu$, where $a$, $b$ and $Nu$ are empirical mass transfer coefficients (e.g. Allen, 1986; Harbeck & Meyers, 1970; Blaney & Criddle, 1950; Penman, 1948). Penman (1948) used the first form to solve for $PE$ when he experimented with thermometers placed 2m above the surface in the UK. The final form of $f$(u) resulted in the following relationship (Shaw, 1994):

$$PE = 0.35(0.5 + \frac{u_2}{100})(e_s - e_d) \qquad (4.2)$$

In Australia and the USA, $f(u)$ has also been determined in the form of $Nu$ to help calculate evaporation from water bodies, with empirically determined $N$ values ranging from 0.0105-0.0120 (Harbeck & Meyers, 1970). The vapour flux and eddy transfer methods (Shaw, 1994) are other forms of the generic mass transfer method. A second method is the simplified energy balance equation which may be written as:

$$PE = R_n - H - G_0 \qquad (4.3)$$

where $PE$ = energy for evaporation, $R_n$ = net radiation (i.e. heat energy available), $H$ = energy for heating the air and $G_0$ = soil heat flux. The values of $LE$ and $H$ can be defined by the aerodynamic parameters in Equation 4.3 and $G_0$ is often ignored as a minor component of the energy balance. A third $PE$ method is the combined mass transfer-energy balance method of which the Penman (1948) method is a very good example. Its improved variant, the Penman-Monteith model, constitutes the method used in this study.

## 4.2 Data and Methods

Table 4.1 shows a summary of meteorological data logged at 10-minute intervals in 2002 and 2004 (GLOWA-Volta database) and aggregated into daily values. A 40-year record (1961-2000) of monthly temperature and rainfall has also been compiled from the Ghana Meteorological Office database for the same purpose. A summary of this record is shown in Table 4.2.

Table 4.1 Summary of daily meteorological parameters at Tamale GLOWA-Volta site

| | | Temperature ($^0$C) | Relative humidity (%) | Wind speed (m s$^{-1}$) | Soil heat flux (W m$^{-2}$) | Rainfall (mm) |
|---|---|---|---|---|---|---|
| **2002** | Minimum | 17.86 | 28.97 | 1.42 | 0.11 | 0.00 |
| (182 | Maximum | 31.07 | 74.90 | 4.79 | 9.86 | 63.77 |
| days) | **Mean** | **23.18** | **56.31** | **2.68** | **3.69** | **3.02** |
| | Std deviation | 2.75 | 10.55 | 0.62 | 2.61 | 291.07 |
| **2004** | Minimum | 18.68 | 27.80 | 1.19 | 0.10 | 0.00 |
| (137 | Maximum | 29.55 | 73.71 | 5.52 | 9.98 | 43.06 |
| days) | **Mean** | **23.96** | **53.31** | **2.42** | **4.03** | **2.75** |
| | Std deviation | 2.86 | 11.60 | 0.62 | 2.59 | 187.19 |
| | | Pressure (mbar) | Net radiation (W m$^{-2}$) | PAR radiation (W m$^{-2}$) | | Global radiation (W m$^{-2}$) |
| **2002** | Minimum | 984.37 | 19.35 | 4.29 | | 39.38 |
| (182 | Maximum | 992.68 | 207.98 | 66.98 | | 366.28 |
| days) | **Mean** | **988.98** | **107.05** | **37.53** | | **212.95** |
| | Std deviation | 1.97 | 40.36 | 9.78 | | 51.09 |
| **2004** | Minimum | 966.00 | 10.18 | No data | | 29.50 |
| (137 | Maximum | 997.96 | 235.73 | No data | | 544.63 |
| days) | **Mean** | **990.59** | **110.85** | No data | | **229.25** |
| | Std deviation | 4.93 | 51.78 | No data | | 68.33 |

Source: Modified after GLOWA-Volta (2004). PAR = Photosynthetic Active Radiation
**Note:** Where as the 2002 raw dataset consisted measurements for a total of 285 days, the 2004 consisted measurements for 137 days. To present a more meaningful statistical summary, continuous data records for 182 and 137 days, respectively, were used in this table.

### 4.2.1 Penman-Monteith Equation

The Penman-Monteith (Allen *et al.*, 1998; Monteith, 1965) equation is a widely used method for calculating *PE* from meteorological data (Ward, 2000; FAO, 1998; Shaw, 1994). It builds on Penman's initial ideas which combine the physical principles described in Equations 4.1 and 4.2. For catchment hydrology, agriculture and forestry applications, the FAO (1998) recommends the Penman-Monteith method as the sole important method for determining *PE* from meteorological data. The method requires radiation, air temperature, air humidity and wind speed as input data.

Table 4.2 Summary of monthly meteorological parameters at the Tamale station (1961-2000)

| | | **January** | **February** | **March** | **April** | **May** | **June** |
|---|---|---|---|---|---|---|---|
| **Rainfall** | Minimum | 0.0 | 0.0 | 0.0 | 3.1 | 30.1 | 55.1 |
| | Maximum | 60.0 | 91.2 | 145.3 | 239.8 | 351.8 | 314.5 |
| | **Mean** | **3.2** | **9.0** | **46.7** | **81.0** | **122.7** | **155.7** |
| | Std deviation | 10.7 | 16.9 | 35.9 | 52.6 | 53.4 | 66.3 |
| **Temperature** | Minimum | 24.9 | 27.9 | 30.4 | 28.6 | 27.6 | 26.0 |
| | Maximum | 29.1 | 31.8 | 33.1 | 33.3 | 30.7 | 28.5 |
| | **Mean** | **27.5** | **30.2** | **31.6** | **30.8** | **29.2** | **27.3** |
| | Std deviation | 1.05 | 0.85 | 0.76 | 1.14 | 0.78 | 0.64 |
| **Pan** evaporation (Average of nine years: 1976-1993) | Minimum | 239.2 | 267.4 | 278.4 | 243.1 | 229.5 | 191.7 |
| | Maximum | 363.3 | 342.4 | 382.8 | 325.0 | 289.6 | 257.3 |
| | **Mean** | **281.6** | **297.6** | **333.3** | **299.5** | **247.7** | **206.9** |
| | Std deviation | 45.0 | 24.8 | 31.0 | 25.7 | 25.5 | 19.7 |
| | | **July** | **August** | **September** | **October** | **November** | **December** |
| **Rainfall** | Minimum | 20.8 | 45.2 | 111.3 | 4.6 | 0.0 | 0.0 |
| | Maximum | 365.5 | 401.3 | 495.8 | 243.3 | 90.7 | 33.0 |
| | **Mean** | **154.7** | **200.1** | **226.0** | **88.4** | **10.1** | **2.8** |
| | Std deviation | 69.5 | 84.2 | 76.9 | 58.7 | 19.6 | 6.6 |
| **Temperature** | Minimum | 25.7 | 25.3 | 25.3 | 26.7 | 27.0 | 24.8 |
| | Maximum | 27.3 | 27.1 | 27.6 | 29.0 | 30.1 | 28.7 |
| | **Mean** | **26.4** | **26.2** | **26.4** | **27.7** | **28.2** | **27.1** |
| | Std deviation | 0.46 | 0.45 | 0.58 | 0.56 | 0.83 | 1.03 |
| **Pan** evaporation (Average of nine years: 1976-1993) | Minimum | 142.3 | 129.3 | 149.6 | 46.7 | 189.3 | 188.0 |
| | Maximum | 193.5 | 184.9 | 260.4 | 214.3 | 237.3 | 288.0 |
| | **Mean** | **164.1** | **154.4** | **176.0** | **174.6** | **210.5** | **222.7** |
| | Std deviation | 16.4 | 18.5 | 33.3 | 49.8 | 16.7 | 27.5 |

Source: Ghana Meteorological Services Department (2004)

The first procedural requirement of the Penman-Monteith combination method is described by the following relationship:

$$PE = \frac{\Delta(R_n - G_0) + \rho_a c_p \dfrac{(e_a - e_a)}{r_a}}{\Delta + \gamma\left(1 + \dfrac{r_s}{r_a}\right)} \qquad (4.4)$$

where $R_n$ = net radiation, $G_0$ = soil heat flux, $(e_s - e_a)$ represents the vapour pressure deficit of the air, $\rho_a$ = mean air density at constant pressure, $c_p$ = specific heat of the air, $\Delta$ = slope of the saturation vapour pressure-temperature relationship, $\gamma$ = psychrometric constant, and $r_s$ and $r_a$ are the (bulk) surface and aerodynamic resistances.

The transfer of heat and water vapour from the evaporating surface into the air above the vegetation canopy is determined by the aerodynamic resistance as:

$$r_a = \frac{\ln\left[\frac{z_m - d}{z_{om}}\right]\ln\left[\frac{z_h - d}{z_{oh}}\right]}{k^2 u_z} \qquad (4.5)$$

where $r_a$ aerodynamic resistance (s $m^{-1}$), $z_m$ = height of wind measurements (m), $z_h$ = height of humidity measurements (m), $d$ = zero plane displacement height (m), $z_{om}$ = roughness length governing momentum transfer (m), $z_{oh}$ = roughness length governing transfer of heat and vapour (m), k = von Karman's constant (0.41) [-] and $u_z$ = wind speed at height $z$ (m $s^{-1}$). This equation is restricted to neutral stability conditions, i.e. where temperature, atmospheric pressure and wind velocity distributions follow nearly adiabatic conditions (i.e. no heat exchange). Using hypothetical conditions as a function of leaf area index (LAI), the bulk resistance ($r_s$) parameter of Equation 4.5 can reasonably be defined as follows (FAO, 1998):

$$r_s = \frac{r_l}{LAI_{active}} \qquad (4.6)$$

where $r_s$ = bulk surface resistance (s $m^{-1}$), $r_l$ = bulk stomatal resistance of the well-illuminated leaf (s $m^{-1}$), $LAI_{active}$ = (sunlit) leaf area index [$m^2$ (leaf area) $m^{-2}$ soil surface)]. From a wide range of field experiments (FAO, 1998) further simplifications of Equations 4.5 and 4.6 result in $r_a = 208/u_2$ and $r_s = 70$ s $m^{-1}$. Thus, from Equations 4.4 - 4.6, the Penman-Monteith method can be simplified (Allen *et al.*, 1998) as:

$$PE = \frac{0.408\Delta(R_n - G_0) + \gamma \dfrac{900}{T_a + 273.16} u_2 (e_s - e_a)}{\Delta + \gamma(1 + 0.34u_2)} \qquad (4.7)$$

where $PE$ = reference crop evapotranspiration [mm $day^{-1}$], $R_n$ = net radiation at the vegetation surface [MJ $m^{-2}$ $day^{-1}$], $G_0$ = soil heat flux density [MJ $m^{-2}$ $day^{-1}$], $T_a$ = mean daily air temperature at 2m height [$^0$C], $u_2$ = wind speed at 2m height [m $s^{-1}$], $e_s$ = saturation vapour pressure [kPa], $e_a$ = actual vapour pressure [kPa], $(e_s - e_a)$ = saturation vapour pressure deficit [kPa], $\Delta$ = slope vapour pressure curve [kPa $^0$C] and $\gamma$ = psychometric constant [kPa $^0$C]. The next section describes how the parameters defined in Equation 4.7 are determinable from measured meteorological data (Appendix 4.1).

## 4.2.2 Derivation of Model Inputs

### *4.2.2.1 Mean Saturation Vapour Pressure ($e_s$)*

Saturation vapour pressure ($e_s$) is a function of air temperature ($T_a$). Thus, $e_s$ can be calculated from air temperature following this relationship:

$$e^o(T_a) = 0.6108 \exp\left[\frac{17.27T_a}{T_a + 237.3}\right] \tag{4.8}$$

where $e^o$ = saturation vapour at the air temperature [kPa]. Due to the non-linearity of the above equation, the mean saturation vapour pressure for a day, week or month needs to be computed from the mean of the saturated vapour pressure at the mean daily maximum and minimum air temperature (Doorenbos & Pruitt, 1977) and was adopted as follows:

$$e_s = \frac{e^o(T_{\max}) + e^o(T_{\min})}{2} \tag{4.9}$$

### *4.2.2.2 Slope of Saturation Vapour Pressure Curve (Δ)*

The slope of the relationship between saturation vapour pressure-temperature ($e_s$ – $T_a$) curve is required for accurate estimation of *PE*. The slope of the curve (Δ) was calculated following Equation 4.10 using data from the GLOWA-Volta Project, whereas the coefficients were taken from published FAO data (FAO, 1998) as:

$$\Delta = \frac{4098\left[0.6108 \exp\left(\frac{17.27T_a}{T_a + 237.3}\right)\right]}{(T_a + 237.3)^2} \tag{4.10}$$

#### *4.2.2.3 Actual Vapour Pressure ($e_a$)*

The actual vapour pressure can be derived from any of the following three data sources: (1) dew point temperature; (2) psychrometric data (i.e. dry and wet bulb temperatures); and (3) relative humidity (Shaw, 1994; FAO, 1998). Appendix 4.1 provides mean daily relative humidity (*%RH*) values for the Tamale station. The relationship between $e_a$ and *%RH* given by Equation 4.11 was adopted as follows:

$$e_a = \frac{RH_{mean}}{100}\left[\frac{e^o(T_{\max}) + e^o(T_{\min})}{2}\right] \qquad (4.11)$$

#### *4.2.2.4 Vapour Pressure Deficit ($e_s - e_a$)*

As noted above, the vapour pressure deficit is the difference between the saturation ($e_s$) and actual ($e_a$) vapour pressure for a given time period. In this case, the formula shown as Equation 4.8 was applied.

### 4.2.3 Conversion of Units for *PE* Calculation

For many ground stations, measured meteorological data need to be converted into standard units desirable for accurate calculation of *PE*. Appendix 4.1 is a good example, where surface parameters, e.g. net radiation ($R_n$) and soil heat flux ($G$) were measured in Watts per square metre (W $m^{-2}$). These data had to be converted into MJ $m^{-2}$ $day^{-1}$. Detailed conversion tables for this and other input parameters have been published by the FAO (1998). An extract is reproduced as Appendix 4.2.

### 4.2.4 Crop Evapotranspiration ($PE_c$)

Accurate derivation of actual evapotranspiration from *PE* can present several challenges. First, factors such as vegetation-soil albedo, vegetation characteristics, irrigation status, aerodynamic and canopy surface resistances need to be separately or interactively accounted for and determined for different vegetation types (FAO, 1998). For small areas (e.g. agricultural fields), acceptable accuracy has been achieved using the crop coefficient ($K_c$) approach. In the case of complex vegetated catchments, this remains a huge research task. In the past, $K_c$ values ranging between 0.3 - 0.8 have been empirically determined for several single-tree-species woodlands, with varying degrees of accuracy (Snyder *et al.*, 1989; Rogers *et al.* 1983). However, the applicability of this approach to a wide range of landscapes, including (complex) heterogeneous woodlands, is yet to be determined (FAO, 1998). For tropical savannah landscapes, a reasonable approach is aggregating vegetation into very broad classes (e.g. mixed bushes and savannah woodland) and assigning a common correction factor to them ($K_c$ = 1.1; see p.106). Alternative approaches include cross-validation of *PE* with local evaporation measurements e.g. pan evaporation, and application of simple soil moisture deficit models (see below).

## 4.3 Application of Empirical Models

In the literature, several empirical models have previously been developed to calculate evapotranspiration with varying degrees of applicability, success and accuracy (Ward, 2000; Shaw, 1994). Here, an experiment was carried out to examine the

robustness of the Thornthwaite method as an alternative approach for the more data-intensive Penman-Monteith model.

### 4.3.1 Thornthwaite *PE* Method

The Thornthwaite model (Thornthwaite, 1948) was developed empirically in the USA principally to establish a relationship between monthly precipitation-evaporation ratio (*P/E*) and temperature. The method is important for two reasons: (1) mean daily or monthly temperature is the sole requirement to implement the model (Burt & Shahgedanova, 1998; Shaw, 1994), and so the method is potentially applicable to data-stressed environments such as the savannah Volta. (2) The model was originally developed to assess potential evapotranspiration (*PE*) in respect of warm dry catchments in Eastern USA, which makes it potentially useful for areas with similar environmental conditions. The Thornthwaite model which estimates *PE* on a monthly basis is given by:

$$PE = 16N_m(\frac{10T_m}{I})^a \qquad (4.12)$$

where $m$ = months 1, 2, 3, ....12, $N_m$ = monthly adjustment factor related to hours of daylight, $T_m$ = monthly mean temperature ($^0$C) and $I$ = heat index for the year, given by:

$$I = \sum\left(\frac{T_m}{5}\right)^{1.5} \qquad \text{for } m = 1,.....12 \qquad (4.12a)$$

and:

$$a = 6.7x10^{-7} I^3 - 7.7x10^{-5} I^2 + 1.8x10^{-2} I + 0.49 \qquad (4.12b)$$

### 4.3.2 Grindley's Soil Moisture Deficit Model

Evapotranspiration does not always proceed at the potential rate (*PE*) since it depends very much on a continuous supply of water. When the vegetation is unable to abstract water from the soil, then the actual evaporation becomes less than the potential (Shaw, 1994). Thus, the relationship between *AE* and *PE* depends on the soil moisture content. On this basis, the Grindley (1970) soil moisture accounting method was examined as a combined approach with the Thornthwaite and Penman-Monteith models. The Grindley's method, even though originally developed for Keele in the UK, has been credited for its capability to accurately model both *AE* and soil moisture (e.g. Burt & Shahgedanova, 1998), which provides some justification for this research. Given the rather intricate procedure of this derived approach, it is probably convenient to provide detailed explanation in tandem with its results in Section 4.4.2.

## 4.4 Results and Discussion

### 4.4.1 Daily *AE* Modelling & Up-scaling

Figure 4.2 shows daily *PE* calculated from Equation 4.7 for fifty-five days. It was not possible to examine the whole year due to discontinuities in the GLOWA-Volta database resulting from equipment and power failure, and human error (Mark Andreini, GLOWA-Volta Coordinator, personal communication, 2004). The important point here however is similarity of the results for the two years, which is further illustrated by the statistical summary in Table 4.3.

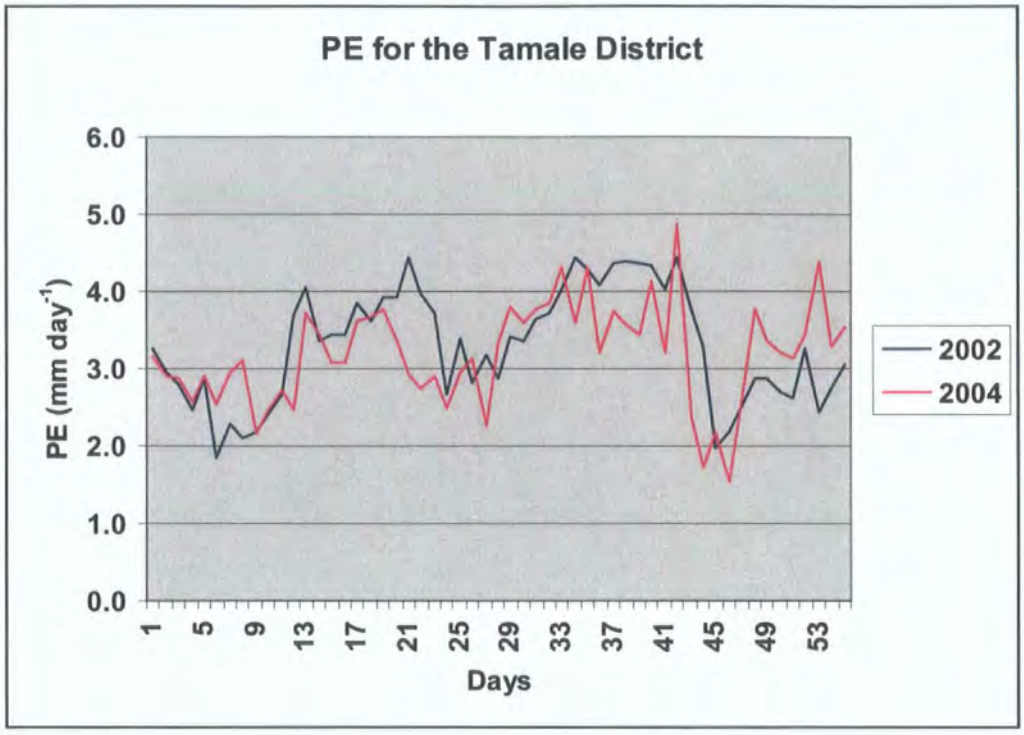


Figure 4.2 Reference evapotranspiration (*PE*) calculated for the Tamale savannah ground station. *PE* is calculated based on Equation 4.7 showing a similar daily *PE* trend for 2002 and 2004.

Table 4.3 PE statistics for Tamale

| | 2002 | 2004 |
|---|---|---|
| Total ET (mm) for 55 days | 181.14 | 175.10 |
| Mean | 3.29 | 3.18 |
| Maximum | 4.44 | 4.87 |
| Minimum | 1.85 | 1.53 |
| Standard deviation | 0.73 | 0.66 |
| Coefficient of variation | 0.22 | 0.21 |

Whether results in Table 4.3 reflect the longer-term daily evapotranspiration rate in the area is not conclusive from such a limited data set. Nevertheless, consistency of the above results points towards a positive direction. Apart from a few days, *PE* in 2002 remains higher than the subsequent year (2004). How does the bulk aerodynamic

equation (Equation 4.1) help to explain this? Two key parameters are critical drivers for elevated surface evaporation (Shaw, 1994); wind speed ($u$) and saturation vapour pressure deficit ($e_s - e_d$).

Linear interpolation of the raw data was implemented to fill in missing values over 285 possible measurements (footnote of Table 4.1) using *MATLAB interpolation* functions. The results are shown in Figure 4.3. The value of the interpolation method is shown in its confirmation of slightly higher *PE* measurement in 2002. Another important consideration here is definition of the dynamic trend of daily *PE* (Figure 4.3b&c). In both plots, the complexity of *PE* over an annual cycle is prominent. Table 4.4 further illustrates this mathematically.

Table 4.4 Daily reference evapotranspiration (*PE*) trend (datasets for 2002 & 2004)

| | Linear | 2nd Order Polynomial | 3rd Order Polynomial | 4th Order Polynomial |
|---|---|---|---|---|
| **2002** | $y = -0.0032x + 4.0061$ | $y = -5E\text{-}05x^2 + 0.0118x + 3.2884$ | $y = 1E\text{-}06x^3 - 0.0005x^2 + 0.0613x + 2.0971$ | $y = 2E\text{-}09x^4 - 3E\text{-}07x^3 - 0.0002x^2 - 0.0462x + 2.3172$ |
| | *($R^2 = 0.1173$)* | *($R^2 = 0.283$)* | *($R^2 = 0.6024$)* | *($R^2 = 0.6106$)* |
| **2004** | $y = 0.0002x + 2.9349$ | $y = 1E\text{-}05x^2 - 0.0028x + 3.0781$ | $y = 5E\text{-}07x^3 - 0.0002x^2 + 0.0227x + 2.4796$ | $y = -3E\text{-}09x^4 + 2E\text{-}06x^3 - 0.0005x^2 + 0.0395x + 2.2265$ |
| | *($R^2 = 0.001$)* | *($R^2 = 0.0129$)* | *($R^2 = 0.159$)* | *($R^2 = 0.1788$)* |

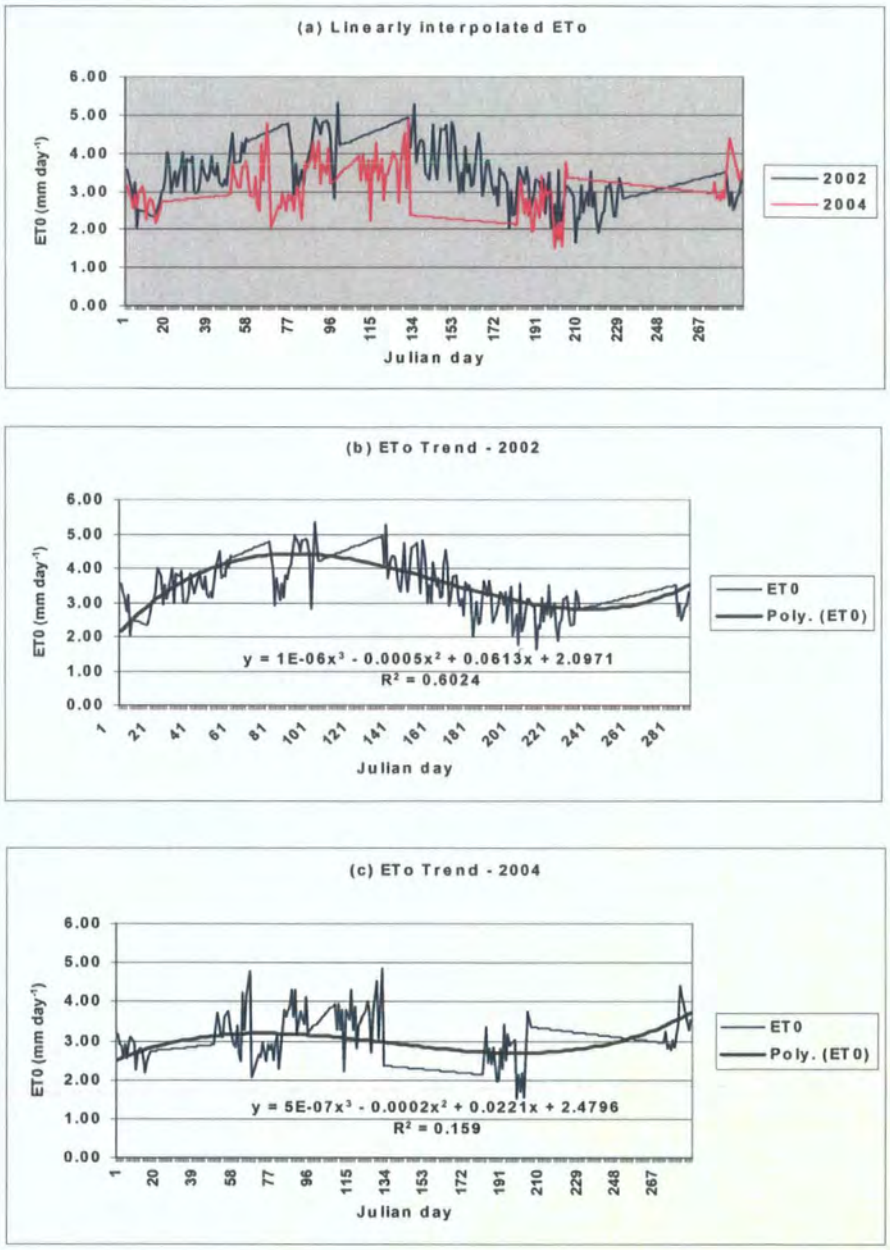


Figure 4.3 Interpolated *PE* over 285 days (Julian day (*J*) is determined for each day (d) of month (m) by J = Integer (275M/9 -30 +d) – 2. If (m<3) then J = J+2; also if (leap year and (m>2)) then J = J+1)

From Table 4.4, a 3rd degree polynomial equation seems to provide the best definition of daily trends in evapotranspiration since its regression value is highest ($R^2$ = 0.60)

compared to a linear or 2nd order polynomial function. It can be concluded that a higher-order polynomial does not only help to define the annual *PE* cycle, but also improves the strength of the trendline ($R^2$); which is better defined in 2002 than 2004 (Figure 4.3b&c). However, a fourth-degree function does not seem to provide any significant improvement on the regression value of ~0.60. Thus, further complexity of the polynomial function has little effect in improving daily *PE* trends. An important question here is: why does the 2002 dataset better reproduce the observed temporal sequence? The total size of measurements points (285 days) for all the input weather parameters in 2002 presents a useful clue. Since there were fewer missing data in 2002 compared to 2004, the linear interpolation method appeared to produce a better prediction. Spatial and temporal interpolation methods are well known to produce greater and more accurate predicted results when raw reconstruction data sets have inherently few missing points (Maidment, 2002).

In order to evaluate the accuracy of the calculated daily *PE*, a 9-year monthly record of Class-A pan measurements (Table 4.5) for the Tamale station was analysed. This forms the best locally available record for this purpose. Daily *PE* results were first aggregated to monthly values and plotted against pan evaporation ($E_{pan}$) (Figure 4.4). $E_{pan}$ was calculated using pan coefficients ($K_p$) derived from FAO (1998) look-up tables, an extract of which is shown in Table 4.6. $K_p$ was derived here in terms of evaporation pan type (Class-A pan), local wind speed, relative humidity and land cover type in the pan area. Results from a linear regression model between $E_{pan}$ and *PE* are shown in Figure 4.5.

Table 4.5 Monthly statistics (mm) of pan evaporation (Tamale) summarised from aggregated daily values over a 9-year period (1976-80 & 1990-93)

| | Jan | Feb | Mar | Apr | May | Jun | Jul | Aug | Sep | Oct | Nov | Dec |
|---|---|---|---|---|---|---|---|---|---|---|---|---|
| Minimum | 239.0 | 267.4 | 278.4 | 243.1 | 229.5 | 191.7 | 142.2 | 129.3 | 149.6 | 146.7 | 189.3 | 188.0 |
| Maximum | 363.0 | 342.4 | 382.8 | 325.0 | 288.0 | 257.3 | 193.5 | 184.9 | 260.4 | 214.3 | 239.2 | 288.0 |
| Mean | 281.2 | 297.9 | 327.1 | 296.2 | 253.3 | 209.1 | 160.8 | 154.4 | 176.0 | 185.0 | 213.7 | 230.6 |
| Standard deviation | 45.0 | 24.6 | 34.3 | 28.7 | 26.2 | 19.3 | 17.5 | 18.5 | 33.3 | 19.7 | 19.3 | 32.2 |

As expected, the 2002 *PE* results show better correlation with $E_{pan}$ ($R^2 = 0.56$) than 2004 ($R^2 = 0.20$) (Figures 4.4 & 4.5). Again, the greater number of ground measurements in 2002 are a factor of this result. This confirmation is significant for two main reasons: (1) subsequent estimation of monthly actual evaporation; and (2) provision of comparative results for empirical models.

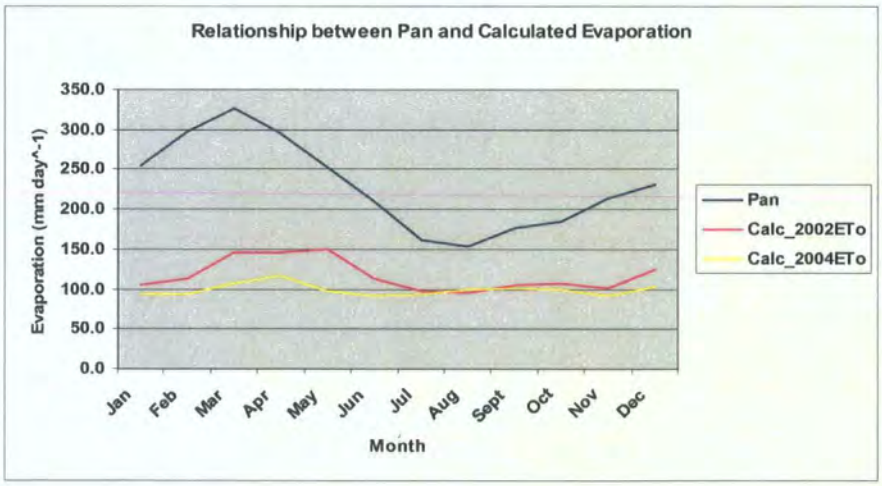


Figure 4.4 Evaluation of reference evapotranspiration (*PE*) using Class-A pan measurements ($E_{pan}$).

Table 4.6 Pan-A coefficient ($K_p$) for Tamale estimated from FAO (1998) look-up tables (LUT)

| Pan is installed on a natural short grassy vegetated surface | | | |
|---|---|---|---|
| | Rank | Value | FAO LUT $K_p$ value |
| Windward side distance of natural vegetation (m) | Moderate | 100 | |
| Wind speed (m $s^{-1}$) | Moderate | 2-5 | **0.60** |
| Relative humidity (%) | Medium | 40-70 | |

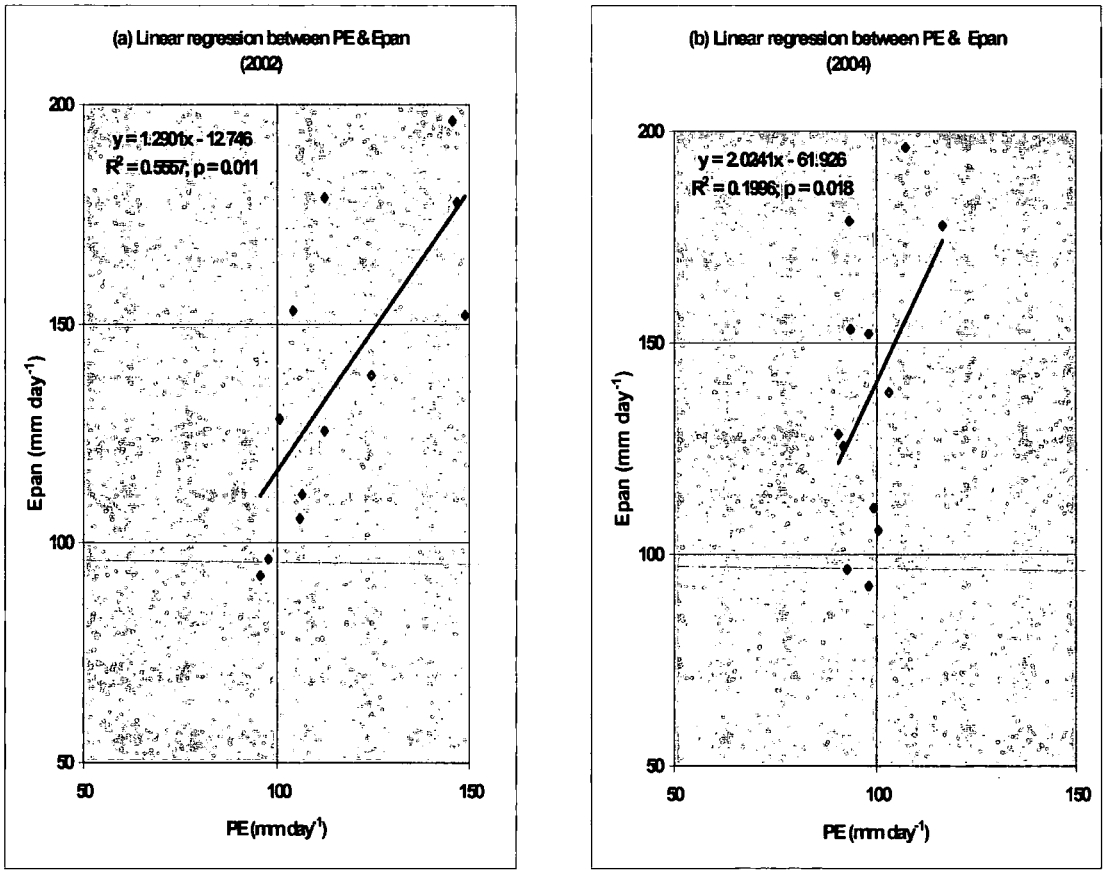


Figure 4.5 Linear regression between $PE$ and $E_{pan}$

Where evaporation pans are sited in non-agricultural environments (e.g. natural grassland surfaces) and local environmental conditions differ significantly from FAO look-up tables, further $K_p$ adjustments of 5 - 10% are recommended (FAO, 1998). Figure 4.6 shows $E_{pan}$ sensitivity to varying $K_p$ adjustments (5, 8 and 10%) and their overall accuracy relationship with *PE*. The results show that beyond 5%, no further adjustments to pan coefficients can accurately reflect evapotranspiration in the Tamale district. Other important deductions are possible from Figure 4.6. The first one is over-estimation of evapotranspiration during dry (winter) months (November – April) when day temperatures in the savannah Volta may reach up to $35^0$C (Table 4.2). At this season, the use of pan evaporation as an analogue of evaporation losses from a dry catchment area becomes questionable. The limitations of the pan method and its susceptibility to extreme temperatures are widely acknowledged (Shaw, 1994). Furthermore, the use of look-up tables and adjustment factors accentuates the insufficiency of the pan method to fully account for all the local conditions that most likely influence $K_p$. This is where establishment of an accurate regression coefficient (Figure 4.5) can play a significant role for calibration purposes. For accurate $E_{pan}$ measurements, a number of local conditions must be satisfied (FAO, 1998): (1) the pan should be installed inside a short green cropped area with a square size of at least 15 x 15m. (2) The pan should not be installed in the centre but at a distance, at least 10m from the green cropped edge in the general upwind direction. (3) Where observations of wind speed and relative humidity variable ($K_p$ parameters) are interpolated from nearby climatic stations, the values should be averaged for the computation period and $E_{pan}$ also averaged for the same period. In most developing (tropical) countries, these conditions

are rarely achieved, which partly explains why pan measurements may not precisely measure evaporation for the Tamale catchment (Figure 4.6). In addition, lack of regular pan maintenance and/or replacement leads to corrosion which can negatively affect pan measurements. Thus, available pan data are very unlikely to present a satisfactory picture of evaporative losses.

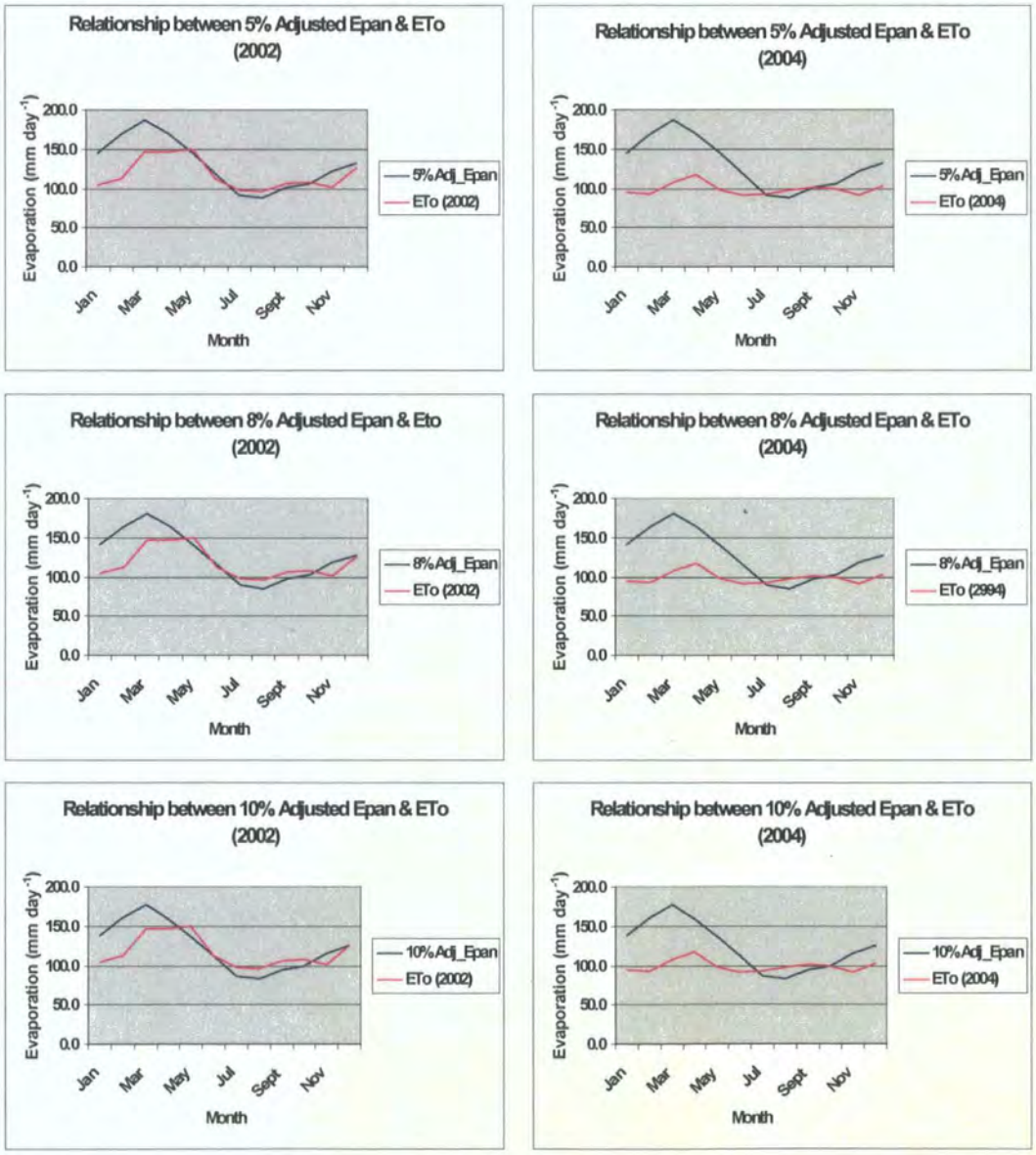


Figure 4.6 $E_{pan}$ sensitivity to $K_p$ adjustment and its overall temporal relationship with *PE*. The plots on the left and right-hand side represent 2002 and 2004 data sets, respectively.

To estimate evapotranspiration for wooded savannah vegetation, the crop coefficient ($K_c$) method is indispensable. That most of the effects of weather conditions get incorporated into *PE* estimates has already been established by Jensen *et al.* (1990). Whereas *PE* represents an index of climatic demand, $K_c$ varies predominantly with the specific crop characteristics and only to a limited extent with climate (Wright, 1982); hence, the transfer of standard values of $K_c$ between locations and between climates. This explains the primary reason for global acceptance of the $K_c$ approach and developed coefficients for wider applications (FAO, 1998).

Agyepong *et al.*, (1999) have reported that for more than 85% of the Volta savannah area, two key land cover classes are distinguishable: mixed (complex) grass-bush and savannah woodlands. Therefore, it is justifiable to ignore minor land cover classes and to use the above classes as a basis of determining the regional $K_c$ factor. But this is not simple, since a suitable single crop coefficient for such complex surfaces is hard to find in the literature. The FAO (1998) has recommended that empirical crop coefficients of single crops can only be extended to land cover classes if the majority of the land cover within a cell equals this crop type or a crop type with comparable evaporative characteristics. As a result empirical crop coefficients developed by van Deursen and Kwadijk (1994) for a tropical region in Asia were examined for adoption in this study. In their studies, both spindly-to-broad leaf thorny bushes and savannah woodlands classes were assigned a crop coefficient of 1.1. Figure 4.7 shows the estimated crop evapotranspiration ($PE_c$) results using this coefficient value. $PE_c$ was calculated on the basis that $K_c$ is a direct ratio between $PE_c$ and *PE*, i.e. $PE_c = K_c * PE$.

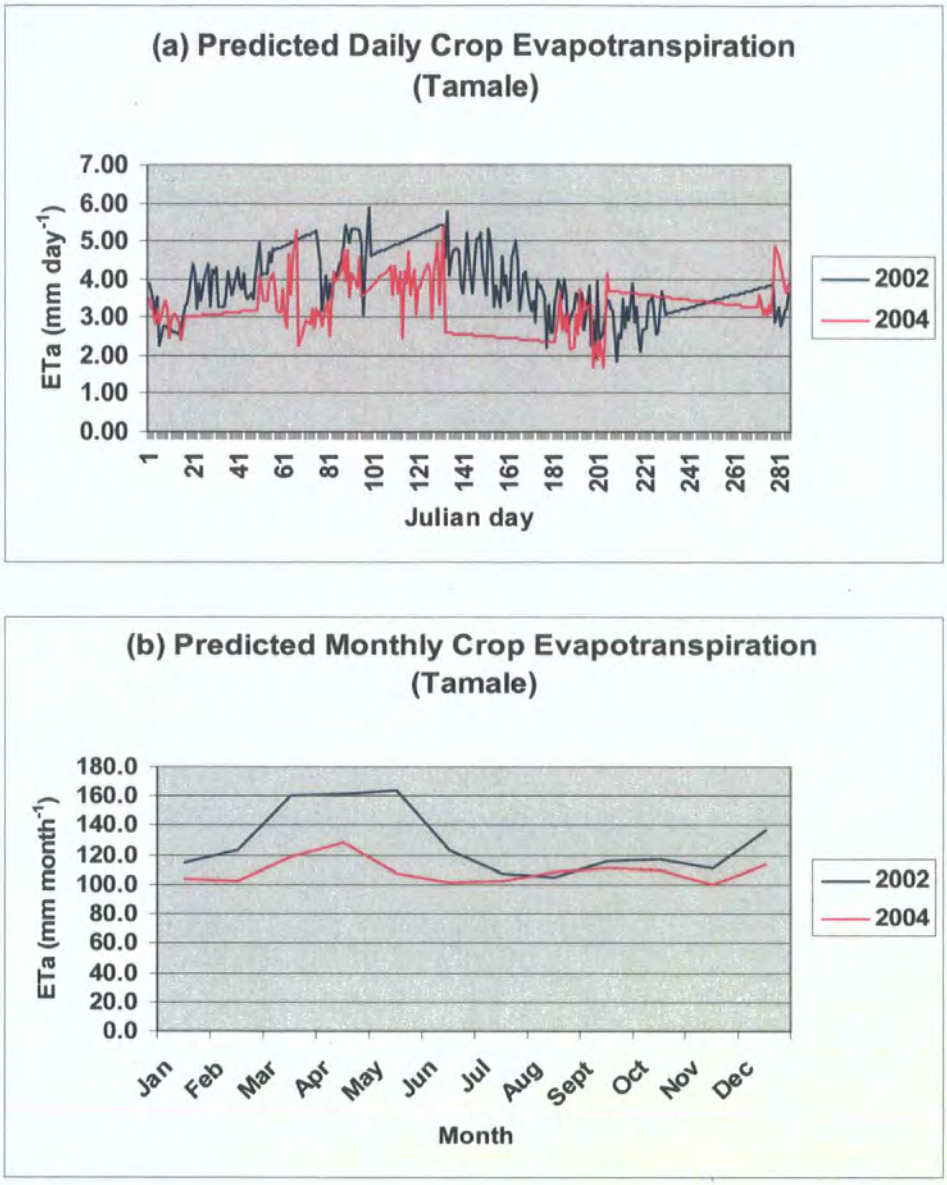


Figure 4.7 Predicted crop evapotranspiration - savannah Tamale district

Using the 2002 results as an example, Figure 4.7a predicts an average daily $PE_c$ (over an annual cycle) of 1.82 – 5.86 mm day$^{-1}$ with a mean of 3.90 mm day$^{-1}$, (approx. 117.0 mm month$^{-1}$) which is in close proximity with *PE* results shown in Figure 4.2 and Table 4.3. This prediction compares favourably with recent aggregated 10-minute latent

heat flux ($\lambda ET$) measurements recorded by the GLOWA-Volta team using the Dutch-type scintillometer instrument (http://ww.glowa-volta/publications..html). This report shows that the mean daily (06:00 – 18:00 hours) scintillometer $\lambda ET$ measurement for a similar vegetated surface near Tamale in December 2001 was 108.2 $Wm^{-2}$, which converted into $PE_c$ is approximately 3.81 mm $day^{-1}$, nearly the same result predicted by the Penman-Monteith model. It is significant to note how the $K_c$ adjustment factor improves $PE$ predictions for savannah vegetation but fails to overcome complexities of the (mixed) natural landscape. Three main reasons account for this: (1) the $K_c$ factor assumes unlimited soil water supply to vegetation, which is hardly the case in the Tamale area; (2) the $K_c$ factor was primarily designed to estimate evapotranspiration for single or dual crop stands, which makes application for complex natural landscapes difficult; and (3) the key environmental conditions such as vegetation height, canopy resistance, vegetation-soil albedo, etc. are hard to satisfy in natural catchments. These constraints notwithstanding, the Penman-Monteith-$K_c$ adjustment approach has been successfully applied to a variety of humid catchments with variable degrees of accuracy (FAO, 1998; Shaw, 1994; Allen *et al.,* 1992).

An important question is the extent to which the above results are representative of the Guinea savannah area in Ghana, and the wider context of West Africa. This is probably best addressed by spatial $AE$ estimates from remotely sensed imagery, which indeed provides the focus for subsequent chapters. In the context of West Africa, further research is necessary. Nevertheless, the current results provide useful insights into evaporation losses of the Guinea savannah region.

### 4.4.2 Empirical *AE* Modelling

Burt & Shahgedanova (1998) have shown in their research in England which analysed hydro-meteorological data from the Radcliffe Observatory (Oxford) that the Grindley (1970) soil moisture balance method is one of most appropriate ways for estimating local-scale *AE* and water balance. The key inputs to the Grindley model are rainfall and *PE* data (Burt & Shahgedanova, 1998; Shaw, 1994). To see whether this method is applicable in the context of dry savannah West Africa, two *PE* approaches were examined, namely the Penman-Monteith and Thornthwaite methods.

In the former case, aggregated *PE* results derived from the preceding section and monthly rainfall for 2002 constituted the input data. The 2002 data set was used mainly to cover the annual cycle. In the latter case, *PE* was calculated using a 40-year record of mean monthly rainfall and temperature for the Tamale district (see Table 4.2) based on the procedure described in Section 4.3.1. Figure 4.8 shows the relationship between pan evaporation measurements and Thornthwaite's model results. It is easy to see how the Thornthwaite model closely reproduces unadjusted pan measurements ($R^2 = 0.80$). The poor fit of Figure 4.8 (top graph) between November and March and the relative scatter of the bottom graph is probably a good justification why the integration of a soil moisture balance model proposed by Grindley (1970) may be a good approach for estimating evaporation in this region.

For catchment areas, water loss does not always proceed at the potential rate but depends on continuous supply of soil water. It is in this context that the Grindley method helps to track vegetation soil moisture abstraction and its relationship with potential and actual water loss. On a monthly time-scale, it is also feasible to evaluate

drought occurrence as well as soil field capacity thus, $AE < PE$ when vegetation is unable to abstract water from the soil, and $AE = PE$ when the soil is at field capacity (Shaw, 1994). Table 4.7 highlights this point and provides further details about the $AE$ calculation procedure.

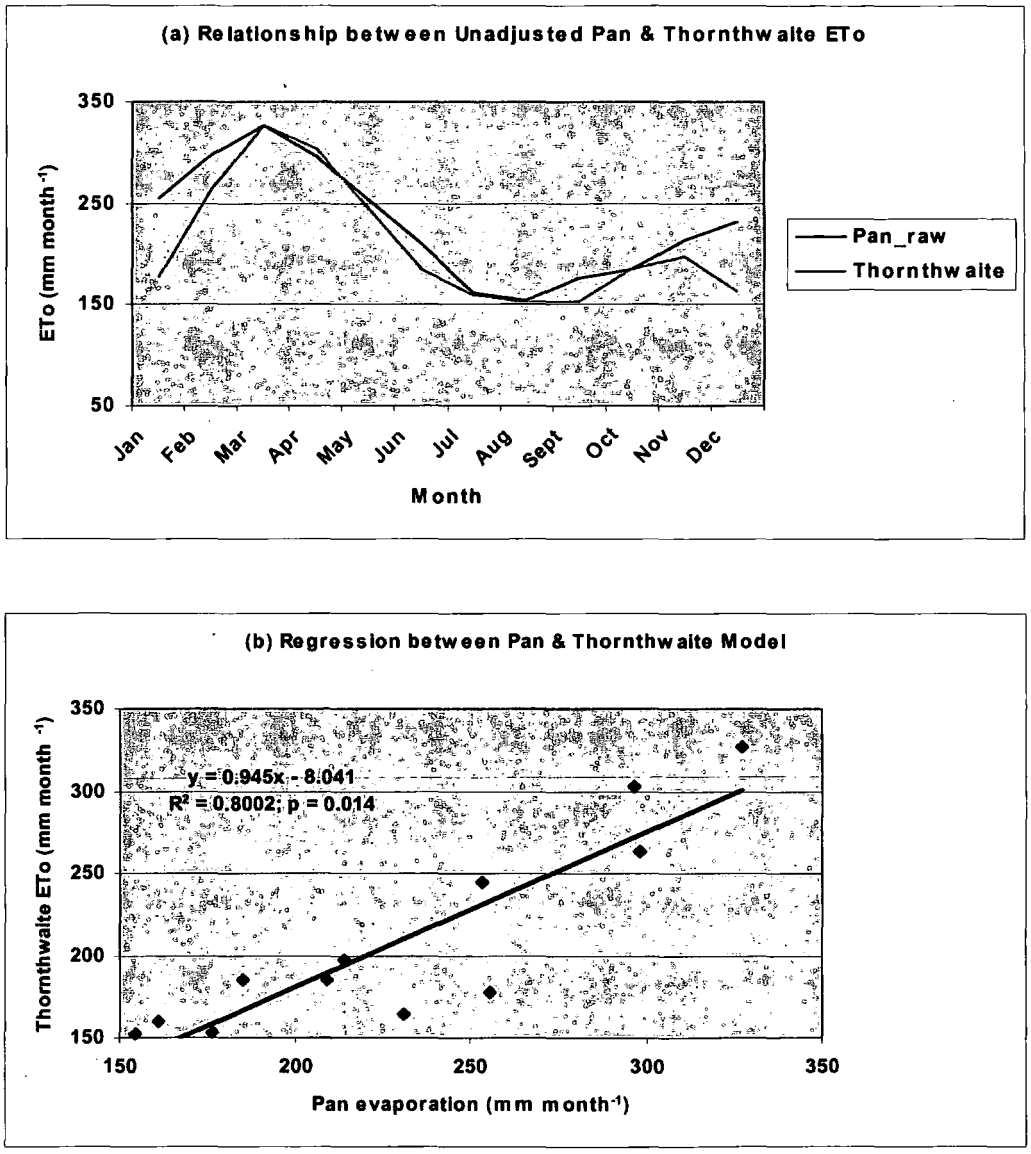


Figure 4.8 Relationship between Pan Evaporation and Thornthwaite model results

Table 4.7 Calculation of soil moisture deficit (SMD) and *AE* for Tamale district (Thornthwaite-Grindley approach)

| | Rainfall (*P*) | Potential evaporation (*PE*) | *P – PE* | Potential soil moisture deficit ($P_{SMD}$) | SMD at 200mm root constant ($RC_{200}$) | Actual evapo-transpiration (*AE*) |
|---|---|---|---|---|---|---|
| | *1* | *2* | *3* | *4* | *5* | *6* |
| **January** | 3.2 | ***177.2*** | -174.1 | 335.1 | 245.0 | ***6.8*** |
| **February** | 9.0 | ***263.6*** | -254.6 | 589.6 | 255.0 | ***19.0*** |
| **March** | 45.6 | ***326.8*** | -281.2 | 870.8 | 269.0 | ***59.6*** |
| **April** | 81.0 | ***302.5*** | -221.4 | 1092.3 | 279.0 | ***91.0*** |
| **May** | 122.7 | ***244.5*** | -121.8 | 1214.0 | 283.0 | ***126.7*** |
| **June** | 155.7 | ***185.6*** | -29.8 | 1243.8 | 285.0 | ***157.7*** |
| **July** | 154.7 | ***160.3*** | -5.6 | 1249.4 | 285.0 | ***154.7*** |
| **August** | 200.1 | ***152.1*** | 48.0 | 1201.4 | 280.0 | ***195.1*** |
| **September** | 226.0 | ***153.2*** | 72.8 | 1128.7 | 281.0 | ***227.0*** |
| **October** | 88.4 | ***184.9*** | -96.4 | 1225.0 | 284.0 | ***91.4*** |
| **November** | 10.1 | ***196.7*** | -186.6 | 1411.6 | 296.0 | ***22.1*** |
| **December** | 2.8 | ***163.8*** | -160.9 | 1572.5 | 300.0 | ***6.8*** |

The detailed procedure for calculating *AE* based on the Thornthwaite-Grindley combination method (Grindley, 1970) is shown in Shaw (1994).

The following provides a stepwise explanation of how results in Table 4.7 were compiled and/or calculated.

***Step 1:*** Column 1 represents mean monthly rainfall compiled from Table 4.2. Based on this, Column 2 (*PE*) was calculated using Equation 4.13 (a-c) in combination with mean daily sunshine (*N*) coefficients for (savannah) latitude $10^0$N published by FAO (1977) and reproduced as Appendix 11.1.2 by Shaw (1994, p.270).

***Step 2:*** Column 3 was then calculated as the difference between monthly rainfall and Thornthwaite's reference evaporation (Column 1 – Column 2).

***Step 3:*** Potential soil moisture deficit ($P_{SMD}$) is defined as the moisture deficit that would result if the potential evaporation was always fulfilled. It is the aggregate of the difference between *P* and *PE* considered as a deficit and is assumed to apply to the riparian lands or above field capacity (Shaw, 1994). The actual soil moisture deficit ($A_{SMD}$) follows the $P_{SMD}$ until it reaches the woodland zone of approximately 250mm.

That means every month is potentially unsaturated in terms of soil moisture. Thus, Column 4 returns aggregated $P_{SMD}$ for all the succeeding months (here, January adds an assumed average figure for the preceding December). For example, the $P_{SMD}$ for May is calculated as sum total of all deficits from January to April, and so on.

***Step 4:*** Based on the previous assumption that the main vegetation class for Tamale district is grass-bush/savannah woodland with a root constant value of 250 mm, actual soil moisture deficits (Column 5) were re-constructed from published look-up tables (UK Met Office Hydrological Memorandum No. 38) and reproduced by Shaw (1994) in her hydrology textbook as Appendix 11.3.1. There is difficulty in applying these tables for very large $P_{SMD}$ values >450 mm. As a result, a linear regression equation ($y = 0.8736x + 223.62$ [$R^2 = 0.9904$]) was developed from Shaw's (1994) tables to derive $A_{SMD}$ ($y$) from $P_{SMD}$ ($x$) up to about 1600 mm to fully take account for all potential water stresses. The extrapolation approach did not present much problems based on the assumption that vegetation rooting depth was more important for soil moisture abstraction than climatic conditions over daily time periods.

***Step 5:*** The actual evapotranspiration ($AE$) (Column 6) for a particular month was then calculated as the change in soil moisture deficit plus the rainfall. For example, $AE$ for June was calculated as: $AE = SMD\ June - SMD\ May + June\ rainfall = 278.0 - 276.0 + 155.7 = 157.7\ mm$. Since actual soil moisture deficit at the root zone ($SMD_{200}$) is lower than the potential for each month it is assumed here that soil water uptake is maximum for each period. The model has also been tuned for January $AE$ to take the value of December given the close similarity of the climatic conditions and vegetation cover for both months (see Table 4.7 Column 1).

Following the above procedure, *AE* prediction driven by the Penman-Monteith approach was implemented. The results are shown in Table 4.8 and Figure 4.9. Figure 4.9 is particularly significant for a number of reasons. First of all, the monthly *AE* for both methods is quite similar ($R^2 = 0.95$) even though the magnitude of their *PE* input is substantially different.

Table 4.8 Calculation of soil moisture deficit (SMD) and *AE* for Tamale district (Penman-Monteith-Grindley approach)

| | Rainfall (*P*) | Potential evaporation (*PE*) | *P* – *PE* | Potential soil moisture deficit ($P_{SMD}$) | SMD at 200mm root constant ($RC_{200}$) | Actual evapo-transpiration (*AE*) |
|---|---|---|---|---|---|---|
| | *1* | *2* | *3* | *4* | *5* | *6* |
| **January** | 0.0 | ***104.2*** | -104.2 | 228.8 | 226.0 | ***4.0*** |
| **February** | 0.0 | ***112.6*** | -112.6 | 341.4 | 245.0 | ***19.0*** |
| **March** | 2.0 | ***145.7*** | -143.7 | 485.1 | 251.0 | ***8.0*** |
| **April** | 92.5 | ***146.7*** | -54.2 | 539.3 | 255.0 | ***96.5*** |
| **May** | 122.6 | ***148.8*** | -26.2 | 565.5 | 256.0 | ***123.6*** |
| **June** | 142.3 | ***112.5*** | 29.8 | 535.7 | 255.0 | ***141.3*** |
| **July** | 146.1 | ***97.7*** | 48.5 | 487.2 | 251.0 | ***142.1*** |
| **August** | 206.8 | ***95.8*** | 111.0 | 376.2 | 248.0 | ***203.8*** |
| **September** | 217.6 | ***105.9*** | 111.7 | 264.5 | 239.0 | ***208.6*** |
| **October** | 98.0 | ***106.6*** | -8.6 | 273.1 | 240.0 | ***99.0*** |
| **November** | 0.9 | ***100.8*** | -99.9 | 373.0 | 248.0 | ***8.9*** |
| **December** | 0.0 | ***124.6*** | -124.6 | 497.6 | 252.0 | ***4.0*** |

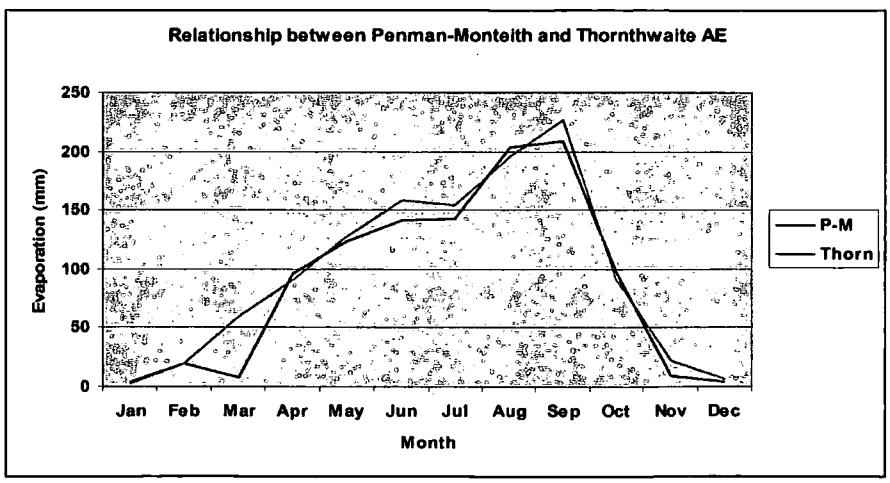


Figure 4.9 Relationship between Penman-Monteith and Thornthwaite *AE* prediction based on the Grindley soil moisture deficit integrated method

Whereas statistical "averaging-out effect" of the long-term data may account for the performance of the Thornthwaite method, the more rigorous energy balance Penman-Monteith method probably explains its effectiveness. Furthermore, the similarity of the rainfall inputs (in each case) imposes equal weight on the soil moisture accounting procedure, which means the observed differences are as a result of variations in the *PE* modelling approach. Nevertheless, given the availability of detailed climatic and environmental data, the Penman-Monteith method is preferred because of its better predictive power. But under data-stress conditions, the Thornthwaite-Grindley integrated approach (hereafter called TG method) may prove a satisfactory alternative to the data-intensive Penman-Monteith-Grindley approach (hereafter referred to as the PMG method). Secondly, Figure 4.9 tends to confirm previous conclusion by Burt & Shahgedanova (1998) that the Grindley model is an appropriate method for estimating *AE* and soil water balance.

An important way of evaluating the above results is comparing with the region's water balance. On this basis, the annual (regional) water balance for the White Volta basin (~10, 986 $km^2$) was calculated using results from Table 2.13 of Chapter 2. It is worth mentioning that the White Volta encompasses the Tamale district. Over annual time scales, the water balance of a large catchment may be approximated (Shaw, 1994) as the difference between rainfall and evaporation, in terms of soil moisture storage ($\Delta S$) or deficit (*SMD)*. Table 4.9 compares the water balance of Tamale and the White Volta basin.

Table 4.9 Annual water balance of the White Volta basin and Tamale district

| | | Annual rainfall (P) (mm) | Annual evaporation (AE) (mm) | Annual (actual) soil moisture deficit (P-AE) (mm) | % Annual soil moisture deficit |
|---|---|---|---|---|---|
| White Volta River basin | | 1083.1 | 1204.9 | -121.8 | 11.2 |
| Grindley combination method (Tamale) | Thornthwaite PE | 1099.3* | 1154.4** | -55.1 | 5.0 |
| | Penman-Monteith PE | 1028.8* | 1058.8** | -30.0 | 2.9 |

*Annual rainfall in the first two cells of this table was compiled from long-term records (see Table 4.2) and the bottom cell was compiled from the 2002 data set only. **The evaporation rate was also calculated as the sum total of monthly *AE* shown in Column 6 of Tables 4.7 & 4.8.

Apart from *AE*, Table 4.9 emphasizes the value of the Grindley approach for regional water balance prediction under tropical conditions. In fact, this method can be a useful, rapid and cost-effective means of estimating evaporative losses from large complex landscapes if the following conditions are satisfied: (1) availability of time series (monthly) rainfall and temperature records; (2) accurate derivation of root constants; and (3) accurate derivation of soil moisture deficits either from published look-up tables or regression equations.

### 4.4.3 Comparative Discussion of Evaporation Methods

The purpose of this section is comparative discussion of the three main *PE* evaporation methods applied in this research, namely the Penman-Monteith, Thornthwaite and pan methods, and also the Grindley (integrated) soil moisture balance method. Figure 4.10 compares their predictive outputs, which provide several important lessons: (1) up-scaling may lead to aggregated errors, if for instance daily *PE* is

converted to monthly values; (2) non-linearity in energy and vapour transfer processes globally affect measurement techniques regardless of the evaporating surface; pan measurements in the case of open water, and Penman-Monteith and Thornthwaite in the case of natural landscapes; and (3) the $K_c$ adjustment factor may not be entirely robust for warm dry (natural) vegetated surfaces (Allen *et al.,* 1998; FAO, 1998; Deursen and Kwadijk, 1994).

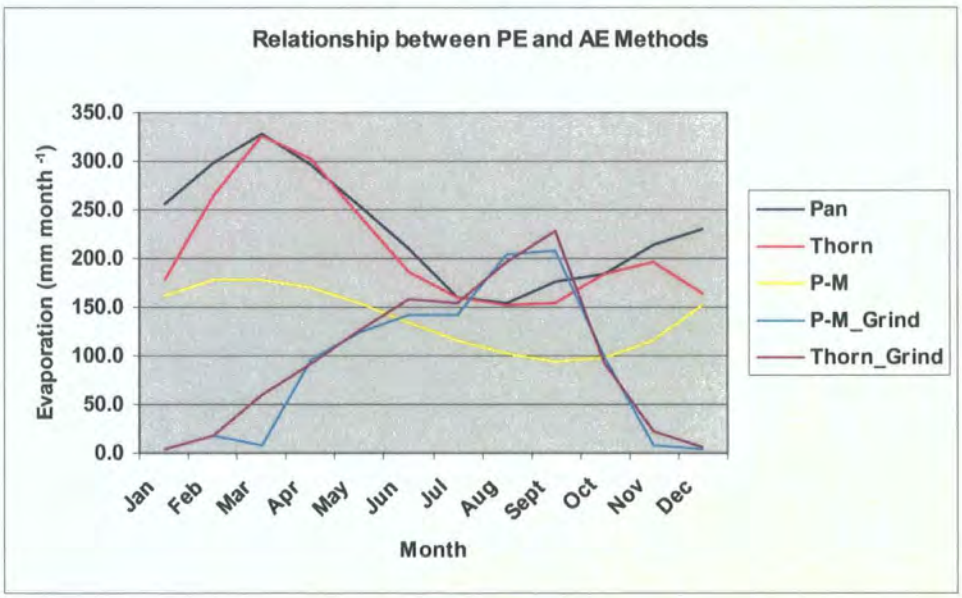


Figure 4.10 Comparison between (a) unadjusted Pan, Thornthwaite and Penman-Monteith *PE* methods, and (b) PMG and TG integrated *AE* and soil moisture balance methods.

Linking Figure 4.10 and Table 4.10, the annual regional *PE* for the area can be easily compared. Table 4.10 shows for instance, that *PE* for Tamale is approximately 1415.0 mm, which means the pan and Thornthwaite methods may potentially exaggerate *PE* measurements up to 90% in comparison with the Penman-Monteith model. The most plausible explanation is the sensitivity of the pan and Thornthwaite methods to

extreme temperatures. In the tropics, water overheating resulting from extreme temperatures is a major source of pan error. From Figure 4.10, extreme temperatures during the "winter" months do not only explain *PE* overestimation using the pan method, but also the Thornthwaite and Penman-Monteith methods. As shown in this example, a reasonable way of resolving this error is accounting for soil moisture and calculating actual evapotranspiration (*AE*) using the PMG and TG methods.

Table 4.10 PE results estimated from various methods

| Evaporation method | Annual Potential (*PE*) Evaporation (mm) | % Departure from Estimated *PE* (Volta basin) |
|---|---|---|
| Pan measurements | 2759.3 | 95.0 |
| Thornthwaite | 2511.2 | 77.0 |
| Penman-Monteith | 1655.6 | 17.0 |
| Water balance method - Volta basin)* | 1415.0 | 0.0 |

*Estimated evaporation for the Volta basin published by AGRHYMET (1998), Table 2.1 of Chapter 2. The other values were extracted from Figure 4.9.

In India for instance, evaporation pans are often painted white to increase radiation reflection which helps to overcome overheating problems; some studies have also recommended setting the pan in the ground (Shaw, 1994). The conditions at Tamale make pan overheating a huge possibility. Regarding the Thornthwaite model, its simple assimilation of air temperature (being the sole model input data) may potentially diminish its effectiveness to estimate *PE* precisely, since important surface conditions such as aerodynamic factors are often ignored in the evaporation process. On account of *PE*, the Penman-Monteith method is much superior and its strength lies in

its ability to account for a wide range of meteorological factors such as momentum, radiation and vapour pressure.

As noted in the previous section, the application of the Grindley method in combination with the Penman-Monteith and Thornthwaite models (Figure 4.9) is instructive in several ways: (1) it is a means of tracking soil moisture deficits or surpluses; (2) it shows how vegetation water uptake contributes to *AE*; and (3) it shows how the above may constitute significant information for agricultural food security and water resources management. The importance of Figure 4.9 is accentuated by water balance results recently published by the GLOWA-Volta team (Braimoh, 2004) for similar savannah catchments (Figure 4.11). Comparing Figures 4.9 – 4.11, it is easy to see how the current conclusions are in close harmony with Braimoh's (2004) findings, which suggest *PE* and *AE* elevation for at least seven dry months and five wet months, respectively. Furthermore, both results model a distinctive *AE* peak in August/September; the period of peak rainfall in the region. Indeed, this is the point where the *PE* predictions break down, giving further justification for integrated soil moisture balance models. Figure 4.11 also supports the current and widely accepted view that the Penman-Monteith equation is a better *PE* predictor even under warm dry conditions than the pan and Thornthwaite methods (FAO, 1998).

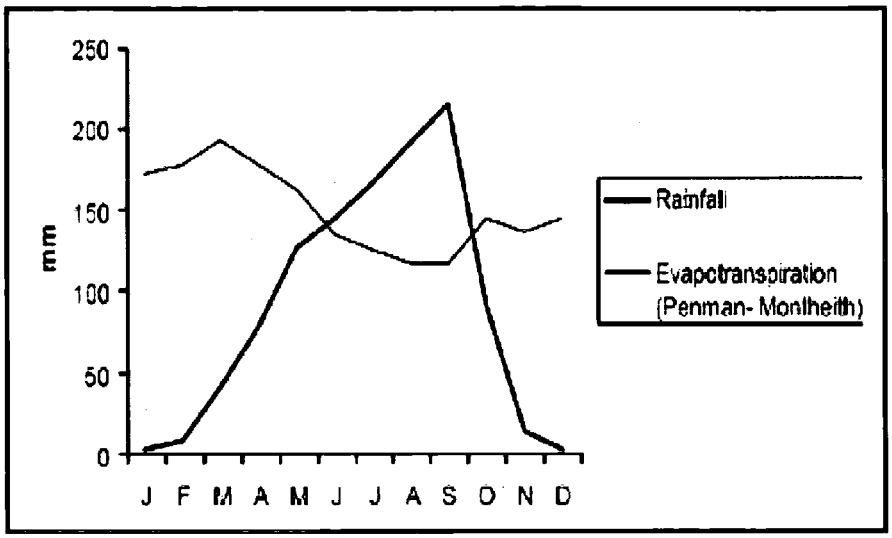


Figure 4.11 Monthly rainfall-ET relationship produced by the GLOWA-Volta research team, after Braimoh (2004)

## 4.5 Summary

For the first time, detailed meteorological data (better than hourly measurements courtesy of the GLOWA-Volta Project) have become available for accurate estimation of actual evapotranspiration (*AE*) in Guinea savannah catchments in West Africa (Figure 4.12). In this chapter, potential evapotranspiration (*PE*) was calculated for the Tamale savannah district using the widely used Penman-Monteith equation. The key model input parameters included daily radiation, air temperature, air humidity and wind speed. As a first step, daily *PE* was calculated for 55 coincidental days in 2002 and 2004. Secondly, a linear function was used to interpolate both data sets to examine a possible annual cycle.

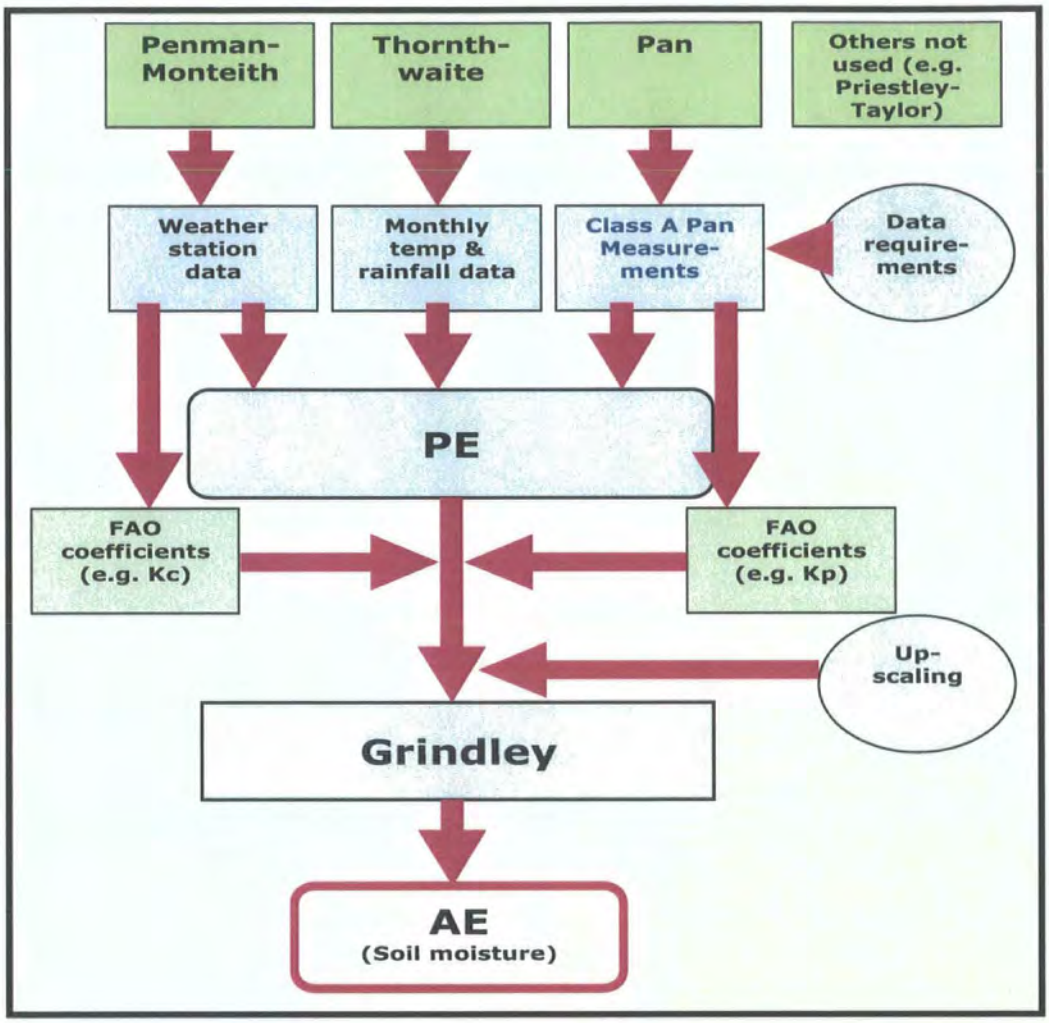


Figure 4.12 Schematic model for *AE* estimation in the Volta basin

To test the accuracy of the Penman-Monteith output, *PE* results were aggregated to monthly values and evaluated using local Class-A pan evaporation records over a 9-year period. The pan values consistently exaggerated *PE*, which made the application of the FAO pan coefficient ($K_p$) method necessary. An adopted $K_p$ value of 0.60, based on pan location and environmental conditions presented a reasonable correction factor. In order to calculate vegetation evapotranspiration ($PE_c$), the FAO crop coefficient ($K_c$)

method was also applied. The predicted *PE* for wooded savannah vegetation using an adjustment of $K_c$ = 1.1 averaged 3.23 mm day$^{-1}$, which is very close to scintillometer observations (3.81 mm day$^{-1}$) by GLOWA-Volta project. As a third step, the results were compared with the Thornthwaite empirical *PE* method; the Thornthwaite incorporates monthly temperature and rainfall records as sole model inputs. Here, *PE* was calculated from mean values using a 40-year rainfall and temperature record. In comparative terms, the Penman-Monteith performed much better than the Thornthwaite method since the latter consistently exaggerated *PE* predictions. For example, whereas estimated *PE* by the Penman-Monteith method for December averaged 117 mm month$^{-1}$, similar to ground (scintillometer) observations, the Thornthwaite method overestimated this by about 46.8 month day$^{-1}$ (see Table 4.7).

To establish the importance of empirical models for *AE* calculation, monthly *PE* from the Thornthwaite and Penman-Monteith methods were incorporated into the Grindley (1970) soil moisture balance model. Interestingly, both approaches produced similar *AE* and soil moisture estimates ($R^2$ = 0.95), which also compared favourably (1058 – 1154 mm a$^{1}$) with available water balance data (1204 mm a$^{-1}$) (Table 4.9). The current results are, however, inconclusive and require further research. Nevertheless, for data-stress areas such as the West African savannah, the above results show the Thornthwaite-Grindley (TG) integrated method as a useful approach for estimating *AE*.

# Chapter 5

# Regional-scale Evapotranspiration Modelling: Remote Sensing Methods

## 5.1 Introduction

Remote sensing is an attractive option to help obtain or model regional or global coverage of the Earth's surface heat and moisture fluxes. The usefulness of other methods such as scintillometer measurements (1-5km) (de Bruin *et al.*, 1996) and [1]SWAP models (Droogers, 2000) has been widely recognised in literature; however, they are limited in relation to scale, time, cost and the need for extensive field work. Although remote sensing techniques cannot measure surface fluxes directly, they can do so indirectly or help to extend point measurements or empirical relationships such as Penman-Monteith (FAO, 1998; Priestley-Taylor, 1972) to much larger areas including areas where measured meteorological data are very sparse (Engman, 2004). The question of how to do this has been addressed in several ways, such as temperature-vapour pressure modelling using linear regression (Davies & Tarpley, 1983), analytical solution of horizontal surface temperature-evaporation changes (Kustas *et al.*, 1990), extrapolation of energy fluxes from thermal and reflectance imagery (Humes *et al.*, 1994) and parameterisation of land surface schemes using reflectance and thermal imagery (Su *et al.* 2000; Bastianssen *et al.*, 1998a).

In the last decade, a number of remote sensing-based land surface schemes (algorithms) have also been developed to assess energy and moisture fluxes. These algorithms differ depending upon the type of land use information requirements, satellite

[1] SWAP = Soil-Water-Atmosphere-Plant model

band wavelength, optimization with meteorological data, and choice of numerical models (Bastiannssen *et al.* 1998a). The Surface Energy Balance Algorithm for Land (SEBAL) developed by Bastiannssen *et al.* (1998a) is one such example that has been widely applied (Mekonnen, 2005; Chemin *et al.*, 2000; Su *et al.*, 1999). The SEBAL algorithm has been validated with large field experiments in Spain, Niger and China (Bastiannssen *et al.*, 1998b) and proved to be applicable and deliver good results. A key advantage of the SEBAL algorithm is its minimal data input requirement for calculating pixel-based actual evapotranspiration (*ET*) (Mekonnen, 2005; Su *et al.*, 1999). The main data requirements are satellite-based visible, near-infrared and thermal data, optimized by local meteorological measurements (air temperature, wind speed and net radiation). The main purpose of this chapter is to provide a detailed description of the methodological approach for the parameterisation of the SEBAL algorithm for calculating *ET* at the regional scale; its full application is discussed in Chapter 7.

## 5.2 Parameterisation of the SEBAL Algorithm

Figure 5.1 presents a simplified illustration of how evapotranspiration (*ET*) may be derived from satellite imagery over savannah landscapes. SEBAL calculates actual evapotranspiration at the time of satellite overpass as the left-hand-side term of the regional surface energy balance as follows (Mekonnen, 2005):

$$ET = R_n - H - G_0 \qquad (5.1)$$

where $ET$ = latent heat flux (evaporation), $R_n$ = net radiation, $H$ = sensible heat flux, and $G_0$ = soil heat flux. The units for all the above parameters are $Wm^{-2}$ and the detailed physics of the radiation and energy balance models are illustrated in Figure 5.2.

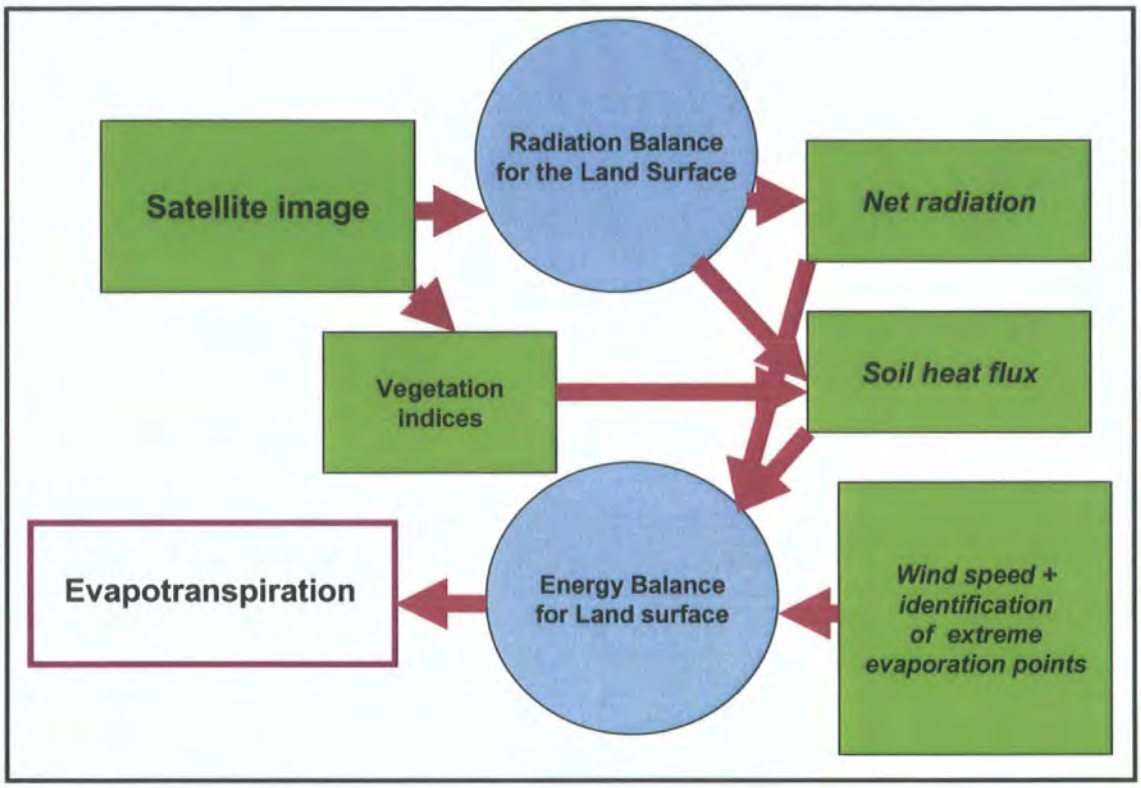


Figure 5.1 Schematic illustration of how evapotranspiration ($ET$) may be estimated from remotely sensed data (Modified after Morse *et al.*, 2000).

The popularity of the SEBAL algorithm is growing (e.g. Brata *et al.*, 2006; French *et al.*, 2005; Mekonnen, 2005; Wang *et al.*, 2004; Chemin, 2003; Morse *et al.*, 2000; Bastiannssen *et al.* 1998b) as a result of its performance in the calculation of energy fluxes over a variety of surfaces. A good example is a recent study by French *et al.* (2005) which compared the Two-Source Energy Balance (TSEB) with SEBAL over the Soil Moisture

Atmosphere Coupling Experiment (SMACEX) site in Iowa (USA). One of their key conclusions was that the TSEB and SEBAL algorithms did not only inter-compare favourably but they also showed systematic agreement with spatially varying surface temperatures and vegetation densities.

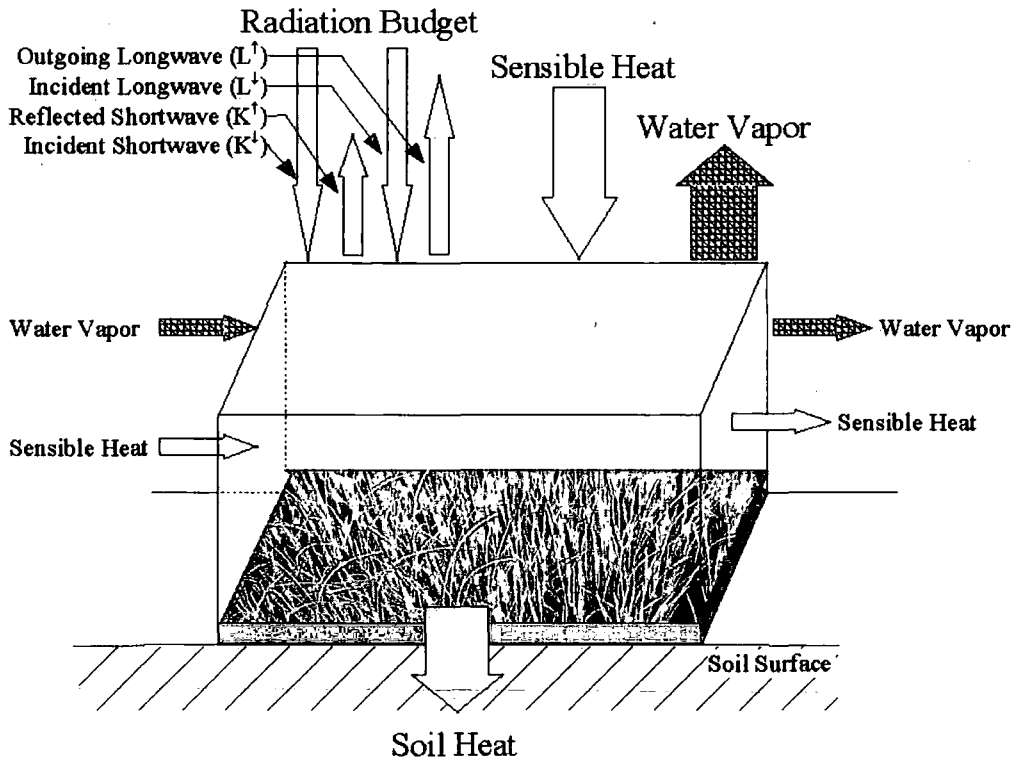


Figure 5.2 Simplified illustration of the regional energy balance model. Source: Chemin (2003)

## 5.2.1 Net Radiation ($R_n$)

The net radiation $R_n$ ($Wm^{-2}$) is the amount of radiation left after all outgoing radiation is subtracted from all incoming radiation. Recognising that albedo ($\alpha$) is a ratio

between incoming and outgoing shortwave radiation, albedo can be used as a function of $R_n$ which is derived as follows:

$$R_n = K_{\downarrow}(1-\alpha) + (L_{\downarrow} - L^{\uparrow}) \qquad (5.2)$$

where $K_{\downarrow}$ = incoming shortwave radiation (0.17 – 4.0 μm), $\alpha$ = albedo (dimensionless) and $L_{\downarrow}$ and $L^{\uparrow}$ are incoming and outgoing long wave radiation (4.0 – 100 μm), respectively.

### *5.2.1.1 Short-wave Radiation ($K_{\downarrow}$)*

The shortwave radiation ($Wm^{-2}$) reaching the Earth's surface under cloud-free conditions is calculated as:

$$K_{\downarrow} = \tau K_{\downarrow}^{toa} \qquad (5.3)$$

where $\tau$ is atmospheric transmissivity and $K_{\downarrow}^{toa}$ is the extraterrestrial solar radiation ($Wm^{-2}$). The extraterrestrial solar radiation at a given point in time is calculated according to the following relationship:

$$K_{\downarrow}^{toa} = G_{SC} E_o (\sin\delta \sin\phi + \cos\delta \cos\phi \cos\varpi) \qquad (5.4)$$

where $G_{SC}$ = solar constant (1367 $Wm^{-2}$), $E_o$ = is eccentricity correction factor (i.e. average/actual Earth-sun distance), $\delta$ = solar declination, $\phi$ = latitude and $\omega$ = hour angle (all angles are in radians). The derivation of these parameters except for latitude, which is

found from the satellite imagery, is given in Table 5.1. Registrations of reflected radiation at the top-of-atmosphere (TOA) by operational Earth observation satellites are usually acquired from a single direction. Corrections for atmospheric interferences can be made, based on detailed information such as temperature, humidity and wind velocity, which are measurable in the field by radiosoundings. Since such information is unavailable in the current research, hemispherical surface reflectance i.e. surface albedo ($\alpha$) has been calculated from broadband planetary reflectance ($r_p$) following Chen & Ohring (1984) as:

$$\alpha = \frac{r_p - r_a}{\tau^2} \qquad (5.5)$$

where $r_a$ = the fractional path radiance and $\tau^2$ = the two-way transmittance for solar radiation ($Wm^{-2}$). The surface albedo ($\alpha$) of the darkest pixel (e.g. deep sea) is usually assumed to take a value of zero. If $\alpha = 0$, it follows from Equation 5.5 that $r_a = r_p$ of a deep sea and by approximation, the darkest pixel target.

Table 5.1 Determination of intermediate radiation balance parameters

| Parameter | Symbol | Unit | Equation |
|---|---|---|---|
| 1. | $K^{\uparrow}_{toa}$ | $Wm^{-2}\ sr^{-1}\ \mu m^{-1}$ | $K^{\uparrow}_{toa} = c12 + (c13 - c12)/255*DN$ |
| 2. | $\delta$ | Rad | $\delta = 0.409*\sin(0.0172*JD - 1.39)$ |
| 3. | $\omega_{(x)}$ | Rad | $\omega_{(x)} = \pi\{t_{(x)} - 12\}/12$ |
| 4. | $t_{(x)}$ | Decimal hours | $t_{(x)} = t + \text{min}/60 + \text{lon}12/\pi$ |
| 5. | ø | Rad | $\text{Cos}ø = \sin(\delta)/\{\text{lat}_{(y)}\} + \cos(\delta)\cos\{\text{lat}_{(y)}\}\cos\{\omega_{(x)}\}$ |
| 6. | $d_s$ | AU | $d_s = 1 + 0.0167\ \sin(2\pi\ (JD - 93.5))/365$ |
| 7. | $E_0$ | Dimensionless | Average/Actual $d_s$ |
| 8. | $K_{\downarrow}^{toa}$ | $Wm^{-2}$ | $K_{\downarrow}^{toa} = K^{\uparrow}_{toa}\ \text{Cos}(ø)/d^2$ (varies with characteristics of radiometer) |
| 9. | $K_{\downarrow}$ | $Wm^{-2}$ | $K_{\downarrow} = G_{SC}\ *\cos\theta*d_r*\tau$ |
| 10. | $r_p$ | Dimensionless | $r_p = \pi\ K^{\downarrow}_{toa}/\ K^{\downarrow}_{toa}$ |
| 11. | $r_a$ | Dimensionless | $r_a = 0.025 - 0.04$ |
| 12. | $L^{\downarrow}$ | $Wm^{-2}$ | $L^{\downarrow} = \varepsilon_a*\sigma T_a^4$ |
| 13. | $\varepsilon_0$ | Dimensionless | $\varepsilon_0 = 1.009 + 0.047\ \ln NDVI$ |
| 14. | $L^{\uparrow}$ | $Wm^{-2}$ | $L^{\uparrow} = \varepsilon_0*\sigma T_s^4$ |
| 15. | $R_n$ | $Wm^{-2}$ | $R_n = K^{\downarrow}\ (1-\alpha) + (L^{\downarrow} + L^{\uparrow})$ |
| ***where*** | | | $r_p$ = planetary reflectance |
| $c_i$ = Parameter number | | | $T_a$ = air temperature |
| $d_s$ = Earth-sun distance | | | $T_s$ = surface temperature |
| $d_r$ = inverse Earth-sun distance | | | $t$ = local time |
| $\sigma$ = Stefan-Boltzmann constant | | | $\delta$ = solar declination |
| ø = sun zenith angle | | | $\omega_{(x)}$ = solar hour angle |
| $JD$ = Julian day | | | $t_{(x)}$ = decimal hours |
| $r_a$ = atmospheric reflectance | | | $\theta$ = solar zenith angle |
| $\varepsilon_0$ = surface emissivity | | | $E_0$ = eccentricity factor |
| $\varepsilon_a$ = atmospheric emissivity | | | Lat/lon = latitude/longitude |

Sources: Tasumi (2003); Bastiannssen *et al.* (1998) and Iqbal (1983)

On a clear dry day, a well-calibrated pyranometer can be used to measure solar radiation ($K_{\downarrow}$) in the field and through this the single-way transmittance $\tau$ can then be derived. The square of this approximation leads to the two-way transmittance[2] value. Tasumi (2003)

[2] Incoming and outgoing solar radiation is higher at the top of atmosphere and lower in the land surface because in both ways, a portion of radiation is absorbed or scattered by air. The amount of the absorption or decrement is explained by using a (one-way) transmittance of air. There is additional reflectance that is observed by sensors above the top of atmosphere because a portion of incoming radiation is reflected, rather than absorbed, before it reaches the earth's surface. This component is called albedo path radiance.

have shown that for a known surface elevation ($z$), the one way transmission ($\tau$) may be predicted as follows:

$$\tau = 0.75 + 2*10^{-5} z \qquad (5.6)$$

Thus, assuming that the average elevation of the Tamale area is 180m, the two-way transmittance ($\tau^2$) is approximately, ***0.568.*** The above report has also shown that the fractional path radiance ($r_a$) ranges from 0.025 – 0.04.

### *5.2.1.2 Incoming Long Wave Radiation ($L_{\downarrow}$)*

The incoming long wave radiation ($Wm^{-2}$) is the downward thermal radiation flux from the atmosphere. It is computed using Stefan-Boltzmann equation as:

$$L_{\downarrow} = \varepsilon_a \sigma T_a^4 \qquad (5.7)$$

where $\varepsilon_a$ = atmospheric emissivity (dimensionless), $\sigma$ = Stefan-Boltzmann's constant ($5.67*10^{-8}$ $Wm^{-2}$ $K^{-4}$) and $T_a$ = near surface temperature ($^0K$), $\varepsilon_a$ may be calculated using an empirical model following Bastiannssen (1995) as follows:

$$\varepsilon_a = 0.85(-\ln \tau)^{0.09} \qquad (5.8)$$

### *5.2.1.3 Instantaneous Outgoing Long Wave Radiation ($L^{\uparrow}$)*

The outgoing long wave radiation ($Wm^{-2}$) is the upward thermal radiation leaving the surface. It is calculated using the Stefan-Boltzmann equation as follows:

$$L^{\uparrow} = \varepsilon_0 \sigma T_s^4 \qquad (5.9)$$

where $\varepsilon_0$ = surface emissivity (dimensionless), $\sigma$ = Stefan-Boltzmann's constant ($5.67*10^{-8}$ $Wm^{-2}$ $K^{-4}$) and $T_s$ = surface temperature ($^0K$) which is calculated from radiant thermal bands using Planck's equation (Section 5.4).

### *5.2.1.4 Surface Emissivity ($\varepsilon_0$)*

Emissivity of an object is the ratio of the energy radiated by that object at a given temperature to the energy radiated by a black body at the same temperature. Since the thermal radiation of the surface is observed in the thermal bands of satellite data, one can compute the surface temperature if the emissivity of the land surface is estimated. In SEBAL, surface emissivity is estimated using NDVI and an empirically-driven (van de Griend & Owe, 1993) method:

$$\varepsilon_0 = 1.009 + 0.047 \ln(NDVI) \qquad (5.10)$$

where NDVI >0; otherwise, emissivity is assumed to be zero (e.g. water) and NDVI is calculated as a ratio of the difference in reflectance for the near infrared band (*NIR*) and the red band (*R*) to their sum as (Goetz, 1997):

$$NDVI = \frac{rNIR - rR}{rNIR + rR} \tag{5.11}$$

In SEBAL, NDVI is calculated based on reflectance ($r$), instead of the brightness ($DN$) values of the original bands.

In remote sensing, different spectral indices and vegetation properties such as the soil-adjusted vegetation index (SAVI), leaf area index (LAI), fractional photosynthetic active radiation ($f$PAR) and fractional vegetation cover ($f$VC) have been used under a variety of atmospheric and landscape conditions as a "measure" of total biomass volume (Steltzer & Welker, 2006; Weng *et al.,* 2003; Qin *et al.,* 1998; Turner *et al.,* 1998). This can then be integrated with empirical models to solve the energy balance equation (Bastiannssen *et al.,* 1998a). However, several uncertainties exist regarding this approach because of the need to correct for a number of physical parameters including solar angles, soil reflectance, canopy and sensor geometry (Steltzer & Welker, 2006; Goetz, 1997). Although the accuracy of the SEBAL method has been widely tested (Brata *et al.,* 2006; Su *et al.,* 1999; Bastiannssen *et al.,* 1998a), its dependence on NDVI as a surrogate variable for biomass volume can be problematic when one attempts to establish independent relationships between biomass and other energy balance parameters such as surface temperature ($T_s$) is ideally suited to study very large heterogeneous basins such as the Volta where there is lack of high quality ground-based observations. The SEBAL approach can not be ignored.

### 5.2.2 Soil Heat Flux ($G_0$)

The soil heat flux ($Wm^{-2}$) is the rate of heat storage in a soil as a result of temperature gradient between soil surface and the underlying topmost soil layers. The temperature gradient varies with the $f$VC and the LAI, as light interception and shadow formation on the bare soil determine radiative heating of the bare soil surface. Under field conditions, $G_0$ can be measured if the soil's thermal conductivity is known (Figure 5.3) based on the following relationship:

$$G_0 = \lambda_s \frac{\Delta T_s}{\Delta z} \qquad (5.12)$$

where $\lambda_s$ = the thermal conductivity of the soil, $\Delta T_s$ = temperature difference between $T_0$ and $T_1$ and $\Delta z$ = depth difference between $z_0$ and $z_1$.

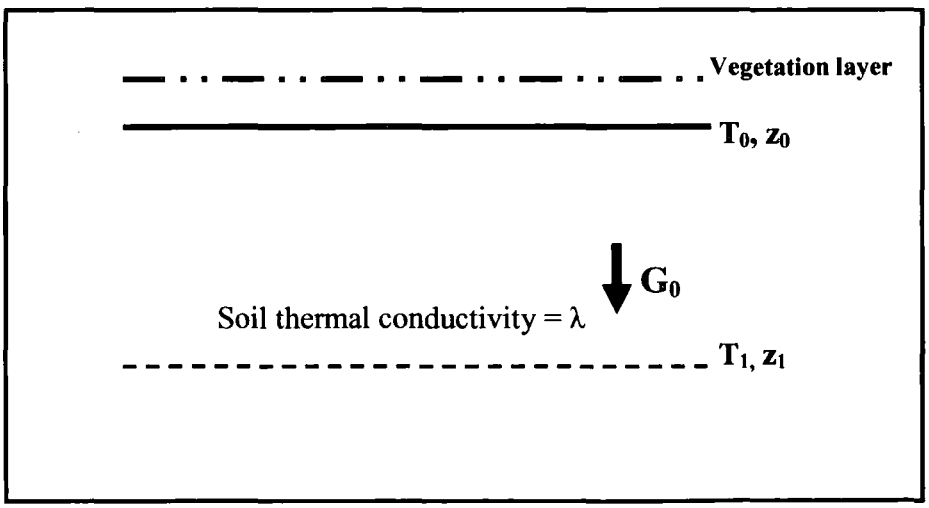


Figure 5.3 Illustration of soil heat flux (modified after Morse *et al.* (2000)

Equation 5.9 is not fully applicable in the context of SEBAL due to lack of spatial information about the soil's thermal conductivity. Therefore, in the Volta application, an empirical equation (Bastiannssen et al. 1998a) is applied to estimate $G_0$ as a function of NDVI, surface temperature and albedo as follows:

$$G_0 = R_n(\frac{T_s - 273}{\alpha})[0.0032(1.1\alpha) + 0.0062(1.1\alpha)^2](1 - 0.978NDVI^4) \qquad (5.13)$$

where NDVI is defined in Equation 5.11

Equation 5.10 is mainly valid for vegetated surfaces; thus, a shorter version which has sole dependence on NDVI has now been developed for more humid environments (Bear River basin in Idaho, USA) by Morse *et al.* (2000). So NDVI is used as a surrogate variable for the amount of radiation that fails to reach the soil surface. The SEBAL equation uses NDVI as an empirical scaling parameter.

### 5.2.3 Sensible Heat Flux (*H*)

Sensible heat flux (*H*) is the rate at which energy is lost from the soil through convection and diffusion processes as a result of temperature difference between the surface and the lowest layers of the atmosphere:

$$H = \frac{\rho_a C_p \Delta T}{r_{ah}} \qquad (5.14)$$

where $\rho$ = density of air (Kg $m^{-3}$), $c_p$ = air specific heat capacity 1004 ($JKg^{-1}K^{-1}$), $\Delta T$ = difference between surface and air temperature ($^0K$) and $r_{rah}$ = aerodynamic resistance for heat transport ($sm^{-1}$), determined by wind speed, surface roughness, displacement height and thermal instability of the atmosphere.

$$r_{ah} = \frac{1}{ku^*}\left[\ln\left(\frac{z_{ref} - d}{z_{oh}}\right) - \psi_h\right] \qquad (5.15)$$

and,

$$u^* = \frac{ku_{blend}}{\left[\ln\left(\frac{z_{blend} - d}{z_{om}}\right)\right] - \psi_m} \qquad (5.16)$$

where $u^*$ = friction velocity, $k$ = von Karman's constant (0.41), $u_{blend}$ = wind speed at the blending height (i.e. mixing layer), $z_{blend}$ = blending height, $z_{oh}$ = roughness length for heat transport, $z_{om}$ = roughness length for momentum transport, $d$ = displacement height and $\psi_h$ and $\psi_m$ = are stability correction factors for heat and momentum transport, respectively.

The temperature difference ($\Delta T$) is predicted in order to estimate $H$ from Equation 5.14 following Bastiannssen *et al.* (1998a):

$$\Delta T = \frac{Hr_{ah}}{\rho_a C_p} \qquad (5.17)$$

In this equation, $H$ and $\Delta T$ are both unknown factors but are directly related to one another, as well as to the value of $r_{ah}$. Therefore, $\Delta T$ is calculated at two extremes, "indicator pixels" (wettest and driest pixels) by assuming values for $H$ at these reference pixels. The wettest pixel is the pixel where $H \sim 0$ (i.e. all the available energy $[R_n - G_0]$ is converted $\lambda ET$ or $\Delta T$ becomes zero), and the driest pixel is where $\lambda ET \sim 0$, so that $H = R_n - G_0$ or $\Delta T$ is maximum. The wettest pixels are selected as pixels with high *NDVI* but with low temperature, while the driest pixels are selected as pixels with high temperature but with low NDVI and albedo. Subsequent to the selection of the wettest and driest pixels, the linear equation which gives value of $\Delta T$ as a function of surface temperature is developed as:

$$T_s - T_a = \Delta T = a + bT_s \qquad (5.18)$$

where $T_s$ = surface temperature, $T_a$ = air temperature (previously defined differently as near surface in Equation 5.7), and $a$ & $b$ are constants. With the values of $T_s$ and $\Delta T$ at the two pixels, $a$ and $b$ may then be solved iteratively, as $r_{ah}$ is also a function of $H$. After solving for $a$ and $b$ the sensible heat flux ($H$) for the whole image is calculated iteratively until convergence is reached. Finally, the latent heat flux ($\lambda ET$) is computed for each pixel as a residual term of the surface energy balance. An equivalent amount of instantaneous $ET$ is also calculated by dividing the latent heat flux by the latent heat of vaporization ($\lambda$).

The context in which $H$ is estimated using remote sensing methods is a challenging one. At the field scale, however, direct $H$ measurements are more easily measured and more widely available using instruments like the scintillometer (eddy correlation) and

energy balance Bowen ratio system. Also, forecasting models such as the European Centre for Medium-range Weather Forecasting (ECMWF) method has wide applicability (Allen *et al.*, 1998; Bastiannssen *et al.*, 1996; de Bruin *et al.*, 1996; Kustas *et al.*, 1990). The biggest advantage of remote sensing methods, however, lies in their ability to make frequent measurements of energy balance components over very large areas.

## 5.3 Evapotranspiration Up-scaling Methods

### 5.3.1 Evaporative Fraction

Remotely sensed measurements such as radiative temperature are only indirectly related to the state of the land surface and the corresponding heat fluxes. Estimation of evaporative fraction ($\Lambda$), which is the ratio of latent heat flux over available energy, is one of the most promising methods for using remote sensing data to evaluate land surface fluxes and in particular, evapotranspiration. Even though there are conflicting reports about evaporative diurnal behaviour (e.g. Gentine *et al.*, 2006), it is often assumed that $\Lambda$ is constant during daytime under fair weather conditions (Bastiannssen *et al.*, 1996; Shuttleworth *et al.*, 1989). This is in contrast to sensible and latent heat fluxes, which show unsteady behaviour during the daytime. Thus, remotely sensed instantaneous evapotranspiration (Section 5.2) may be integrated over a daily time scale using the $\Lambda$ relationship as:

$$\Lambda = \frac{\lambda AE}{\lambda AE + H} = \frac{\lambda AE}{R_n - G_0} \qquad (5.19)$$

From Equation 5.15, the instantaneous evaporative fraction ($\Lambda_{ins}$) and integrated daily evaporative fraction ($\Lambda_{day}$) may be assumed to remain the same as:

$$\Lambda_{ins} = \Lambda_{day} \tag{5.20}$$

### 5.3.2 Daily Net Radiation

Guided by the above principles, net radiation can be aggregated as daily net radiation ($R_{n\text{-}day}$) following the approach of Bastiannssen *et al.* (1996) as:

$$R_{n-day} = (1-1.1\alpha)K^{\downarrow}_{day} - 110\tau_{day} \tag{5.21}$$

where $\tau_{day}$ = daily atmospheric transmissivity for radiation, which is calculated using the Angstrom formula as:

$$\tau_{day} = 0.25 + 0.5\frac{n}{N} \tag{5.22}$$

where $n$ = actual duration of sunshine and $N$ = maximum possible sunshine or daylight hour. The actual (10-hour) and maximum sunshine duration (12-hour) record is readily available from the Ghana Meteorological Office. Daily incoming short wave radiation ($K^{\downarrow}_{day}$) is also calculated using the following relationship:

$$K^{\downarrow}_{day} = 11.5741\tau_{day}K^{toa}_{\downarrow-day} \tag{5.23}$$

where $K_{\downarrow-day}^{toa}$ = daily incoming short wave radiation at the top-of-atmosphere (TOA) calculated using either (1) the sine method or (2) cosine method as:

$$K_{\downarrow-day}^{toa} = \frac{24}{\pi} G_{SC} E_o \sin\delta \sin\phi \left[ \frac{\pi}{180} \omega_s - \tan\omega_s \right] \qquad (5.24a)$$

$$K_{\downarrow-day}^{toa} = \frac{24}{\pi} G_{SC} E_o \cos\delta \cos\phi \left[ \sin\omega_s - \frac{\pi}{180} \omega_s - \cos\omega_s \right] \qquad (5.24b)$$

where $\omega_s$ = sunset or sunrise hour angle (radians). The definition of the remaining parameters is given in Equation 5.4.

### 5.3.3 Daily Actual Evapotranspiration ($ET_{day}$)

A combination of Equations 5.20 and 5.21 allows daily actual evapotranspiration ($ET_{day}$) to be calculated (Bastiannssen *et al.*, 1996):

$$AE_{day} = \frac{\Lambda R_{n-day}}{28.588} \qquad (5.25)$$

### 5.3.4 Monthly Evapotranspiration ($ET_{mon}$)

Based on Equation 5.25, it is feasible to aggregate daily evapotranspiration to monthly values. The procedure depends on two key inputs: (1) daily reference crop evapotranspiration (*PE*); and (2) daily actual evapotranspiration. Two of the commonest approaches to solve this incorporate either the Priestley-Taylor equation (1972) or the FAO Penman-Monteith method (Allen *et al.* 1998). Mekonnen (2005), Parodi (2002) and Bastiannssen & Mekonnen (2000) have applied the Priestley-Taylor equation for similar tropical catchments using an empirically determined albedo ($\alpha$) = 0.23 as follows:

$$PE_{ref-day} = 1.26\left[(1-0.23)K^{\downarrow}_{day} + L_{net-day}\right] \qquad (5.26)$$

where $K^{\downarrow}_{day}$ is represented in Equation 5.23 and $L_{net\text{-}day}$ is daily net long wave radiation determined based on a procedure previously described by de Bruin (1987). The Priestley-Taylor coefficient of 1.26 was originally developed for humid conditions, which may not be fully applicable for dry catchments. The ASCE (1990) has developed a range of constants, 1.32, 1.56 & 1.74 for dry vegetated, sparsely-vegetated and arid environments, respectively. As input to this approach, daily *PE* has already been determined for this area based on the FAO's Penman-Monteith equation and the results are shown as Figure 4.3 in Chapter 4. Assuming that daily relative evapotranspiration remains fairly stable over the month in which the satellite image was acquired in combination with Equation 5.25, the areal monthly actual evapotranspiration ($ET_{mon}$) may be derived as follows:

$$AE_{-mon} = \frac{AE_{-day}}{PE_{ref-day}} * PE_{ref-mon} \qquad (5.27)$$

where $PE_{ref\text{-}day}$ and $PE_{ref\text{-}mon}$ refer to daily and monthly reference evapotranspiration, respectively.

## 5.4 Derivation of Land Surface Temperature from Satellite Imagery

Recognising the importance of surface temperature as key energy source for estimating regional *ET*, the question is: how are temperatures derived from thermal imagery? Figure 5.4 provides a diagrammatic illustration of how this may be achieved. Temperature derivation from new sensor data such as MODIS and AATSR (the key research data here) has been addressed by a number of authors (e.g. Sobrino *et al.*, 2003; Prata, 2002; Wan *et al.*, 2002; etc.).

In all cases, it is impossible to extract temperature from Level 1B radiances without knowing the emissivity of the observed surface object or by performing inter-band comparisons. Here, brightness temperature ($T_B$) (i.e. the temperature for an ideal black body with the observed radiance) is calculated from the Planck's Law as:

$$L = \frac{2hc^2\lambda^{-5}}{\left(e^{\frac{hc}{k\lambda T_B}} - 1\right)} \qquad (5.28)$$

where $L$ = radiance ($Wm^{-2}$ $steradian^{-1}$ $m^{-1}$); $h$ = Planck's constant ($6.620*10^{-34}Js$); $c$ = speed of light ($3.0*10^{8}$ m $s^{-1}$); $k$ = Boltzmann's gas constant ($1.381*10^{-23}$ $JK^{-1}$); $\lambda$ = band or detector centre wavelength (m) and $T_B$ = temperature ($^0K$).

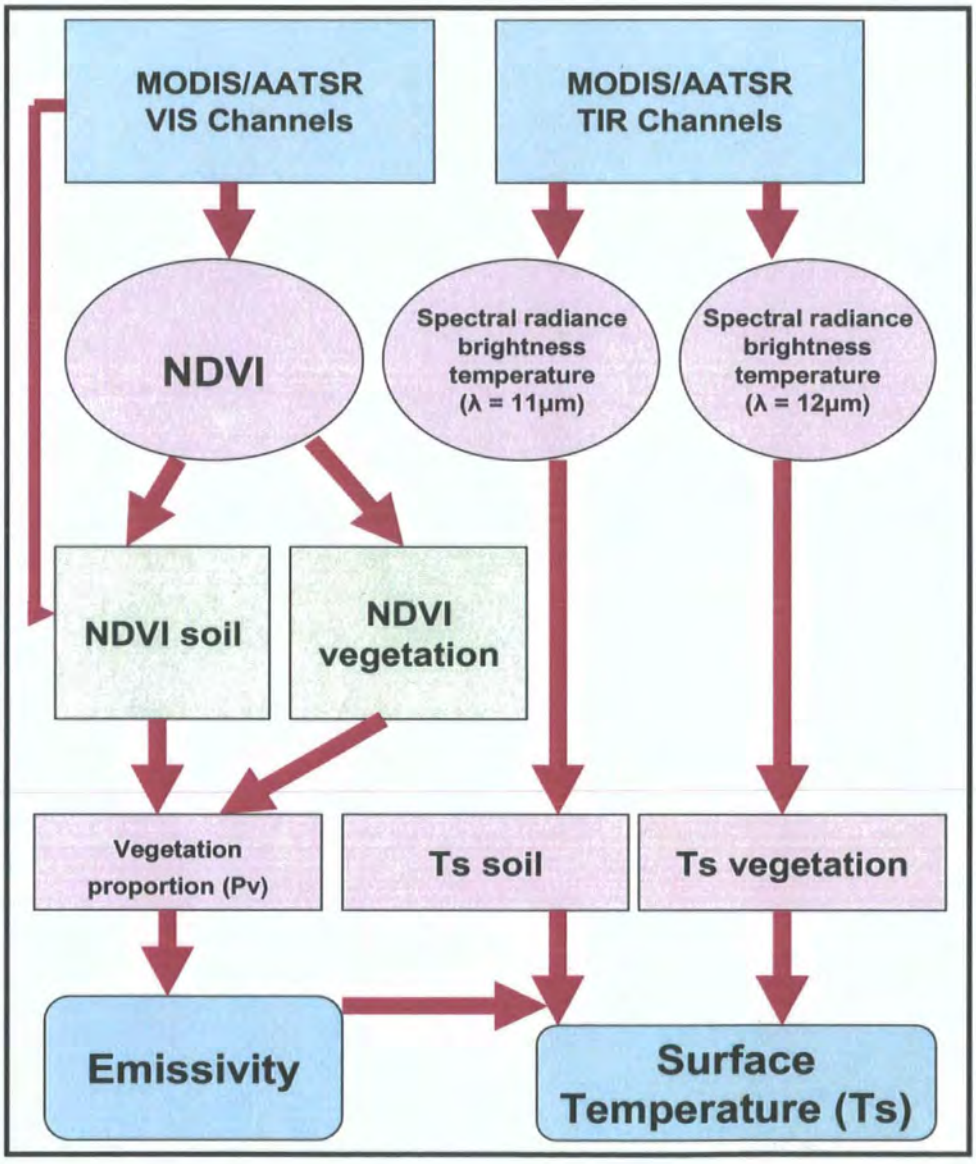


Figure 5.4 Schematic diagram for deriving surface temperature from satellite imagery.

Inverting Equation 5.28 to solve for temperature ($T_B$) results in the following:

$$T_B = \left(\frac{hc}{k\lambda}\right)\frac{1}{\ln\left(2hc^2\lambda^{-5}L^{-1}+1\right)} \qquad (5.29)$$

Several attempts have been made in the past to simplify Equation 5.29 based on approximations and empirical constants in order to correct for atmospheric attenuation of radiance and surface emissivity. However, researchers need to be careful about the general application of these constants to avoid misleading results (McManus, 2004). One of the most widely applied formulae is given by Price (1989) and Creswell *et al.* (1999):

$$T_B = \frac{c_2}{\lambda \ln\left[\frac{c_1}{\lambda^5 L}+1\right]} \qquad (5.30)$$

where $c_1 = 3.74*10^8$ and $c_2 = 1.439*10^4$. It is worth mentioning that AATSR has fully calibrated $T_B$ values, which means that Equation 5.30 has already been applied to the data before it is supplied to the user.

Different methods have been published in order to retrieve $T_s$ from $T_B$, on the basis of correcting $T_B$ for atmospheric effects. A full revision of these is given in Sobrino *et al.*, (2002) and Dash *et al.* (2002). In these reports, three main methods have been distinguished based on whether temperature is retrievable from one or two thermal channels: (1) single-channel method (e.g. Jiménez-Muñoz & Sobrino, 2003; Qin *et al.*, 2001); (2) split-window (e.g. Sobrino *et al.*, 1994; Becker & Li, 1990; Price, 1984); and (3)

dual angle (e.g. Sobrino *et al.*, 2004; Prata, 1994). Whereas the single-channel (mono-window) method uses observation at one spectral band, the split-window employs observations at two different bands within the 10 – 12μm spectral region to estimate and compensate for the influence of atmosphere. The dual angle (DA) method uses observation of the same channel but under two different angles to exploit the different absorption path-lengths. Three or more thermal channel methods have also been demonstrated in literature, e.g. Wan & Li (1997), but are not applied here. It is worth mentioning that many of these studies refer to ocean temperature where it is easy to assume constant emissivity; on land, this is more difficult. Figure 5.3 is an example of the split-window method. For multi-channel thermal imagery, the split-window method has been adopted mainly because of its simplicity and accuracy (Sobrino *et al.* 1996; Prata, 1994; Becker & Li, 1990). Furthermore, in the case of AATSR data the dual angle algorithm may not be appropriate because of pixel re-gridding problems; AATSR image pixels derived from the forward angle acquisition process are rescaled from 1.5 x 2.0 km to 1 x 1 km, which means pixel temperature for heterogeneous landscapes may not represent the actual areas measured (Sòria & Sobrino, 2005).

The effects of land surface emissivity are implicitly taken into account in split-window algorithms. The base algorithm may be stated as follows:

$$T_s = a_0 + b_0 T_{11} + c_0 T_{12} \qquad (5.31)$$

where $a_0$, $b_0$ and $c_0$ are coefficients that depend on: (1) land cover type; (2) vegetation fraction; (3) season and time of day; (4) atmospheric water vapour; (5) satellite zenith

viewing angle; and (6) land surface emissivity, where $T_{11}$ and $T_{12}$ = brightness temperatures (top-of-atmosphere) in MODIS/AATSR 11μm and 12μm channels.

The essence of the algorithm is the recognition that over the land, both atmospheric water vapour effects and surface emissivity effects play important roles in modifying the amount of radiation reaching the satellite-borne radiometer. In this research, the accuracy of two key scenarios based on numerical coefficients recently proposed by Sòria & Sobrino (2005) is examined as follows: (1) $T_s - T_B$ linear split-window (Equation 5.32) and (2) $T_s - T_B$ quadratic split-window algorithms (Equation 5.33).

$$T_s = T_{11n} + (1.01 + 0.53W)(T_{11n} - T_{12n}) + (0.40 - 0.85W) + (63.4 - 7.01W) * (1 - \varepsilon) - (111 - 17.6W)\Delta\varepsilon \quad (5.32)$$

$$T_s = T_{11n} + 0.61(T_{11n} - T_{12n}) + 0.31(T_{11n} - T_{12n})^2 + 1.92 \quad (5.33)$$

where $n$ = satellite nadir viewing angle; $W$ = water vapour content; $\varepsilon$ = emissivity and $\Delta\varepsilon$ = spectral emissivity difference. The advantages of the semi-automated split-window method are also examined in comparison with the fully-automated Simplified Method for Atmospheric Correction (SMAC) (Rahman & Dedieu, 1994). The resulting $T_s$ values are evaluated using field-based surface temperatures before applying the outcome as input to the SEBAL algorithm in Section 5.2.

## 5.5 Remote Sensing Statistics

A strong link exists between statistics and remote sensing. For example, Curran & Atkinson (1998) and Lacaze *et al.* (1994) have demonstrated a range of statistical applications in remote sensing, e.g.: (1) exploration and description of spatial variation in remotely sensed and ground data; (2) designing optimum sampling schemes for image and ground data; and (3) increasing the accuracy with which remotely sensed data can be used to classify land cover or estimate continuous variables.

An important application of statistics in this thesis (see Chapter 7) concerns the derivation of models that correlate between satellite-derived and physically measured geophysical variables. The utility of the Pearson product coefficient ($r$) (i.e. measure of the association between two geophysical variables [e.g. $X$ and $Y$]) is described in this section. The sampling procedure driving the correlation models is also described. The detailed definition of the Pearson product-moment correlation coefficient ($r$) and the coefficient of determination $R^2$ are given in Appendix 5.1. Here, it is necessary to define $R^2$ as the ratio of explained to total variation described by the follow relationship:

$$R^2 = \frac{\sum(\hat{Y} - \overline{Y})^2}{\sum(Y - \overline{Y})^2} \qquad (5.34)$$

where $Y$ = a score on a random variable; $Y$ $\hat{Y}$ = corresponding predicted value of $Y$, given the correlation of $X$ and $Y$ and the value of $X$. As noted above, $R^2$ is mainly used by statisticians as a conventional measure of the association between two random variables. Assuming that changes in surface temperature ($T_s$) in the Volta landscape are strongly

correlated with changes in vegetation cover (NDVI) such that $r = 0.90$, it follows from Equation 5.34 that 81% of the variance in $T_s$ can be "accounted for" or "explained" by changes in NDVI and the linear relationship between NDVI and $T_s$.

It must be noted, however, that the applicability and predictive power of linear correlations between satellite-derived surface variables depends critically on the normality of the frequency distribution of the image data (Lacaze *et al.*, 1994). In this case, histograms of the image outputs were plotted (Figure 5.5) to evaluate their frequency distribution; positively/negatively skewed images were not used in the research.

A number of remote sensing based data sampling techniques have been described in literature, e.g. Curran & Atkinson (1998) and Lacaze *et al.* (1994). These include: (1) optimum spatial sampling; (2) random sampling; (3) systematic sampling; (4) stratified random sampling; and (5) cluster sampling. The simplest definition of random sampling is selection of image pixels from the image (sample) population such that each pixel has an equal chance to be measured. A good selection approach is guided by expert knowledge about field conditions and experience in statistics, such as the utilization of random numbers. The main difference between random and optimum sampling is that in the latter case, all the image pixels are measured. Systematic sampling methods involve selection of for example, every $n^{th}$ pixel of the population ($N$), while stratified sampling involves division of the population into two or more strata and sampling each sub-population using random techniques. The cluster sampling methods also involve division of the population into clusters. A few of the clusters are randomly selected from which exhaustive sampling is carried out.

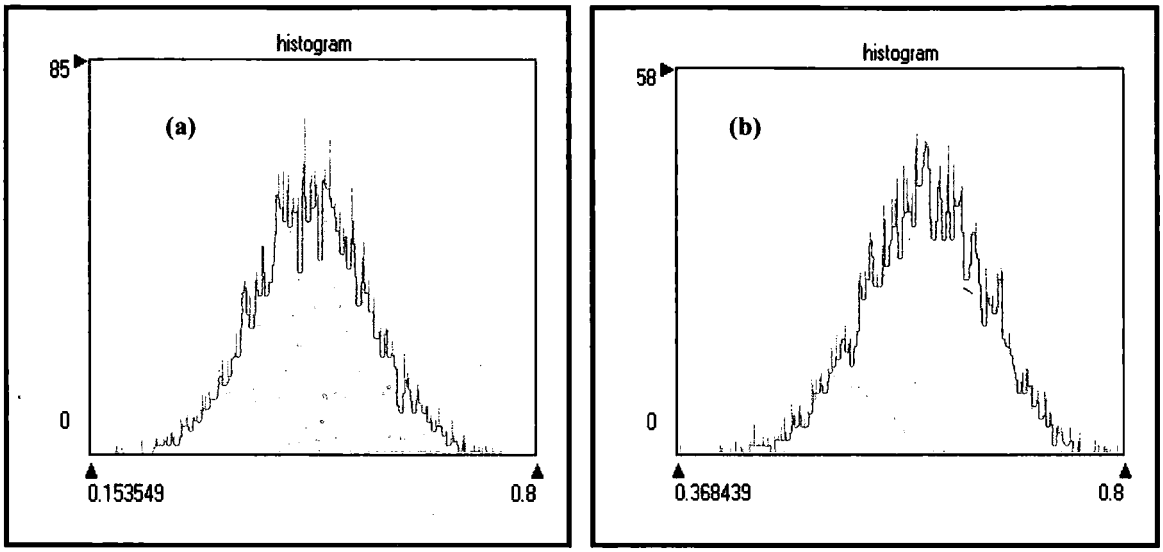


Figure 5.5 Histograms of NDVI values (a) MODIS date: 250105 and (b) AATSR date: 250105. These data sets show examples of normal data representation, which shows the applicability and usefulness of $R^2$ as an association measure between two random geophysical variables.

To account for spatial variability of the savannah landscape, the images have not been sampled, which means that all image pixels (entire population) were used to model relationships between geophysical variables (see Figure 7.3 in Chapter 7). The benefit of this approach is that no sampling bias is encountered. Where this was not entirely feasible, for example, to measure energy fluxes for the Tamale urban area (see north-western part of Figure 3.8a) a two-stage clustered sampling method was used. In that case, the urban area was delimited and guided by a district map, approximately 90% of the district was randomly sampled.

## 5.6 Summary

This chapter has provided a description of the methodological approach for the parameterisation of the SEBAL algorithm for calculating *ET* at the regional scale, for subsequent application to the study area. Although remote sensing techniques cannot measure *ET* directly, it has been shown that they can provide indirect estimates by measuring intermediate parameters (e.g. land cover and surface temperature) over large spatial and temporal scales.

In this case, the Surface Energy Balance Algorithm for Land (SEBAL), a data assimilation scheme developed by Bastiannssen *et al.* (1998a) has been adopted. SEBAL is noted for its promising results and minimal data input requirement; such inputs being satellite-based visible, near infrared and thermal data. The performance of SEBAL is further enhanced by the integration of local meteorological measurements such as air temperature, wind speed and net radiation (Mekonnen, 2005; Bastiannssen *et al.* 1998b). Recognising that surface temperature ($T_s$) is the most critical energy source for heat fluxes, a detailed account of its retrieval methods from thermal imagery has been described. For heterogeneous landscapes, the split-window atmospheric correction has been recognised (Sòria & Sobrino, 2005) as one of the most suitable methods for retrieving spatial temperature from top-of-atmosphere (brightness) temperatures, which are now easy to extract from current sensor data sets. A full discussion of the application of the above approaches is the focus of Chapter 7.

The chapter has also provided a detailed description of the statistical methods used to model the relationships between geophysical parameters in the study area.

# Chapter 6

# Regional-Scale Evapotranspiration Modelling: SEBAL Processing in MATLAB

## 6.1 Introduction

Although satellite sensors cannot directly measure land surface fluxes, recent studies such as Brata *et al.* (2006), Mekonnen (2005) and Chemin (2003) have demonstrated how sensor measurements of instantaneous radiometric temperature, albedo and vegetation cover can be used to derive estimates of daily surface fluxes such as *ET* over wide areas. Understanding the spatial distribution of *ET*, for instance, is not only important for predicting agricultural efficiency and water resources but also successful implementation of global/regional climate models. Description of satellite sensor measurements, up-scaling procedures and regional energy and water balance modelling (right and bottom rings of Figure 6.1) have been given in Chapters 3 and 5. The purpose of this chapter is to build on these methods by providing algorithm for estimating surface energy and water fluxes (e.g. *ET* in Figure 6.1) using a [1]MATLAB-based implementation of SEBAL[2]. The goal is not only to establish a link between general *ET* modelling methods (Chapter 5) and subsequent results (Chapter 7) but also, to provide a critically evaluated stepwise procedure as an aid to future users which

[1] MATLAB is an interactive computer program that serves as a convenient "laboratory" for computations involving matrices. The program is written in FORTRAN and is designed to be readily installed under any operating system which permits interactive execution of FORTRAN programs. In the past couple of decades, the MATLAB language has become the *de facto* standard high-level language in digital signal processing. It is used extensively for analysis and rapid prototyping. MATLAB was created by Prof. Cleve B. Moler, Professor of Computer Science (a specialist in numerical analysis) at the University of New Mexico, USA. It has since spawned several commercial and open-source derivatives of the original MATLAB language. Today, the premier commercial version is MATLAB (R) by The Mathworks, Inc., and the best free, open-source version is probably, OCTAVE.

[2] SEBAL = Surface Energy Balance for Land Algorithm

hopefully, may improve their own SEBAL processing and analysis using a range of satellite imagery.

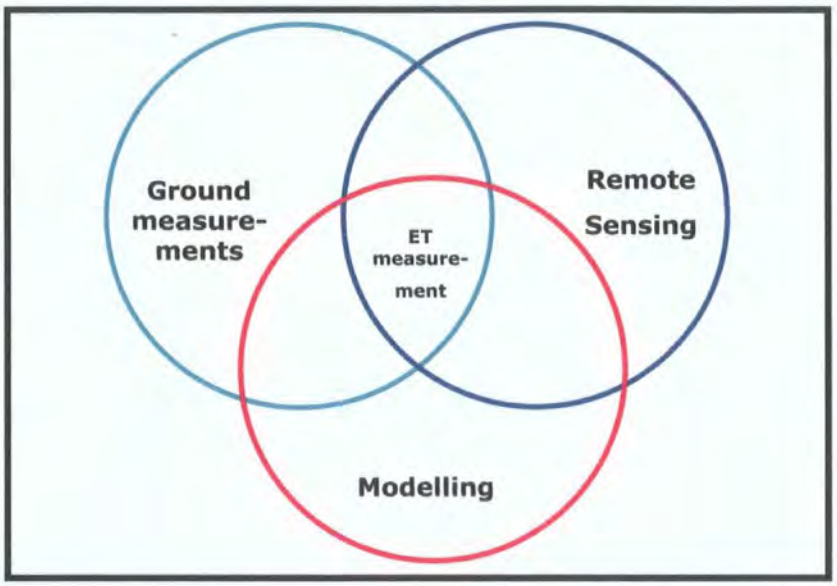


Figure 6.1 Regional *ET* measurement approach using remote sensing

## 6.2 SEBAL Processing

### 6.2.1 SEBAL Re-packaging

Morse *et al.* (2000) provide very useful guidelines for running the SEBAL algorithm in ERDAS-Imagine, following pioneering work by Bastiannssen *et al.* (1998a, b). However, these guidelines fail to address a variety of issues such as computational intensity of repetitive low-resolution satellite imagery, variability in data calibration coefficients, processing and analytical potential of complementary software packages and inter-changeability of data formats. Consequently, the original SEBAL algorithm was first reviewed following data and software demands reported by Makonnen (2005), Chemin (2003) and Morse *et al.* (2000). Secondly, to fit recent

datasets (i.e. Landsat ETM+, MODIS and AATSR) and the SEBAL computational chain to a wide variety of programs, three widely used applications were evaluated: ERDAS-Imagine, *C++* and MATLAB® in greater detail in the following section.

Prior to evaluation, it is important to comment on the organisation of raster and other model variables within these processing tools. Unlike ERDAS, *C++* and MATLAB are structured similarly in the way data are represented and manipulated. For example, they both require that input-output raster data and calibration constants are represented as *data types* (Appendices 6.1 and 6.2). The detailed information about machine-level data representation is described in a number of standard computer science textbooks, e.g. Lippmann *et al.* (2005), Hubbard (2000), etc. For SEBAL processing, however, it is relevant to mention that input-output variables may be stored as *single or double precision floating-point type* (Appendix 6.2). Here, *"single and double precision floating-point"* refers to computer memory storage as 32 and 64 bits, respectively; the size being a determinant of the number of significant digits the *type* value might contain. Whereas the *single precision float* (simply *float*) is generally guaranteed to offer six significant digits, the *double precision float* (simply *double*) is can offer at least 10 significant digits (Lippmann *et al.,* 2005), which is sufficient for SEBAL mathematical computations.

## 6.2.2 SEBAL Processing in MATLAB®

In the last 10 years, SEBAL has been processed using a number of programs. For example, the ITC (1995) previously used ILWIS; ERDAS-Imagine has been used by several authors, e.g. French *et al.* (2005); Chemin (2003); Morse *et al.* (2000); Zu *et al.* (1999) and Bastiannssen *et al.* (1998a, b). Also, the *C* language was used by Mekonnen (2005) and recently, MATLAB® was used by Brata *et al.* (2006). Though

each of these packages is noted for their unique advantages, none of them seems exclusively superior. For example, Morse *et al.* (2000) have reported that some of the difficulties associated with ERDAS-based SEBAL programming are: (1) complicated procedural algorithms (models) using the Model-Maker toolbox (e.g. Figure 6.2) and, (2) computational inefficiency related to SEBAL's extensive iterative steps for calculating sensible heat flux (see Section 5.2.3 of Chapter 5). Though ERDAS-Imagine has proved to be an efficient processing tool for single-date datasets (e.g. Chemin, 2003), its efficiency for repetitive (multi-temporal) imagery is yet to be ascertained.

In this research, an attempt was made to program SEBAL in the *C++* language. Although *C++* has good potential to run SEBAL successfully, three main difficulties were encountered. First, a suitable source-code was hard to find. Secondly, a considerable amount of time was needed for code modification, test-running, correction and re-coding. Finally, a good background in *C++* is needed to successfully run the program.

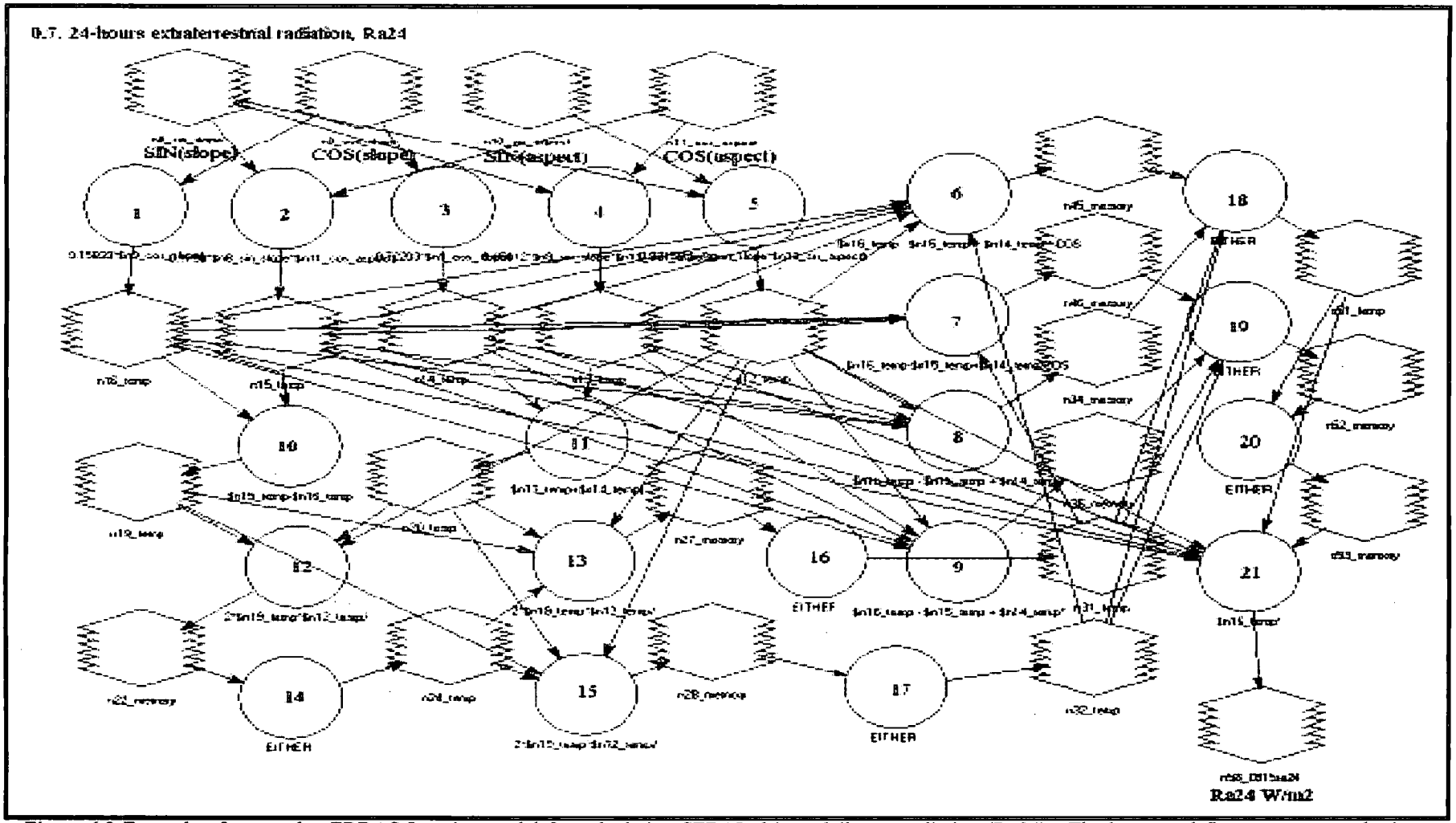


Figure 6.2 Example of a complex ERDAS-Imagine model for calculating SEBAL-driven daily net radiation (Rn24). The hexagonal figures represent the input-output domain for manipulative satellite data while the circles represent the domain for mathematical computations.

An important question is: of what utility is MATLAB for SEBAL processing? Brata *et al.* (2006) have recently demonstrated the capabilities of MATLAB as a comprehensive program for running SEBAL. Their method does not only confirm some of MATLAB's advantages over its predecessors like ERDAS-Imagine, but also its ability to integrate dynamically with Microsoft software suite e.g. MS Access, Word & Excel and to display and output complex illustrations in hardcopy. One of the greatest disadvantages of MATLAB is probably its susceptibility to loss of pixel geolocation attributes (i.e. pixel geographical coordinates), which has the potential to mask verification of specific targets and, thus, validation of results. One way to overcome this is conversion of MATLAB outputs into data formats (e.g. ASCII, TIFF, etc.) using complementary programs such as ENVI, ERDAS-Imagine and ARC-GIS. In other words, geolocation tasks in MATLAB are not automatically managed and have to done with support from other software such as ARC-GIS. Appendix 6.3 shows an example of how the geolocation task can be managed using ARC-GIS, whereas Appendix 6.4 displays the MATLAB graphical user interface (i.e. MATLAB R2006a version 7.2.0.232) whose import-export and format conversion tools support software and data integration.

### *6.2.2.1 Procedural Steps Involved in SEBAL Processing*

**Preparatory Stage 1: Calibration of Image Pixels**

Though MATLAB can successfully read and help the computational steps in raw data calibration, the best result is probably achieved through initial utilization of ERDAS-based spatial (mathematical) models (Model-Maker toolbox). A good example is NDVI modelling, represented by the following equation: NDVI = (NIR-R)/(NIR+R). Over complex vegetated surfaces, there is a good chance that the aggregated response

of red and near infrared light of certain pixels may sum up to zero (i.e. NIR+R = 0, for mixed pixels). Where the denominator of the equation above is equal to zero, solution of an otherwise very simple equation potentially becomes numerically complex over a wide spatial domain. One way to address this is to program intermediate steps likely to preclude zero as a denominator (see Figure 6.3) while at the same time, engaging a wide array of pixel values. Although MATLAB may handle zeros expediently; however, for inexperienced users, the ERDAS option may still be worth considering.

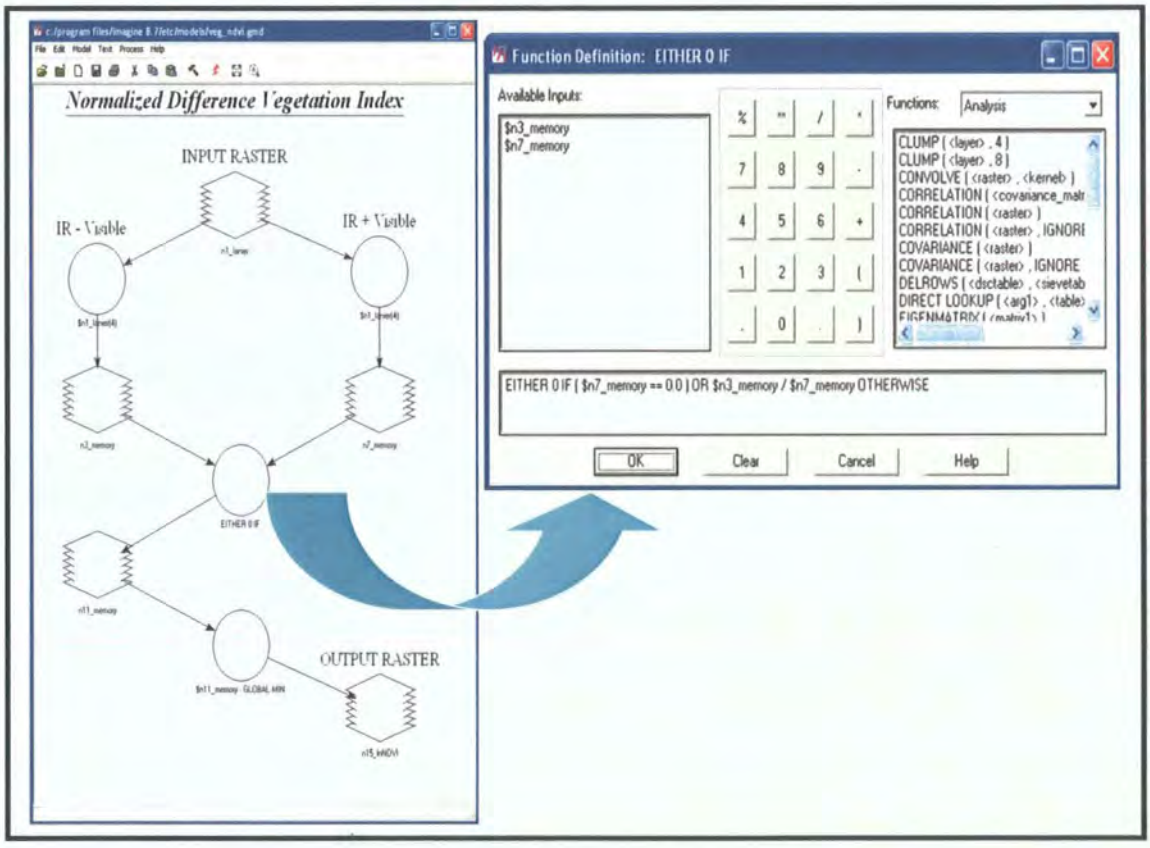


Figure 6.3 ERDAS-Imagine *Function* definition which precludes zero as divisor in the NDVI algorithm. The left and right-hand-side boxes represent the NDVI model and the Function definition, with the intermediate step connected by the arrow.

Another reason why program integration (see, for example, Figure 6.4) could be helpful is avoidance of extensive MATLAB programming loops, which may potentially

increase error propagation into the SEBAL processing chain, especially where a number of calibration uncertainties are connected with raw (first level) satellite data (e.g. MODIS Level 1). Though first level satellite data often deliver good quality information (sometimes free of charge), full calibration to suit local conditions may be unavailable to users. Figure 6.4 illustrates one of several approaches by which the computational steps in raw data calibration using ERDAS-Imagine may potentially be linked with MATLAB. For inexperienced users, this could be a very important and easy step to consider.

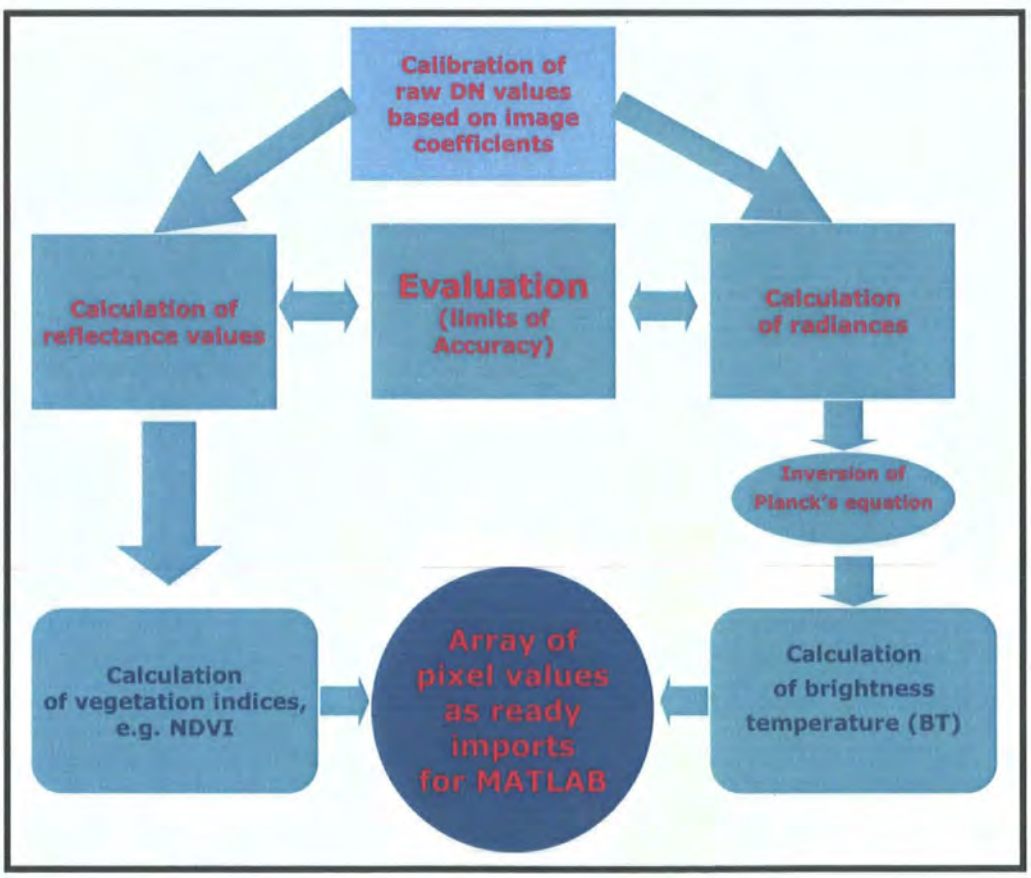


Figure 6.4 Manipulation of Landsat ETM+ and MODIS data for subsequent SEBAL programming in MATLAB

Table 6.1 show some examples of MATLAB mathematical syntaxes for SEBAL processing (see Figure 6.4). Detailed examples of the SEBAL algorithm are given in Appendix 6.1.

Table 6.1 Examples of MATLAB mathematical syntaxes for SEBAL processing (Landsat ETM+)

| Processing Step | MATLAB mathematical syntax |
|---|---|
| %%Calculation of radiance in band 1 (red channel) ($L_1$) (W $m^{-2}$ $ster^{-1}$ $\mu m^{-1}$) | $L_1$ = a+(b-a)*DN/255, where a & b are image constants and DN = digital number |
| %%Calculation of reflectance in band 1 (red) ($rf_1$) (%) | $rf_1$ = ($L_1$*PI*D^2)/(SSI*0.9494), where PI = 22/7, SSI = solar spectral irradiance from look-up tables |
| %%Calculation of brightness temperature ($BT_6$) (K) based on inverted Planck's equation (e.g. Landsat ETM band 6: 11μm) | $BT_6$ = $c_2$/(ln($c_1$/$L_1$+1), where $c_1$ = 666.09 W m^-2 $ster^{-1}$ $\mu m^{-1}$) and $c_2$ = 1282.71K |

Note: The above examples are related to Figure 6.5.

What constitutes the main drawback to this approach? Although the methodology shown in Figure 6.4 can be used to produce accurate calibrated data inputs for MATLAB, the process is not altogether straightforward and may be time-consuming. Thus, for inexperienced programmers, such integration can be difficult. On the other hand, where processing experience is lacking, automation of the integration process can be helpful.

**Preparatory Stage 2: Parameterization of the SEBAL Code**

For different types of satellite data, the SEBAL algorithm (hereafter called SEBAL code) was tuned to account for whether reflectance/radiance values were user-calibrated or not. This explains, for instance, the development of separate SEBAL codes for MODIS and AATSR data shown as Appendices 6.1 & 6.2 respectively. For Landsat ETM+ and MODIS, a similar algorithm was applied since both data sets were calibrated in a similar way based on coefficients retrieved from the raw data and related

publications. For AATSR, reflectance and brightness temperatures were simply imported into MATLAB; fully calibrated values are easily retrievable (Section 5.4 of Chapter 5). In this case, AATSR vegetation indices remained the only input derived from image processing with ERDAS-Imagine software.

**Preparatory Stage 3: Managing the SEBAL Code**

This section describes a stepwise procedure for managing the SEBAL code. In part, the section also describes the key functions of the main MATLAB operational tools.

- **Step 1: Re-writing the SEBAL code**

The SEBAL algorithm source code is now in the public domain in text formats. However, re-organisation of the code may be necessary to suit specific user-needs. In this case, the code was re-written from a hardcopy source having been previously used by Mekonnen (2005). The formulation was carefully verified based on earlier versions implemented via the ERDAS-Imagine modeller toolbox, e.g. Chemin (2003); Morse *et al.* (2000), and Bastiannssen *et al.* (1998a). The FAO (1998) guidelines for calculating regional *ET* were also used as a supplementary check, making references to crucial determinants such as radiation balance constants, vegetation and atmospheric resistances. The final output was saved as a text file in Windows Notepad.

- **Step 2: Inputting the SEBAL Code**

The text file was then copied and pasted into the MATLAB Editor/Debugger. The main function of the Editor/Debugger is to create and debug files (M-files), which are programs written to run MATLAB functions. Creating and editing M-files followed the usual windows instructions such as: *File -> New or File -> Open*, and also

application of the edit function. Further details about the M-Editor/Debugger are available from the MATLAB Users-Guide and the HELP menu.

- **Step 3: Code Analysis**

For SEBAL to run efficiently, the *M-Lint automatic code analyzer* (bottom of Editor – see Appendix 6.4) was utilized to identify problems and to correct SEBAL's mathematical formulation arising from human error. A good example is the radiation balance calculation for which map coordinates and radiation constants had to be converted from decimal degrees to radians. For written codes (inclusive of results), the Editor is also well-suited for sectional evaluation (called cells) and publishing to popular output formats like HTML. Mandatory programming syntax and symbols such as *comments modulus* (%%), *semi-colon terminator* (;) etc. had to be thoroughly observed for SEBAL to run without errors.

- **Step 4: Importing Data**

Following Section 6.2.2, two types of ERDAS-Imagine files were imported into MATLAB: (1) radiance (DN) values; and (2) vegetation indices (i.e. NDVI and SAVI[3]). For single-channel (band) raster data such as NDVI, they are easily importable as TIFF files (single float). This becomes more complex when dealing with multi-channel radiance values (double precision float). To overcome this, the radiance files were converted from TIFF or IMG format to ASCII using ERDAS-Imagine or ENVI file conversion tools. To ensure correct layering of multi-channel data, manual location of a matrix start and end points is necessary. In this case, the matrix position of the starting and ending pixels of each band was queried and recorded. This was

[3] SAVI = Soil Adjusted Vegetation Index defined as $(NIR-R)/(NIR+R+L)(1+L)$, where NIR & R represent reflectance in the near infrared and visible bands, respectively and L = a soil-brightness dependent correction factor that compensates for the difference in soil background conditions; in this case L = 0.5, following Huete *et al.* (1988).

finally built into an array in a band sequential format. The bottom right-hand-side of Table 6.1 presents an example.

Table 6.2 Typical MATLAB function for SEBAL Application. The left part of the table declares the input and output variables which are defined as comments on the right. Note: the right-hand-side of the (function) equation defines both the output file (e.g. PETmodel_ats2) and examples of importable data files.

| **Function** | **Definition** |
|---|---|
| ***function*** [SE, Ts, NDVI, EF, LAI, Rn_24, PET_24, Band4, Band5, Go_ins, H_ins, Ro] =PETmodel_ats2(data, NDVI, savi, JD, D) | *%%* SE=surface emissivity, Ts=surface temp, NDVI=normalised difference vegetation index, Rn_24=daily net radiation, PET_ins=instantaneous PET<br><br>*%%* data=satellite imagery, ConstB1=refl. band1, ConstB2=refl. band2, ConstRF1=corrected refl. band1, ConstRF2=corrected refl. band2, PETmodel=general output model, JD=Julian day and D=Earth-Sun distance constant<br><br>*%%* Imported Data (Manual band sequence – data (1:89) means Band1 has pixel range 1 to 89, and so on).<br>Band1=data (1:89,:);<br>Band2=data (90:178,:);<br>Band3=data (179:267,:);<br>Band4=data (268:356,:);<br>Band5=data (357:445,:);<br>Band6=data (446:534,:); |

- **Step 5: Critical User Decision-making**

A number of critical processing decisions have to be carefully taken by the user to run-error-free SEBAL. Four of the most important ones are described here: (1) determination of prediction algorithms for surface roughness (leaf area index method); (2) selection of appropriate prediction equation for land surface temperature (3) selection of ground-based weather data and development of prediction equations for surface to air temperature differences; and, (4) selection of the driest and wettest indicator pixels as an aid for determining sensible heat flux.

**(a) Surface Roughness Algorithm:** Surface roughness depends very much on leaf area index (LAI) which also has an inverse logarithmic relationship with vegetation index. The choice, therefore, exists for users to apply NDVI or a soil-adjusted

vegetation index (SAVI). The general SEBAL assumption (e.g. Morse *et al.* 2000) is that SAVI better accounts for soil reflectivity than NDVI, which probably leads to a more accurate determination of surface roughness. SAVI was therefore applied in this case. However, further examination has revealed no significant difference between NDVI and SAVI, as illustrated in Chapter 7.

**(b) Prediction Equation for Surface Temperature:** A number of empirical equations have already been developed for predicting surface temperature from brightness temperature (see Section 5.4 of Chapter 5). A good theoretical background is required for the user to choose an appropriate equation. In this research, the widely-used split-window algorithm (Sobrino *et al.,* 1994; Becker & Li, 1990, Price, 1984) was applied.

**(c) Algorithm for Surface to Air Temperature Difference:** This is one of the most difficult approximations for SEBAL users because of the paucity of spatially distributed air temperature. In this case, the mean of five field (point) measurements (i.e. $27.43^0$C) coincidental with satellite overpass was spatially applied, using an empirical relationship developed by Bastiannssen *et al.* (1998a) for similar dry catchments. A first approximation would be to construct Theissen polygons using long-term point measurements. However, this was considered unnecessary because only one ground station exists in the study area. Also, regional ambient temperature variation for tropical areas is often assumed to be insignificant (Shaw, 1994).

**(d) Selection of Driest & Wettest Pixels:** A number of techniques have been developed (e.g. Morse *et al.,* 2000) to avoid undue subjectivity of this process; the ERDAS-based trial-and-error is a popular method. In MATLAB, a *for-else-end* loop function was developed to select pixels with the most extreme values.

- **Step 6: Creating MATLAB Functions**

The next step is creation of MATLAB *Functions*, which not only requires considerable programming skills but also knowledge about mathematical arguments. Mathematical *Functions* may be represented by expressing them as MATLAB or Anonymous *Functions*. The HELP menu provides invaluable support to new users. Table 6.2 illustrates a Mathematical *Function* which was developed to suit the current SEBAL application. Nearly all MATLAB functions are designed to precede and code-written in the Editor. The next important thing is saving the Editor, debugging and running it.

- **Step 7: Running the Function in Command Window**

The Command Window (Appendix 6.4) is essentially designed for users to enter variables to run functions and MATLAB file scripts at the command line or prompt (>>). In MATLAB, the Editor only partially runs the SEBAL code. This task is completed by copying and pasting the *Function* into the Command Window, supplying the *terminator* symbol (;) and hitting the return key (keyboard). MATLAB commands are mostly UNIX-based and their application develops largely through user experience and the HELP menu. A good example of recalling and editing previous statements from the Command Window is by pressing the up-arrow key.

- **Step 8: Saving SEBAL Results**

A successful run of the *Function* results in a number of output files, which are often listed alphabetically in the Workspace (Figure 6.5a). Two main windows characterize this graphical user interface – Current Directory and Workspace. The Current Directory was used to save, edit and open new and existing files. Double-clicking a directory in the Workspace (see *"Name"* column in Figure 6.7a) automatically opens a matrix of SEBAL results in the Array Editor (Figure 6.5b). The Array Editor has two main functions: (1) editing SEBAL results, saving and copying into standard databases

or spreadsheets; and, (2) displaying and analysing the results using appropriate commands in the Command Window.

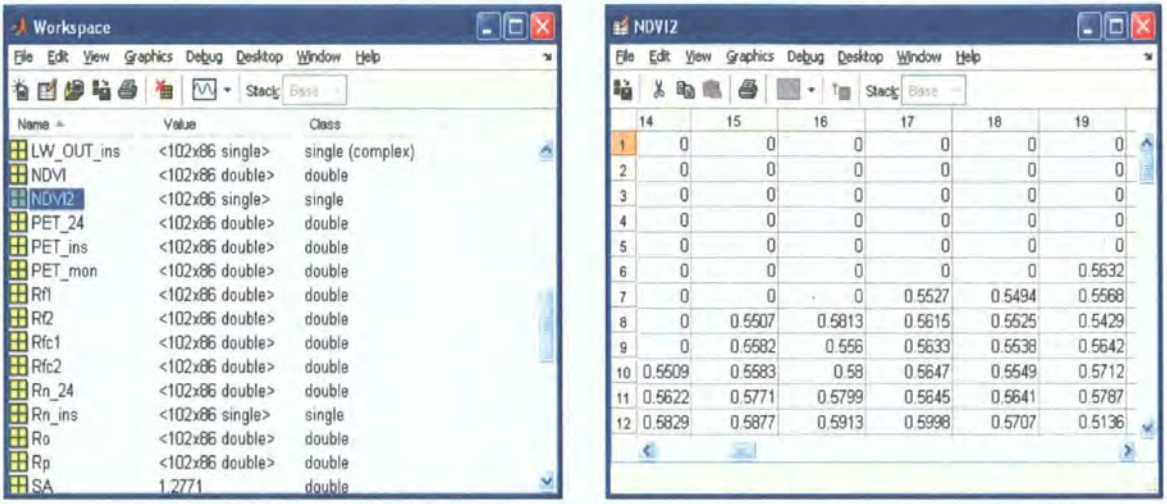


Figure 6.5 Undocked MATLAB (a) Workspace with listed SEBAL parameter files and (b) NDVI values displayed in the Array Editor

- **Step 9: Displaying SEBAL Results**

One of MATLAB's greatest advantages is its output display and analytical capabilities. The most conventional way to display and analyze SEBAL outputs, maps, etc. in ERDAS is via ARC-GIS. In MATLAB, a number of command lines exist to accomplish this. MATLAB is also widely known for its mathematical and statistical capabilities (Brata *et al.,* 2006). Again, the quality of output display and analysis depends on user experience and support from the HELP menu. Examples of MATLAB-derived plots and maps are displayed in Appendix 6.5.

- **Step 10: Keeping Command History**

The Command History (see Appendix 6.4) is an indispensable tool for keeping track of the numerous MATLAB commands. In this research, the Command History was beneficial in a variety of ways: (1) re-introduction of previously used commands; (2)

reviewing the SEBAL code; (3) archiving the code and related commands; and, (4) locating and resolving bugs.

- **Step 11: Running Multi-temporal Imagery**

As noted earlier on, an important feature of MATLAB is its simple programming requirements. Once Stage 3 is set up, it becomes easy to calculate surface fluxes from a series of images by repeating Steps 4 – 11. It is important, however, for users to declare completion of each cycle-run, using the M-*save-clear* command in order to prevent overwriting previous results. Table 6.3 presents an example of the M-*save-clear* syntax.

Table 6.3 Sample MATLAB command for SEBAL programming of multi-temporal images

| M-command | Remark |
|---|---|
| `save aatsr_wsp2c.mat` | Saves image file |
| `[SE, Ts, NDVI, EF, LAI, Rn_24, PET_ins, PET_24, PET_mon, Band4, Band5, Go_ins, H_ins, Ro]=PETmodel_ats(data, NDVI2, savi, JD, D);` | M-Function |
| `clear` | Removes previous result |

## 6.2.3 Challenges in SEBAL Processing

SEBAL is composed of more than 20 operational steps and as seen in Figure 6.5a, may potentially deliver several individual outputs depending on user needs. Some of the processing steps require decision-making by the user such as accurate prediction of surface roughness and surface to air temperature differences, use of microclimate data, etc. (see Step 5). These decisions are crucial and challenging in that they do not only influence accuracy of the SEBAL output but they also require good a theoretical knowledge about: (1) regional energy and radiation balance modelling; (2) the region's microclimate; (3) the local bio-physical environment, e.g. vegetation cover, soil

physical conditions, etc.; (4) physics of the SEBAL algorithm; and (5) computing power, programming knowledge and allied resources. Though the above may not be limited to MATLAB processing, development of MATLAB and related skills is also a challenge.

It is also important to note the presence of other challenges such as determination of general robustness of the SEBAL algorithm (code) for surface flux estimation. However, this has been reserved for full consideration in Chapter 7.

## 6.3 Summary

This chapter has provided a procedural account of how surface energy and water fluxes (e.g. *ET*) may be derived using MATLAB-based SEBAL processing. The purpose is to establish a procedural link between previous *ET* modelling methods and subsequent results discussed in Chapter 7. The goal is to provide a critically evaluated stepwise procedure as a guide to future users.

The first part of the chapter reviewed the contrast between previous SEBAL processing methods e.g. ILWIS and ERDAS-Imagine (French *et al.* 2005; Chemin, 2003; Morse *et al.* 2000; Zu *et al.* 1999; Bastiannssen *et al.* 1998a) and more recent ones such as stand-alone *C*-program and MATLAB application (Brata *et al.* 2006; Makonnen, 2005). Although ERDAS-based SEBAL processing has been widely applied, its ability to account for spatial multi-temporal satellite imagery has not been fully addressed.

The second part of the chapter has established a case for integrated MATLAB-based SEBAL processing. Indeed, Brata *et al.* (2006) have recently demonstrated MATLAB's potential to derive regional energy and water fluxes using repetitive MODIS and NOAA/AVHRR data. Their work made exclusive use of MATLAB

functions. This approach has potential to produce geographically distorted outputs, which can mask opportunities for results validation; this has been addressed in this thesis.

The final part of the chapter has provided a detailed step-wise procedure for SEBAL processing, while at the same time addressing the key assumptions driving the most uncertain prediction equations. The most important challenges to the current approach have also been discussed.

# Chapter 7

# Regional-Scale Evapotranspiration Modelling: Results & Discussion

## 7.1 Introduction

This chapter discusses spatial estimation of energy and water fluxes over the Volta catchment area using SEBAL-based energy balance modelling and up-scaling methods driven by radiometric measurements from satellite sensors (i.e. Landsat ETM+, MODIS and AATSR). Remote sensing inputs to the SEBAL algorithm are brightness temperatures (*BT*) and NDVI which, in the context of this research, is applied as a metric for biomass density. The emphasis on NDVI will be explained later; here, it is sufficient to note that other tangible metrics for biomass density are widely reported in the literature. For example, there is substantial empirical evidence to suggest that percentage vegetation cover (*PVC*), fraction of photosynthetically active radiation (*fPAR*) and leaf area index (*LAI*) are more suitable indices for ground canopy cover than NDVI and therefore provide better estimates of *ET* over vegetated surfaces [e.g. Tucker (1979); Asrar *et al.* (1984); Wiegand *et al.* (1991); Goward & Hummerich (1992)]. Nevertheless, a number of published papers also suggest that a strong linear relationship exists between the above metrics on one hand and NDVI on the other [see Choudhury (1987); Myneni & Williams (1994); El Mayaar & Chen (2006)]. Also, Curran (1983) and Tucker & Sellers (1986) have demonstrated linear relationships between percentage vegetation cover and leaf area index and how these are closely correlated with NDVI. Thus, for practical purposes, NDVI may be used as a surrogate for biomass or ground cover (El Mayaar & Chen, 2006).

Indeed, NDVI is one of the most widely calibrated vegetation indices, which can be routinely derived from satellite data. This means that for large river basins, such as the Volta where no systematic in-situ (ground-based) measurements exist, NDVI may be applied as a practicable index for ground cover. Furthermore, NDVI has been successfully used for modelling *ET* across a variety of landscapes using the SEBAL method, significant examples being Niger in West Africa (Bastiannssen *et al.*, 1998 a&b), Sri Lanka in Southeast Asia (Chemin, 2003), the Roxo district in Portugal (Mekonnen, 2005) and the Southern Great Plains in USA (Brata *et al.*, 2006). In all these studies, the modelling task presented various challenges, the most important being how to derive surface emissivity across vegetated landscapes. This remains a key research issue, but as noted above, the principal concern here is detailed discussion of regional *ET* modelling, the context of which is illustrated in Figure 7.1 and Table 7.1. The figure illustrates how each of the modelling steps fits with the other and their data parameterisation strategy. Following this, the table provides a detailed explanation about the various uses of the satellite and ground truth data.

The chapter is organised in the following way. The first part presents results derived from sensor radiometric measurements and energy balance modelling followed by their validation, while the second part discusses these results. Both sections are developed along an analytical sequence as follows: (1) establishment of relationships between land cover distribution and surface parameters; (2) radiation balance modelling and evaluation of the model uncertainties; (3) derivation of regional-scale energy fluxes and validation methods; and (4) sensor inter-comparison.

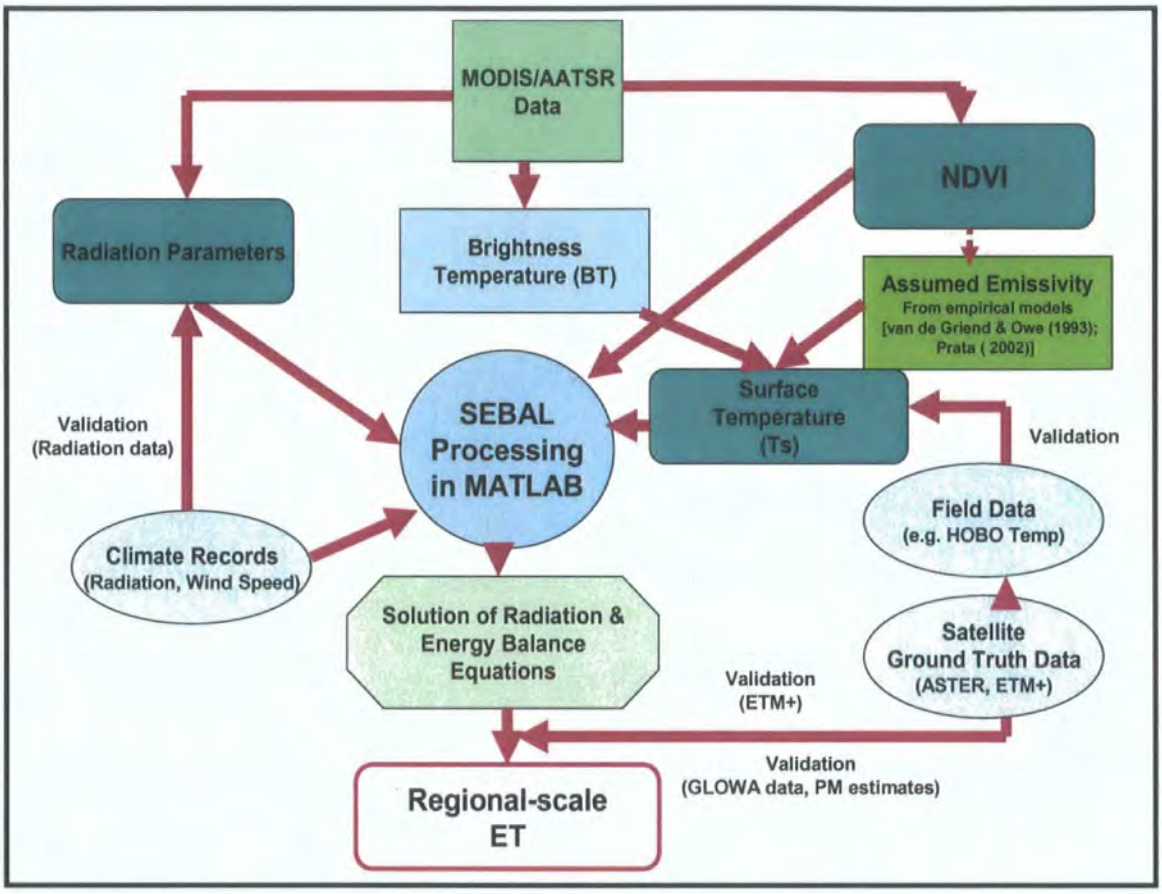


Figure 7.1 Flow chart showing how *ET* and related water and energy balance parameters have been modelled from MODIS and AATSR data; the role of ASTER, Landsat ETM+ and ground information as complementary and validation data are indicated. Note: SEBAL assumes constant emissivity in order to estimate $T_s$ using the split-window approach (see further details in Section 7.2.1.2).

## 7.2 Results

There exists widespread interest in distributed energy fluxes and their feedback responses with land cover, water resources and crop yields. This explains the importance of regional energy balance models (Kalluri & Townsend, 1998) and why researchers continue to develop, test and improve upon various remote sensing methods, including: (1)

Two-source Energy Balance (TSEB) by French *et al.* (2005); (2) Surface Energy Balance System (SEBS) by Su (2002); (3) Single-source Energy Balance (SSEB) by Kalluri & Townsend (1998); and, (4) Surface Energy Balance for Land (SEBAL) by Bastiannssen *et al.* (1998a). The current results are based on the SEBAL method.

Table 7.1 Satellite and ground data used for regional-scale *ET* estimation and validation

| *Data Type* | | *Use of the Data* |
|---|---|---|
| Satellite data | MODIS/AATSR time series imagery | The MODIS and AATSR provided the key instantaneous data needed for energy and water balance modelling (net radiation, NDVI, BT) |
| | A Landsat ETM+ scene acquired on 5th January 2004 | The Landsat image was used as a source of detailed land use/cover classification and ET maps for various purposes: (1) location of sites for installing thermal loggers; (2) mapping wet and evaporation points to guide SEBAL-based energy balance modelling; and (3) as a source of validation for MODIS & AATSR *ET* estimates |
| | An ASTER scene acquired on 27th December 2000 | The ASTER image was used as a detailed source of ground location in the selection of test sites and for generating ground control points for classifying the Landsat ETM+ data. |
| Satellite-based intermediate parameters | Brightness temperatures (*BT*) | *BT* was derived from satellite data but only served as intermediate data sources for energy balance modelling |
| Climate Records (from local and global data archives) | Radiation data and constants | These were used to: (1) validate the MODIS/AATSR net radiation data; and (2) up-scale satellite-based net radiation from instantaneous measurements |
| | Wind speed ($u$) | Wind speed was used as a source of momentum data for SEBAL-based energy balance modelling |
| | Air temperature ($T_a$) | $T_a$ was used as a data source for solving the temperature difference ($T_s - T_a$) in SEBAL energy balance modelling |
| Data from fieldwork | HOBO logger temperatures | Field temperatures were used as a source of validation data for satellite-based estimates before using the output for SEBAL-based processing |
| | GPS geo-location data | The GPS geo-location data were used to guide field trekking, selection of test sites and image classification using Landsat ETM+ data |
| | Vegetation characterisation data | The vegetation characterisation data (e.g. tree height) were used as data source to guide the selection of training samples which in turn, were used for land use/cover classification (Landsat ETM+ image). |
| *ET* validation data | GLOWA-Volta field data | The GLOWA data was used as one of the main sources of validation for satellite-derived net radiation and energy fluxes (e.g. *ET*) |
| | Penman-Monteith estimates (Tamale district) | The Penman-Monteith estimates were used as additional source of validation data for satellite-derived *ET* |

### 7.2.1 Relationships between NDVI & Surface Parameters

This section describes spatial relationships between satellite-derived NDVI and other surface variables (e.g. $T_s$) using linear and multiple regression models. To achieve this, histogram plots were first used to examine the distribution of the image results. Attempts have been made to analyse full image scenes, however, in a few cases, pixels over the Tamale district have been selected and a detailed study undertaken. The reason is that much of the ground data needed for validating the satellite-based results are available in this area. The detailed data sampling approach is given in Section 5.5 of Chapter 5. As noted above, NDVI is used as a surrogate variable for vegetation cover following the strong empirical relationships reported by Curran (1986), Tucker & Sellers (1986), Myeni & Williams (1994) and El Mayaar & Chen (2006).

#### *7.2.1.1 NDVI and Surface Temperature*

The radiation emitted from any given surface in the thermal infrared (*TIR*) part of the electromagnetic spectrum wavelength is a function of both its surface temperature and emissivity (see Equation 5.9). This means that surface temperatures cannot be derived from radiance values without knowing land surface emissivity ($\varepsilon$). This is an important challenge in SEBAL, which explains why many users apply empirical model approaches such as those described by van de Griend & Owe (1993) and Cihlar *et al.* (1997). Other methods such as the thermal emissivity separation (TES) method (Kealy & Hook, 1993) and the constant emissivity approach (Prata, 2002) have also been described in the literature. However, they generally depend on reference emissivity coefficients which in turn depend on knowledge of biospherical and sensor characteristics such as land cover

types, atmospheric water vapour, solar zenith angle and satellite viewing angle. Such precise data are unavailable in the study area, which means direct application of the TES method may introduce several uncertainties in the $T_s$ model. For this reason, emissivity was assumed to be constant based on the empirical relationship that exists between emissivity and the logarithm of NDVI (van de Griend & Owe, 1993; Equation 5.10) in the range of 0.96-0.99 (Prata, 2002). This was subsequently applied in the $T_s$ split-window algorithm (see Section 5.4 of Chapter 5). Notably, an NDVI range of 0.3-0.7 corresponded with the range of emissivities, which were found to correspond to published emissivities (0.94-0.99) observed for similar heterogeneous landscapes (Sutherland, 1986; Labed & Stoll, 1991; Owe & van de Griend, 1994; Wittich, 1997). Although this approach is crucial for $T_s$ modelling, it is imperfect and remains one of the most important limitations of the SEBAL method.

In SEBAL, estimates of soil and canopy temperatures are needed to model fluxes in soil and sensible heat (Equations 5.12 & 5.14 of Chapter 5). Previous studies such as Nemani & Running (1989), Carlson *et al.* (1990), Price (1990) and Kalluri & Townsend (1998) show that the relationship between percentage of vegetation canopy cover and measured surface temperatures is linear. Here, the physical basis of NDVI is that plant pigments absorb at red wavelengths and reflects strongly at near-infrared wavelengths. It is the difference between red and near-infrared wavelengths which is used to express the density of canopy cover and is the basis for the results displayed in Figure 7.2. The geographical context for discussing these results is given in Figure 2.1. Analysis of estimated land surface temperature ($T_s$) data suggests that vegetated areas are cooler than non- or less-vegetated areas (Brata, *et al.* 2006; Kalluri & Townsend, 1998; Price, 1990).

Kalluri & Townsend (1998) attribute this to the differences in evapotranspiration and thermal properties of bare soil and vegetation. The results from the Volta savannah (Figure 7.3) tend to support this hypothesis.

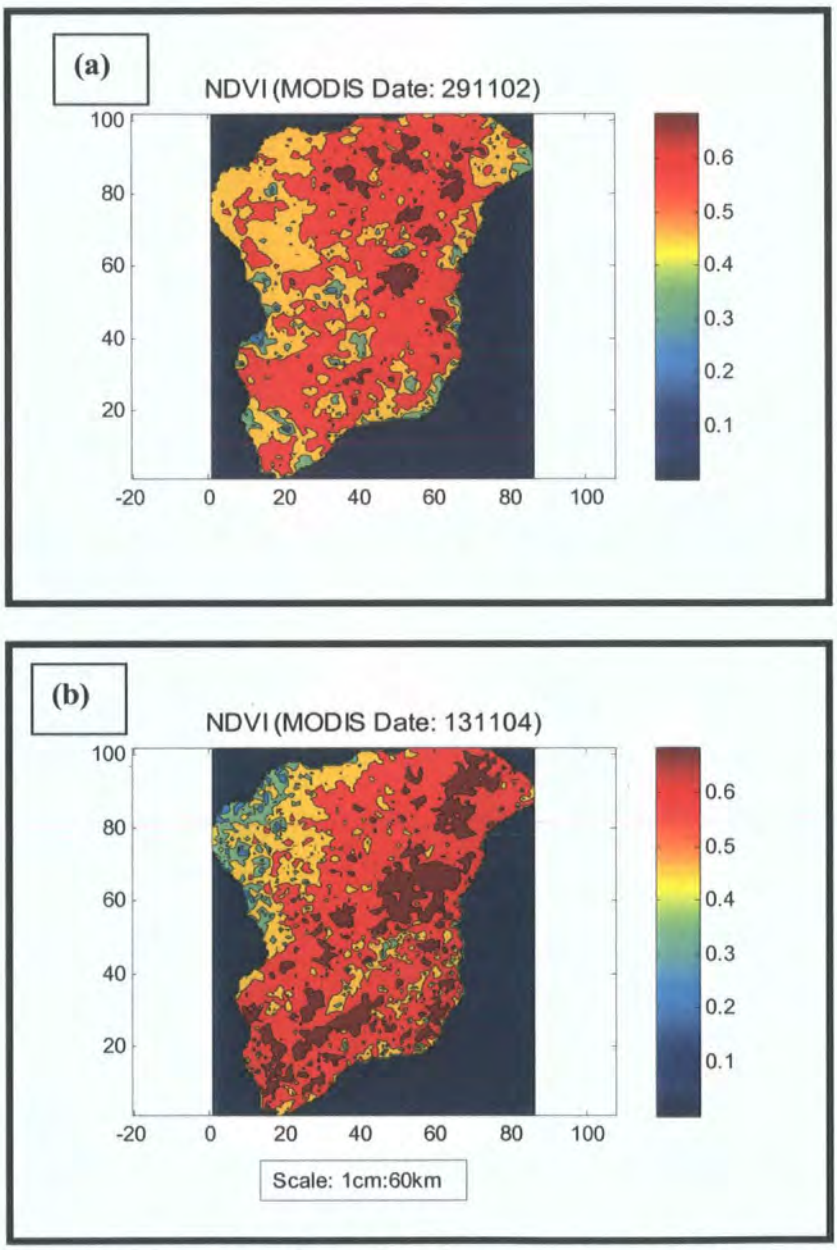


Figure 7.2 Spatial variation of NDVI over the study area (see Figure 2.1). Based on NASA's MODIS data, vegetation cover change is shown over a two-year period (b) 291102 and (c) 131104. Higher soil moisture in mid-November probably explains the increased total biomass volume in 2004 with the exception of the Tamale urban area (top-left corner of the images).

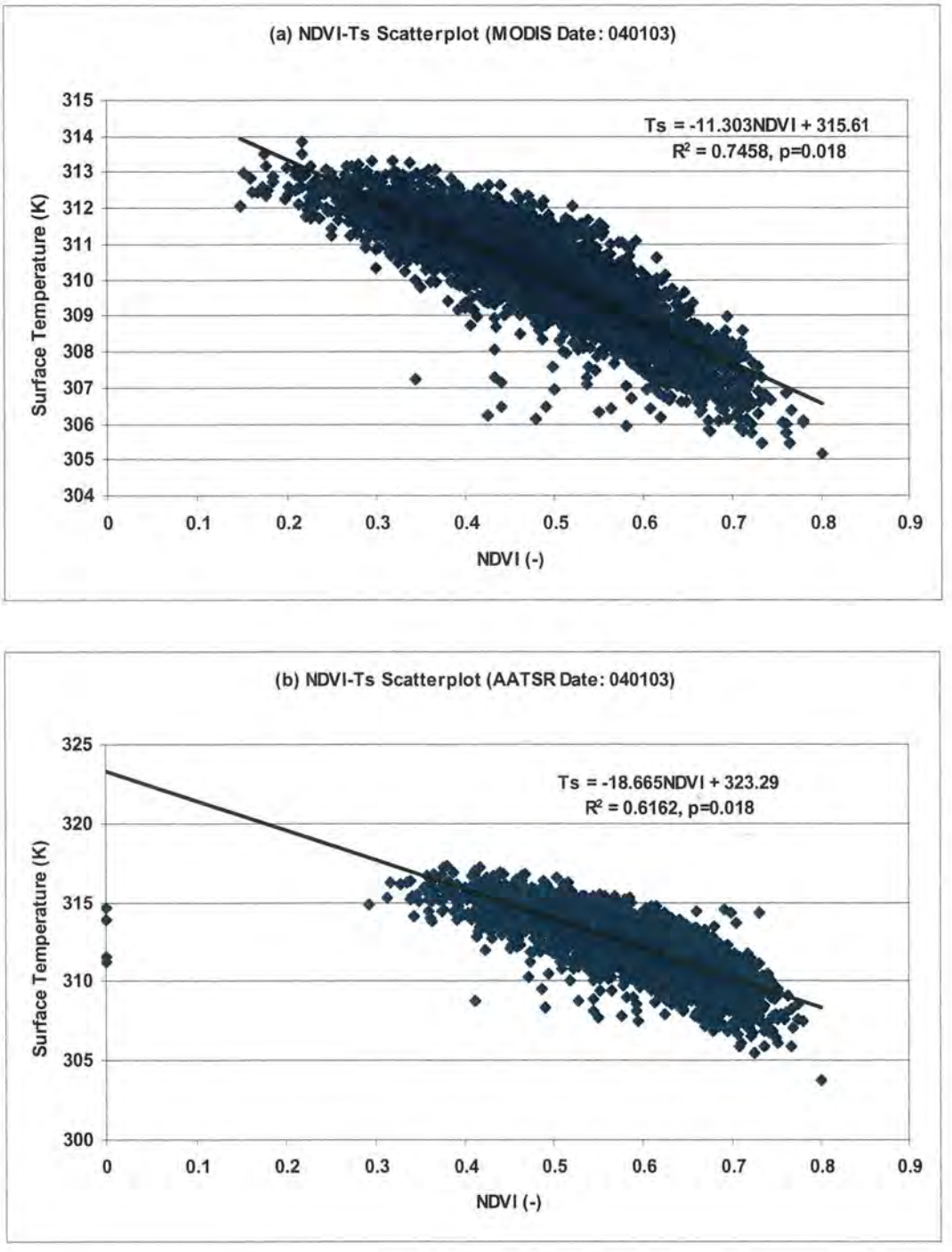


Figure 7.3 Regression models between NDVI and surface temperature ($T_s$). The models are derived from full MODIS ($N$ = 5486 pixels) and AATSR ($N$ = 4139 pixels) scenes, (a) $T_s$ = -11.303NDVI + 315.61; $R^2$ = 0.7458, $p$ = 0.018; RMSE = 0.051; and (b) $T_s$ = -18.655NDVI + 323.29; $R^2$ = 0.6162, $p$ = 0.018; 04993. The data sampling procedure is described in Section 5.5.

Figure 7.3 supports previous observations by Brata *et al.* (2006) and Kalluri & Townsend (1998) that NDVI is negatively correlated with $T_s$. Measurements taken over two dry areas in the Southern Great Plains (USA) by Brata *et al.* (2006) and over the Manhattan FIFE[1] site by Kalluri & Townsend (1998) demonstrate that the precision of the NDVI-$T_s$ relationship may vary considerably based on surface and atmospheric conditions, sensor-type (e.g. AVHRR) and ground measurement techniques.

Is there always a linear relationship between NDVI and $T_s$ especially for tropical savannah areas? Also, how do we assess, for instance, the capabilities of satellite sensors such as MODIS and AATSR? Previous research by Kalluri & Townsend (1998), recently confirmed by El Mayaar & Chen (2006) tries to address these questions. The above authors have demonstrated that NDVI and $T_s$ measured from coarse-resolution sensors like AVHRR, MODIS and AATSR over heterogeneous land surface areas may be described by linear equations following models derived by Nemani *et al.* (1993) and Price (1990) as:

$$T_0 = fT_c + (1-f)T_s \qquad (7.1a)$$

$$NDVI_0 = fNDVI_c + (1-f)NDVI_s \qquad (7.1b)$$

where the subscripts *0*, *c* and *s* represent the variables measured over a full canopy, bare soil and mixed land surface, respectively. Thus, $T_0$ and $NDVI_0$ measured from the satellite at a coarse resolution can be considered as a linear mixture of contributions from the canopy and bare soil weighted by their fractional amount ($f$) in each pixel. In fact, the relationship between NDVI and $T_s$ is not unique to mixed grasslands (Kalluri & Townsend, 1998). Such relationships have also been observed over agricultural areas as well as forest

[1] FIFE = First International Satellite Land Surface Climatology Project (ISLSCP) Field Experiment

landscapes (Nemani & Running, 1989; Nemani *et al.*, 1993; El Mayaar & Chen, 2006). For forest areas, extrapolating the regression line to the NDVI of bare soil and full canopy helps to estimate their respective surface temperatures. Table 7.2 shows typical NDVI values measured from coarse-resolution sensors (e.g. AVHRR, MODIS, etc.) over a variety of land surface types.

Table 7.2 Measured NDVI over various land surface types

| Land Surface | Measured NDVI range (Dimensionless) | Source (s) |
|---|---|---|
| Bare soil | 0.00 – 0.20 | Colby & Keating (1998) |
| Grassland | 0.05 – 0.55 | Brata *et al.* (2006); Kalluri *et al.* (1998); Nemani *et al.* (1993) |
| Tropical grains and arable crops | 0.10 – 0.64 | Nemani *et al.* (1993) |
| Open canopy forest | 0.28 – 0.65 | Nemani *et al.* (1993); Goward *et al.* (1991) |
| Closed canopy forest | 0.60 – 0.80 | Goward *et al.* (1994) |

Accurate measurement of the NDVI-$T_s$ relationship from satellite sensors remains a formidable challenge. Among the well-known problems is sensor calibration and inter-calibration, which does not appear to be unique to the older sensors (e.g. AVHRR), but also more recent ones such as MODIS and AATSR. Improvements over the MODIS Level-1 products are now available to help specific applications. For example, the Level-3 (MOD 13A1) 16-day 500 m products can be used to derive improved vegetation indices. Over the Volta basin, this is a critical issue especially during the wet season. Apart from

this, atmospheric effects and surface anisotropy remain as factors detrimental to retrieving accurate measurements of surface and canopy properties from remote sensing.

### *7.2.1.2 NDVI and Soil Heat Flux*

In remote sensing studies, soil heat flux ($G_0$) is commonly assumed to be negligible (Jacobsen & Hansen, 1999; Seguin & Itier, 1983). This approximation is appropriate because ground-based measurements of the soil heat flux cannot be extrapolated to large areas since its measurement depends on soil moisture and the amount of vegetation cover. However, when extrapolating near-midday estimates of the energy balance components, the values of $G_0$ are not always negligible (Jacobsen & Hansen, 1999). Over tropical regions, a significant portion of the soil surface is exposed to solar radiation, especially around midday, and so a significant amount of energy may be conducted into the soil (Kustas *et al.*, 1990). Equation 5.12 of Section 5.2.2 (Chapter 5) shows that $G_0$ may be conveniently estimated from satellite data. However, a key requirement is that $G_0$ should be proportional to another component of the energy balance such as net radiation ($R_n$). $R_n$ is often used because it may be extrapolated to large areas by combining multi-spectral estimates of reflected shortwave and emitted longwave radiation with ground-based measurements of incoming shortwave and longwave radiation (Kustas *et al.* 1989).

The main factors controlling the $G_0/R_n$ ratio are plant physiological parameters, such as biomass, leaf area index and percentage vegetation cover (Kustas and Daughtry 1990). The plant parameters are correlated with spectral vegetation indices and several studies have found strong relationships in the case of semi-tropical vegetation (e.g. Batra *et al.*, 2006; Bastiannssen et al., 1998; van de Griend & Owe, 1993). $G_0/R_n$ over bare soil

ranges from 0.20± 0.50 depending on the soil moisture (Idso *et al.* 1975), and from 0.05± 0.30 for surfaces with varying amounts of vegetation cover (Clothier *et al.* 1986, Kustas and Daughtry, 1990). However, for dry and sparsely vegetated surfaces, soil moisture is considered a factor of lesser importance in comparison with vegetation cover (Jacobsen & Hansen, 1999; Kustas *et al.* 1994). Furthermore, the magnitude of $G_0/R_n$ at midday is essentially a function of the amount of vegetation cover (Jacobsen & Hansen, 1999).

Because plant physiological factors controlling $G_0/R_n$ are related to spectral vegetation indices, a conceptual model of NDVI versus $G_0/R_n$ can be regarded as a physically-based relation (El Mayaar & Chen, 2006; Bastiannssen *et al.* 1998a). Simplified and empirical relations between LAI and $G_0/R_n$, as well as LAI and NDVI, allow for an acceptable analytically-based formula of a non-linear relationship between $G_0/R_n$ and NDVI (Kustas *et al.* 1993). Empirical studies show, however, that crop height, LAI and spectral vegetation indices (e.g. NDVI) often make a better fit to a linear expression when directly related to the $G_0/R_n$ ratio (Kustas *et al.* 1993; Kustas & Daughtry 1990; Choudhury *et al.,* 1987). Figure 7.4 shows the observed relationship between NDVI (vegetation cover) and $G_0/R_n$ (soil heat flux-net radiation ratio) over the study area.

A number of points need to be considered in relation to Figure 7.4. For example, it has to be shown whether the derived results are consistent with published data. First of all, there is a large degree of variance in the results represented by the wide scatter of points around the mean, which manifests in very low $R^2$ values (0.0 – 0.1). This may be related to the variation of vegetation types and their associated ground cover. The second point concerns the theoretical relationship between NDVI-$G_0/R_n$ and soil water content (Kustas *et al.* 1993). In the Volta basin, soil water content during the dry period is critical in terms

of groundwater recharge. Droughts in the area affect the soil's thermal conductivity and moisture diffusivity and their interaction has a pronounced effect on heat capacity. From November until March, increased soil temperature is invariably the most critical factor that affects the phase changes between soil water and vapour pressure (Jacobsen & Hansen, 1999; Shaw, 1994) leading to depressed capacity for savannah vegetation to withdraw soil water. The second point is that vegetation stress in the area may not only be associated with vapour pressure deficit but also the soil's thermal and hydraulic conductivity. Although the relationship between surface temperature and soil heat flux is complex over vegetated surfaces (Jacobsen & Hansen, 1999) (Figure 7.5), a number of studies have reported strong correlations between surface temperature, soil heat flux and crop biomass, a good example being Carlson *et al.* (1990).

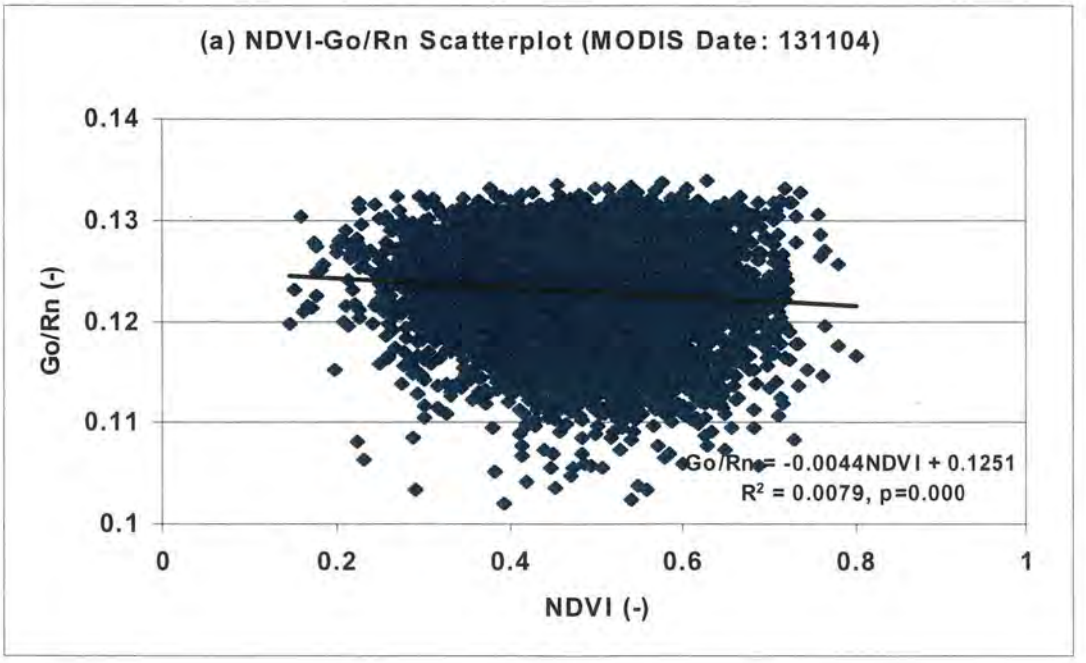


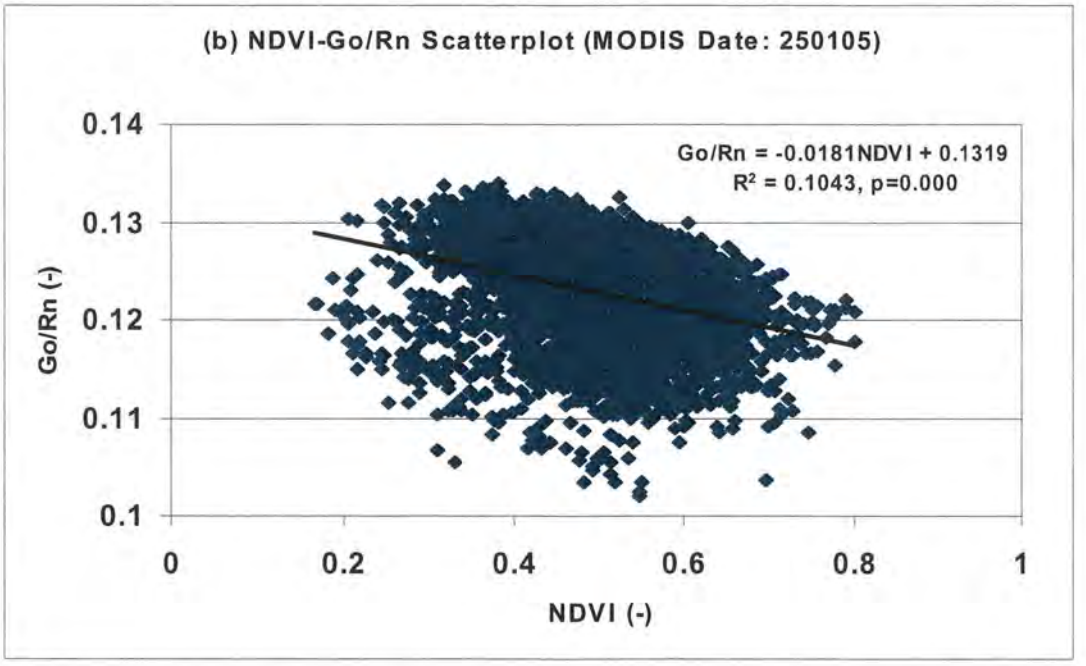


Figure 7.4 Relationship between NDVI and $G_0/R_n$ over the savannah Volta (a) MODIS date 131104: $N = 5486$; $R^2 = 0.0079$, $p = 0.001$; RMSE = 1.0076; $G_0/R_n$ = -0.0044NDVI + 0.1251 (b) MODIS date 250105: $N = 5486$; $R^2 = 0.1403$, $p = 0.000$; RMSE = 0.08521; $Go/R_n$ = -0.0181NDVI + 0.1319.

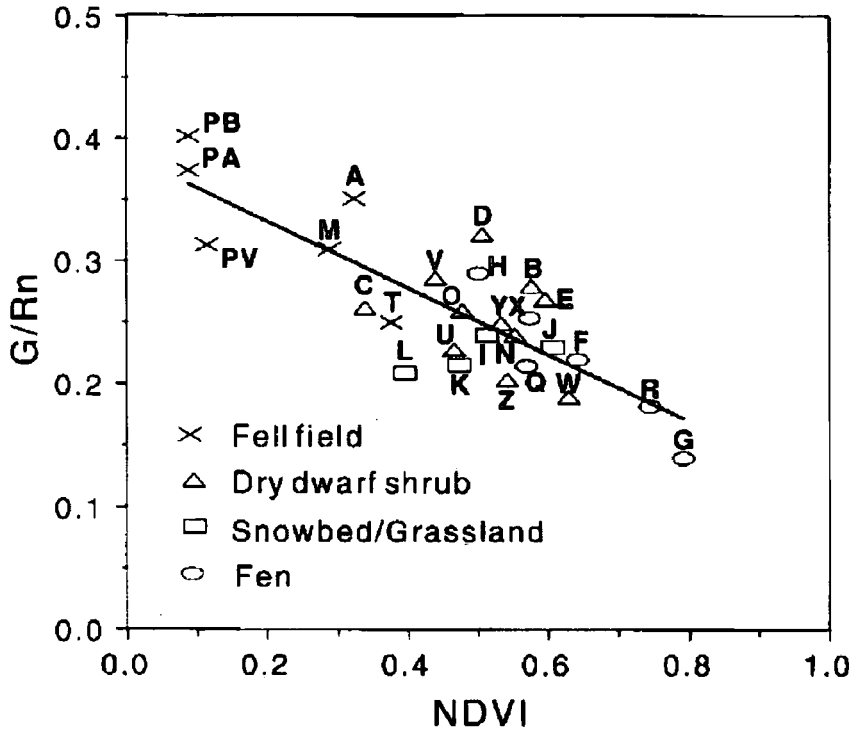


Figure 7.5 Linear regression of NDVI on $G_0/R_n$ representing 27 locations of different vegetation types in the Zackenberg National Park in Greenland, $R^2$ = 0.66. Source: Jacobsen & Hansen (1999).

## 7.2.2 Net Radiation Modelling from Satellite Data

### *7.2.2.1 Extrapolation of Instantaneous Net Radiation*

Instantaneous net radiation ($R_n$) is of little significance to energy and water balance modelling unless it is extrapolated over an entire catchment area. There have been many attempts to accomplish this by combining remotely sensed observations with ancillary surface and atmospheric data (e.g. Ma *et al.*, 2002; Jacobs *et al.*, 2000; etc.). Islam *et al.* (2003) have reported methods for regionalizing net radiation by interpolating ground observations. A recently developed methodology by Bisht *et al.* (2005) eliminates the

need for ancillary ground data to provide spatially distributed instantaneous and diurnal cycle of $R_n$ map over a large heterogeneous area for clear sky days. In the current research, instantaneous $R_n$ (W $m^{-2}$) was evaluated in terms of its components of downward and upward shortwave radiation fluxes, and downward and upward long-wave radiation fluxes based on Equation 5.2 (see Section 5.2.1 of Chapter 5).

The physics governing Equation 5.2 closely follows Zillman's (1972) parameterization scheme to obtain downward shortwave radiation, Prata's (1996) parameterization scheme along with air temperature to obtain downward long-wave radiation, and the approach of Bastiannssen *et al.* (1998) who used land surface emissivity ($\varepsilon_0$) and surface temperature to estimate upward long-wave flux. Figure 7.6 displays an example of instantaneous energy fluxes measured from the MODIS and AATSR sensors on 25$^{th}$ January 2005, which forms the basis for modelling the diurnal pattern of net radiation, which in turn, can be used to derive an estimate of regional evapotranspiration.

### *7.2.2.2 Diurnal Estimation of Net Radiation*

There are questions as to what extent instantaneous $R_n$ results, e.g. Figure 7.6, could reflect the diurnal cycle of the study area in the Volta landscape. Also, it is important to know how diurnal $R_n$ models can be used to predict and/or validate regional evapotranspiration. Brata *et al.* (2006) and Bisht *et al.* (2005) have proposed a sinusoidal model to estimate the diurnal cycle of net radiation on the basis of instantaneous sensor measurements. Their method was originally proposed by Lagouarde & Brunet (1993), who used it to derive diurnal surface temperatures from AVHRR data.

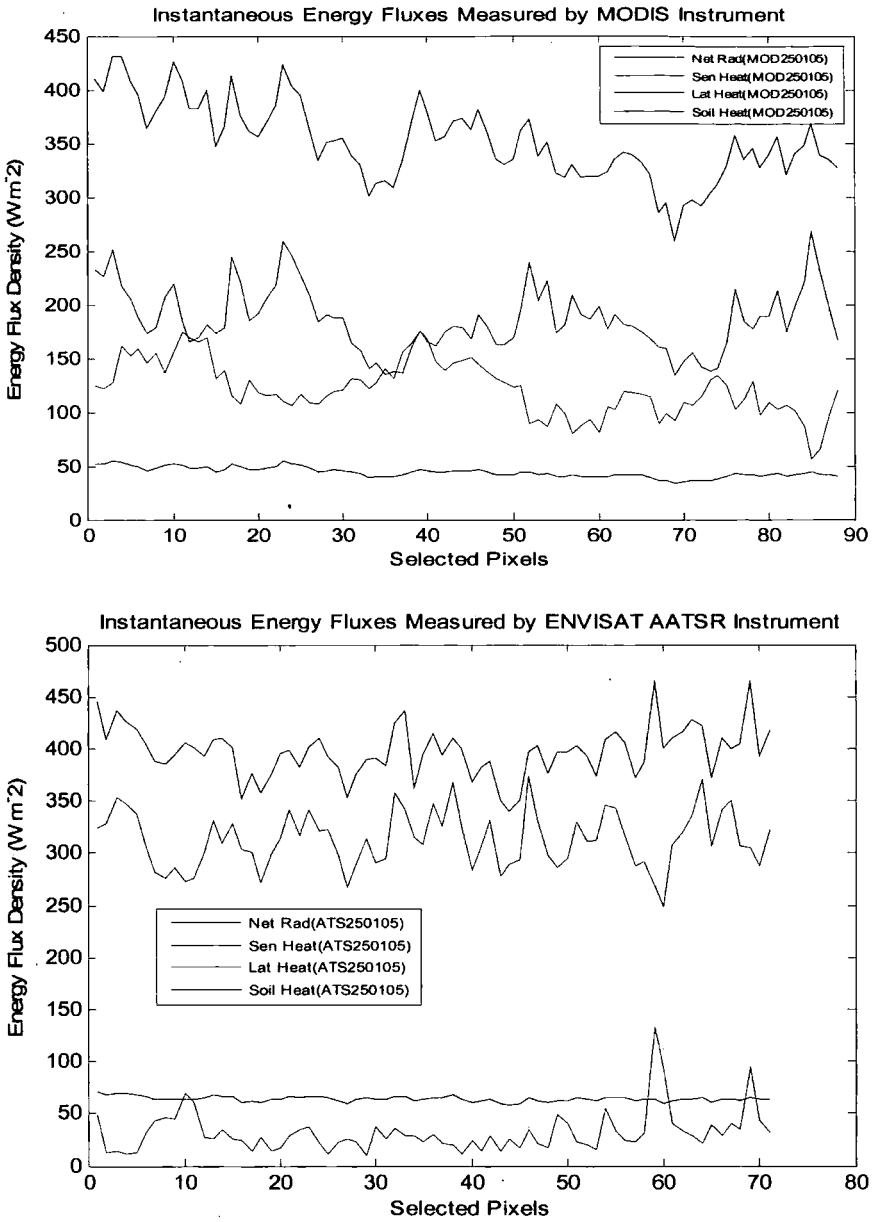


Figure 7.6 Instantaneous energy flux regime of the Volta savannah measured from MODIS and AATSR on 25/01/05. The average energy flux measurements over the study area are net radiation = 394 W $m^{-2}$; sensible heat = 276 W $m^{-2}$; latent heat = 150 W $m^{-2}$ and soil heat flux = ~ 50 W $m^{-2}$. (Sensor inter-comparison and error assessment follows in Section 7.5). Note: Eighty to ninety pixels were used for this analysis mainly to cover the Tamale district where validation data were available. Sensor differences explain the shortage of AATSR pixels.

The sinusoidal model of Bisht *et al.* (2005) is given by:

$$R_n(t) = R_{n-\max} \sin\left[\left(\frac{t - t_{rise}}{t_{set} - t_{rise}}\right)\pi\right] \qquad (7.2)$$

where $R_{n\text{-max}}$ = maximum value of $R_n$ estimated during the day, $t_{rise}$ and $t_{set}$ = local times at which $R_n$ becomes positive and negative, respectively. For a given study day, satellite overpass time ($t_{overpass}$), sunrise time ($t_{rise}$) and sunset time ($t_{set}$) are known, the value of $R_{n\text{-}max}$ is obtainable from the corresponding value of instantaneous net radiation. In the present case, Equation 7.2 was tested using two clear-sky dates of MODIS data over the Tamale district of Ghana because of the need for validation data (see Figure 2.2). The accuracy of the method was validated using local scintillometer observations (ZEF, 2004) and published results over a similar area in Central Nigeria by Jegede (1995). Figure 7.7 displays the results. Data on the sunrise and sunset times for the area coincidental with the Terra (MODIS) instrument overpass time for the study area were obtained from the US Naval Observatory (Astronomical Application Department) website (http://aa.usno.navy.mil/); see Table 7.3.

Table 7.3 Satellite overpass, sunrise and sunset time (GMT) for study days

| Image Date | Time of Satellite Overpass | | *Sunrise | Sunset | Hours of Sunshine |
|---|---|---|---|---|---|
| | MODIS | AATSR | | | |
| 291102 | 10:52 | 10:08 | 06:03 | 17:40 | 11:37 |
| 191202 | 10:37 | 10:05 | 06:13 | 17:48 | 11:35 |
| 040103 | 10:27 | 10:14 | 06:20 | 17:56 | 11:36 |
| **131104** | **10:32** | **10:05** | **05:57** | **17:39** | **11:42** |
| 021204 | 11:02 | 10:08 | 06:05 | 17:41 | 11:36 |
| **250105** | **10:27** | **10:11** | **06:25** | **18:06** | **11:41** |

* The solar data was compiled from the US Navy website: http://aa.usno.navy.mil/. The highlighted dates represent test dates.

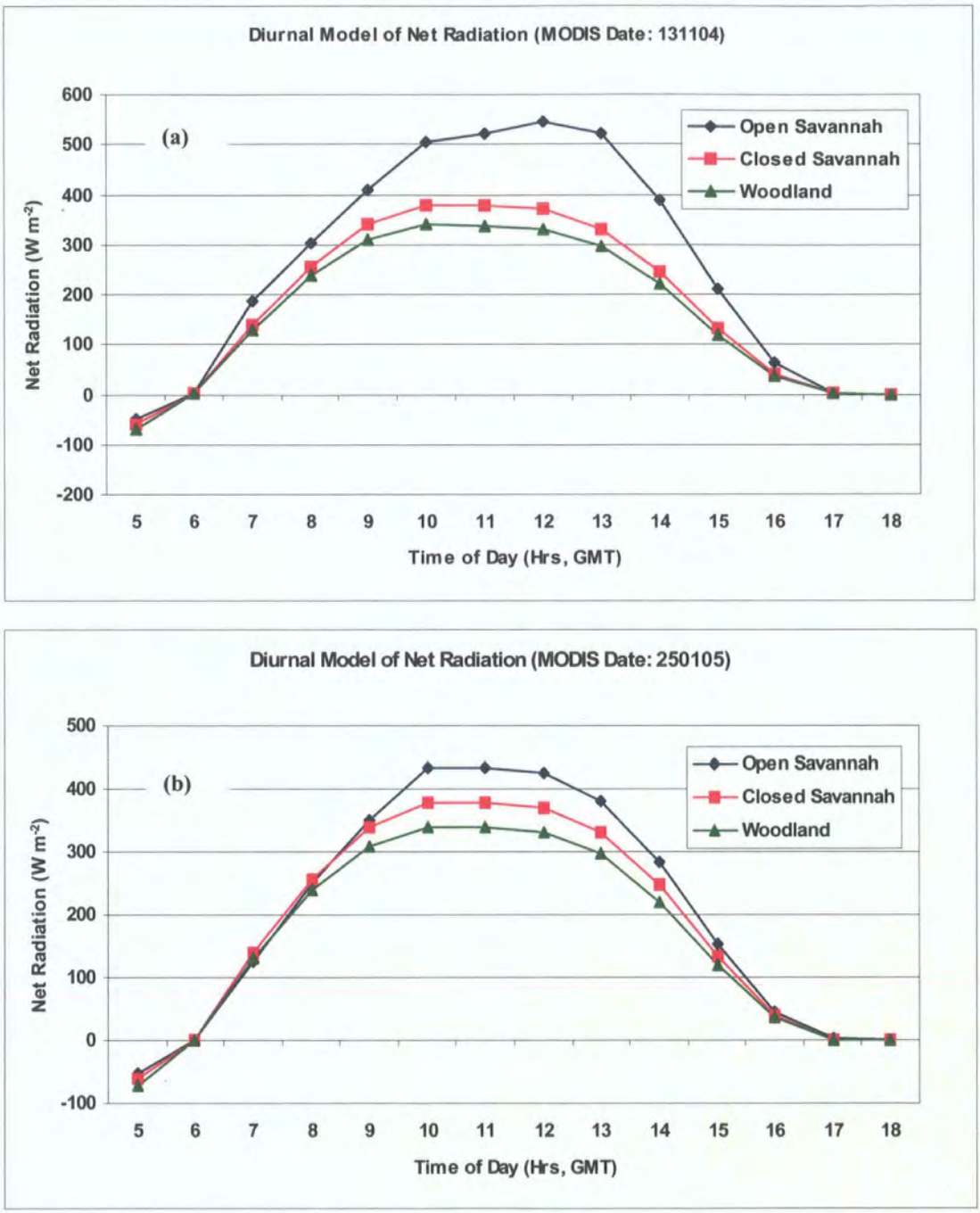


Figure 7.7 Sinusoidal model of diurnal net radiation derived from MODIS measurements dated (a) 131104 and (b) 250105 over a vegetated Guinea savannah landscape in West Africa.

It is necessary to comment on the key assumptions of the sinusoidal approach. First, $R_n$ is assumed to rise within 15 - 30 minutes after sunrise ($t_{rise}$) and it becomes less than zero within 15 – 30 minutes before sunset ($t_{set}$) for tropical areas (e.g. Batra *et al.*, 2006). Secondly, it is assumed that the variation in sunshine duration for most of the dry period is negligible (see the last column of Table 7.3).

### *7.2.2.3 Validation of the Volta Diurnal Net Radiation Model*

The primary source of validation data for Figure 7.7 was obtained from local scintillometer energy flux observations (ZEF, 2004), which is shown in Figure 7.8. Other validation data were obtained from published sources (Jegede, 1995) covering daily variation of net radiation over the Osu catchment in Central Nigeria and observed locally from radiometers; see Figure 7.9.

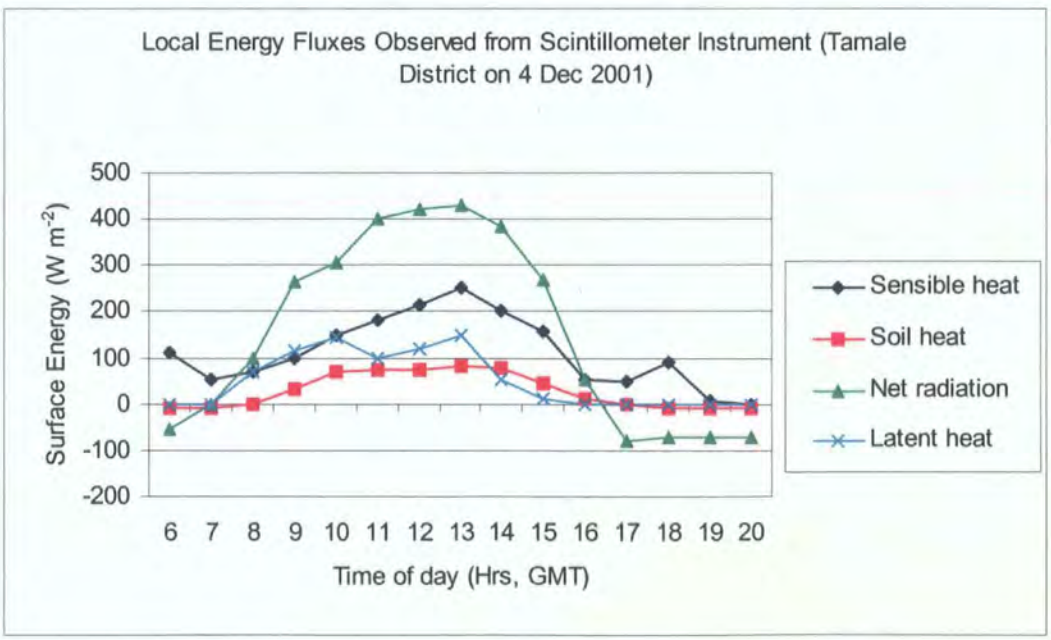


Figure 7.8 Local energy flux observations from the Dutch-type scintillometer instrument. Source: Reproduced from ZEF, (2004)

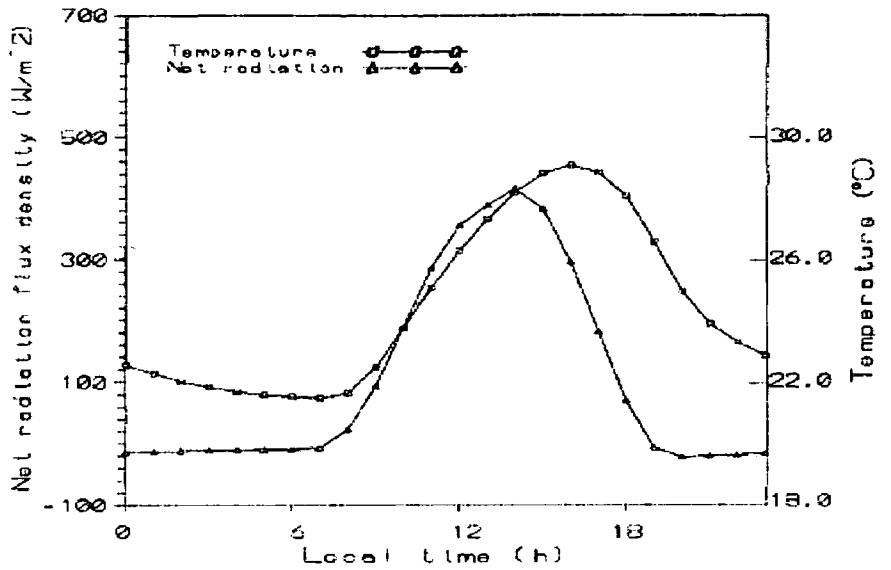


Figure 7.9 Mean daily variation of the net radiation and air temperature for Osu (Central Nigeria, 7.43°N, 4.58°E) in 1995. Source: Jegede (1995)

A comparison of Figures 7.8 - 7.10 shows that the sinusoidal model developed from Equation 7.2 is a reasonable approximation of diurnal hydro-climatic parameters observed in West African savannah regions. It can be concluded from Figure 7.10, for example, that instantaneous radiation measurements from satellites are potentially useful to estimate regional net radiation both in time and space. Indeed, the plots in Figure 7.10 show that the MODIS net radiation measurements show a strong positive correlation with field observations ($r$ = 0.89; RMSE = 41.216 W $m^{-2}$).

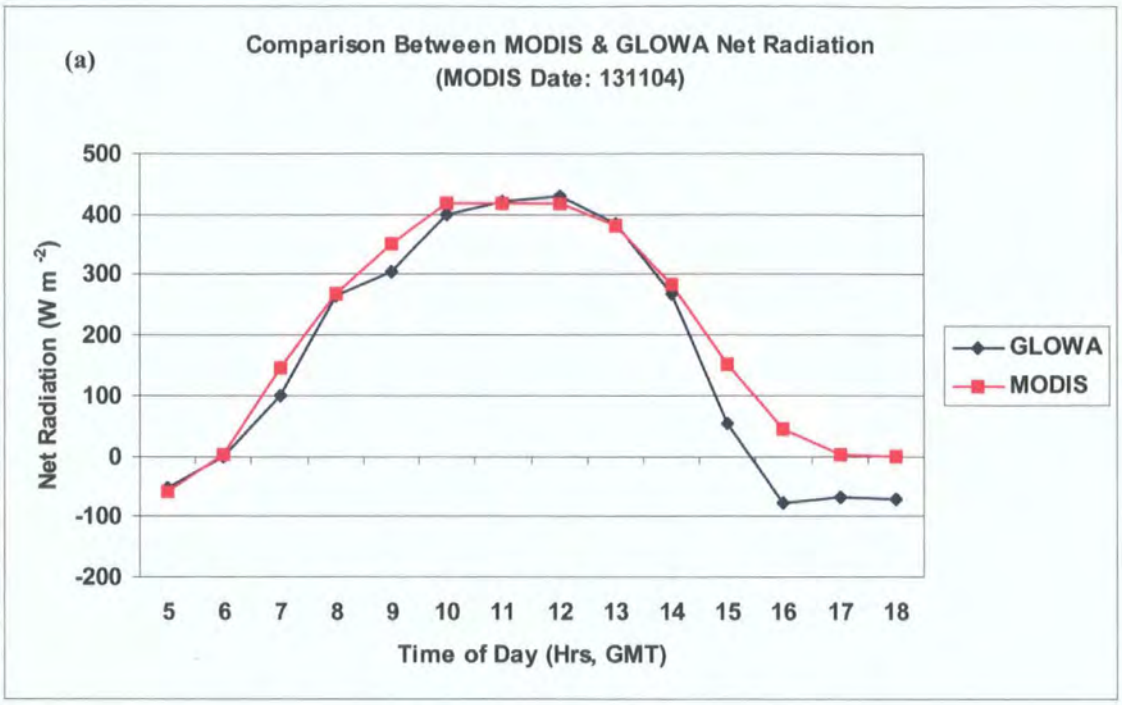


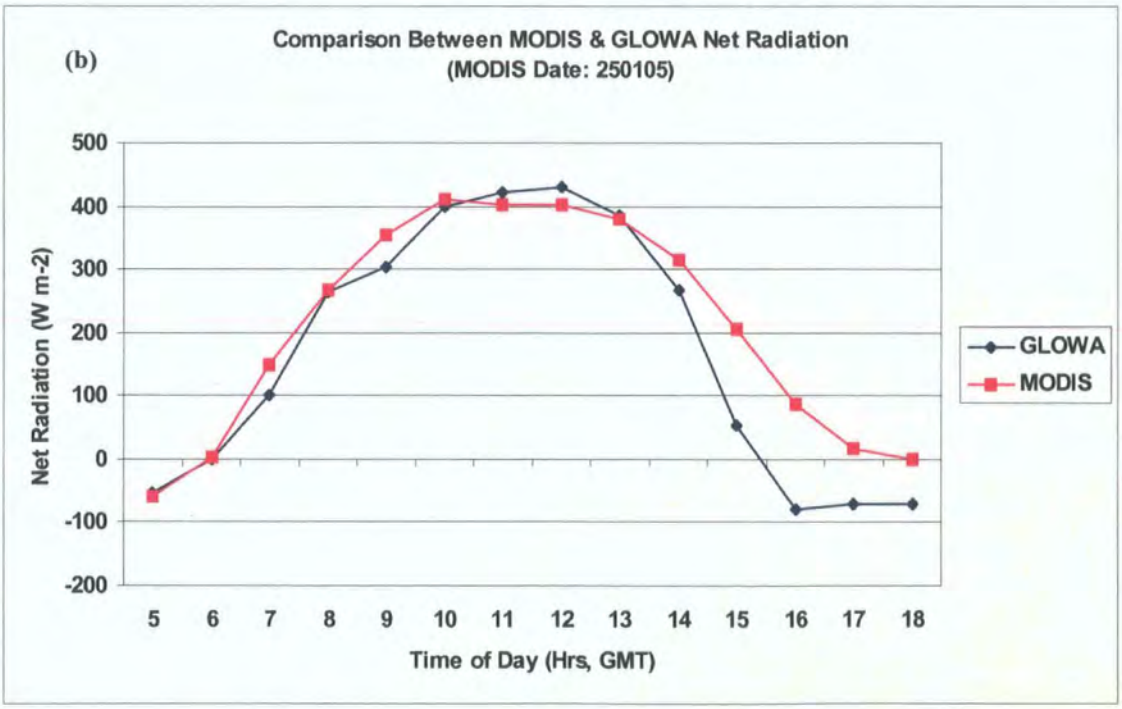


Figure 7.10 Mean diurnal net radiation (a) MODIS date: 131104 and (b) MODIS date: 250105 compared with GLOWA-Volta's (2002) local net radiation ($r = 0.89$). These plots are similar to Figure 7.7 except that they are averaged over the two dates and compared with the net radiation data in Figure 7.8.

### 7.2.3 Diurnal Temperature Modelling

A useful extension of the net radiation model is diurnal temperature modelling. In this case, the $R_n$ term in Equation 7.2 was replaced with $T_s$ and temperature predictions made for various diurnal times as follows: 06:00, 12:00, 15:00 and 18:00. The results are displayed in Figure 7.11. As expected, the north-western urban areas (Figure 7.11) are warmer than the forested river valleys in the south. From a visual perspective, it is not easy to distinguish the spatial changes in temperature because of scale limitations. However, quantitative analysis has shown that the temperature range at 06:00, 12:00, 15:00 and 18:00 hours are as follows: 298.4-312.2 K; 307.8-322.0 K; 308.1-322.3 K; and 296.4-310.0 K, respectively. This diurnal thermal model tends to reflect the "cool-warm-cool" conditions of the area and is important for two main reasons. First, it provides useful information about water stress over the diurnal cycle, which may be used for water resources management studies. Secondly, the spatial distribution of surface temperatures can be used as inputs for environmental models such as regional/global climate change, numerical weather prediction, drought assessment, and crop forecasting models. A detailed discussed follows in Section 7.3.

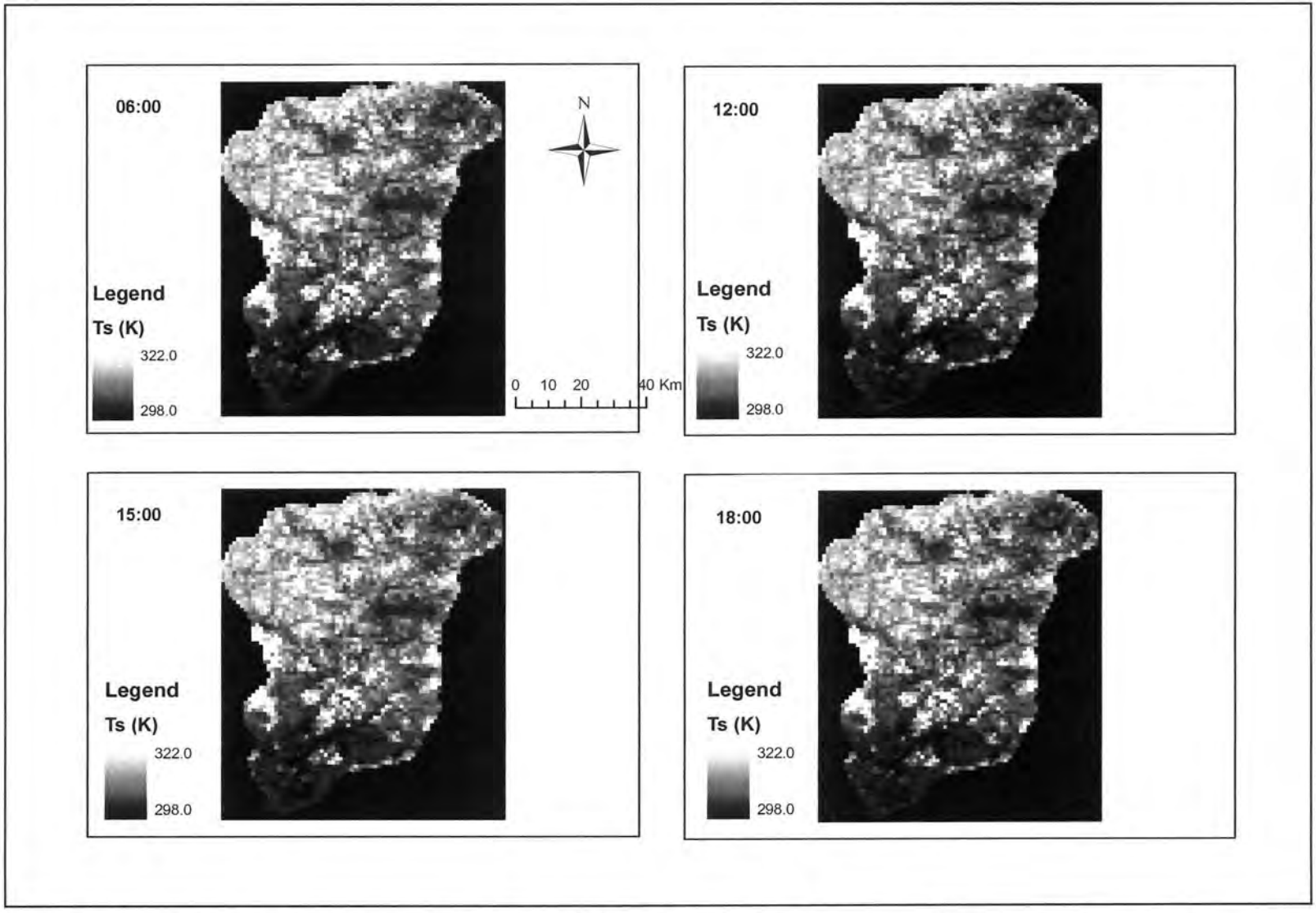


Figure 7.11 Diurnal (06:00 – 18:00) temperature distribution on 13th November 2004. Note the warm sparsely vegetated north-western urban areas in contrast with the cool forested woodlands and river valleys in the south.

### 7.2.4 Diurnal *ET* Modelling from $R_n$ and Evaporative Fraction (*EF*)

Another important extension of the sinusoidal $R_n$ method is diurnal *ET* modelling based on the evaporative fraction (*EF*) method previously proposed by Bastiannssen *et al.* (1998) and defined in Equation 5.25 (Section 5.3.3 of Chapter 5). From Figure 7.7, the mean *EF* from three main land cover types (i.e. grassland, open and closed woodland) was calculated as *0.2978*. For each time *t*, Equation 5.25 was applied as 0.2978**t/k*; where *k* has been empirically determined for dry landscapes in Niger as 28.588 by Bastiannssen *et al.* (1998). Since the *EF* method is often defined in terms of daily evaporation (mm $day^{-1}$), for purposes of comparison, the final results were converted to standard energy units (W $m^{-2}$) for latent heat using the following relationships: 2.45 MJ $m^{-2}$ $day^{-1}$ = 1mm $day^{-1}$ equivalent evaporation, and 1 W $m^{-2}$ = 0.0864 MJ $m^{-2}$ $day^{-1}$ (FAO, 1998). Figure 7.12 compares the final result with local observations of latent heat (see Figure 7.8).

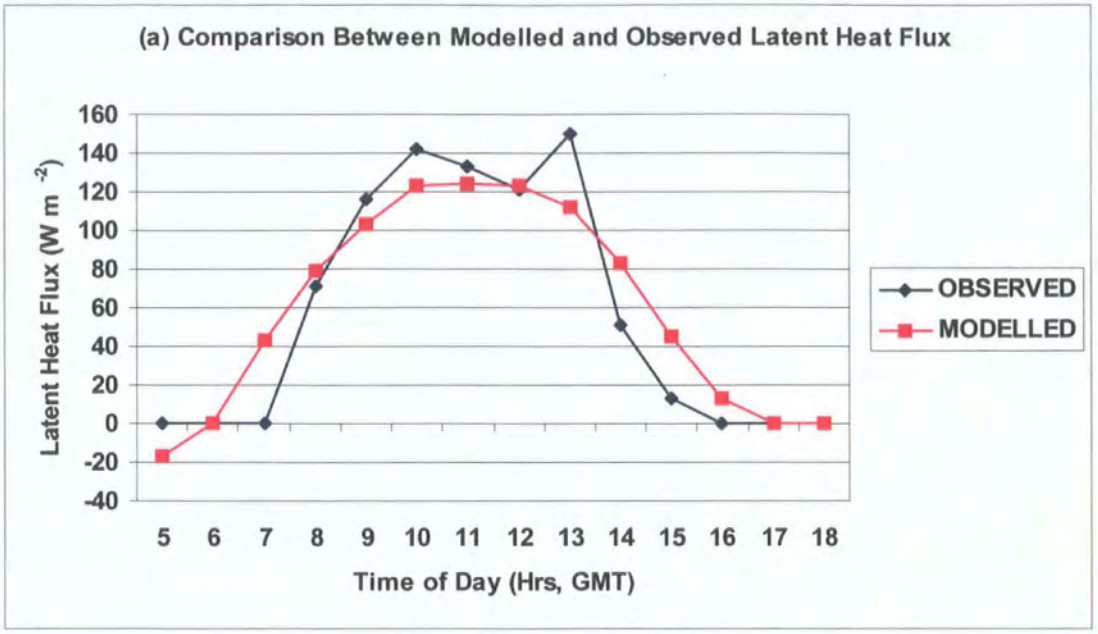


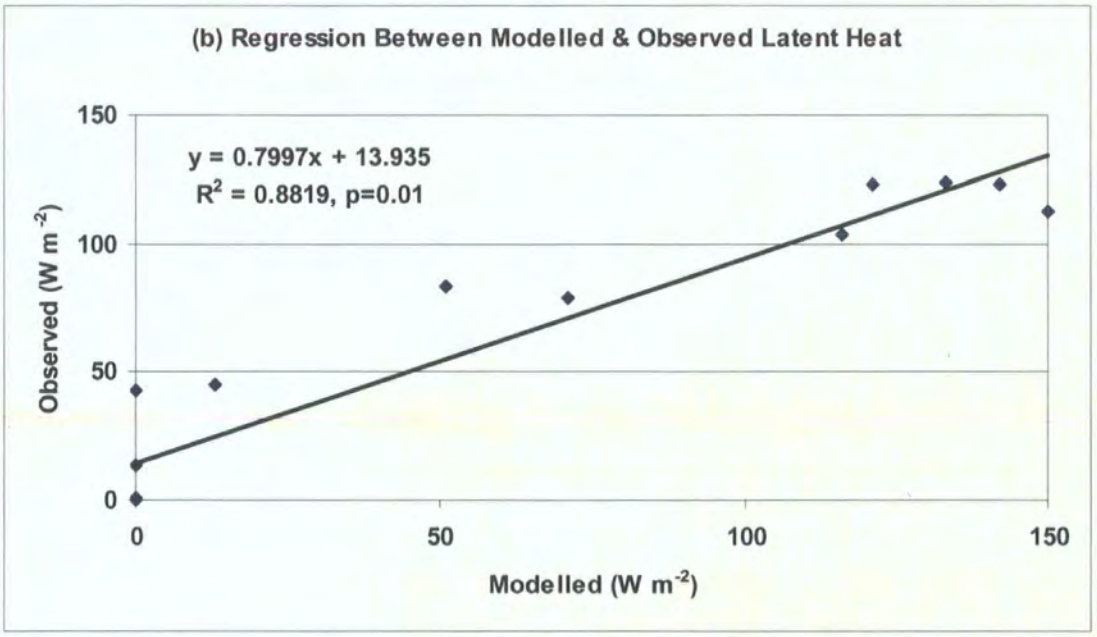


Figure 7.12 Diurnal latent heat flux (i.e. *ET*) modelled from MODIS instantaneous measurements and compared with observation from GLOWA-Volta's scintillometer observation. $N = 14$; $R^2 = 0.88$, $p = 0.01$; RMSE = 22.376 W m$^{-2}$.

The above method presents preliminary results, which may require further verification. However, the approach is interesting for two important reasons. First, it is a simple but innovative method which can be used to derive diurnal *ET* cycles from instantaneous sensor measurements. Secondly, the method presents an alternative to the Penman-Monteith method for estimating *ET*.

## 7.2.5 Regional Estimation of *ET* from Satellite Data

### *7.2.5.1 Instantaneous ET Measurement - the SEBAL Approach*

The principal objective of this thesis is regional estimation of *ET* over the Volta savannah region. The details of how this was achieved constitute the focus of this section. Reference to other parts of this thesis is relevant to put the full discussion into context. First, the satellite data sets analysed here were described in Chapter 3. Secondly, the energy and water balance modelling (SEBAL) approach from which results were derived was detailed in Chapter 5 (in particular Equations 5.2 & 5.25). Thirdly, the methods for processing and implementing the SEBAL algorithm (e.g. MATLAB programming tools) were described in Chapter 6.

Figure 7.13 (a-c) presents examples of spatial estimation of *ET* over the Volta savannah from different satellite sensors (i.e. MODIS, AATSR and Landsat ETM+). There is general qualitative agreement among the sensors in terms observing higher evaporation over the more vegetated southern part of the study area and lower evaporation over the urbanized north-western section (the Tamale metropolis). Further quantitative analysis has been done in Section 7.3.

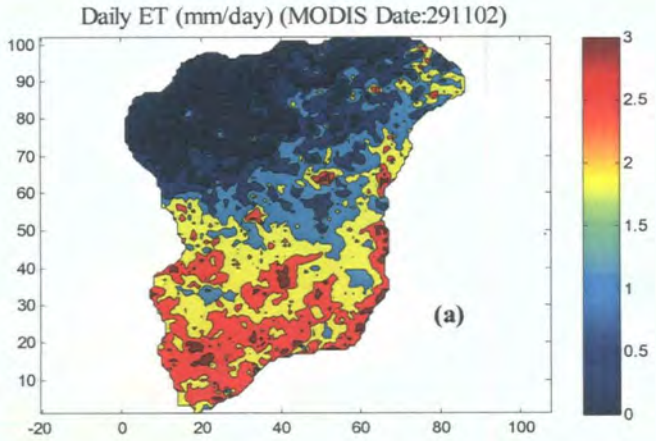


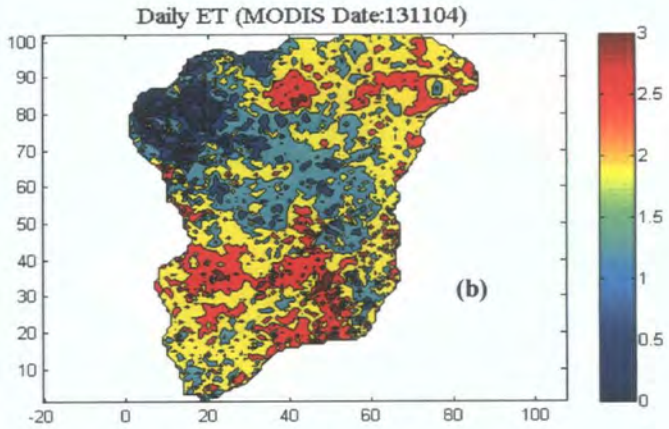


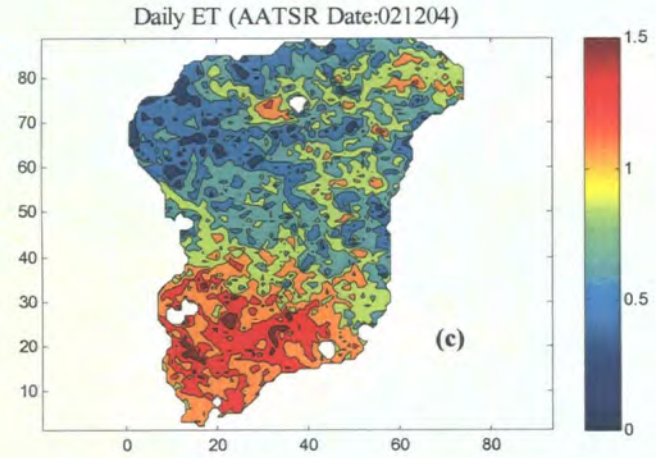


Figure 7.13 (a-c) Distributed *ET* estimated from the MODIS & AATSR sensors on 29/11/02, 13/11/04 and 02/12/04, respectively, within the savannah Volta basin; the blank (white) spaces in (c) represent missing data.

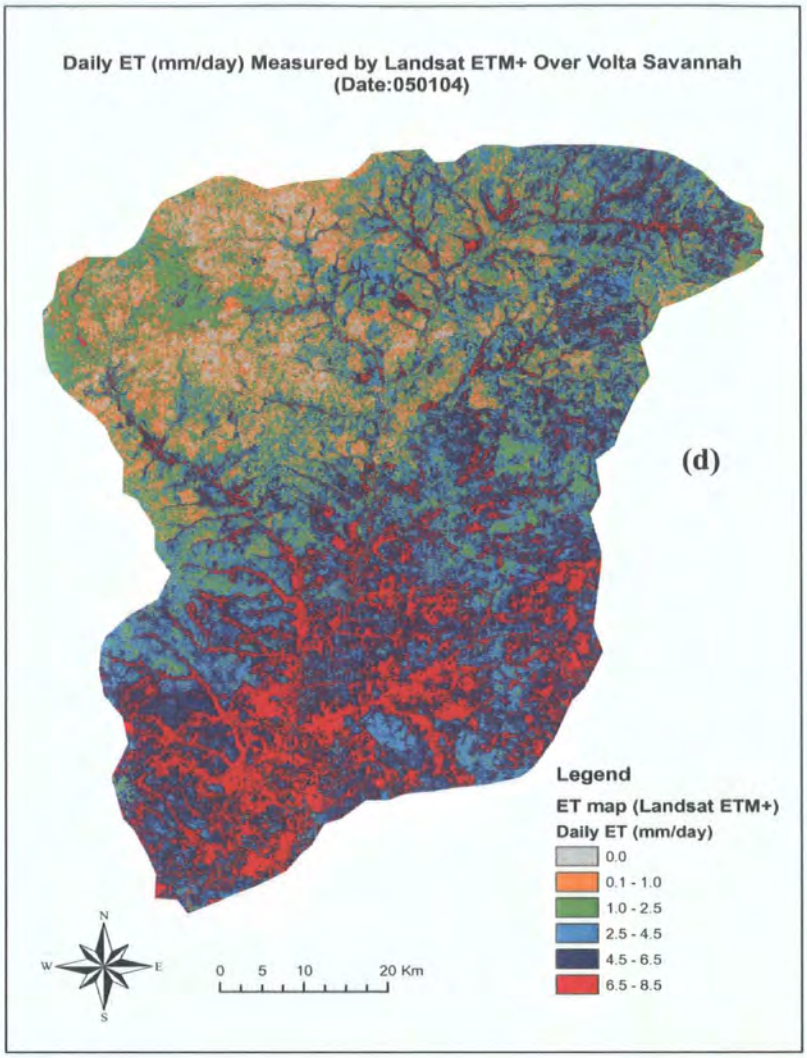


Figure 7.13(d) Distributed *ET* predicted from the Landsat ETM sensor on 05/01/04 within the savannah Volta basin.

Figure 7.13d is important for a variety of reasons. First, it was produced using the ERDAS Imagine-ARC-GIS software packages to solve a practical problem. GIS is widely available so that linked with Figure 7.14, the data can easily be updated in Africa in subsequent studies. MATLAB (used for maps a-c) is not readily available in Africa. Also, linking the Landsat with the MODIS/AATSR results helps to reveal land surface

information of hydrological interest. For example, the *ET* estimates closely follow vegetation distribution even though the pixel sizes of the Landsat ETM+ (30 m) and the MODIS/AATSR (1 km) sensors are very different. The land cover distribution was validated using a land cover map which was acquired nearly at the same time of the coarse-resolution data (see Figure 7.14).

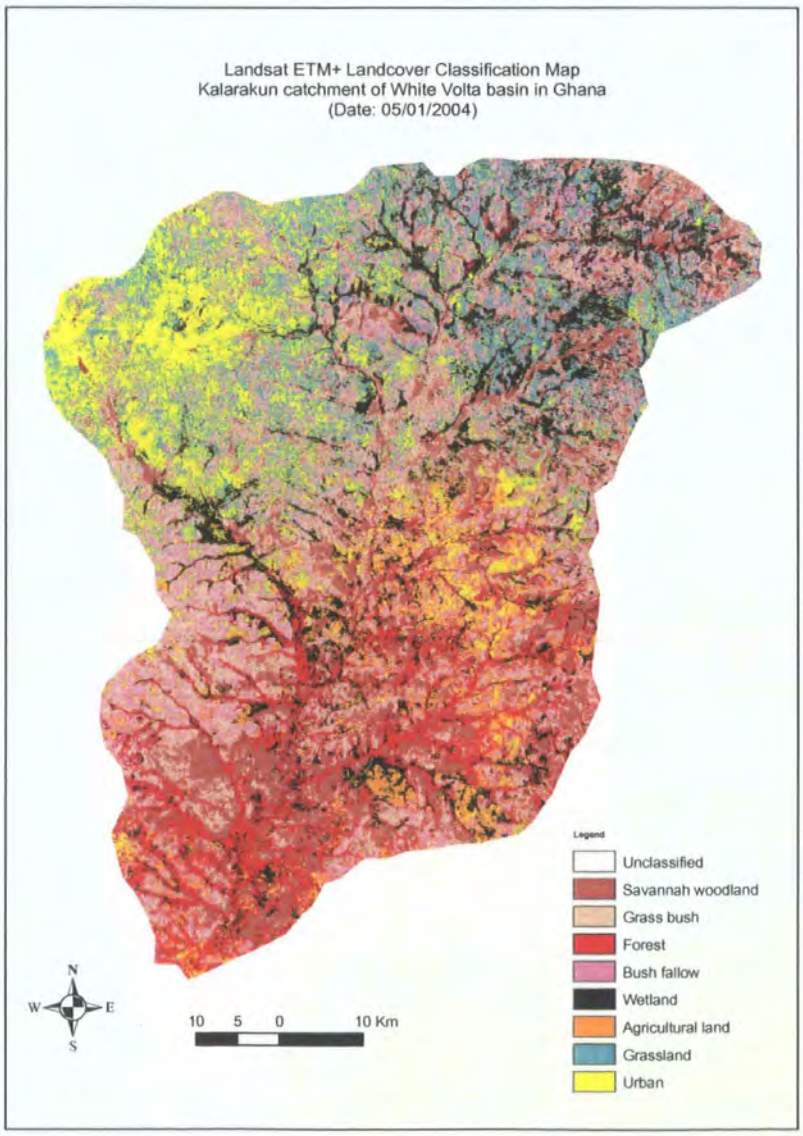


Figure 7.14 Land cover map of the study area based on Landsat ETM+ image acquired on 5th January 2004. The overall classification accuracy based on 178 ground control points using GPS (see Section 3.9.1.2 of Chapter 3) is 71.4%.

The detailed classification procedure which was used to derive the land cover map has been described in Section 3.9.1.2. Here, it is important to briefly describe why the map is helpful. First of all, the image scene was acquired in January in order to capture the mid-drought season; a period when variation and feedback responses between the region's hydro-climatic conditions and land cover are most pronounced. Secondly, the high spatial resolution of the Landsat instrument provides sufficient land cover details to help validate results from the MODIS and AATSR sensors. A visual comparison of Figures 7.13 and 7.14 shows that the *ET* estimates appear strongly correlated with the land cover map as observed independently by the Landsat ETM+ data. This is expected given the detailed spatial resolution of the Landsat sensor.

An important question is whether the quality of the land cover map (Figure 7.14) is sufficient for evaluating the *ET* estimates. Table 7.4 shows that the classified map was produced with an overall accuracy of 71.4% and a Kappa coefficient of 0.69 (the accuracy assessment and Kappa methods are explained in Section 3.9.1.2 of Chapter 3). For such a large study area (~5,300 $km^2$), the above result appears to be reasonable and consistent with published results. In their research which investigated different land cover classification methods (e.g. maximum likelihood, minimum distance, Mahalanobis, etc.) based on Landsat-5 TM data, Colby & Keating (1998) reported overall classification accuracy ranges of 65.1 – 79.7% (Kappa coefficient = 0.48 – 0.61) for sparsely vegetated Ecuadorian catchments, and 77.8 – 82.1% (Kappa coefficient = 0.62 – 0.74) for their counterpart catchments in Costa Rica.

Table 7.4 Land cover classification accuracy for the savannah (Volta) Kalarakun catchment using Landsat ETM+ image acquired on 5th January 2004. The percentage accuracy for each class is highlighted in the table. The main class definitions are given in Section 3.9.1.2 of Chapter 3.

| Land cover classes | | Reference data (Field and ancillary data) | | | | | | | | |
|---|---|---|---|---|---|---|---|---|---|---|
| | | Wood land | Bush | Forest | Fal-low | Wet-land | Agric | Grass-land | Urban | Row Total (%) |
| Classified data based on the Maximum Likelihood method | Wood-land | **78.8** | 2.4 | 13.9 | 1.8 | 0.0 | 1.2 | 1.9 | 0.0 | 100.0 |
| | Bush | 3.1 | **80.2** | 0.8 | 6.1 | 0.4 | 2.2 | 6.8 | 0.4 | 100.0 |
| | Forest | 10.9 | 0.8 | **76.0** | 2.5 | 0.0 | 0.0 | 1.6 | 8.2 | 100.0 |
| | Fallow | 1.4 | 11.4 | 9.6 | ***51.2*** | 21.3 | 2.2 | 2.8 | 0.1 | 99.7 |
| | Wet-land | 0.2 | 0.0 | 0.0 | 8.7 | **70.3** | 11.8 | 8.1 | 0.9 | 100.0 |
| | Agric | 0.0 | 0.3 | 0.0 | 20.7 | 0.4 | **72.2** | 3.7 | 2.7 | 100.1 |
| | Grass-land | 0.6 | 1.1 | 0.0 | 8.8 | 1.3 | 4.4 | **69.2** | 14.7 | 99.9 |
| | Urban | 5.0 | 3.7 | 0.0 | 0.2 | 6.3 | 5.8 | 5.9 | **73.0** | 99.9 |
| Column Total | | 100.0 | 99.9 | 100.3 | 100.0 | 100.0 | 99.8 | 100.0 | 100.0 | |

The accuracy of each class was calculated as the number of correctly classified pixels expressed as a ratio of the total number of pixels (see highlighted diagonals). The overall accuracy was therefore calculated as the average of correctly classified classes along the matrix diagonal, which is approximately 71.4%. Detailed classification methods, signature definition, classification accuracy and error measurements are given in the 7th Edition of ERDAS Field Guide (2003), Chapter 7, pages 221 - 264. Mapping bush fallow is most incorrect (51% accuracy) mainly because of the presence of a wide range of vegetation types (tree crops, bushes, grasses, grain stubble, etc.)

A second important characteristic of Figure 7.13 is linked with the spatial organisation of land cover in the study area (Figure 7.14). As expected, both maps show that *ET* is generally high over vegetated surfaces where soil moisture appears to be also high (e.g. river valleys). Thirdly, Figure 7.13 tends to support the widely accepted view that remote sensing is useful for regional estimation of energy fluxes in dry catchments (e.g. Brata *et al.*, 2006; Kondoh & Higuchi, 2001; Di Bella *et al.* 2000). Fourthly, the figure portrays the complementary capabilities of different sensors for mapping energy fluxes over complex surfaces. In fact, the high resolution Landsat land cover map is a potentially useful data set to validate its medium resolution (MODIS and AATSR) counterparts.

### 7.2.6 Relationship between *ET* and Surface Biophysical Variables

Several studies have established strong correlations between *ET* and other biophysical parameters such as NDVI and land surface temperature ($T_s$) using multivariate analysis (e.g. Tucker and Sellers, 1986; Goetz, 1997; Di Bella *et al.* 2000; Brata *et al.* 2006). Di Bella *et al.* (2000), for example, have reported a linear relationship between $T_s$, NDVI and AVHRR-derived *ET* over the Argentine Pampas as follows:

$$ET = -88.3439 + 1.77636T_s + 286.406NDVI \qquad (7.3)$$

where $T_s$ = land surface temperature ($^0$C) and the units of *ET* is mm day$^{-1}$ ($R^2$ =0.7535; $N$=41; $p$<0.0001). The above study showed that the percentage variance in *ET* caused by $T_s$ and NDVI data was similar to that obtained by other authors, such as Seguin *et al.* (1994) and Smith *et al.* (1990). In order to demonstrate how *ET* is related to the interaction of key biophysical parameters (e.g. NDVI, $T_s$, aerodynamic resistance to heat transport ($R_{ah}$) and daily net radiation ($R_{n\_24}$)), a multivariate experiment was performed over the Tamale district (Figure 2.2) using a clear-sky MODIS image acquired on 13$^{th}$ November 2004 (see Section 5.5 of Chapter 5). The purpose was to describe the surface conditions of the Tamale area (i.e. *urban* land cover class in Figure 7.14) knowing that the district presents the widest range of NDVI values (Figure 7.2b) by which sensitivity compared to other parameters can be determined. The results are shown in Table 7.5 and further discussed in Section 7.3.2.

Table 7.5 (a) Multivariate analysis between *ET* and related biophysical parameters

| I | Coefficient | Standard Error | t-Statistic | P-value | Lower 95% | Upper 95% |
|---|---|---|---|---|---|---|
| **Intercept** | ***92.0729*** | 10.5926 | 8.6922 | 2.47E-13 | 71.0083 | ***93.1376*** |
| **NDVI (-)** | -24.0687 | 5.56.27 | -4.3268 | 4.15E-05 | -35.1306 | -13.0067 |
| **$T_s$ (K)** | -0.2333 | 0.0277 | -8.4064 | 9.28E-13 | -0.2884 | -0.1781 |
| **$R_{ah}$ (s $m^{-1}$)** | -0.1161 | 0.0400 | -2.8997 | 0.0047 | -0.1957 | -0.0365 |

| II | Coefficient | Standard Error | t-Statistic | P-value | Lower 95% | Upper 95% |
|---|---|---|---|---|---|---|
| **Intercept** | ***75.3308*** | 9.3528 | 8.0543 | 4.72E-12 | 56.7317 | ***93.9299*** |
| **NDVI (-)** | -8.4778 | 1.1245 | -75392 | 5.03E-11 | -10.7141 | -6.2416 |
| **$T_s$ (K)** | -0.2280 | 0.0300 | -7.5882 | 4.02E-11 | -0.2878 | -0.1629 |
| **$R_{n\text{-}24}$ (W $m^{-1}$)** | 0.0017 | 0.0036 | 0.4799 | 0.6325 | -0.0054 | -0.0089 |

| III | Coefficient | Standard Error | t-Statistic | P-value | Lower 95% | Upper 95% |
|---|---|---|---|---|---|---|
| **Intercept** | ***11.5483*** | 9.5843 | 1.2049 | 0.2316 | ***-7.5112*** | ***30.6079*** |
| **NDVI (-)** | -12.4708 | 11.1473 | -1.1187 | 0.2664 | -34.6384 | 9.6968 |
| **$R_{n\text{-}24}$ (W $m^{-1}$)** | -0.0027 | 0.0062 | --0.4424 | 0.6594 | -0.0149 | 0.0095 |
| **$R_{ah}$ (s $m^{-1}$)** | -0.0552 | 0.0741 | -0.7448 | 0.4585 | -0.2024 | 0.0921 |

| IV | Coefficient | Standard Error | t-Statistic | P-value | Lower 95% | Upper 95% |
|---|---|---|---|---|---|---|
| **Intercept** | ***62.1408*** | 9.1101 | 6.8210 | 1.3E-09 | 44.0243 | ***80.2573*** |
| **$R_{n\text{-}24}$ (W $m^{-1}$)** | -0.0033 | 0.0034 | -0.9824 | 0.3287 | -0.0109 | 0.0034 |
| **$R_{ah}$ (s $m^{-1}$)** | 0.0505 | 0.0076 | 6.6185 | 3.21E-09 | -0.0353 | 0.0656 |
| **$T_s$ (K)** | -0.2069 | 0.0307 | -6.7481 | 1.8E-09 | -0.2679 | -0.1459 |

Note: NDVI=Normalised Difference Vegetation Index; $T_s$=Surface Temperature; $R_{n\text{-}24}$=Daily net radiation; $R_{ah}$=Aerodynamic resistance for heat transport

(b) Summary regression statistics

| | I | II | III | IV |
|---|---|---|---|---|
| Multiple Regression | ***0.8125*** | ***0.7919*** | 0.6130 | 0.7675 |
| $R^2$ | ***0.6602*** | ***0.6272*** | 0.3758 | 0.5892 |
| Adjusted $R^2$ | 0.6481 | 0.6138 | 0.3535 | 0.5745 |
| Standard Error | 0.3613 | 0.3784 | ***0.4897*** | 0.3972 |
| No. of Observations | 88 | | | |

(c) Analysis of variance (ANOVA)

| I | df | SS | MS | F | Significance F |
|---|---|---|---|---|---|
| Regression | 3 | 21.3019 | 7.1006 | ***54.4012*** | 1.2E-19 |
| Residual | 84 | 10.9639 | 0.1305 | | |
| Total | 88 | 32.2658 | | | |

| II | df | SS | MS | F | Significance F |
|---|---|---|---|---|---|
| Regression | 3 | 20.2373 | 0.7457 | 47.1088 | 5.9051E-18 |
| Residual | 84 | 12.0284 | 0.1432 | | |
| Total | 88 | 32.2657 | | | |

| IV | df | SS | MS | F | Significance F |
|---|---|---|---|---|---|
| Regression | 3 | 12.1249 | 4.0146 | ***16.8563*** | 1.17E-08 |
| Residual | 84 | 20.1408 | 0.2398 | | |
| Total | 88 | 32.2659 | | | |

| IV | df | SS | MS | F | Significance F |
|---|---|---|---|---|---|
| Regression | 3 | 19.0105 | 6.3368 | 40.1575 | 3.39E-16 |
| Residual | 84 | 13.2522 | 0.1578 | | |
| Total | 88 | 32.2657 | | | |

### 7.2.7 Inter-comparison of Geophysical Variables by MODIS and AATSR Sensors

There is no generally accepted methodology to compare and validate the spatial distribution of *ET* over large areas measured from different satellite sensors. The biggest problem is mismatch in sensor pixel size (i.e. point spread function). Random measurement errors may be different and could arise on account of varied usage of sensors, measurement techniques and system calibration methods (Brata *et al.*, 2006; Jiang & Islam, 2001). Notwithstanding, sensor inter-comparison has several benefits, such as data accuracy checks and improvements, feedback from the data-user community to data providers, vital market decisions on spatial data (e.g. types, cost and quantity of satellite imagery) and sharing of key technical information among researchers and operational users. In this section, *ET*, NDVI and $T_s$ measurements from the MODIS and AATSR sensors are compared with the first part of the results displayed in Table 7.6.

Table 7.6 Variation of surface temperature ($T_s$), normalised difference vegetation indeed (NDVI) and daily evapotranspiration ($ET$) over the Volta savannah from MODIS & AATSR sensors ($N = 71$ pixels)

| Date of image acquisition [Julian day] | MODIS 131104 [318] | MODIS 021204 [337] | MODIS 250105 [25] | AATSR 131104 [318] | AATSR 021204 [337] | AATSR 250105 [25] |
|---|---|---|---|---|---|---|
| ***Land Surface Temperature ($T_s$)*** | | | | | | |
| Maximum | 309.476 | 309.650 | 310.390 | 317.037 | 323.089 | 322.356 |
| Minimum | 302.078 | 302.616 | 306.691 | 308.623 | 308.750 | 312.347 |
| **Mean** | **304.383** | **306.217** | **308.586** | **312.463** | **318.970** | **319.050** |
| Std Deviation | 1.594 | 1.999 | 0.965 | 1.871 | 2.890 | 1.882 |
| ***NDVI*** | | | | | | |
| Maximum | 0.727 | 0.720 | 0.661 | 0.751 | 0.701 | 0.693 |
| Minimum | 0.387 | 0.326 | 0.312 | 0.519 | 0.461 | 0.488 |
| **Mean** | **0.620** | **0.566** | **0.489** | **0.639** | **0.587** | **0.582** |
| Std Deviation | 0.066 | 0.079 | 0.068 | 0.045 | 0.074 | 0.046 |
| ***Daily Evapotranspiration ($ET_{24}$)*** | | | | | | |
| Maximum | 2.297 | 3.082 | 2.831 | 0.987 | 1.471 | 0.706 |
| Minimum | 0.020 | 0.025 | 0.904 | 0.000 | 0.300 | 0.000 |
| **Mean** | **0.918** | **1.469** | **2.052** | **0.283** | **0.965** | **0.170** |
| Std Deviation | 0.609 | 0.840 | 0.400 | 0.213 | 0.282 | 0.140 |

### *7.2.7.1 Sensor Inter-comparison of $T_s$*

Accurate assessment of $T_s$ measured from different sensors is valuable for a number of reasons. The most important of them is better understanding of microclimatic changes and how they affect human, ecological and hydrological changes of catchment areas. Also, to utilize remote sensing methods, scientists do not only need to evaluate the quality of sensor data, but also to make important decisions concerning availability of the data, scale issues and cost. In Table 7.6 the MODIS and AATSR sensors are compared, which in part, may help researchers to assess the potential of the instruments.

Consideration of Table 7.6 shows that the average difference between AATSR and MODIS $T_s$ is about 10.4 K. To ascertain which of the sensors more accurately measures surface temperature two types of validation are necessary. The first one is evaluation of the image thermal calibration methods and the second one is verification of the results from independent data sources, such as global climate data and/or field observations.

From Sections 3.6 and 5.4 of Chapters 3 & 5, it can be seen that MODIS and AATSR imagery have been subjected to similar thermal processing procedures; where image radiances were first converted to brightness temperature ($T_B$) using the inverted Planck's equation and subsequent derivation of surface temperature ($T_s$), using the split-window algorithm. The main difference here is that whereas the AATSR Level 1B product was obtained as calibrated $T_B$ data, the MODIS Level 1B product was obtained as raw radiance data; the $T_B$ was retrieved applying calibration coefficients provided by the data suppliers. The effect of this was investigated on the basis of $T_B$ statistics shown in Table 7.7.

Table 7.7 Temporal statistics of MODIS & AATSR brightness temperatures ($T_B$)

| Date of image acquisition [Julian day] | 131104 [318] | | 021204 [337] | | 250105 [25] | |
|---|---|---|---|---|---|---|
| | **MODIS** | | | | | |
| | **11μm** | **12μm** | **11μm** | **12μm** | **11μm** | **12μm** |
| Maximum | 301.8 | 299.3 | 303.2 | 301.6 | 309.1 | 306.3 |
| Minimum | 281.4 | 289.8 | 291.6 | 294.3 | 298.0 | 299.9 |
| **Mean** | **296.0** | **292.0** | **299.3** | **292.7** | **302.2** | **300.8** |
| Std. Deviation | 1.231 | 1.032 | 0.853 | 1.110 | 1.543 | 1.276 |
| | **AATSR** | | | | | |
| | 131104 [318] | | 021204 [337] | | 250105 [25] | |
| | **11μm** | **12μm** | **11μm** | **12μm** | **11μm** | **12μm** |
| Maximum | 303.2 | 297.6 | 314.8 | 312.2 | 317.7 | 313.3 |
| Minimum | 292.6 | 289.2 | 299.6 | 298.4 | 307.7 | 302.8 |
| **Mean** | **298.9** | **294.8** | **305.0** | **303.3** | **309.1** | **304.7** |
| Std. Deviation | 1.055 | 0.807 | 2.276 | 2.078 | 1.441 | 1.511 |

From Table 7.7, the average brightness temperatures ($T_B$) measured by the AATSR sensor (full-scenes) are slightly higher than MODIS in the 11 and 12μm thermal bands (channels) at nadir viewing angles; the average $T_B$ difference between the thermal bands is about 4.9K (Table 7.7). Over large heterogeneous surfaces, the above $T_B$ difference may be considered sufficiently large (Coll *et al.*, 2004) to show the magnitude of $T_s$ deviations in

Table 7.6. This seems to confirm that the above $T_s$ deviations may not be due to errors produced from processing the MODIS thermal bands but differences in sensor and instrument characteristics.

In the second (evaluation) case, Table 7.8 was extracted from a record of field soil temperatures observed from the Tempcon® HOBO-H8 thermal data logger (see Appendix 3.8) coincidental with the time of the satellites overpass and evaluated against the two sensors. There were no field temperatures for 25/01/05 since the fieldwork concluded before this date. Differences are expected between field-based and radiometric temperature, which is precisely the case in Table 7.8 and Figure 7.15; further details are given in Section 7.3.3. Figure 7.15 shows that the MODIS sensor is more precise ($R^2$ = 0.73) than AATSR ($R^2$ = 0.41).

Table 7.8 Surface (including soil) temperatures (K) observed from thermal data logger at the time or near MODIS & AATSR overpass. The thermal loggers named here as A-E were sited in locations defined in Figure 3.8. The land cover types of the locations (Figure 7.15) were urban, grassland bush, open woodland, agriculture and closed woodland, respectively.

| | Logger A | Logger B | Logger C | Logger D | Logger E |
|---|---|---|---|---|---|
| **Date: 131104** | | | | | |
| Time 10:12 | 309.19 | 310.21 | 309.19 | 308.72 | 307.58 |
| 10.32 | 309.27 | 310.32 | 309.97 | 308.86 | 307.97 |
| 11:12 | 309.27 | 310.29 | 309.92 | 308.45 | 308.49 |
| Av. Temp (K) | **309.24** | **310.29** | **309.69** | **308.68** | **307.95** |
| **Date: 021204** | | | | | |
| Time 10:12 | 312.67 | 312.08 | 312.39 | 308.11 | 307.88 |
| 10.32 | 312.98 | 312.21 | 312.33 | 308.07 | 307.70 |
| 11:12 | 312.98 | 312.29 | 312.38 | 308.64 | 308.66 |
| Av. Temp (K) | **312.88** | **312.19** | **312.37** | **308.27** | **308.08** |

**Note:** Only two days coincidental with fieldwork have been used for the current analysis. The short period of fieldwork as well as data loss due to bush fires and bad weather (heat wave) prevented more data to be collected.

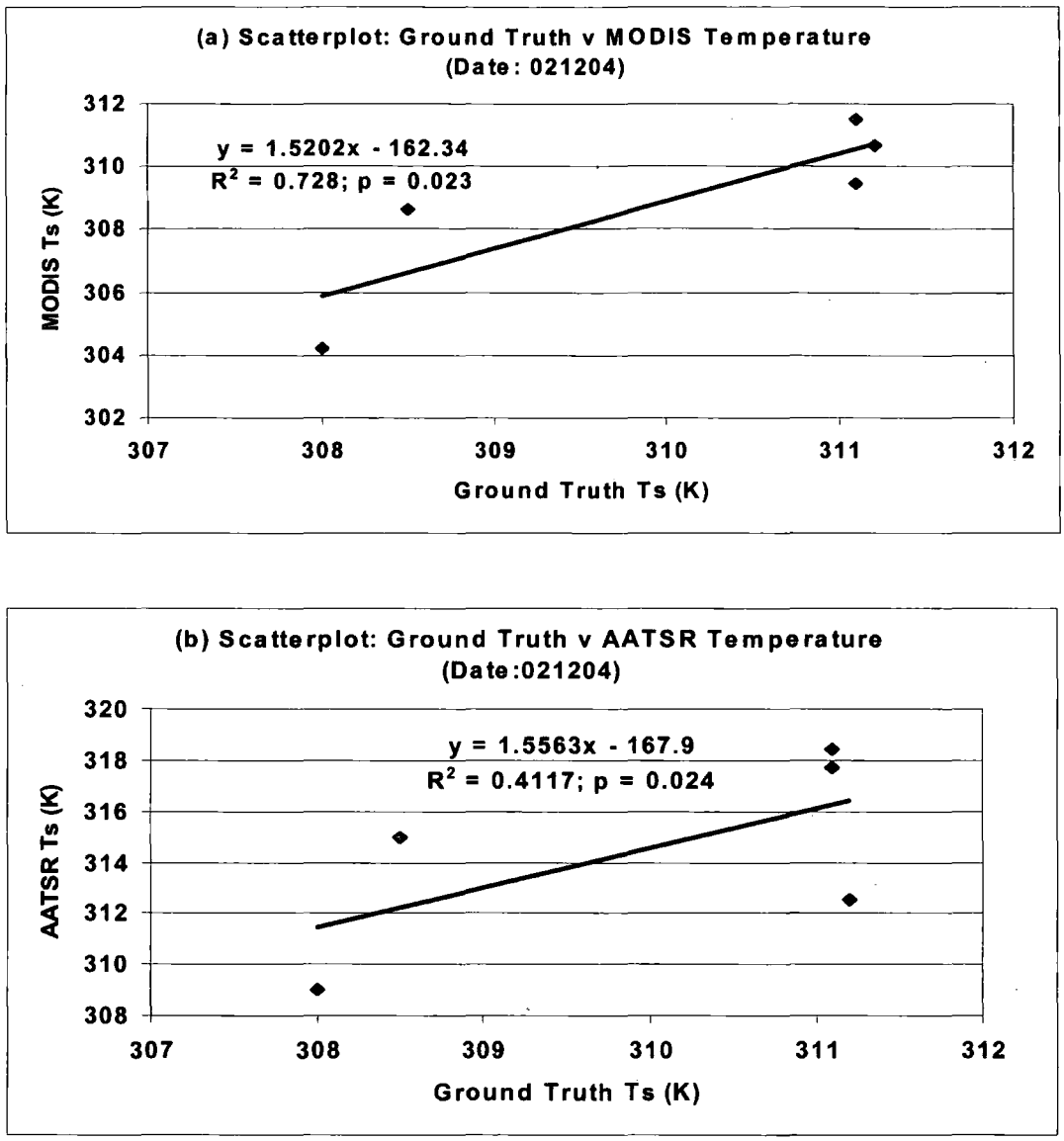


Figure 7.15 Correlation between ground truth (HOBO logger) data and satellite surface temperatures.

As further verification of the results in Figure 7.15, simple statistical error analysis was performed on the data for 2nd December 2004 using the ground truth information in Table 7.8. As a first step, the mean observed (HOBO) temperature was calculated and the result

was used to calculate the sensor accuracy ($A$) (i.e. mean of error) as $A = \frac{\sum d}{n}$ where $d$ = deviation (error) of the sensor pixel temperature from the mean observed (HOBO) temperature, which was 310.76 K, and $n$ = 4142. Similarly, the sensor precision ($P$) (i.e. standard deviation of error) was calculated as $P = \sqrt{\frac{\sum d^2}{n-1}}$. The results are shown in Table 7.9 below. Table 7.9 tends to confirm the precision of the MODIS temperature measurement compared to the AATSR sensor, which is discussed later.

Table 7.9 Accuracy and precision statistics determined on the basis of ground truth (HOBO logger) data; the mean local temperature was 310.76K. The sensor temperatures are in Kelvin and $N$ = 4142 pixels. The observation date was 021204.

| Sensor | Sample mean | Mean of error (Accuracy level) | Standard deviation of error (Precision level) |
|---|---|---|---|
| MODIS | 307.06 | +3.69 | 2.47 |
| AATSR | 318.75 | -7.99 | 1.95 |

An important question is: how are the two sensors correlated in terms of temperature measurement? Figure 7.16 presents a correlation plot between the MODIS and AATSR sensors, which shows that for the above purpose, the sensors appear poorly correlated in this example.

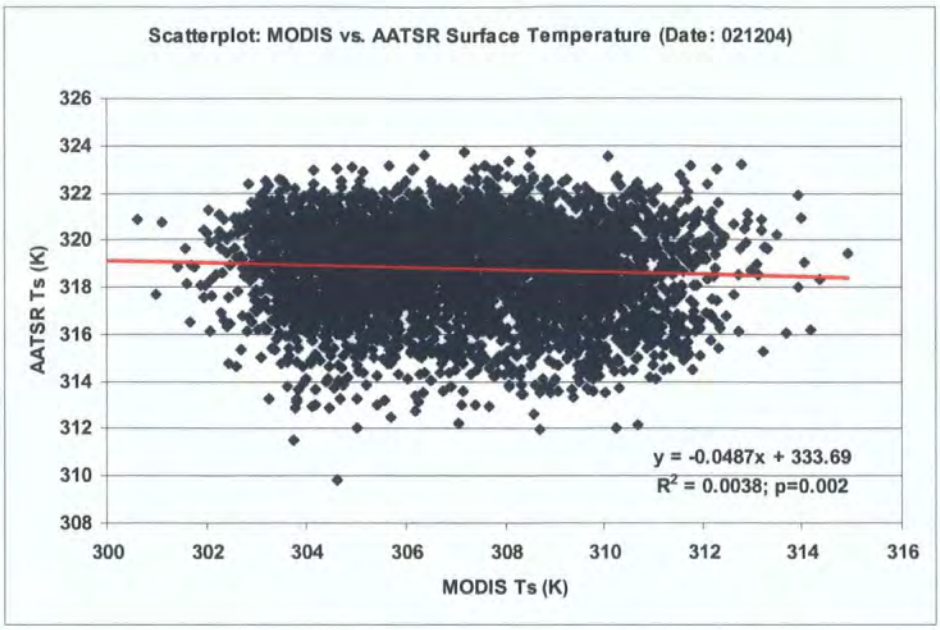


Figure 7.16 Correlation between MODIS and AATSR surface temperatures

### *7.2.7.2 Sensor Inter-comparison of NDVI*

Degradation of vegetation cover in the savannah region resulting from factors such as climate and land use change, droughts, extreme variability in surface and groundwater hydrology has been reported by many local researchers, e.g. Duadze (2004) and Gyau-Boakye & Tumbulto (2000). The temporal variation in NDVI (Table 7.6) probably shows this trend more consistently from the MODIS sensor than the AATSR. This is further exemplified by the wider range of the MODIS NDVI values (~0.36) in comparison with the AATSR sensor (~0.22). For medium resolution (1x1 km) satellites, an NDVI difference of nearly 0.15 may cover an extremely wide range of ground cover, vegetation types and biomass volume. This shows the advantage of the MODIS visible and near-infrared bands over its AATSR counterpart for estimating NDVI; a large variance is not expected for the identical measurement period indicated in Table 7.6.

#### *7.2.7.3 Sensor Inter-comparison of ET*

Hydrologists often obtain *ET* as the unknown term of the regional energy and water balance equation mainly because of its critical value in terms of water availability. *ET* over- or underestimation can lead to severe consequences on water resource management which makes sensor inter-comparison a necessity. Similar to NDVI and $T_s$, Table 7.6 compares the temporal statistics of *ET* measured from the MODIS and AATSR sensors over the Tamale savannah district. The standard deviations in *ET* (Table 7.6) linked with Figure 7.13 tend to show how *ET* is spatially estimated by both sensors. The main sensor differences are further discussed in Section 7.3.3.

## 7.3 Discussion

### 7.3.1 Bio-geophysical Relationships

Vegetation abundance, represented by the NDVI ratio (Figure 7.2), is one of the most influential factors in the control of $T_s$ through partitioning of solar radiation into fluxes of sensible and latent heat and by limiting the proportions of vegetation and the ground within a sensor's instantaneous field-of-view (IFOV). NDVI can be particularly useful for predicting seasonal variability of *ET* and soil moisture status (Nemani *et al.*, 1989). Keeping meteorological and canopy transpiration factors (e.g. canopy resistance) constant over short periods, *ET* and soil moisture are expected to be higher on 13$^{th}$ than 29$^{th}$ November (Figure 7.2), knowing that groundwater recharge from the October rainfall (see Table 4.2, Section 4.2 of Chapter 4) precedes the seasonal droughts in the region. This reason explains why *ET* and soil moisture was higher in 2004 than 2002 (Figure 7.2).

For very large ungauged tropical areas without prior knowledge of site conditions, derivation of seasonal time-series NDVI maps hold promise for *ET* and soil moisture prediction. Knowing the strong relationship between NDVI and *ET* and also $T_s$ and *ET*, it follows that a well calibrated model between NDVI and $T_s$ for both the dry and wet seasons may help to establish an annual trend between NDVI and *ET*, which may potentially be used for assessing water stress.

As expected, the NDVI-$T_s$ curve (Figure 7.3) shows a strong negative relationship between NDVI and surface temperature ($R^2$ = ~0.70; $p$ = 0.018), which generally represents canopy cooling effects from evapotranspiration processes; the greater the plant biomass, the lower is $T_s$. Such strong correlation in savannah catchments could be used to derive linear regression models which then may be applied for predicting $T_s$ over wide areas for such applications as global change, hydrology and agronomy. This may not be needed if thermal remote sensing technology is well developed; however, for areas where NDVI may be the only available satellite-based product, this approach may be worth considering. However, there is both lack of consistency in the scatterplots and coherence between the MODIS and AATSR curves. In both cases, several pixel values lie well outside the (trend) prediction line, even though the MODIS sensor shows a much better result ($R^2$ = 0.74). Divergence between the sensors may be explained by differences in sensor characteristics (see details in Section 7.2.7.2); however, extensive field checks are needed to fully explain outliers in the scatterplots (Figure 7.3). The warm but poorly-vegetated surfaces (see Figure 7.2) are probably wide bare surfaces such as urban places, sand/stone winning areas (for construction) or extensive rock outcrops; the cool, well-vegetated surfaces are probably wetlands. Apart from surface heterogeneity (Weng *et al.*,

2004), differences in the NDVI-$T_s$ curve may be attributed to increased soil moisture depletion and drought. For instance, no rainfall event was recorded over the 8-week period (Figure 7.2b) preceding the 4$^{th}$ January data (Figure 7.3). This probably explains why large exposed surfaces (NDVI<0.2) appear to emit large amounts of radiated energy (see Figure 7.3b). Although a linear relationship fits well for the data in this study, incoherent outliers in the NDVI-$T_s$ scatterplots need to be resolved before such a linear model could be transferred to other catchments for predicting $T_s$ or savannah biomass. This can be important in developing countries where satellite data or image processing facilities are not readily available.

The plots in Figure 7.4 are important for two main reasons. First, the negative relationship between NDVI-$G_0/R_n$ is expected since generally, a greater amount of radiant energy is conducted into exposed soil surfaces than vegetated areas, which somewhat describes observations in the Volta catchment area. Secondly, soil moisture depletion as in the case of the dry period of study (Figure 7.4) is a critical factor which first, controls predictions of the $G_0/R_n$ ratio and secondly, the relationship between the $G_0/R_n$ ratio and vegetation cover. Published research such as Jacobsen & Hansen (1999) seems to suggest strong linear correlation between NDVI and $G_0/R_n$ (see Figure 7.5). However, conditions in the Volta basin do not follow this pattern precisely, showing very low correlation between NDVI and $G_0/R_n$ ($R^2$=0.10). Whereas the relationship is better portrayed under the Arctic/Tundra conditions in Figure 7.5, drought conditions appear to mask the West African example (Figure 7.4). The plots in Figure 7.5 (Jacobsen & Hansen, 1999) show that large $G_0/R_n$ and small NDVI values represent very sparse vegetation (Fell fields with moraine ridges), which is characterised by bare soil and crusts. This seems to correspond

well with the patterns seen in Figure 7.4 in the urban and senescent grassland areas where vegetation is sparse, which means such parcels are more strongly related to $G_0/R_n$. In other words, depression in the $G_0/R_n$ ratio may be strongly associated with abundance of vegetation biomass and vice versa, which invariably is related to soil moisture status (Jacobsen & Hansen, 1999).

The above point is related to the third important characteristic of Figure 7.4. At the field scale, measurement of land surface temperature ($T_s$) is not hugely problematic since $T_s$ may be measured with instruments such as the forward-looking infrared (FLIR) sensor. This is also a rapid and non-destructive method. Such is not the case for $G_0$, which requires a heat flux plate and frequently simultaneous measurements of $G_0$ and vegetation cover at several undisturbed locations. Figure 7.4 shows how remote sensing methods can achieve this in a convenient way. Fourthly, the NDVI-$G_0/R_n$ regression presents a simplified way of classifying and discriminating vegetation water stress, which is of importance not only to catchment hydrology, but also forestry and agriculture.

In the literature, different $G_0/R_n$ ratios have been published for a variety of land surface conditions. For example, Jacobsen & Hansen (1999) measured daily $G_0/R_n$ over dry *Cassiope* heath with a mean value of 0.18 over a 20-day experimental period. Kustas *et al.* (1993) found a daily $G_0/R_n$ ratio of 0.16-0.18 over Central USA, and Rouse (1984) observed 0.16-0.24 in Hudson Bay. Daily observations for tropical areas are not easily obtainable but this may not be a big problem since near-midday magnitude of $G_0/R_n$ ratio is of greater importance than the daily magnitude because a diurnal variation from 0.05 – 0.50 may be observed for many naturally vegetated surfaces (Kustas *et al.*, 1993). This shows that the current observed $G_0/R_n$ ratio (0.10 – 0.13) is a reasonable result.

Why the observed correlation between $G_0/R_n$ and NDVI is so low ($R^2$=0.10) is not easy to explain. It should be noted that vegetation biomass cannot be regarded as the only parameter that governs the magnitude of the $G_0/R_n$ ratio. Indeed, Jacobsen & Hansen (1999) and Kustas & Daughtry (1990) have reported that differences in soil surface conditions and vegetation are likely to alter the slope in the regressions. A closer view of increasing $T_s$ from November – January (see Table 7.6) suggests that soil heat transfer in the Volta catchment area is controlled by $T_s$ rather than vegetation cover. Although the NDVI method is designed to remove, to some extent, zenith angle effects on the vegetation index derived, it is likely that some of the explanation for the low $R^2$ value is to be found here.

### 7.3.2 Diurnal $T_s$ Modelling

In the dry season, diurnal models of $T_s$ are important for a variety of reasons. Such information may be used to guide health and safety policy functions, and operational early warning systems for both crop harvesting and bushfire monitoring. Obtaining regional-scale temperature information is not easy in the Volta basin because of the sparse distribution of ground monitoring stations. This leaves remote sensing as the only practicable way of achieving this. Figure 7.11 shows an example of how the MODIS data could be used for this purpose. The figure tends to follow the sinusoidal model (see Equation 7.2), which is characterised by a steep rise in warming between 06:00am and 12:00 noon (10 K), which peaks and stabilises after midday followed by steady cooling until sunset.

In terms of hydrology, a useful example which applies diurnal thermal maps for water stress assessment has been shown by Viau & Jang (2005) over Southern Quebec in Canada. Combining diurnal-scale NDVI with NDWI (normalized difference water index), these authors derived a new vegetation index called the normalized moisture index (NMI) after which they plotted the moisture index against $T_s$ to examine trends in vegetation hydrothermal conditions. The NDWI is given by: (NIR-SWIR)/(NIR+SWIR). From their 2D trapezoid plots, Viau & Jang (2005) arrived at conclusions quite similar to the Volta example (Figure 7.3), in which they observed that well-watered vegetation was strongly correlated with high moisture index and depressed canopy temperature. The physical basis of this is that the difference in reflectance between the shortwave infrared (SWIR) and near infrared (NIR) bands expresses vegetation moisture content, knowing that the shortwave infrared (SWIR) band is sensitive to canopy water content in contrast with the near infrared (NIR) band (Tucker, 1980). The conclusion here is that remotely derived thermal maps are potentially useful data both for assessing water stress in the savannah Volta basin and for monitoring key environmental processes such as bushfires and carbon circulation.

### 7.3.3 *ET* Modelling and Interactions with Catchment Factors

From Figure 7.6, the average instantaneous heat fluxes (derived over the Tamale district) can be summarized as follows: net radiation ($R_n$) = 394 $Wm^{-2}$; sensible heat ($H$) = 276 $Wm^{-2}$; latent heat ($LE$) = 150 $Wm^{-2}$; and soil heat ($G_0$) = 50 $Wm^{-2}$, which when integrated over a diurnal cycle has been shown to compare well with examples shown in Figure 7.7 – 7.10. The models shown in Figure 7.10 particularly show a good correlation ($R^2$ = 0.79) between MODIS and ground measurements; the main discrepancy is sensor

overestimation of net radiation (~130 $Wm^{-2}$) towards sunset. This error may be due to several factors, among which include sensor calibration problems and the time difference between radiation measurement and sunset (~8hrs). Furthermore, uncertainties associated with the sinusoidal extrapolation may account for part of the observed error. However, the cumulative error margin (~40.268 W $m^{-2}$) for the full day appears to be consistent with published results. For example, Brata *et al.* (2006) have recently reported large deviations (53W $m^{-2}$) between satellite-based net radiation and ground measurements over the dry Southern Great Plains (SGP) in the USA. Jiang & Islam (2001) have also reported a difference between 28.9 - 35.3W $m^{-2}$ when they utilized AVHRR data over parts of the SGP. But of greatest significance is the diurnal *LE* (i.e. *ET*) prediction shown in Figure 7.12. The large error margin (>100 W $m^{-2}$) at sunset may be explained by factors such as poor sensor calibration at this time, weaknesses in the sinusoidal model by Bisht *et al.* (2005) or further approximations based on the evaporative fraction approach adapted from the original method by Bastiannssen *et al.* (1998). The general agreement between the model and observed values ($R^2$ = 0.88) may also explained by the sparseness of the observation series ($N$ = 14). These notwithstanding, the daily bias (22.4 $Wm^{-2}$) in relationship with published results such as Brata *et al.* (2006) and Jiang & Islam (2003) suggests that the approach is a reasonably quick and effective method for estimating regional energy balance in West Africa, which could be used for a number of studies including regional climate change, hydrology and agronomy.

The general (qualitative) agreement in the spatial organisation of *ET* and land cover in Figures 7.13 & 7.14 may be explained in a number of ways. First of all, relatively higher soil moisture status in clearly defined river valleys (see Figures 7.13d & 7.14) tends

to support withdrawal of soil water by riparian forests, which in turn promotes active transpiration processes in comparison with less vegetated areas including the Tamale district (Figure 2.2). Even at a coarse-scale (Figure 7.13 a-c), it is much easier to determine *ET* from the wet southern forest and woodland areas than the dry northern grasslands where it is difficult to distinguish among vegetation types. An important conclusion here is that in the Volta valley bottoms, *ET* is largely controlled by transpiration processes because of higher residual soil moisture (deep clayey soils), but in (shallow soil) upstream catchments, *ET* is generally controlled by $T_s$. Also, both high (e.g. Landsat ETM+) and medium-resolution sensors (e.g. MODIS) can reasonably measure these important catchment processes using the SEBAL method. As explained before, the observed differences in Figure 7.13 (a-d) are mainly due to differences in sensor characteristics. To examine the temporal variation in *ET* estimates, two images processed for November 2002 and 2004 were included in the analysis. Here, the spatial organisation of *ET* appears to be quite similar; particularly, in the Tamale district (north-western part of images). However, quite large differences occur in the southern-most forested river valleys and the north-eastern section (compare Figures 7.13 a&b). Why this happens is not very easy to explain without detailed field checks; however, errors in the modelling technique, vegetation changes in response to seasonal rainfall and environmental conditions at the time of satellite overpass may account for the observed discrepancies. Vegetation proliferation in response to rainfall (i.e. higher soil moisture withdrawal) appears to be a tangible reason, conscious of the fact that annual rainfall was generally higher in 2004 than 2002 (MSD, 2004).

In heterogeneous catchments *ET* relationships with NDVI and $T_s$ (Table 7.5) may not consistently follow theoretical concepts. For example, the sparsely vegetated surfaces (such as urban areas in Figure 7.13) are generally expected to be warmer; other things being equal, which should also result in elevated *ET* (e.g. Di Bella *et al.* 2000). However, such areas depict depressed *ET*. This may be explained by rapid evacuation of drainage water leading to soil moisture deficit for evapotranspiration. Another explanation is that in most urban areas in the tropics, the greater part of daytime radiant energy is absorbed by a wide variety of dark metallic, wooden or concrete roof top materials rather than being emitted, which probably represents a striking example of regional apparent thermal inertia (ATI). ATI may be defined as the ratio between surface albedo and the difference between the maximum and minimum diurnal temperatures of surface targets (Sabins, 1987). During the day, dark urban targets (low albedo) are likely to absorb more solar energy which could lead to elevated kinetic temperature and radiant thermal energy (Sabins, 1987). This probably results in instantaneous and/or diurnal depression of atmospheric vapour pressure. Thus, urban evaporation is likely to result from small open surfaces, which are also unaccounted for by both the sensor and the SEBAL energy balance method. The relatively poor distribution of vegetation cover within the urban areas (Figure 7.14) compared with the southern woodlands is also a good explanation why *ET* is low within areas of human habitation.

Consideration of Table 7.5 shows that the interaction between NDVI, $T_s$ and $R_{ah}$ ($R_{ah}$ = aerodynamic resistance for heat transport) produces the strongest effect on regional *ET* amount and distribution ($R^2$ = 0.66) and followed by NDVI-$T_s$-$R_n$ ($R^2$ = 0.63) (see Table 7.5b). As expected, the exclusion of $T_s$ in the analysis (Table 7.5a, Part III) most

significantly constraints the regression model ($R^2$ = 0.38), while the other variables remain fairly stable, as can be seen in the *F*-values of the ANOVA table (Table 7.5c). Similarly, the exclusion of NDVI in the analysis appears to depress the correlation coefficient; however, the NDVI may not be as influential as $T_s$ (see Table 7.5b). The main conclusion here is that the interaction between temperature and vegetation constitutes the most influential factor which drives regional water loss over short temporal scales (e.g. daily to monthly). The next section discusses sensor effects on the organisation of key geophysical variables.

## 7.3.4 Sensor Characteristics and Effects on Measured Variables

### *7.3.4.1 Sensor Effects on $T_s$*

Analysis of Tables 7.6 - 7.8 shows that the average range of temperature measured by the MODIS sensor instrument was 304.4 - 306.2 K compared to 312.5 - 318.9 K by the AATSR sensor. The MODIS sensor showed a very strong correlation ($R^2$ = 0.89) with ground truth data (Figure 7.15) compared with its AATSR counterpart ($R^2$ = 0.44), which confirms that the MODIS sensor has a greater potential for measuring $T_s$ in the Volta basin. This is exemplified by Table 7.9, which shows that the MODIS sensor has a smaller mean error margin (3 K) on the strength of ground observations compared with AATSR (8 K). Contrary to expectation, however, the AATSR appears to be more precise given its lower standard deviation of error (1.95 K) compared with MODIS sensor (2.5 K). It is difficult to find a reason for this; however, their respective engineering design, sensor calibration and the satellite overpass time gap (~60 minutes) may partly explain the differences. It must also be noted that the observed differences are consistent with their engineering

design efficiency and published results. For example, comparing $T_s$ measurements from the MODIS and NOAA-14 sensors, Brata *et al.* (2006) recently observed a difference of 25 K within satellites overpass gap of 2 – 3 hours. Other technical factors may also explain the observed differences, e.g. sensor characteristics, atmospheric correction and the spectral response function of the thermal infrared channels (Brata *et al.,* 2006; Donoghue *et al.,* 2004; Goetz, 1997). The last point appears to be a convincing one because the design characteristics of most optical sensors possess limited capabilities to measure the "skin" temperature of bare soils (Sobrino & Jiménez-Muñoz, 2005; Prata, 2002). It is important to note that the results displayed in Table 7.8 encompass soil surface temperatures in contrast with radiant temperature measured by the sensors. Theoretically, these two measurements are quite different but are often compared for the sake of practicality (McManus, 2004; Sabin, 1987). Sobrino & Jiménez-Muñoz (2005) have reported that over rough vegetated surfaces, a wide range of differences (such as the above) are not unexpected between radiant and soil surface temperatures. Indeed, the infrared channels of MODIS and AATSR can be considered as well suited to measure surface temperatures but only to the degree of their design efficiency, which is rarely better than 3 K (Salomonson *et al.,* 2002). The plot in Figure 7.16 is an attempt to investigate how well the MODIS and AATSR sensors are correlated. The figure shows that both sensors are very poorly correlated ($R^2$ <0.01) in terms of measuring $T_s$ over the study area. As noted above, differences in sensor design and calibration may explain the lack of correlation between the two sensors. It must also be noted that, whereas MODIS was designed to measure land surface temperature, AATSR was designed primarily, to measure sea surface temperature. Given the above analysis, it can be concluded that the MODIS

sensor has greater capabilities of measuring surface temperature compared with its AATSR counterpart over complex savannah catchments, which may be explained by factors such as differences in sensor design and calibration as well as peculiarities of field conditions at the time of satellite overpass.

### *7.3.4.2 Sensor Effects on NDVI*

Both Figure 7.2 and Table 7.6 show that the AATSR sensor generally measures a shorter range on the NDVI scale, which may be due to the sensor's narrower bandwidth (see Table 3.1, Section 3.2 of Chapter 3). Table 3.1 confirms that the red (*R*) and near infrared (*NIR*) bands of MODIS are more clearly separated than those of AATSR. Whereas the MODIS *R* band has a bandwidth of 0.50 μm (see Table 3.1 for detailed sensor characteristics), the AATSR *R* band has a bandwidth of 0.20 μm. Also, the MODIS *NIR* band has a bandwidth of 0.35 μm while the AATSR *NIR* has a bandwidth of 0.20. Previous studies (e.g. Brata *et al.*, 2006; Goetz, 1997; Huete, 1989) have shown that multiple widths of the reflective solar bands are closely related with the spectral sensitivity of green vegetation. Sabins (1987) has further shown with a range of spectral reflectance curves that the percentage of incident energy reflected by vegetation is a function of wavelength, which also explains why vegetation reflectance increases significantly over the *NIR* region. The wider the *NIR* region, the more variable vegetation discrimination can be over large areas. It should be noted, however, that the primary purpose of the AATSR sensor (unlike MODIS) is measurement of global sea surface temperature (Prata, 2002; Prata, 1994). Thus, the optical range of the AATSR sensor has not been as fully calibrated and widely validated on land compared with MODIS (Brata *et al.*, 2006). The conclusion

here is that though MODIS and AATSR may both derive reasonable $T_s$ measurements over sparsely vegetated surfaces; however, their NDVI products are not equivalent because of differences in their solar bands, sensor and inter-calibration, and atmospheric correction. In this case, the AATSR may not be as suitable as MODIS for hydrological applications. However, further research would be needed to verify this conclusion especially using the AATSR Level 2 product.

### *7.3.4.3 Sensor Effects on ET*

From Table 7.6, the AATSR sensor underestimates *ET* by about 32% in comparison with the MODIS sensor. Since data from both sensors have been processed in the same way, a plausible explanation for this observation is aggregated errors from the main independent variables closely related with the *ET* model namely, $T_s$, NDVI and net radiation ($R_n$). Whereas the MODIS instrument measures regional *ET* value of approximately 1.48 mm $day^{-1}$, the AATSR sensor measures only 0.47 mm $day^{-1}$, which represents a difference of 1.01 mm $day^{-1}$. Thus, for one AATSR pixel (1x1 km), the cumulative difference in water loss is approximately $2.45*10^6$ MJ $km^{-2}$ day; assuming that 1.0mm $day^{-1}$ evaporation is equivalent to 2.45MJ $m^{-2}$ $day^{-1}$. Over very large areas, a large amount of moisture loss could be underestimated.

In Section 7.2.5, remotely measured *ET* was assessed qualitatively. To better understand sensor differences, a quantitative evaluation is pursued here using calculated values from the Penman-Monteith method, ground (scintillometer) observations and Landsat ETM+ spatial measurements as the main sources of validation. The range of estimated *ET* values for the Tamale district based on the Penman-Monteith method (in

2004) was 1.5 – 4.8 mm $day^{-1}$ (see Figures 4.2 & 4.3 of Chapter 4; Section 4.4.1). It must be noted that sensor evaluation based on point data may not always be the most convenient way (El Maayar & Chen, 2006). However, this can still provide a good way of comparing different sensors against an independent indicator in the absence of extensive field validation at the time of satellite overpass. Based on the geographic extent of (x-y coordinates) of the Tamale area, a linear interpolation model (see Section 4.4.1) was derived covering an approximate area of 70$km^2$. The mean *ET* value for Tamale, geo-referenced from MODIS and AATSR *ET* maps (see Figure 7.13) was compared. Here, both sensors underestimated regional *ET* by an average of 2.0 mm $day^{-1}$. This large difference may be attributed to the difference in pixel size (point spatial function).

Scintillometer observations (ZEF, 2004) extracted from Figure 7.8 were used as further basis for comparison. In this case, the daily average latent heat for December 2001 (i.e. 50.87W $m^{-2}$) was converted into daily evaporation units; the result being 1.79 mm $day^{-1}$. In this example too, the MODIS and AATSR sensors underestimated *ET* for the region by about 1.29 mm $day^{-1}$. The last evaluation method utilized spatial estimates from the Landsat ETM+ sensor based on the same SEBAL energy balance modelling approach. Figure 7.17 displays results from the regression models.

Although spatial mismatch remains a difficult issue when validating medium-scale measurements using high resolution sensor data (El Maayar, 2006), Figure 7.17 reveals a reasonably good agreement between Landsat ETM+ and MODIS ($R^2$ = 0.71) in comparison with AATSR ($R^2$ = 0.13). Careful consideration of Table 7.6 and Figure 7.17 shows that the discrepancy of *ET* measured from the AATSR sensor could be approximately 0.6 mm $day^{-1}$ compared with the MODIS instrument (0.3 mm $day^{-1}$). This

seems to confirm the initial suspicion (Section 7.2.5) that (AATSR) errors may have aggregated from the measurement of the model intermediate parameters such as $T_s$, NDVI and net radiation ($R_n$). Why this happens may be related to problems in sensor calibration for land targets, atmospheric correction and/or poorly derived coefficients for the NDVI algorithm. The last point has indeed, been speculated by an AATSR expert (Adam Keith (ESA), personal communication, February 2006). Table 7.10 presents a summary of *ET* measurements from different methods discussed in this chapter.

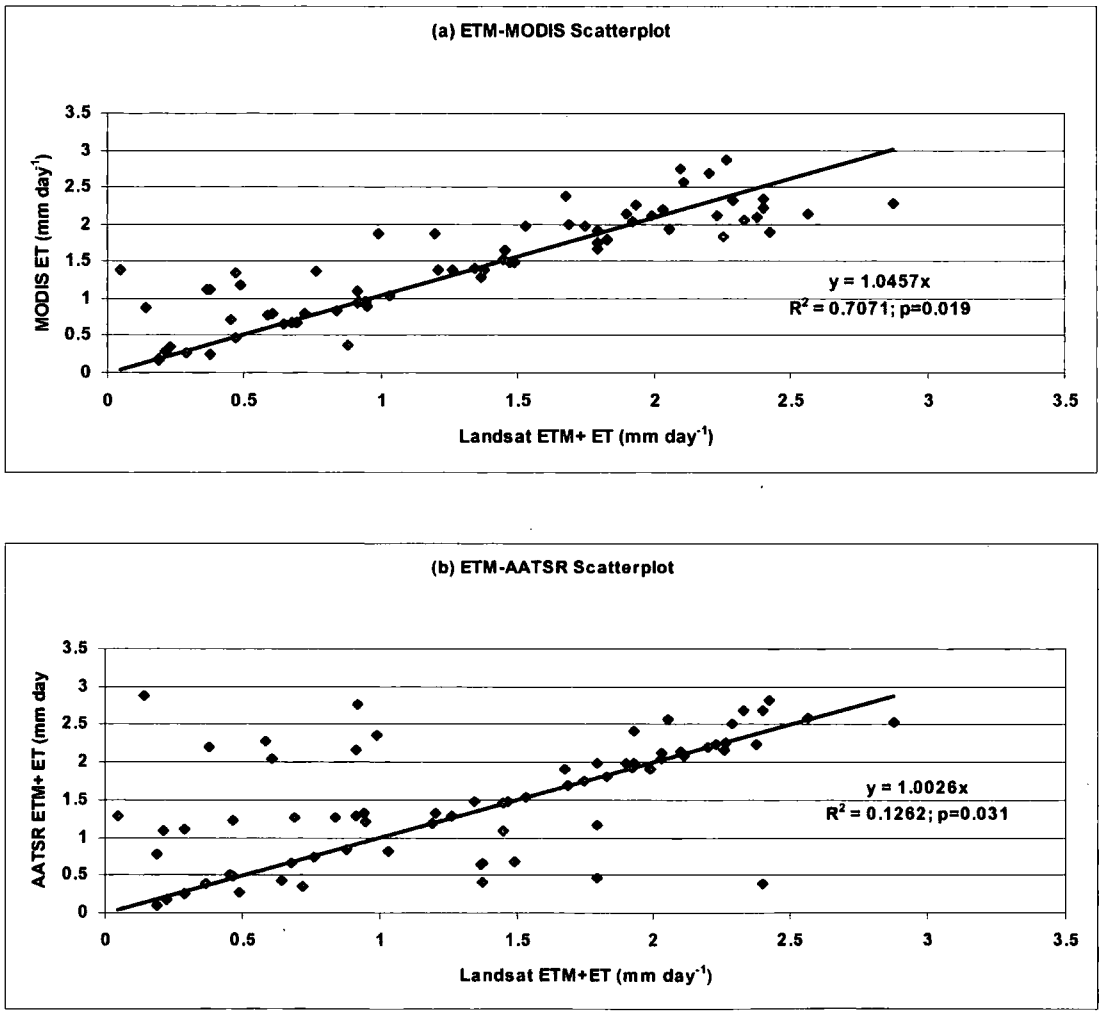


Figure 7.17 Regression models between ETM+ *ET* and (a) MODIS; y = 1.0457x; $R^2$ = 0.7071, $p$ = 0.019; RMSE = 0.3359; and (b) AATSR: y = 1.0026x; $R^2$ = 0.1262, $p$ = 0.031; RMSE = 0.6211. Note: $N$=71 pixels because analysis covered the Tamale district where validation data is available. The sampling procedure is described in Chapter 3 and explained in Section 7.2.4.

Table 7.10 Summary of measured *ET* (mm $day^{-1}$) using different methods and data sets (Tamale district)

| Method | Scale | Range | Mean | Standard deviation |
|---|---|---|---|---|
| Penman-Monteith | Local (Tamale) | 1.53 – 4.87 | 3.90 | 0.66 |
| Scintillometer | Local (Tamale) | - | 1.79 | - |
| Landsat ETM+ | Regional | 0.15 – 2.93 | 2.10 | 0.42 |
| MODIS | Regional | 0.05 – 2.83 | 2.07 | 0.37 |
| AATSR | Regional | 0.01 – 2.09 | 1.21 | 0.86 |

Considering Figure 7.17 and Table 7.10, the MODIS sensor has much greater potential for measuring energy and water fluxes over the savannah region than its AATSR counterpart. Indeed, the AATSR sensor may underestimate *ET*, which means for hydrological applications, users have to apply the product with caution. It may be necessary to apply further calibration corrections to the solar bands of the AATSR Level 1 product in order to derive an accurate vegetation cover map.

## 7.4 Summary

This chapter has discussed the spatial organisation and interrelationships of surface fluxes over the Guinea savannah landscape in West Africa. The results were derived from energy balance modelling and up-scaling methods driven by radiometric measurements from satellite sensors. Evaluation of the model results was achieved based on published data, field observations, detailed satellite measurements and Penman-Monteith estimates.

The capabilities of the MODIS and AATSR data to parameterize the SEBAL energy balance algorithm have been evaluated. It has been shown that satellite-derived instantaneous net radiation ($R_n$) can not only be used for modelling diurnal cycles of net radiation, but also for deriving diurnal *ET* using improved empirical models. Correlations of $R^2 = 0.66$ were found between *ET* and key independent variables such as NDVI, surface

temperature ($T_s$), aerodynamic resistance to heat transport ($R_{ah}$) and daily net radiation ($R_n$) revealing the complexity of their feedback responses and interrelationships with regional water loss over short time (daily to monthly) scales. It has also been demonstrated that the MODIS sensor particularly estimates daily *ET* with strong spatial correlation of $R^2 = 0.71$ with Landsat ETM+ estimates, but underperforms with large deviations (~2.0 mm $day^{-1}$) when evaluated against point observations e.g. the Penman-Monteith method and scintillometer observations, mainly because of scale mismatch.

On the question of sensor inter-comparison, it can be concluded that the MODIS sensor has much greater potential to derive reasonable estimates of key surface fluxes, e.g. $T_s$ and $R_n$ over sparsely vegetated surfaces than AATSR. The AATSR sensor potentially underestimates both NDVI and regional *ET*, probably because of differences in the visible and near-infrared bands and sensor calibration.

# Chapter 8

# Improved Data Management Tools for Driving Hydrological Models in the Volta Basin

## 8.1 Introduction

The first part of this chapter uses the *ET* model to demonstrate how it may be used to predict runoff. This is followed by an analysis the sensitivity of flow to declining scenarios of biomass volume. The second part deals with development of improved data assimilation methods required for driving low-data-input hydrological models such as the modified Pitman model (Hughes *et al.*, 2006). This section also includes a treatment on the key limitations, challenges and prospects of the modelling approach.

In the savannah Volta basin, estimation of fluctuations in surface flows (Figure 1.1 in Section 1.1.2 of Chapter 1) is a major problem because of the scarcity of spatially-derived hydrometeorological data (Jung, 2006; Washington *et al.*, 2006). The most important concern here is quantification of inflows to the Volta Lake, on which local communities depend for energy, agriculture and water supply. Spatial rainfall estimates, data assimilation methods and availability of calibrated low-data-input hydrological models are critical ingredients for lake-flow prediction (Gan *et al.*, 1997); the potential of remote sensing to help address some of these issues constitutes the main concern of this chapter.

## 8.2 Regional Runoff Modelling

### 8.2.1 Assumptions & Analytical Framework

Within vegetated river basins, runoff may be generated in a number of ways as shown in Figure 8.1. Although the figure represents a simplification of runoff processes in tropical savannah regions, it still exemplifies the key flow processes within large river basins on basis of the generalized water balance equation given in Equation 3.3 (Section 3.8 of Chapter 3).

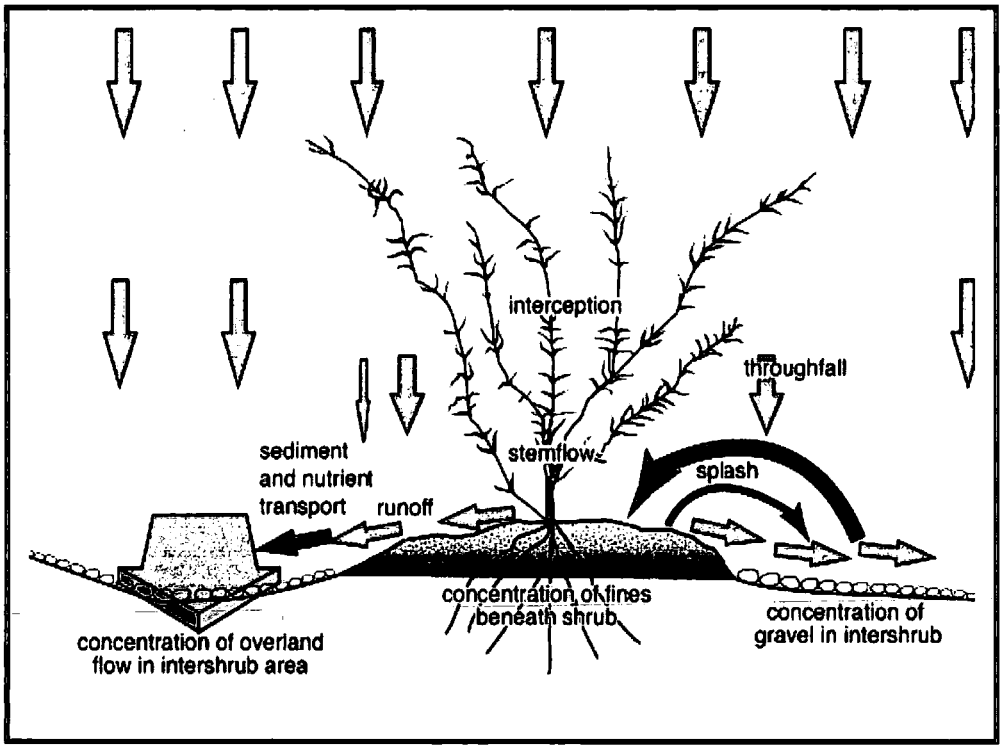


Figure 8.1 Basic interactions between vegetation and water movement over vegetated landscapes. Source: Modified after Wainwright *et al.* (2000).

Figure 8.1 is linked with Equation 3.3 in the sense of their common emphasis on rainfall as the principal driver for basin-wide flow, in which case key processes such as soil moisture storage are assumed to be constant over an annual time scale (Shaw, 1994). The arrows in the above figure represent the direction of key flow processes

such as interception, stemflow and overland flow (runoff), which may occur over instantaneous to daily time periods (Wainwright *et al.*, 2000). Often, this is not the case for groundwater seepage because that may take several days. Over large tropical basins such as the Volta, groundwater seepage may be assumed to be constant over monthly to annual time scales (Kesse, 1985). Following this, runoff ($Q$) can be considered as a function of rainfall ($P$) and evapotranspiration ($ET$), assuming that soil evaporation is negligible over the vegetated areas during the dry period (November – March). Liu *et al.* (2002) have shown in China that soil evaporation may be reduced by 30% in crop fields covered by tasselled maize (leaf area index ~ 4.8). In the southern part of the study area where ground cover is dense (see Figures 7.2 and 7.15), soil evaporation may probably be much lower. Given this background, runoff in November 2002 was estimated on 1 x 1 km basis following the relationship: $Q = P - ET$; where all the units are in millimetres (mm) and spatial rainfall estimates ($P$) are derived from the interpolation of November rainfall observed from ground stations located upstream of the Volta Lake (Figure 8.2a); the main study area is shown as an inset in Figure 8.2b. The above period was chosen because of the availability of daily rainfall records, satellite images (from which $ET$ estimates could be derived) and measured discharge data for validation purposes.

On the basis of the Surface Energy Balance Algorithm for Land (SEBAL) method (see Section 5.2 of Chapter 5), an estimate of distributed $ET$ was derived from a MODIS image dated 29$^{th}$ November 2002. This image was selected in order to coincide with available rainfall data (November 2002) for modelling purposes. This output was integrated over a 30-day period following methods described by Tasumi *et al.* (2000) and Bastiannssen *et al.*, (1998a), which was found to be similar to another MODIS scene acquired on 13$^{th}$ November 2004. The main reason why the 2004 image

was chosen was to solve the problem of unavailable cloud-free MODIS scenes for other dates in November 2002 or 2003.

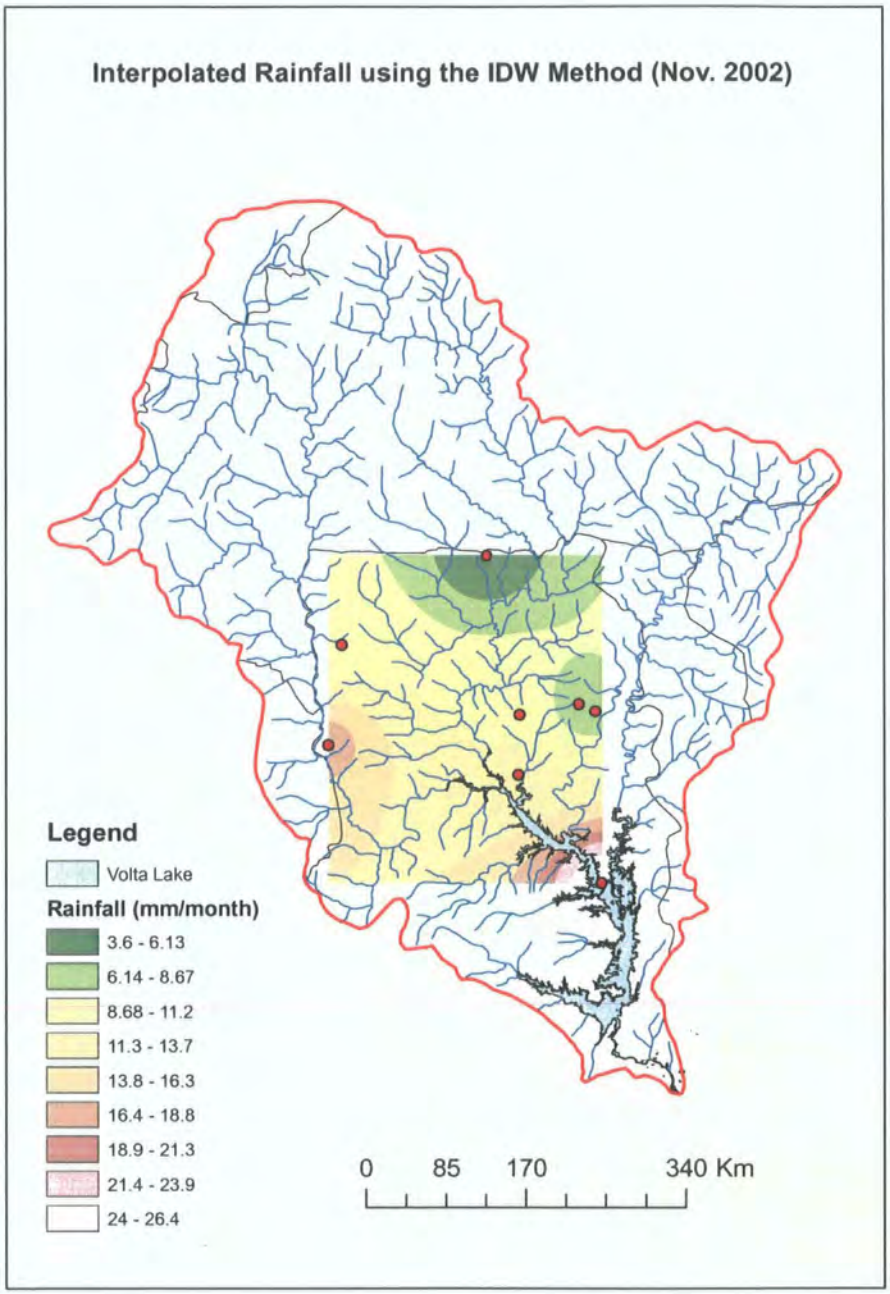


Figure 8.2a Interpolated (IDW) rainfall (mm) for November 2002 covering observation stations (shown as dots) upstream the Volta Lake. Stations lacking full daily observations (see Figure 8.2b) were imputed from time-series monthly records covering 1961 – 2000.


Figure 8.2b The main study area is shown as an inset within the spatial rainfall area. In the absence of reliable data for the Digma and Tijo stations, the average of a 40-year record for November was applied as a substitute (see Table 8.1 for further details).

The NDVI ratio was calculated using Equation 5.13 (Section 5.2.2) for the 29th November image and assumed to be constant over 30 days. November is the rainiest month in the dry season in the Volta basin, but daily rainfall records are not always available. Unreliable rainfall data from two stations (marked with asterisks in Table 8.1) were substituted with a long-term average (1961 – 2000) for November 2002, after which data from a total of eight stations (Figure 8.1) were interpolated (1 $km^2$ pixels) to cover the study area using the inverse distance weighted (IDW) method. Where the ground station networks are few and their location distances have no spatial correlation, as in this case, the IDW method may produce more accurate results than co-kriging (e.g. Thiessen polygon) and spline methods (Oliver, 1990) (see Section 3.10 of Chapter 3 for more details). Wilk *et al.* (2006) found that the IDW approach was more successful than the co-kriging method when estimating rainfall spatially over the Okavango basin in Southern Africa. Details of the interpolation procedure, data processing and manipulation of data formats using MATLAB and ARC-GIS functions are described in Chapters 3. Section 8.2.2 presents spatial estimates of runoff and their sensitivity to various scenarios of vegetation decline, which is followed by a discussion and evaluation in the context of published and local information.

Table 8.1 Names of rainfall stations, their geographic locations and aggregated observations for November 2002

| Local rainfall station | Lon. (decimal degrees) | Lat. (decimal degrees) | Mean rainfall (Nov) (mm) |
|---|---|---|---|
| Yendi | 0.09 | 9.43 | 8.30 |
| Tamale | 0.82 | 9.40 | 10.40 |
| Bole | -2.65 | 9.11 | 17.30 |
| Wa | -2.52 | 10.07 | 9.20 |
| Navrongo | -1.13 | 10.93 | 3.60 |
| Kete Krachi | 0.03 | 7.78 | 26.40 |
| *Tijo | 0.25 | 9.50 | 7.35 |
| *Digma | 0.83 | 8.82 | 12.35 |

*Gaps in daily records were substituted with time series (1961 – 2000) monthly records. The names of these stations are indicated on Figure 8.2b.

### 8.2.2 Results

Figure 8.2 shows interpolated rainfall estimates for November 2002 based on the ground station data presented in Table 8.1. Table 8.2 also displays a statistical summary of the 30-day *ET* result (Figure 8.3) and runoff response (Figure 8.4), which was calculated as the difference between the spatial rainfall estimates displayed in Figure 8.2 and the *ET* output in Figure 8.3.

Table 8.2 Descriptive statistics of regional *ET* (top row) and runoff (*Q*) (bottom row) for the Kalarakun catchment of the Volta basin (all units are in mm month$^{-1}$).

| Period | Parameter | Minimum | Maximum | Mean | Standard Deviation |
|---|---|---|---|---|---|
| November 2002 | *ET* | 3.85 | 135.00 | 86.27 | 16.69 |
| | *Q* | -29.48 | 12.58 | 0.0 | 39.09 |
| *November 2004 | *ET* | 0.0 | 123.93 | 38.07 | 45.24 |
| | *Q* | -12.75 | 25.74 | 0.0 | 65.12 |

*Note: November 2004 image data was used mainly because of the absence of cloud-free scenes for similar dates in 2002 and 2003.

In order to understand whether changes in total savannah biomass may influence the quantity of runoff, a sensitivity experiment was carried out using the NDVI ratio as a surrogate metric for vegetation density. Using MATLAB-based processing functions, NDVI value for each pixel reduced (depreciated) in 10% increments in the range of 10 – 80% were run against predicted runoff (Figure 8.4); the test results are shown in Table 8.3. Similar to Table 8.2, the NDVI was calculated from the MODIS scene dated 29$^{th}$ November 2002 was assumed to be constant over 30 days. The descriptive statistics of the NDVI product are as follows: minimum = 0.207, maximum = 0.811, mean = 0.519 and standard deviation = 0.0328.

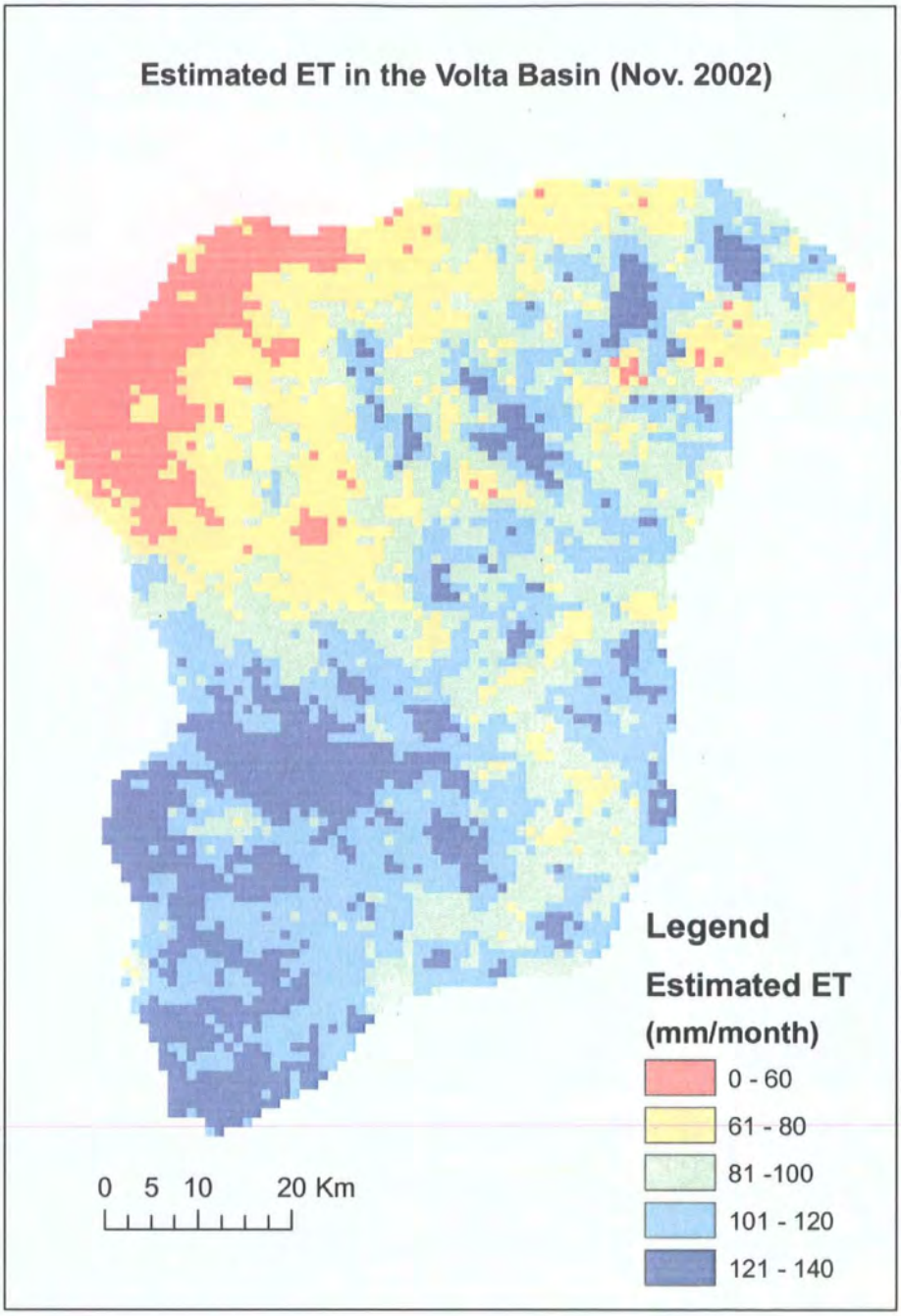


Figure 8.3 *ET* estimates for November 2002 (Kalarakun Volta catchment) derived from 1x1 km MODIS L1B image acquired on 29th November 2002. As expected, the Tamale district (north-west part of image) displays the lowest estimates of *ET*. Note: This map shows monthly aggregated *ET* values derived in the same way as the examples shown in Figure 7.13.

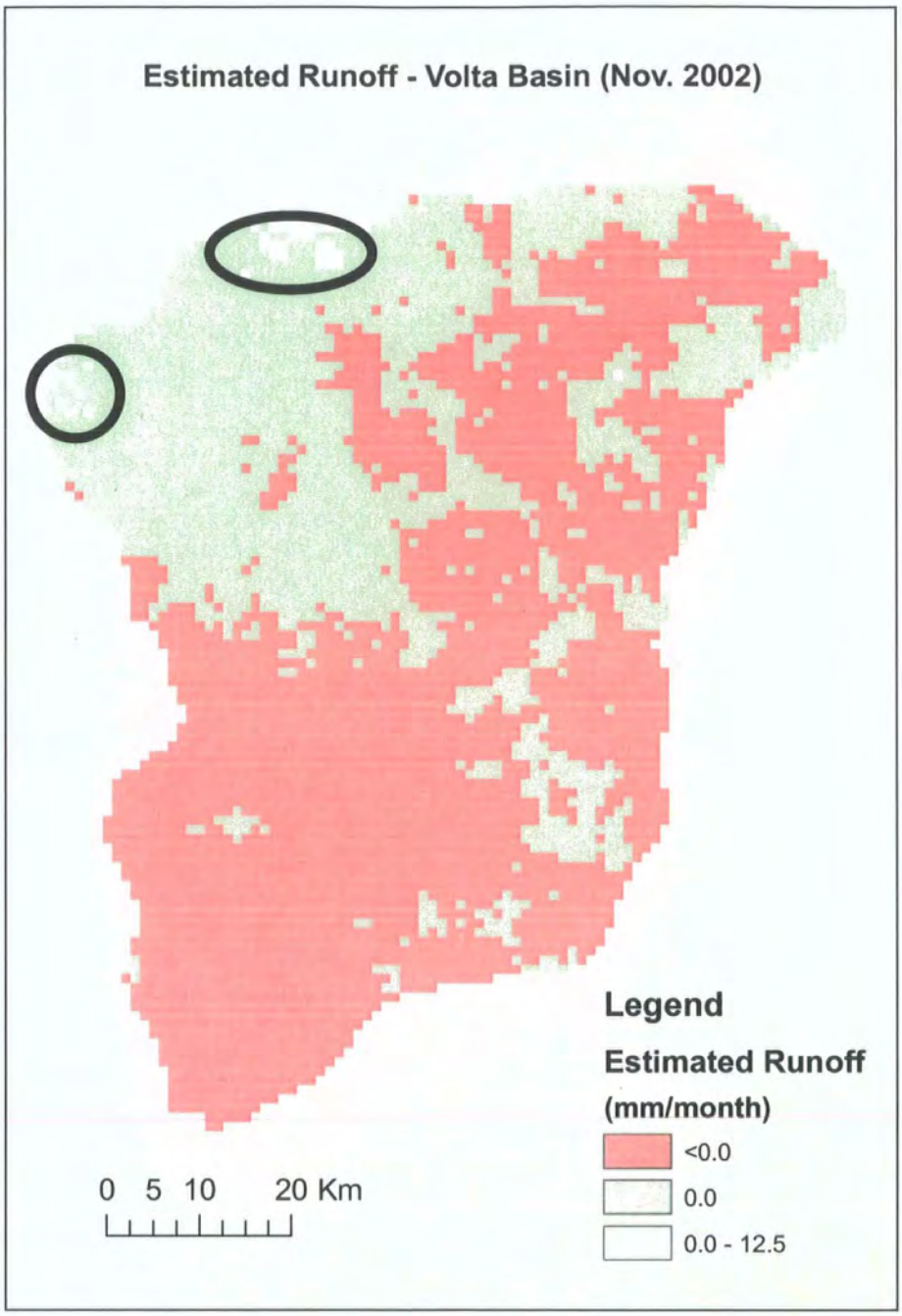


Figure 8.4 Spatial estimates of runoff in the Kalarakum Volta catchment area. As expected, runoff was negative or zero for most pixels of 1km$^2$, except the less vegetated Tamale airport area (north-western corner of the image). Note: The few pixels with positive runoff in the Tamale district are marked with black circles.

Table 8.3 Sensitivity of runoff (mm) to decline in vegetation density using NDVI as a surrogate metric.

| % NDVI depreciation | Absolute range of NDVI values | Minimum runoff | Maximum runoff | Mean runoff | Standard deviation |
|---|---|---|---|---|---|
| 10 | 0.18 – 0.72 | 0.0 | 126.05 | 0.0 | 21.46 |
| 20 | 0.16 – 0.64 | 0.0 | 126.21 | 0.0 | 21.44 |
| 50 | 0.10 – 0.40 | 0.0 | 126.87 | 0.0 | 21.34 |
| 60 | 0.08 – 0.32 | 0.0 | 127.20 | 0.0 | 21.29 |
| 70 | 0.06 – 0.24 | 0.0 | 127.63 | 0.0 | 21.22 |
| 80** | 0.04 – 0.16 | $-3.38*10^6$ | $1.76*10^6$ | $-5.10*10^5$ | $7.0*10^5$ |

**The model is ineffective when the entire catchment is reduced to bare soil (i.e. maximum NDVI<0.2) thus, result of 75% NDVI reduction was found to be similar to 80%. Note: Only a few pixels in the Tamale district predict positive runoff with an extreme value of 127 mm; there is no runoff for over 99% of the basin because rainfall is very limited in November.

### 8.2.3 Discussion

Although Figure 8.2 shows a sparse coverage of rainfall stations, the interpolated results appear to follow expected trends of decreasing rainfall along a latitudinal gradient from south ($8^0$) to north ($10^0$). Here, interpolated rainfall tends to follow vegetation distribution in terms of density and type (see Figure 7.2, Chapter 7). In the dry winter months (November to March) when rainy days are few, levels of rainfall are low (Table 8.1) and precipitation intensities are low, interception, storage and evaporation from plant canopies may be considered as the most dominant processes in relation to throughfall, stemflow and runoff (Figure 8.1) (Shaw, 1994). Similarly, soil evaporation can be considered to be more dominant than infiltration over un-vegetated parts of the catchment area (Agyare, 2004). This probably explains why the simple rainfall-runoff model predicts that runoff is absent for >46% of the catchment (e.g. Tamale district) in November. Measured runoff over the Tamale district (Figure 8.5) closely agrees with current synthesis (Figure 8.4); both results suggest that runoff is minimal or absent ($Q = 0.0$) throughout the dry period.

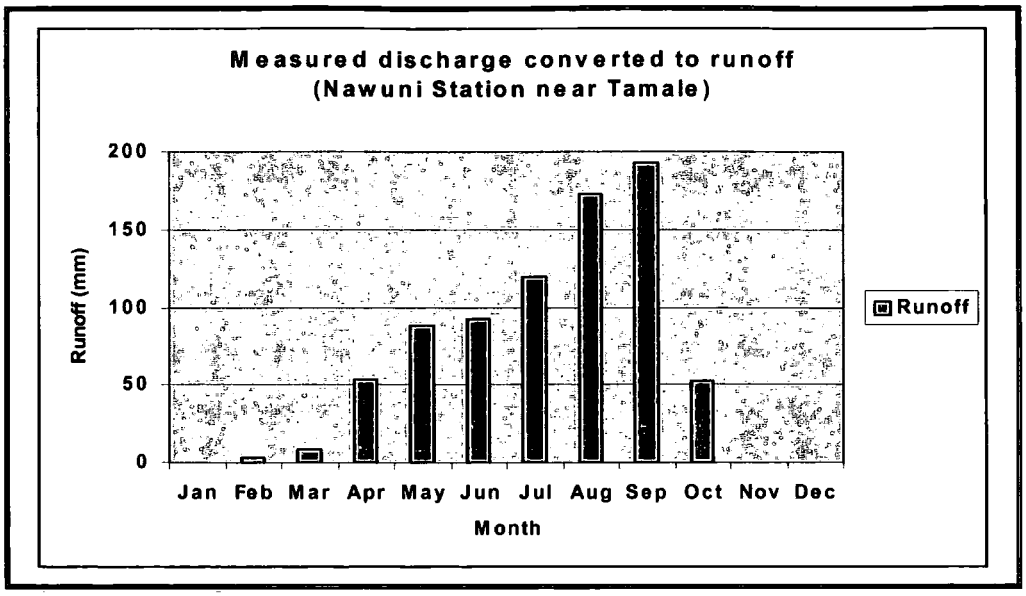


Figure 8.5 Observed runoff over the Tamale district (savannah Volta) for a 15-year period from 1985-2000. This data was extracted from Figure 2.14c of Section 2.2.4 in Chapter 2.

From Figure 8.4, >53% of the catchment is predicted as having experienced "negative" runoff (<0.0) probably because of model simplification and elevated *ET* inputs, which may have resulted from aggregating instantaneous *ET* to daily, and daily to monthly output. As noted in Section 8.2.1, several boundary conditions (e.g. constancy of soil evaporation) were set in order to operate the model (Equation 3.3). In this case, the absence of a soil evaporation component particularly limits the performance of the model. It is significant to note, however, that "negative" runoff is predicted over the more vegetated areas, particularly the southern parts of the area (Figure 8.4). This may be explained in two ways: first, the southern parts remain wet in early November, which may indicate soil moisture availability to sustain evapotranspiration. Secondly, the area is covered by deep-rooted woodlands and riparian forests (see Figure 7.2); extensive root anatomy has potential to facilitate groundwater abstraction (though not considered in the model) can still play a significant role in transpiration processes. Both Figures 8.3 and 8.4 show an expected inverse relationship between *ET* and runoff.

In simple quantitative terms, a high *ET* input to the model would depress surface flow (model output) when rainfall recharge is minimal; this appears to describe the conditions of the study area in November very well. Research by Roberts (2000) has shown that stomatal conductance, hydraulic conductivity and water uptake is stronger in areas covered by woody vegetation than in grasslands. Apart from canopy temperature, the above provides additional explanation why a sharp contrast exists between spatial estimates of *ET* and runoff. Runoff is positive (1 – 12.5 mm) over the north-western sub-catchments in Figure 8.4, which incidentally, is the location of the Tamale Airport and Military Air-force Base. Why runoff is highest in this location may possibly be due to poor drainage or discharges from large water supply reservoirs. Since the model does not account for direct reservoir evaporation, the above estimate is to be expected. Another important question is how streamflows and groundwater recharge occur in the dry season. In West Africa, stream desiccation is a common occurrence in the dry winter months (Jung, 2006). In the study area, however, perennial streams have been observed while carrying out field measurements (vegetation, soil and water measurements) in support of this research (Chapter 3). Apart from this, flows in the main river channels are not uncommon (see Figure 7.13c). If runoff is largely absent in the dry season, streamflows are probably due to discharge from groundwater sources (Ajayi, 2004), which requires further study. It is particularly important to know how this fits into the widely held view that groundwater remains the only source of river flow in most West African catchments (Ayibotele, 1993; Kesse, 1985).

Over large river basins where precise quantification of vegetation density (total biomass) is not always possible, the NDVI is a useful metric that may be used as an approximation (up to about NDVI = 0.8) for total biomass: see Gamon *et al.* (1995) for

example. Boulain *et al.* (2006) have also shown that temporal losses of Sahelian vegetation increases surface runoff, which agrees with the widely accepted view that depression in plant biomass may directly result in increased surface runoff (Roberts, 2000).

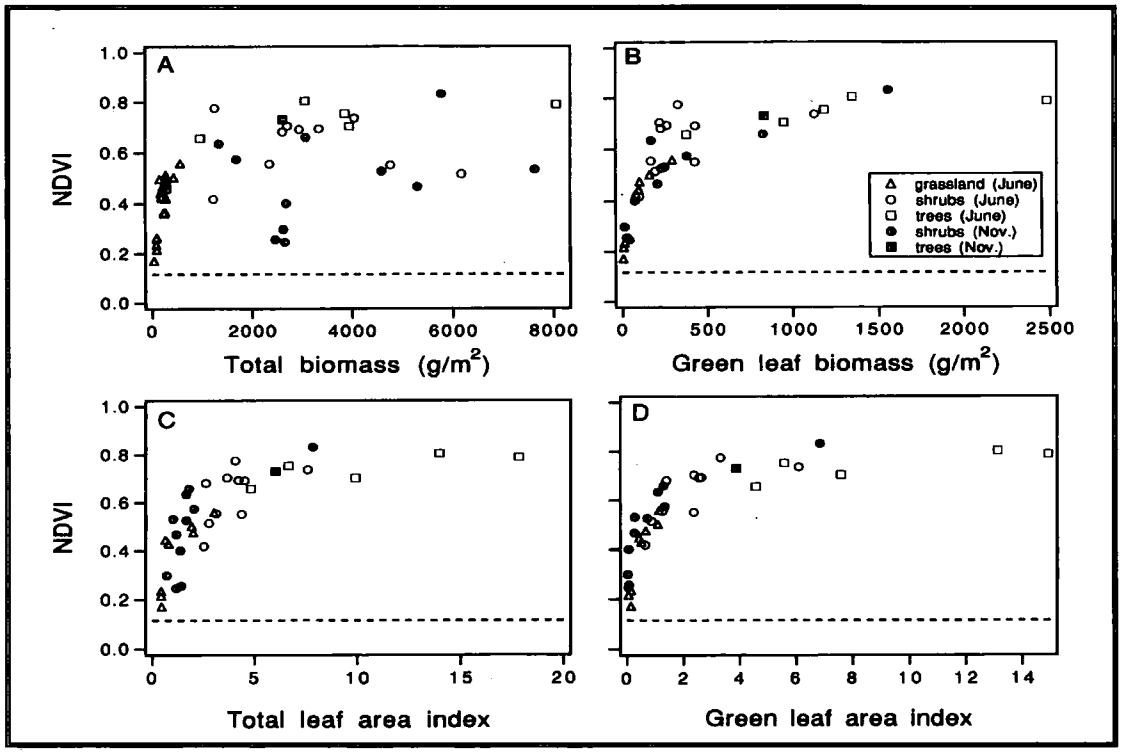


Figure 8.6 Relationships of NDVI to total biomass (A & B) and LAI (C & D) for grassland, trees and shrubs in California at different seasons; the dashed line represents NDVI for bare soil. Source: Gamon *et al.* (1995)

This hypothesis is investigated in the Volta study area and the results are shown in Table 8.3. Although the runoff model has boundary conditions that assume constancy in key variables such as soil moisture and deep drainage, both Table 8.3 and Figure 8.7 reveal useful information about runoff response in the low flow period, which can be relevant for basin planning. For example, the maximum runoff estimates (~126 mm month$^{-1}$) are large and suggest that runoff could exceed infiltration and evaporation

during peak flows, which may result in localised flooding in the Tamale district. Also, calibration of the NDVI-biomass model over an annual cycle may have the potential to be used to indicate possible changes in flow patterns.

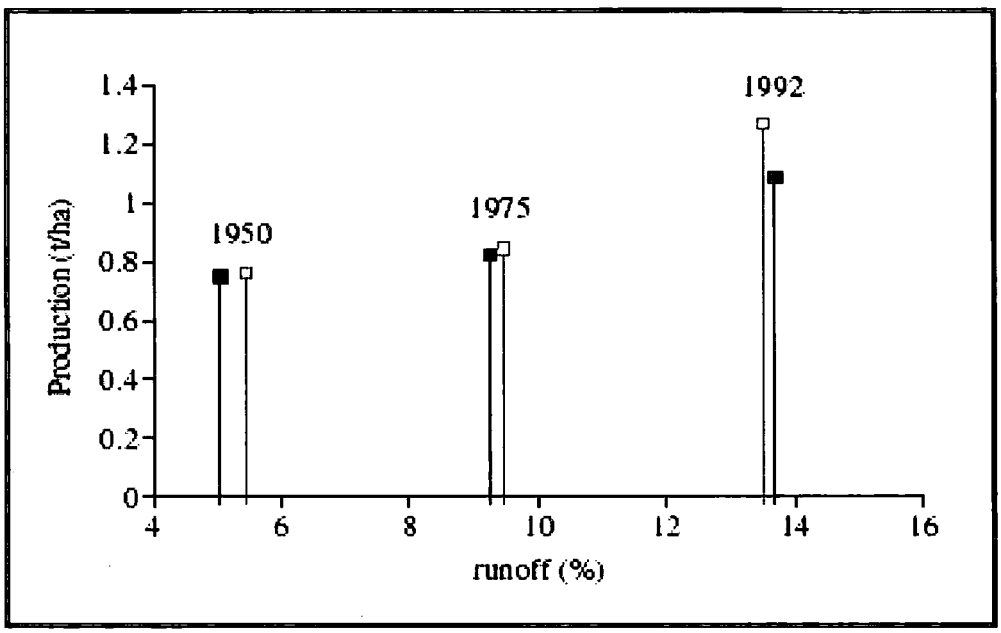


Figure 8.7 Land use uptake of total biomass (t $ha^{-1}$) (left to right) versus seasonal runoff coefficient (% of total rainfall) in the Wankama catchment (180$km^2$) in eastern Niamey (West Africa); the black and grey squares represent rainfall conditions for 1992 and 1997, respectively. Source: Boulain *et al.* (2006)

Table 8.3 further shows that the model begins to predict runoff when the NDVI value becomes less, particularly within the 0.4 – 0.7 range. From Figure 7.2 (Chapter 7), this NDVI range represents a variety of savannah land cover types, e.g. mixed clusters of grasslands, woodlands and riparian forests. It is not easy to derive total biomass from the NDVI method. However, linking Table 8.3 with Figure 8.6 (similar vegetation types from different locations) provides quite useful information on biomass type and volume. For example, an absolute drop of NDVI from 0.6 to 0.4 is represented by 20 – 50% reduction in Table 8.3, which when related with the plot in Figure 8.6A, shows an approximate loss of 2 kg $m^{-2}$ (i.e. 2 tonnes $ha^{-1}$) of shrub vegetation. It can also be seen

from Figure 8.7 that about 0.4 tonnes loss of land cover may lead to approximately 0.8% increase in runoff per year, which means an estimated loss of 2 tonnes of Volta savannah (preceding analysis) is likely to increase annual surface runoff by about 4%, assuming that rainfall conditions remain stable for two decades.

It is not easy to support such biomass-flow results with locally published data; however, the above synthesis shows that remote sensing may have operational value for detecting flow response to vegetation changes in West Africa using the NDVI ratio as a metric. In the case of the Volta basin, it is worth noting the existence of a vegetation density threshold (e.g. NDVI<0.2), beyond which the water balance model may not make any meaningful predictions (see bottom row of Table 8.3). At this point, the model probably assumes the complete absence of vegetation (see Figure 8.5), which means that rain would be transported entirely as runoff, precluding other key processes such as soil evaporation, infiltration and soil moisture storage. Given that soil temperatures are very high (see Table 7.8, Chapter 7) and savannah vegetation is generally sparse, a more sophisticated model is needed to model soil evaporation in order to improve the current results. This is particularly important knowing that below a catchment NDVI average of 0.2, the regional water balance model may not be a useful approach for detecting savannah runoff; the model probably operates better if NDVI average is >0.5.

In summary, runoff is practically absent over most parts of the savannah Volta basin during the dry season, except a few un-vegetated areas in the Tamale district. It is notable that runoff response in this region appears to be strongly dependent on biomass density, which can be represented by the NDVI ratio. Unfortunately, the current synthesis is limited by a number of parameters, of which lack of high quality spatially distributed rainfall estimates is the most critical; how this can be addressed is

one the principal objectives of Section 8.3. Over very large areas, several other parameters need to be integrated into a runoff model, for example, soil infiltration and soil moisture storage. The failure to discriminate vegetation types, the inability to calculate actual plant biomass from NDVI (assumed to be constant over 30 days) and the absence of an annual cycle of sensor data, are other important limitations; methods described in Section 8.3 are designed to help address these issues.

### 8.2.4 Annual Runoff Prediction Based on the *ET* Model

An important question is whether the above *ET* model can be used to estimate annual runoff in the study area. This is achievable; however, two key issues need to be addressed to obtain good results. First of all, monthly estimates of *ET* need to be derived from aggregated daily satellite images. This is not always possible because of the operational constraints of most satellites, the presence of cloud-cover and the cost of obtaining and processing large amounts of image data. The most feasible option is, to approximate monthly *ET* values from a few cloud-free scenes obtained within that particular month (see Section 8.2.1). The second issue concerns spatial interpolation of rainfall records on a monthly basis to cover the annual cycle. In this case, the approach described in Section 8.2.1 can be adopted; the only problem is the cost of data processing. To examine the usefulness of the current *ET* model for annual runoff prediction, Table 8.4 has been reproduced from previous results displayed in Table 4.8 (see Section 4.4.2 of Chapter 4) and Table 8.2 (this chapter). Although the highlighted values in Table 8.4b represent the average regional estimate of *ET* for the entire study area, the results (especially 2004) closely resemble the local *ET* estimate for the Tamale district (see Table 8.4a).

Table 8.4a Estimated soil moisture deficit (SMD) and actual evapotranspiration (*AE*) for the Tamale district using the Penman-Monteith-Grindley method (all units in mm month$^{-1}$)

| | Rainfall (*P*) | Potential evaporation (*PE*) | *P – PE* | Potential soil moisture deficit ($P_{SMD}$) | SMD at 200mm root constant ($RC_{200}$) | Actual evapo-transpiration (*AE*) |
|---|---|---|---|---|---|---|
| | 1 | 2 | 3 | 4 | 5 | 6 |
| January | 3.2 | 177.2 | -174.0 | 335.0 | 245.0 | 6.8 |
| February | 9.0 | 263.6 | -254.6 | 589.6 | 255.0 | 19.0 |
| March | 45.6 | 326.8 | -281.2 | 870.8 | 269.0 | 59.6 |
| April | 81.0 | 302.5 | -221.5 | 1092.3 | 279.0 | 91.0 |
| May | 122.7 | 244.5 | -121.8 | 1214.1 | 283.0 | 126.7 |
| June | 155.7 | 185.6 | -29.9 | 1244.0 | 285.0 | 157.7 |
| July | 154.7 | 160.3 | -5.6 | 1249.6 | 285.0 | 154.7 |
| August | 200.1 | 152.1 | 48.0 | 1201.6 | 280.0 | 195.1 |
| September | 226.0 | 153.2 | 72.8 | 1128.8 | 281.0 | 227.0 |
| October | 88.4 | 184.9 | -96.5 | 1225.3 | 284.0 | 91.4 |
| ***November*** | *10.1* | *196.7* | *-186.6* | *1411.9* | *296.0* | ***22.1*** |
| December | 2.8 | 163.8 | -161.0 | 1572.9 | 300.0 | 6.8 |

Table 8.4b Descriptive statistics of regional *ET* (mm month$^{-1}$) for the entire Kalarakun catchment of the Volta basin

| Period | Parameter | Minimum | Maximum | ***Mean*** | Standard Deviation |
|---|---|---|---|---|---|
| November 2002 | *ET* | 3.85 | 135.00 | ***86.27*** | 16.69 |
| November 2004 | *ET* | 0.0 | 123.93 | ***38.07*** | 45.24 |

The resemblance of the November results in the above tables are important for two reasons: first, it tends to confirm the previous conclusion in Chapter 7 that satellite data are generally useful for deriving regional estimates of *ET*. Also, the satellite-based methods are quite comparable to the Grindley empirical methods for estimating actual evapotranspiration. Secondly, it shows that the current *ET* model may potentially be used for predicting both dry and wet-season runoff. The details of how this may be achieved are discussed in Section 8.3.

## 8.3 Improved Data Integration Methods for Driving Hydrological Models

The focus of this section is to review data assimilation methods for driving low-data-input hydrological models such as the modified Pitman model (Hughes *et al.*, 2006). The purpose is to suggest improvements to water balance modelling as discussed in Section 8.2 and also to address key data needs, including how spatial rainfall estimates may be derived from satellite data.

### 8.3.1 Modelling Research in the Context of West Africa

Hydrological models may be defined as representations of the processes involved in the transformation of climate inputs, e.g. rainfall, solar radiation and wind, through surface and subsurface transfers of water and energy into hydrological outputs, typically, streamflow, soil moisture and groundwater (Shaw, 1994). Models are the only practical solution to logistical problems and costs associated with repetitive sampling of surface and groundwater required to quantify their distribution in space and time.

A full review of modelling research in the context of West Africa is a difficult task given the vastness of the topic. However, a few of the most important and recent model applications are as follows: (1) fully-distributed [1]TOPLATS model by Bormann & Diekkrüger (2003) in central Benin; (2) coupled lumped-semi-distributed [2]IBIS and SHE models by (Kim & Eltahir, 2004) over the Guinea ($9^0$N) and Sahel ($13^0$N) region; (3) distributed TOPMODEL model by Messager *et al.* (2006) over the Sudano-Guinean

[1] TOPLATS = Topography, Land and Atmosphere Transfer Scheme
[2] IBIS = Integrated Biosphere Simulator; SHE = Système Hydrologique Europeènne

(Burkina Faso/Niger) region; (4) distributed (meso-scale) [3]SWAT model by Schuol & Abbaspour (2006) over the Senegal, Volta and Niger basins; and (5) coupled distributed (climate-hydrology) [4]MM5-WaSiM model over the savannah Volta basin by Jung (2006). The SWAT and WaSiM applications are particularly relevant because of their specific reference to the Volta basin.

Schuol & Abbaspour (2006) have demonstrated value of the SWAT mesoscale approach for predicting freshwater availability in West Africa. But as shown in Figure 8.8, their predictions of the Niger River ($\text{Nash-Sutcliffe}_{\text{calibration}}$ = -1.16 and $\text{Nash Sutcliffe}_{\text{validation}}$ = -0.63) are constrained by uncertainties and discontinuities in the input rainfall and temperature data. The Nash-Sutcliffe (NS) coefficient is a measure of model optimization or uncertainty, which is a ratio between observed and simulated discharges, where a coefficient value closest to zero represents a very good simulation fit. In Figure 8.8 the top plots show better simulation fit for the Gambia River ($\text{Nash-Sutcliffe}_{\text{calibration}}$ = 0.82 and $\text{Nash Sutcliffe}_{\text{validation}}$ = 0.54) than the Niger River because time-series hydrometeorological data were more readily available in the Gambian basin than the Niger basin. The authors have reported that discharge simulations using generated data were found to be even better than simulations using available data measured from local climatic stations. This serves to highlight the problems associated with the scarce distribution of ground station networks (WMO, 2003), and also raises important questions about the accuracy of local measurements. Jung (2006) experienced similar problems in his application of the WaSiM model to the Sourou catchment of the White Volta basin (Burkina Faso). While model calibration was required for 1962-69, daily discharge data were available for only 1968/69 hydrological year (i.e. March – February); in contrast, there were 20 rainfall stations. The full

[3] SWAT = Soil and Water Assessment Tool
[4] MM5 = Mesoscale Meteorological Model (Version 5); WaSiM = Water Balance Simulation Model

complement of ground stations in the Sourou catchment (~39,000 km$^2$) were as follows (Jung, 2006): 20 temperature observations stations, 18 relative humidity stations, 19 wind velocity stations and 12 sunshine observation points. Conditions in the Volta Lake basin are far worse (see Figure 8.1). The reason why Jung's model simulations showed a good fit in Figure 8.9 may be explained by model optimization using a complex algorithm - the non-linear Parameter ESTimation tool (PEST) to derive a set of "best-fit" parameters on the basis of the "equifinality" theory (Beven, 2006).

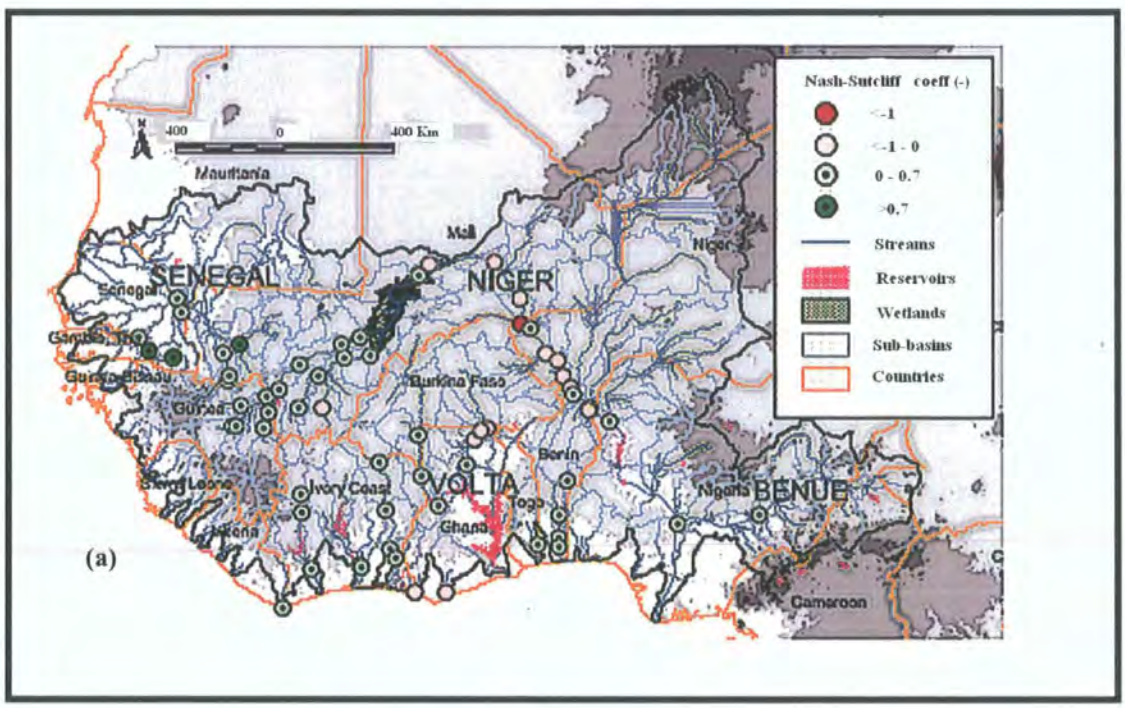


Notes: (1) Yellow lines = National boundaries; (2) Blue lines = Main rivers; (3) Purple polygons = Reservoirs; (4) Green circles = Discharge stations; (5) Brown circles = irrigation reservoirs; and (6) Red circle = AGRHYMET Station in Niamey.

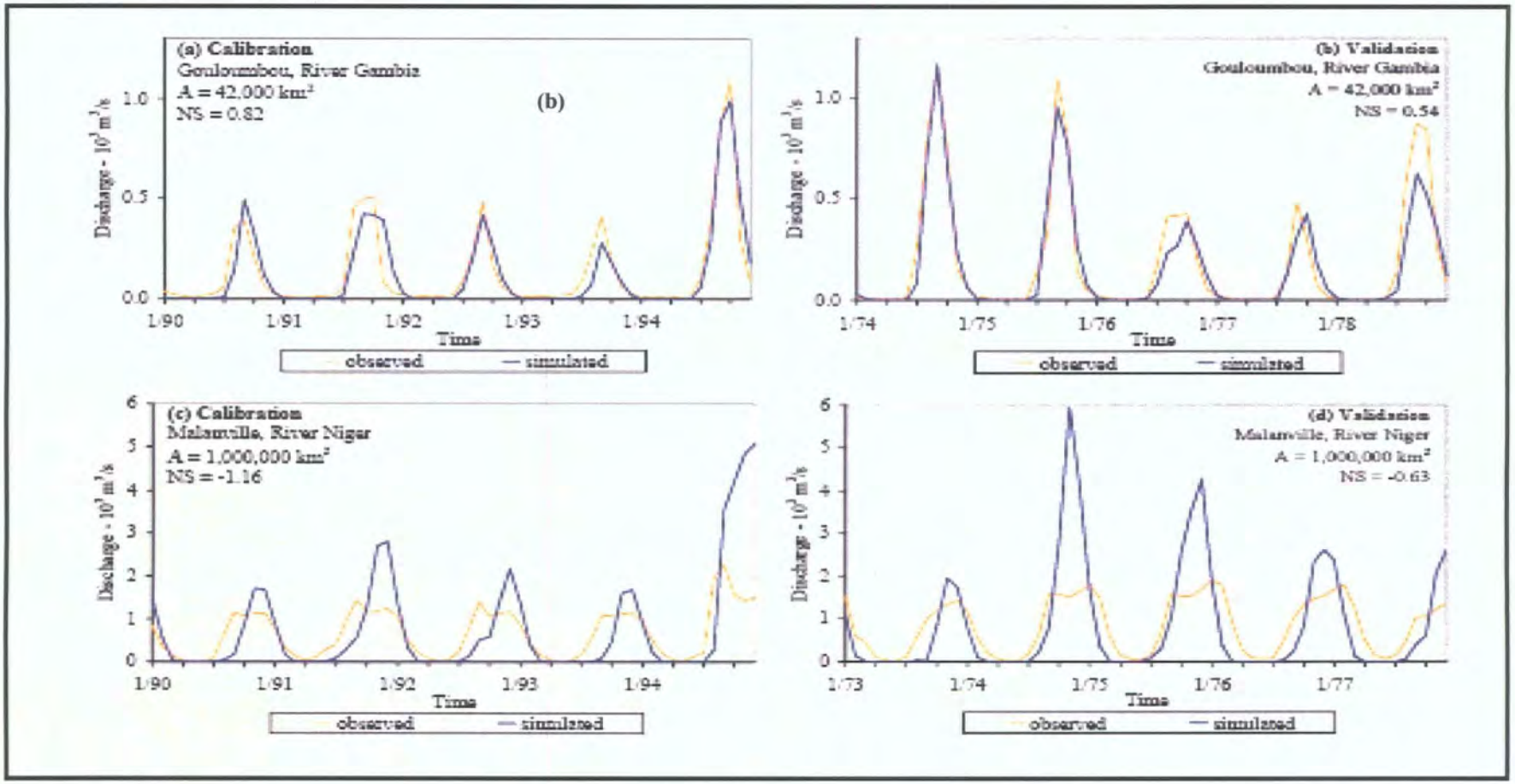


Figure 8.8 (a) Nash-Sutcliff (NS) coefficient of monthly rainfall validation for 64 discharge stations, (b) wide range of quality in SWAT model fit ranging from very good fit (e.g. Gouloumbou on River Gambia: $NS_{calibration} = 0.82$ and $NS_{validation} = 0.54$) to very poor fits (e.g. Malanville on River Niger: $NS_{calibration} = -1.16$ and $NS_{validation} = -0.63$). Source: Schuol & Abbaspour (2006)

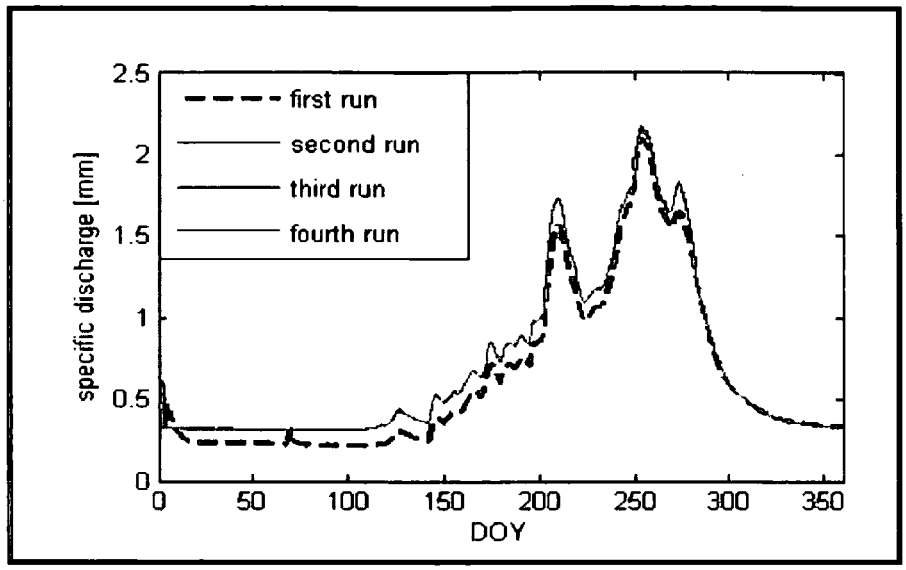


Figure 8.9 Iterative WaSiM runs: Simulated discharge (mm) of the Sourou catchment of the White Volta basin, optimized by the PEST "best-fit" method Source: Jung (2006)

Equifinality simply refers to the finite domain of optimal parameter space from which the best set of parameters may be selected for model optimization. The PEST method uses a gradient-based non-linear parameter estimation algorithm following the Gauss-Marquardt-Levenberg method (Kunstmann *et al.,* 2005), which in turn follows a least-squares fit approach. Jung's calibration uncertainties further raise questions about current modelling strategies, which probably strengthen the case for improved information management which takes advantage of new data sets (e.g. Earth observation satellite data) to drive hydrological models. As a first step, there is a need to identify models with structural efficiency for low levels of input data. Such models should be: (1) easily transferable from one basin to other basins with similar environmental and climatic conditions; (2) modest in their input requirements (hydro-meteorological records); and (3) sufficiently flexible to assimilate a variety of data sets, including satellite-based observations. The modified Pitman model (Hughes *et al.,*

2006) is an example of such a model, and constitutes focus of discussion in the next section.

### 8.3.2 The modified Pitman Model

The principal data requirements of the (conceptual) modified Pitman rainfall-runoff model (Hughes *et al.*, 2006) are monthly rainfall and PET, land-use/cover, soil and geology maps. Its application to savannah catchments in Southern Africa has been successful compared to physically-based models (Wilk *et al.*, 2006). Details about model acquisition, set-up and operation are given by Hughes *et al.* (2006). Since its initial development (Pitman, 1973), the calibration process has focussed on several key problem areas, particularly Africa's lack of high quality hydro-meteorological observations, hence the need to explore new approaches. The model consists of storages linked by functions designed to represent the main hydrological processes prevailing at the basin scale. The modified version (Hughes *et al.*, 2006) includes important changes such as a more explicit groundwater recharge/discharge function (Hughes, 2004). In addition, Hughes (2002) defined several components of the model where modifications could enhance the model's ability to address the requirements of regional water resources assessment of many river basins in Africa. This flexibility allows incorporation of a reservoir water balance model, which has successfully been applied to the Okavango delta, Botswana (Wolski *et al.*, 2006). The detailed structure of the composite model is reproduced from Hughes *et al.* (2006) in Figure 8.10.

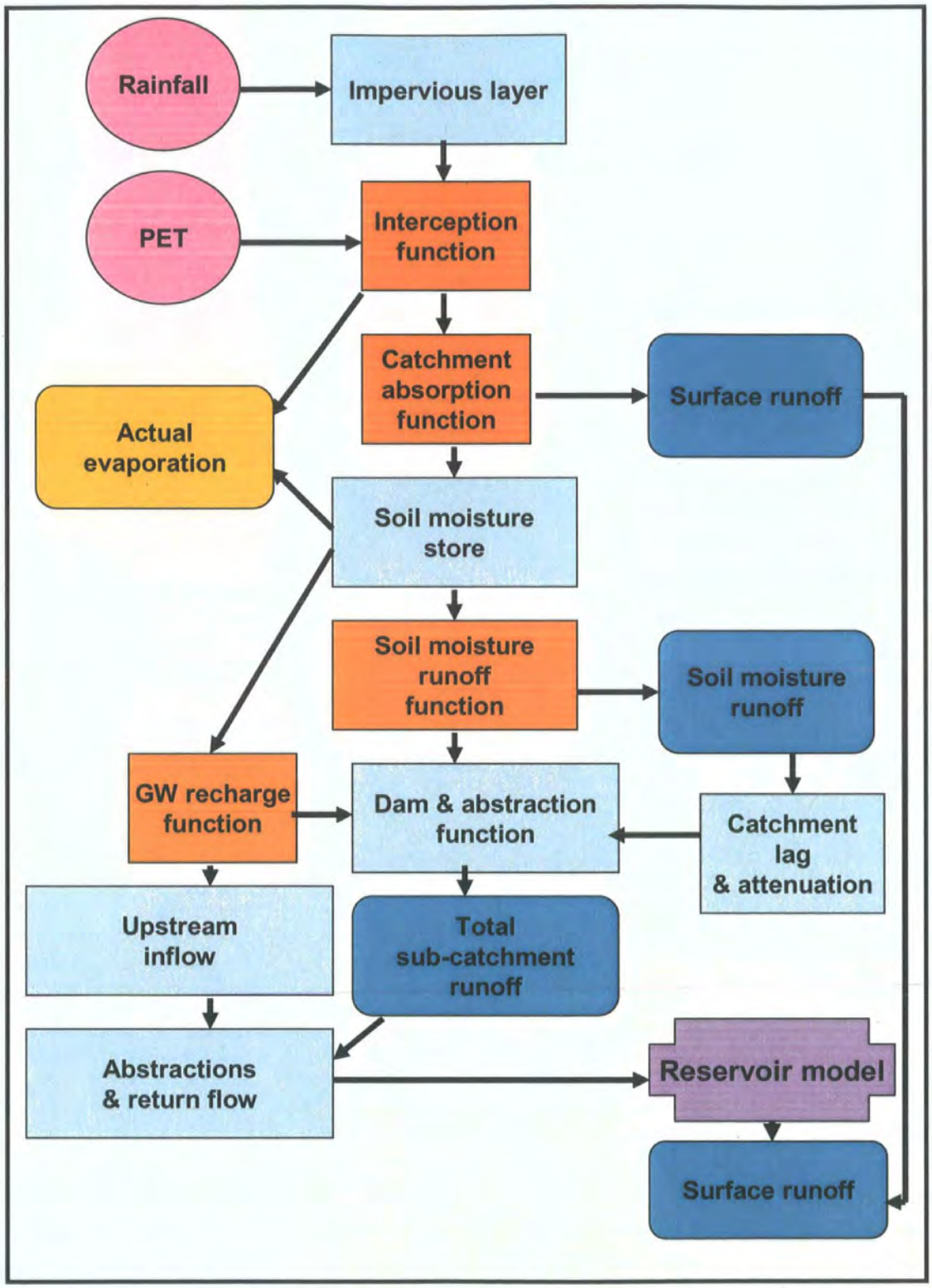


Figure 8.10 Flow diagram of the main components of the modified Pitman-reservoir model. Source: modified after Hughes *et al.* (2006). Note the colour differences of the model units. Red = remote sensing inputs; ash = local and global ground data inputs; orange = sub-models from literature; blue = model outputs.

### *8.3.2.1 Model Parameters and Operation*

Figure 8.10 represents a composite framework of the Pitman's rainfall-runoff and reservoir water balance models; their main interconnection is shown in the bottom right corner of the figure. Although they may be maintained separately for specific needs, their integration has potential uses for the Volta Lake, where quantitative water resources assessment of is of critical importance. Table 8.4 provides a list of the parameters for the integrated model, with brief explanations of their purpose. Compulsory data requirements for the rainfall-runoff component include the following: (1) catchment area; (2) a time series of catchment average rainfall; and (3) a time series of PET (or an annual value and monthly relative distributions). Optional requirements include: (1) seasonal distributions of irrigation water requirements and other water abstractions; (2) time series of upstream inflow; (3) transfer inflow; and (4) downstream compensation flow requirements. The model operates over four iterations and the distribution of the total monthly rainfall is controlled by an *S*-curve function that depends on total rainfall and the rainfall distribution function (*RDF*) parameter. Lower values of RDF result in a more even distribution of rainfall, the effect being more pronounced for higher rainfall totals (Hughes *et al.*, 2006). The interception function is based on the interception capacity parameter (*IP*), which, in addition to being seasonally variable, can be given for the two most dominant vegetation types in the area (Table 8.5). The depth of rainfall intercepted in any month is based on an empirical relationship between the relevant *IP* and rainfall depth, while interception storage satisfies the evaporation demand at the potential rate (Hughes, 2004). Figure 8.10 and Table 8.5 represent a spatially-distributed implementation of the model, whereby all identified sub-catchments are modelled with independent compulsory (see above list) parameter sets and input time series.

Table 8.5 Modified Pitman and reservoir model parameters

| Parameter | Units | Pitman model parameter description |
|---|---|---|
| RDF | | Rainfall distribution factor. Controls the distribution of total monthly rainfall over four model iterations |
| AI | Fract. | Impervious fraction of sub-basin |
| PI1 and PI2 | mm | Interception storage for two vegetation types |
| AFOR | % | % area of sub-basin under vegetation type 2 |
| FF | | Ratio of potential evaporation rate for Veg2 relative to Veg1 |
| PEVAP | mm | Annual sub-basin evaporation |
| ZMIN | mm month$^{-1}$ | Minimum sub-basin absorption rate |
| ZAVE | mm month$^{-1}$ | Mean sub-basin absorption rate |
| ZMAX | mm month$^{-1}$ | Maximum sub-basin absorption rate |
| ST | mm | Maximum moisture storage capacity |
| SL | mm | Minimum moisture storage below which no GW recharge occurs |
| POW | | Power of the moisture storage-runoff equation |
| FT | mm month$^{-1}$ | Runoff from moisture storage at full capacity (ST) |
| GPOW | | Power of the moisture storage-GW recharge equation |
| GW | mm month$^{-1}$ | Maximum ground water recharge at full capacity (ST) |
| R | | Evaporation-moisture storage relationship parameter |
| TL | months | Lag of surface and soil moisture runoff |
| CL | months | Channel routing coefficient |
| D.Dens | | Drainage density |
| T | m$^2$ d$^{-1}$ | Ground water transmissivity |
| S | | Ground water storativity |
| Slope | | Initial ground water gradient |
| AIRR | km$^2$ | Irrigation area |
| IWR | Fract. | Irrigation water return flow fraction |
| EFFECT | Fract. | Effective rainfall fraction |
| RUSE | Ml yr$^{-1}$ | Non-irrigation demand from the river |
| MDAM | Ml | Small dam storage capacity |
| DAREA | % | Percentage of sub-basin above dams |
| A, B | | Parameters in non-linear dam area-volume relationship |
| IRRIG | km$^2$ | Irrigation area from small dams |
| Parameter | Units | Reservoir model parameter description |
| CAP | Mm$^3$ | Reservoir capacity |
| DEAD | % | Dead storage |
| INIT | % | Initial storage |
| A, B | | Parameters in non-linear dam area-volume relationship |
| RES1–5 | % | Reserve supply levels (percentage of full capacity) |
| ABS | Mm$^3$ | Annual abstraction volume |
| COMP | Mm$^3$ | Annual compensation flow volume |

Source: Hughes *et al.* (2006)

However, not all sub-basins need the optional input requirements specified and if missing, they are assumed to be irrelevant to that specific area (Hughes *et al.*, 2006). To allow for attenuation of the seasonal hydrograph in lower sub-basins (e.g. Volta Lake), where incremental flow contributions are negligible, riparian areas that are assumed to be fed by seepage from the river, and from which water is assumed to evaporate, are modelled as open water surfaces (i.e. dummy reservoirs) Hughes *et al.* (2006). The compulsory requirements for the reservoir water balance model are monthly distributions of normal drafts (fraction of annual abstraction requirement, *ABS* in Table 8.5) and compensation flow requirements (fractions of annual requirement,

determined by the parameter, *COMP*), as well as monthly distributions of drafts and compensation flow for up to five reserve supply levels (defined by parameters RES1 – RES5). A detailed explanation of the parameterization scheme is given in Hughes *et al.* (2006); Hughes (2006) and Wilk *et al.* (2006). In West Africa, the Pitman model may be more suitable in comparison with, say, the WaSiM, given its modest input data requirements. However, it is necessary to emphasize data availability through management and technical innovation, rather than model choice and efficiency. Attention is paid to this in the next section.

### 8.3.3 Data Management Tools

Figure 8.11 illustrates a data management tool which may be used to drive hydrological models (e.g. modified Pitman model). The left, middle and right parts of the framework describe point, satellite-based and ancillary (mixed) data sources. The data correction and validation strategy (left part of Figure 8.11) proposes improvements to previous models (Section 8.3). Further details are given in the next section, which also discusses data generation, accessibility and utilization.

#### *8.3.3.1 Ground Hydrometeorological Data*

Nearly 50 years (1951 – 2000) of monthly rainfall and temperature records observed from gauging stations have been processed and analysed with examples shown in Table 4.2 (Chapter 4). Monthly PET (Figure 8.10) has also been derived using the Thornthwaite empirical method (see Section 4.3.1 of Chapter 4). The Thornthwaite model seems to predict PET well (see Section 4.4.2 of Chapter 4) over the Volta basin and should therefore provide reasonable input data for the Pitman model.

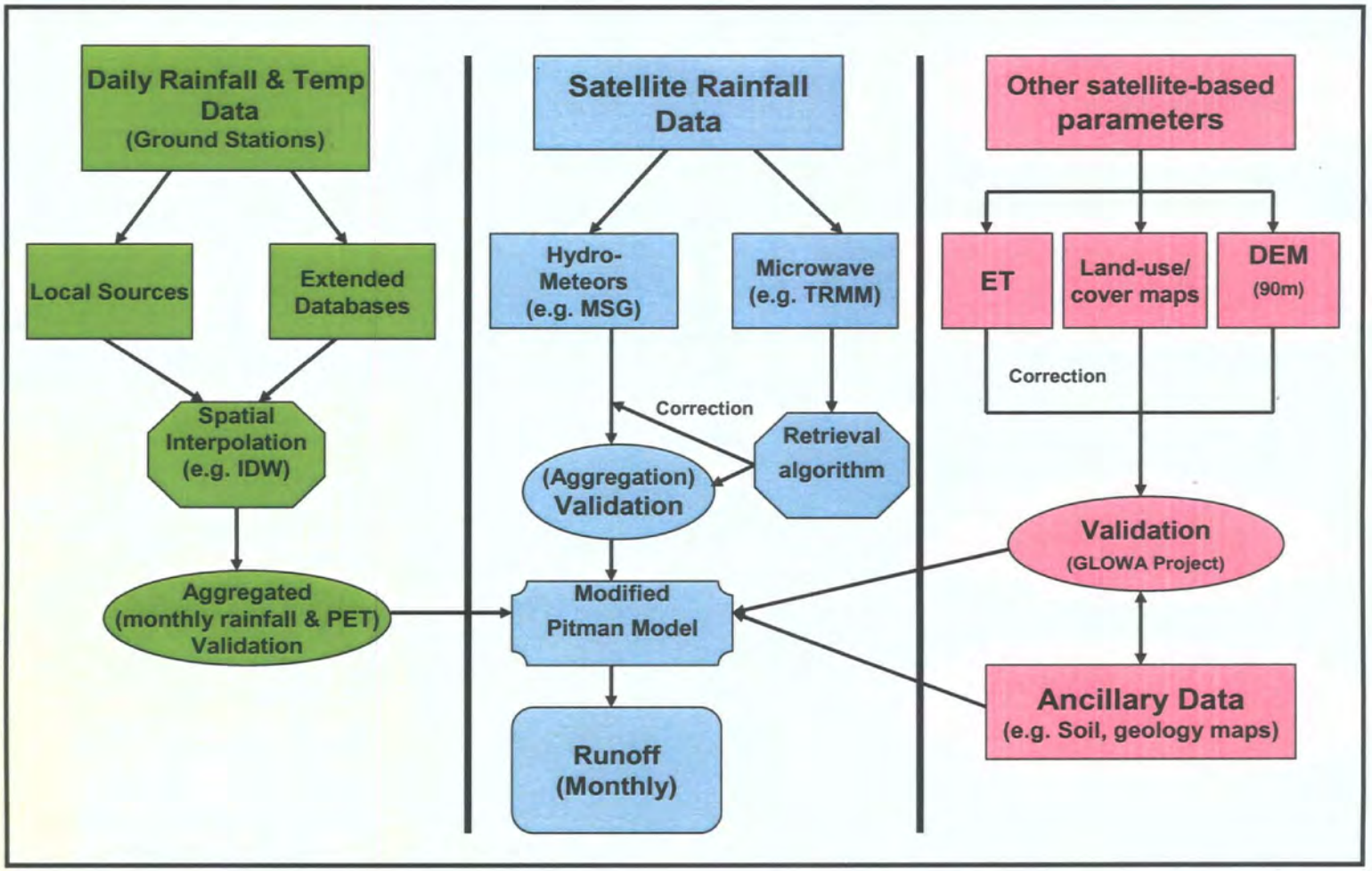


Figure 8.11 A conceptual data management tool for driving hydrological models. The first part (left-hand-side) focuses on ground-based hydrometeorological records, while the second and third parts propose assimilation of satellite-based inputs.

Although the Nicholson African monthly rainfall database (NARD) (Wilk *et al.*, 2006) has not been processed in the current research, its value for the Okavango research has been recognised (Wilk *et al.*, 2006). The NARD is an example of an "extended database" (left part of Figure 8.11). This expression has been used because of the extrapolation methods employed in the generation of Nicholson's database. A useful way of benefiting from the NARD and similar databases (e.g. AGRHYMET Sahel database, etc.) is through geo-statistical interpolation methods, an example of which is shown earlier on in Figure 8.2.

There are also nine river discharge gauging stations in the Volta Lake basin. In contrast to rainfall, the temporal record of discharges are more discontinuous, especially from 1960 – 1990, which also coincides with the period of extreme droughts, and economic and political instability in West Africa. There were probably many more pressing economic needs at this time than investments in gauging stations. Continuous time-series monthly discharges (a total of nine years) have been processed and analysed, which is a valuable validation database. Amisigo & van de Giesen (2005) have demonstrated the utility of the Expectation-Maximisation (EM) algorithm as geo-statistical approaches for improving the temporal coverage of discharge measurements in the Volta basin. An example of their results is displayed in Figure 8.12 and may be easily adapted for other sub-basins of the Volta.

### *8.3.3.2 Satellite-based Observations*

Global or near-global datasets of a wide range of terrestrial information derived from satellite imagery are becoming increasingly available and accessible. The type of information available includes not only relatively static characteristics, such as land cover (d'Herbès and Valentin, 1997), but also time series variations, such as

temperature (Xiang and Smith, 1997), evapotranspiration (Kite and Droogers, 2000), soil moisture (Valentijn *et al.*, 2001) and precipitation (WCRP, 1986).

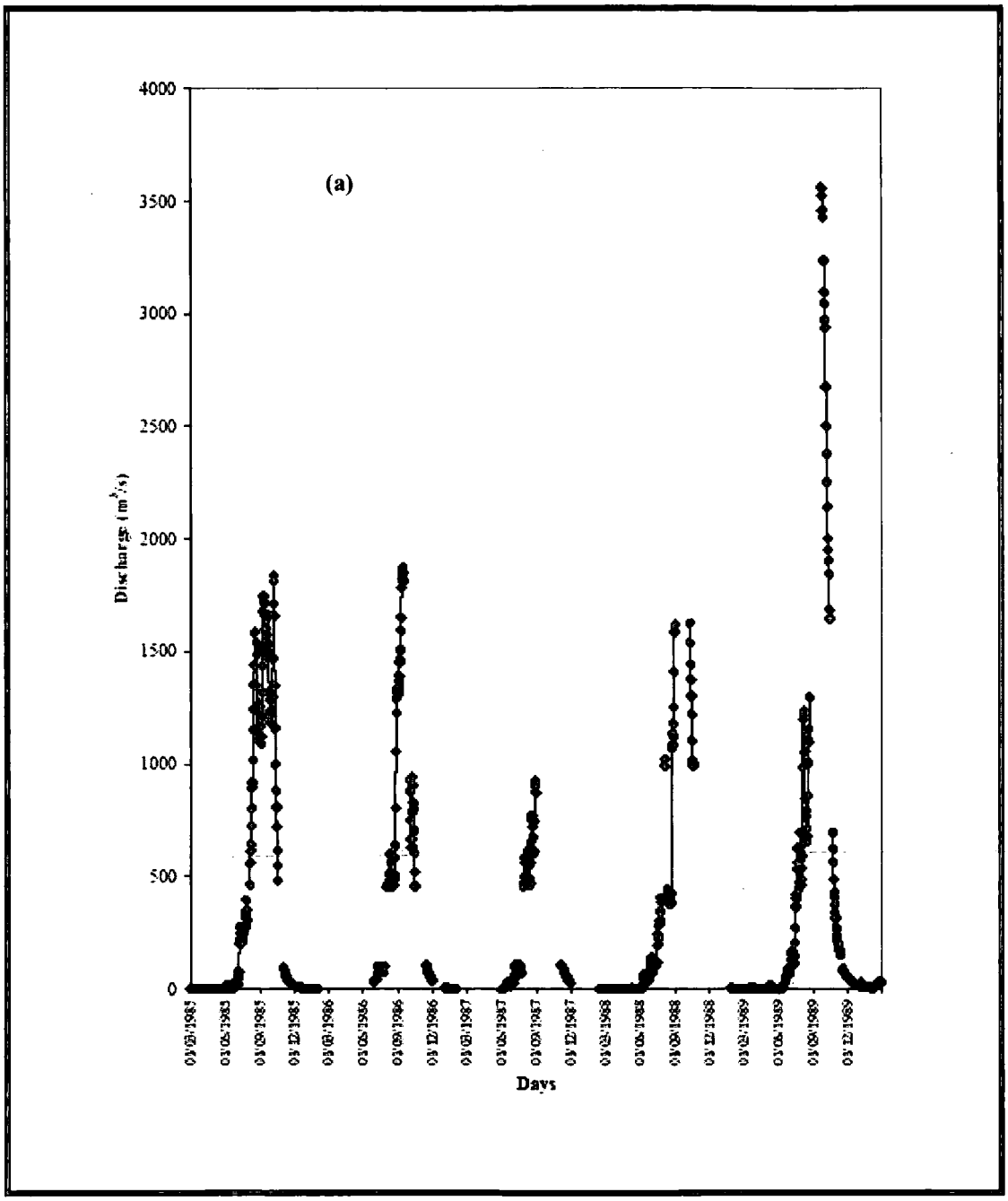

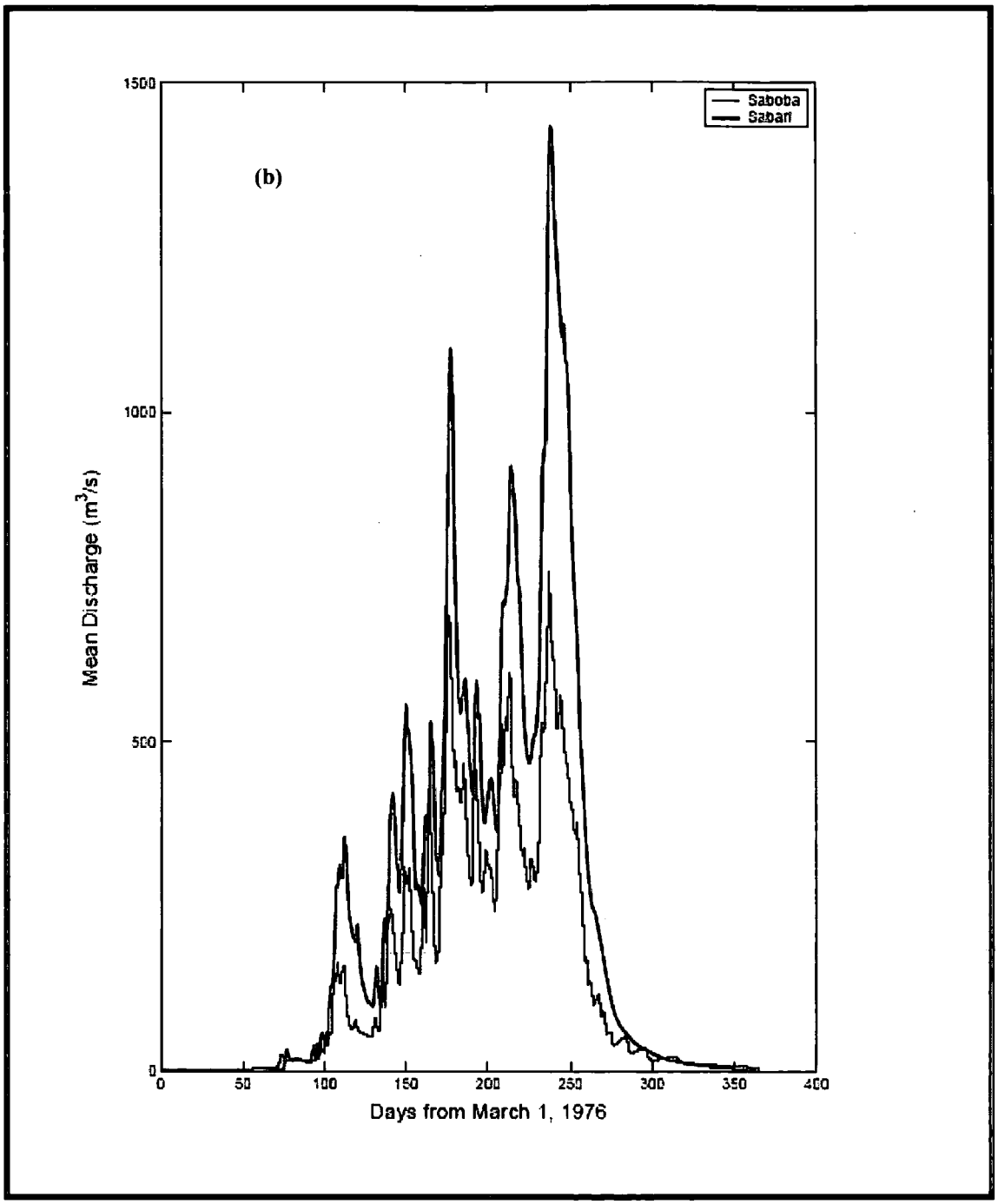


Figure 8.12 EM method for patching gaps in discharge measurements ($m^3$ $s^{-1}$) in 1976 (a) Typical pattern of gaps considered in the spatio-temporal modelling (b) Modelled daily hydrographs of two stations on the Oti-Volta River. Note: The top and bottom graphs represent Saboba and Sabari discharge stations, respectively. The legend shows the same stations Source: Amisigo & van de Giesen (2005)

Many of the above have the potential to fill some of the information gaps and provide input data for water resource estimation models in developing regions (Hughes, 2006).

There are several practical considerations that need to be addressed if such products are to be used successfully and with confidence (Hughes, 2006): (1) existing hydrological models are often calibrated against historical gauged data, which makes re-calibration necessary; (2) satellite data have a relatively short period of record and do not cover the various cycles of wet and dry periods frequently found in hydrological records; (3) the previous two points suggest that, ideally, gauged and satellite data need to be used together and so the relationships between the two data sources need to be quantified and clearly understood; (4) the data have to be accessible to water resource practitioners in the developing countries; (5) the techniques required to make effective use of the data should not be excessively complex or difficult to understand since the resources available for data analysis and processing are frequently limited in developing countries.

### *8.3.3.3 Near-global Satellite Rainfall Products*

There are a number of references to satellite rainfall estimation methods and products in the hydrological and meteorological literature. These include [5]TAMSAT (Grimes *et al.*, 1999 and Thorne *et al.*, 2001), TOVS (Susskind *et al.*, 1997), GPCP (Huffman *et al.*, 1997 and Huffman et al., 2001) and PERSIANN (Hsu *et al.*, 1999 and Sorooshian *et al.*, 2000). The two that appear to be the most straightforward to access (via internet links) and process into readily usable information are the GPCP and

[5] TAMSAT = Tropical Applications of Meteorology using SATellite; TOVS = TIROS Operational Vertical Sounder; PERSIANN = Precipitation Estimation from Remotely Sensed Information using Artificial Neural Networks.

PERSIANN data sets. The GPCP (Global Precipitation Climatology Project) 1DD dataset is based on merged information from several sources:

- GPCP Geostationary Satellite Precipitation Data Centre (IR $T_b$ histograms),
- GPCP Merge Development Centre (GPCP SG Merged precipitation estimate and GPROF 6.0 SSM/I fractional occurrence), and
- GSFC Satellite Data Utilization Office (TOVS precipitation estimates – (Huffman *et al.*, 2001)).

The temporal resolution is 1 day, the spatial resolution 1° and the period of record of available data is currently October 1996 to January 2005. Various groups prepare rainfall estimates from individual data sources, while the GMDC (GPCP Merge Development Centre at the NASA Goddard Space Flight Centre) are tasked with combining these into the final product. Each data file (7.4 MB) on the website (www1.ncdc.noaa.gov/pub/data/gpcp/1dd/data/) consists of 1 month of data for the entire globe and it is a relatively simple matter to develop a computer program to extract the data required for a specific region.

The PERSIANN datasets have a temporal resolution of 6h, a spatial resolution of 0.25° and cover regions between 50°N and 50°S (Hsu *et al.*, 1999). The estimates are based on grid infrared images from geosynchronous satellites (GOES-8, GOES-9/10, GMS-5, Metsat-6 and Metsat-7) and instantaneous rain from the NASA TRMM TMI instrument. The 6h data files (2 MB) for complete months can be downloaded (between 112 and 124 individual zipped files) from the University of California, Irvine website (hydis8.eng.uci.edu/persiann) and, as with the GPCP data, are straightforward to process and extract the required data. An inspection of the individual 6h data indicates that there are missing data in most of the months for Africa. However, they are frequently single 6h periods, not biased to any specific time of the day or season of

the year and result in less than 5% of the accumulated days being missing. It is assumed this they will not substantially affect accumulated monthly totals (Hughes, 2006). The PERSIANN data are available for March 2000 to December 2004. For both satellite data sources, the amount of time to download the complete datasets is quite substantial and at commercial internet fee rates, can be very expensive. It does not seem to be currently possible to select a specific region on the websites and download only the data for a specific region of interest.

New algorithms are also being explored, such as the University of Sussex algorithm that has been used to extract satellite rainfall estimates for 1991–1997 using a combined TRMM (Tropical Rainfall Measuring Mission), SSM/I (Special Sensor Microwave Imager) and METEOSAT data. The application of such data sets in the Okavango basin (Southern Africa) has still been confronted with the problem of accuracy in terms of ground observation records (Wilk *et al.*, 2006). The eventual objective is to be able to use a combination of historical gauge and satellite derived rainfall data as inputs to hydrological models (Figure 8.10). In that regard, perhaps the best approach for assessing the satellite rainfall data would be to calibrate the model using historical gauge data and then apply the model using the satellite data (Figure 8.11). However, Hughes (2006) thinks a pair-wise comparison of the gauge data with the satellite data (and in some cases comparisons between gauges in close proximity and between the sources of satellite data) is a quicker and easier method. Even then, he recognises questions about spatial correlation between point rainfall and areal estimates from satellite sensors. Spatial interpolation methods (Section 8.4.1) may partly address this issue.

Another issue is that overlaps between the gauge data and the satellite data may not be sufficiently long to allow meaningful comparisons. Hughes (2006) addressed

this problem using a two-way inference method. First of all, he referenced the relationships between the gauge and PERSIANN data from existing gauge and GPCP data; then between the GPCP and PERSIANN data, based on single 1° × 1° grid squares extracted from the GPCP data, the equivalent of 0.25° grid squares of the PERSIANN data. He developed a grid numbering system to achieve this, while ensuring coverage of all available gauges within the area. Although several uncertainties remain about Hughes' approach, his work has shown very promising correlation results between satellite estimates and gauge station observations, an example of which is shown in Figure 8.13. Perhaps, a combined approach based on Hughes' method and the spatial interpolation method shown in Figure 8.4 may potentially improve model outputs.

Accurate delineation of catchment areas is one of the compulsory requirements of the Pitman model (Section 8.3.2), which depends very much on topographic characteristics of the area. An example of a DEM produced from NASA's Shuttle Radar Topography Mission is illustrated in Figure 3.3 (Section 3.3.1 of Chapter 3). The precision of this product needs further verification before it can be used for other applications such as calculating the topographic index of the catchment area.

### 8.3.4 Geographical Data

Landsat ETM+, MODIS and AATSR sensor data (e.g. Figure 7.13, Section 7.2.5 of Chapter 7) have been used to derive land-use/cover maps both as input and validation sources (Figure 8.11). The current maps have been verified using GPS field surveys and the GLOWA-Volta land-use/cover classification system, which may be useful for regional studies. Other essential geographical variables include soil and geology data. Much of this information has been processed from digital map archives

of the Ghana Soil Research Institute and Geological Survey Department (see Sections 2.1.4 & 2.1.5 of Chapter 2) and may be directly assimilated into the Pitman model.

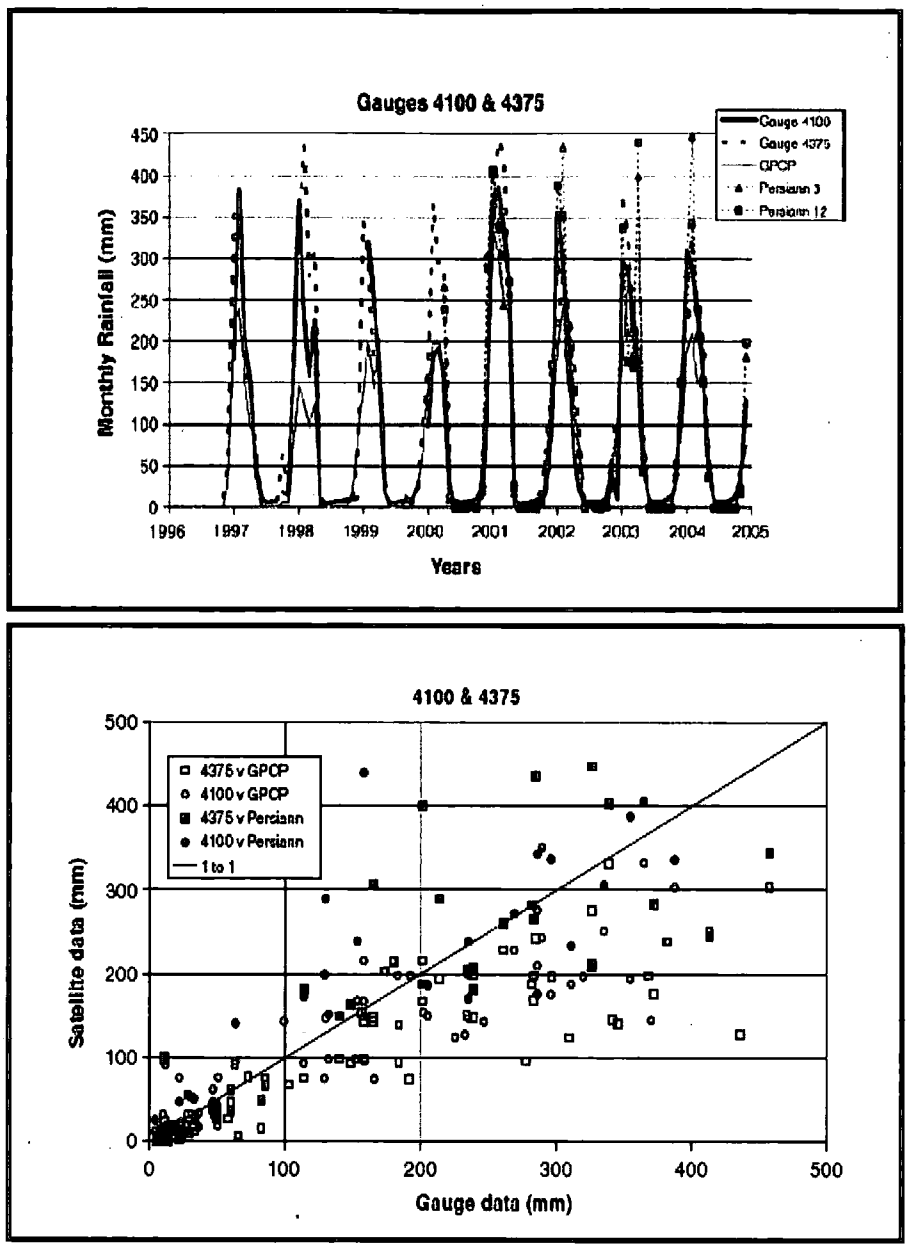


Figure 8.13 Time series comparisons for data associated with the northern grid point in the Kafue River basin, Zambia. Source: Hughes (2006)

It is also worth mentioning that high quality data sets are also available from global sources such as the UN-FAO, USGS and AGRHYMET/Niamey which may be downloaded, processed and utilized without charge.

Satellite-derived *ET* is one of the principal outputs of this research (Chapter 7). Although the Pitman model can assimilate satellite-based rainfall, the assimilation of satellite-derived *ET* has not been achieved. Model calibration of spatially-derived *ET* is therefore an important research topic that needs to be explored in subsequent studies. The next section proposes a conceptual framework for predicting runoff from ungauged basins using the sole input of satellite-derived data. Prior to that, it is important to comment on improvements likely to be made from current modelling strategies.

### 8.3.5 Improvements to Volta Basin Modelling Research

Figure 8.11 proposes a number of improvements to modelling research in the Volta basin. The most important one is substitution of gauged records with satellite rainfall estimates (Wilk *et al.*, 2006). Utilization of satellite rainfall is a crucial modelling step; first, the spatial coverage and temporal frequency of data delivery is often better than ground sources. Secondly, satellite-based rainfall data has the potential to save research costs in developing countries. The substitution of ground-based temperature measurements with satellite-based thermal infrared (TIR) data have not yet been widely explored and must remain the subject of future research. *ET* derivation methods shown in Figure 8.11 and Chapter 7 show potential as a substitute for ground thermal measurements. This can be useful for a variety of hydrological models, e.g. the SWAT (Schoul & Abaspour, 2006), WaSiM (Jung, 2006) and Pitman (Hughes *et al.*, 2006) models.

Spatially-derived *ET* (Figure 8.11) would provide direct benefits to hydrological models, especially the reservoir component of the Pitman model. The right-hand-side of Figure 8.10 shows that satellite sensor data can provide spatial *ET* which may

improve upon pan measurements or data derived from meteorological records based on sparsely distributed network stations.

The validation strategy in Figure 8.11 proposes a substantial improvement in data quality before assimilation into the Pitman model. A close examination of recent applications of the Pitman model (e.g. the Okavango basin by Hughes *et al.*, 2006) shows this as an important "missing link". For example, in the absence of long-term records from Angola (Okavango), proxy data were utilized and validated using global data sources at very low spatial scales. In contrast, Figure 8.11 proposes validation of time-series inputs from instantaneous satellite derived measurements and further verification from hourly meteorological observations such as the GLOWA-Volta database (see Table 4.1, Chapter 4 & Figure 7.8, Chapter 7), before assimilation. This has a huge potential to improve the accuracy of model simulations.

### 8.3.6 Rapid Water Balance Assessment of Ungauged Basins

Integrated data assimilation methods (as shown above) may apply in the case of sparsely-gauged catchments, but not ungauged ones. The purpose of this section is to demonstrate the sole utility of satellite-based observations for rapid water balance assessment of ungauged savannah catchments. Using Figure 8.14 as an example, repetitive processing of satellite rainfall and *ET* products can be a quick and easy way of assessing regional water balance on the basis of the regional water balance approach (Equation 3.3, Section 3.8 of Chapter 3).

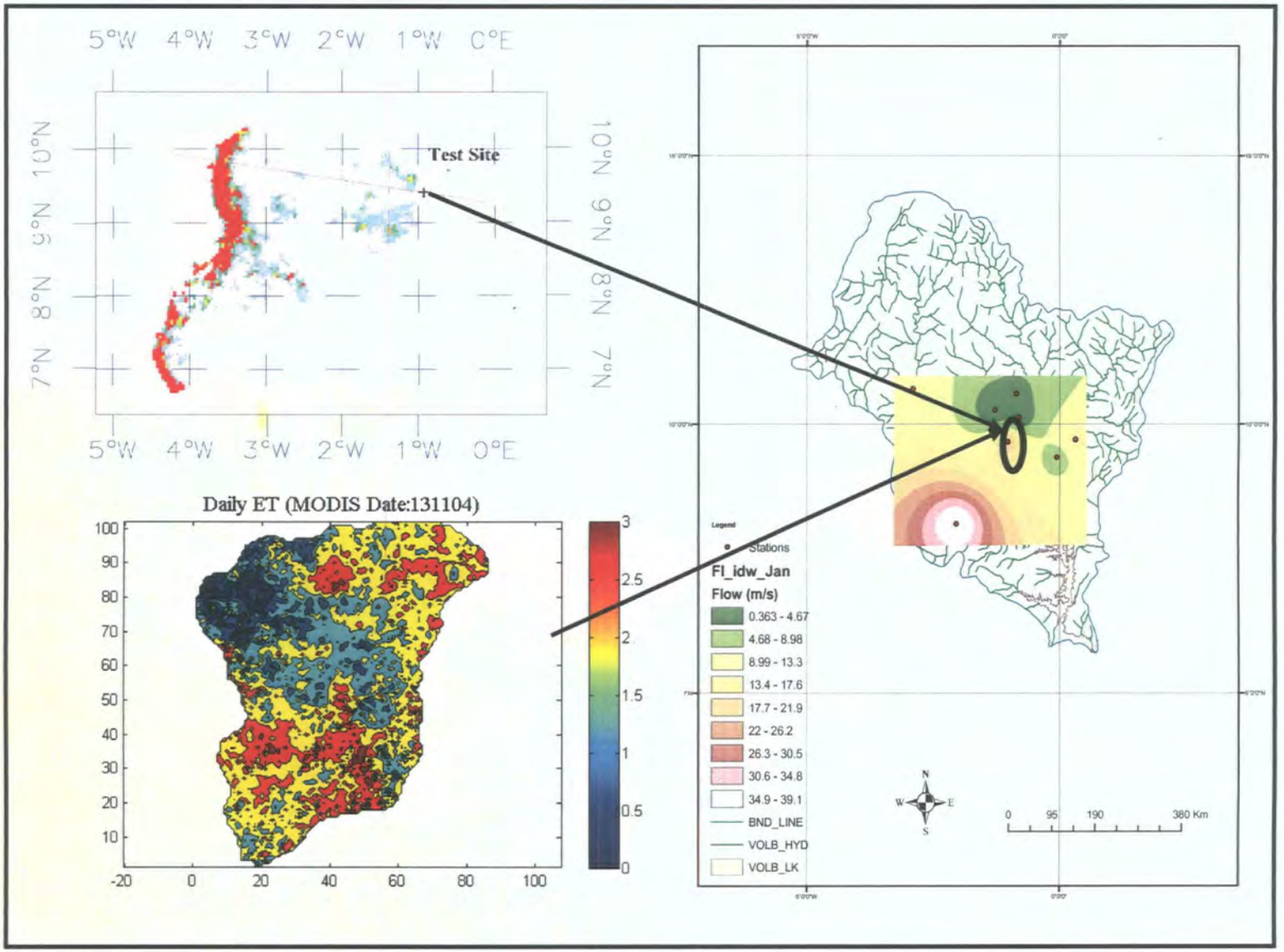


Figure 8.14 Conceptual framework for spatial water balance modelling using satellite rainfall and ET measurements and on the basis of the regional water balance equation. The top left image is a TRMM-based rainfall, the bottom left is MODIS-based ET and the right map is a hypothetically derived runoff map.

The key assumption here is that at very short time-scales (e.g. instantaneous) and over very large areas (regional basins), soil moisture storage ($\Delta S$) remains constant. This means the difference between satellite-based rainfall derived from satellite rainfall products (e.g. TRMM, PERSIANN) and *ET* derived from multi-spectral sensors (e.g. MODIS) (Chapter 7) can produce crude estimates of water balance, which can be beneficial for taking (short-term) water management decisions if catchments are ungauged.

A number of problems need to be resolved before this approach can be successful and operational. First, there is the need to calibrate the satellite imagery to reflect ground conditions, which may probably require installation of expensive instruments (e.g. radiometers, weather stations, etc.) at the time of satellite overpass. Also, there is the need to deal with uncertainties involved in aggregating instantaneous measurements to reasonable hydrological time-scales (e.g. monthly and annual time-scales). Furthermore, complex algorithms need to be developed to correct for atmospheric contaminants in rainfall products (see Figure 8.11). This is particularly difficult regarding the TRMM products (Hughes, 2006; Wilk *et al.*, 2006); much progress has, however, been made concerning the PERSIANN composite product (Section 8.4.2.1).

The top left and bottom left images of Figure 8.14 are examples of TRMM-based rainfall measurement of the Volta basin (ZEF, 2004) and MODIS-based *ET* measurement (this thesis, Chapter 7). The difference between these images (regional water balance equation) is shown as a hypothetical runoff map (right-hand-side of the figure). It is recognised that much work needs to be done on this topic; however, the above approach could be very promising if Earth observation programmes are

sustained. The prospects and challenges of this and related approaches are discussed in the next section.

### 8.3.7 Modelling Limitations & Uncertainties

There are a number of uncertainties about the conceptual runoff model proposed in Section 8.3.6. Principal among them is oversimplification of the regional water balance equation. It is difficult to know, for instance, the effects of some the key model assumptions including constancy of soil moisture storage, deep drainage and soil evaporation. Also, it is not certain how sensitive the model is to any of the above assumptions, neither is immediately known which of them is most critical and needs to be addressed first. Further, more work is needed to see how the model will operate in the wet season and whether indeed the model will perform much better with more rainfall data inputs. Additionally, more work is necessary to test the model in similar catchments in or outside West Africa to examine the robustness of the current method.

The errors in Tables 8.2 & 8.3 and Figure 8.4 are essentially a spill-over from the energy balance modelling approach. For example, the *ET* inputs in Table 8.2 cannot be separated from the aggregated errors observed in Chapter 7. An important source of error is the application of the $T_s$ algorithm. Many key assumptions such as constancy in surface emissivity, uniformity of atmospheric water vapour, grouping of land cover types had to be made in order to operate the $T_s$ split-window algorithm. The effects of emissivity and atmospheric water vapour are extremely difficulty to quantify without ground truth data. Also, the biomass-runoff sensitivity output in Table 8.3 and Figure 8.4 are beset with problems because NDVI is only a surrogate variable for vegetation biomass. Further, the conceptual model is limited by practical problems such as ground station rainfall data, which makes immediate validation of the model

difficult. More details are given in Section 9.3.2 of Chapter 9. These are important limitations; yet, there are good prospects that the models developed here can be improved and applied in hydrological models.

### 8.3.8 Prospects & Challenges

Before the launch of rainfall satellites such as the TRMM, the measurements of the global distribution of rainfall at the Earth's surface had uncertainties of about 50% (NASA website: http://trmm.gsfc.nasa.gov/overview_dir/instrumentfacts.html) (Salomonson *et al.*, 2002). Unless scientists can better define the amount of rainfall and the energy released when rain occurs, there is little chance of estimating water availability or prediction of key global events such as atmospheric warming. Having both passive and active sensors on spaceborne observatories has now greatly improved the measurement of key hydrological parameters of rainfall, soil moisture and land cover. The TRMM instrument, for example, now provides the most comprehensive set of quantitative tropical rainfall data in history (Salomonson *et al.*, 2002).

It has been shown that the modified Pitman model may have the potential to provide estimates of water balance of the Volta Lake, given its simplicity and low demand for input data than previous models (e.g. WaSiM [Jung, 2006]). It has also been shown that much of the compulsory model data, e.g. catchment area, time series of catchment average rainfall and PET land-use/cover, soil, geology maps as well as topographic parameters (DEM) can be provided by current satellite sensors such as the TRMM, PERSIANN composite, MODIS and SRTM.

However, modelling approaches that depend on satellite-based observations (Figure 8.10) can be questionable because of various practical issues. For example, continuous availability of the satellite imagery, scale issues and the excessive demands

on computer and internet facilities, and data processing time. Whereas the PERSIANN rainfall data are only available from 2000 – 2004, the TRMM sources (e.g. Precision Radar and TRMM Microwave Imager) are available from 1997 – 2005. Other multi-spectral sensors, e.g. the MODIS, are also available from 2000 – 2006. Apart from sensor life-span (these sensors are due for decommissioning), it is difficult to say whether future satellites by NASA (USA) and JAXA (Japan) will build on the current data outputs or not. The short operational lifetime of satellite sensors makes it difficult to extend model applications back in history and therefore difficult to link to long-term modelling strategies. For example, Wilk *et al.* (2006) have experienced positive biases in satellite-derived rainfall in respect of the Okavango basin. They had to develop a series of correction equations in order to reconcile satellite rainfall observations with historical gauged data. Furthermore, algorithms to help download and process smaller rainfall files specific to the Volta region of interest are currently non-existent (Hughes, 2004); handling of very large data files (about 120 zipped files for regional catchments [~10,000km$^2$]) can be a huge difficulty because of limited computing and internet facilities in Africa.

## 8.4 Summary

The first part of this chapter dealt with deriving spatial estimates of runoff and establishing their sensitivity to savannah biomass using NDVI as a surrogate for total biomass. The results showed that runoff may be absent ($Q = 0.0$) over most parts of the sub-catchment study area in the dry season, except a few un-vegetated areas in the Tamale district. The analysis also showed that runoff response is a function of vegetation abundance, represented by the NDVI ratio; the approach though useful, may be limited by key parameters such as scarcity of spatially-observed rainfall.

The second part of the chapter reviewed data assimilation approaches for driving low-data-input hydrological models. The most important objective was to suggest development of tools with which to overcome the scarcity of spatially-observed ground data and to prepare a framework for rapid water balance assessment of the Volta Lake basin, with only satellite-derived data as inputs. As a first step, the parameterization of the modified Pitman model was proposed given its simplicity and modest demands for input data in place of previously applied models, e.g. WaSiM (Jung, 2006). For sparsely-networked catchments, an integrated data management system was developed to take advantage of existing ground data, validation sources from a variety of databases (GLOWA Volta, Nicholson's Africa rainfall data, etc.), and satellite-observed rainfall and geographic data sets. For ungauged catchments, it is possible to use satellite-based estimates of rainfall and *ET* to help estimate water balance of the Volta Lake. However, there are several practical issues that need to be addressed if such products are to be used successfully and with confidence (Hughes, 2006). For example, successful calibration of satellite data using ground measurements, improvement of spatial interpolation methods between ground and satellite data, and improvement of data processing and analytical techniques need to be accomplished before local experts can use the data effectively.

# Chapter 9

# Conclusions & Recommendations for Future Research

## 9.1 Introduction

This thesis sought to develop improved methods for measuring regional-scale energy and water fluxes, particularly evapotranspiration (*ET*), from complex savannah landscapes in the Volta basin in West Africa using satellite imagery (i.e. [1]Landsat ETM+, MODIS and ENVISAT/AATSR). The results have been evaluated using a variety of methods including published data, 1-5m scintillometer (eddy correlation) observations and local-scale Penman-Monteith estimates. This chapter is structured in three parts as follows: (1) evaluation of the research aims and objectives; (2) discussion of the limitations of the spatial modelling approach; and (3) discussion of future research directions.

## 9.2 Evaluation of Aims and Objectives

The following section reviews the research aim and objectives outlined in the introductory section of the thesis (Chapter 1). This is followed by a discussion of the outcomes and how the main research problems were addressed. The aim of the research is:

**To use remote sensing methods as a means of providing some of the key data inputs (DEM, *ET*, land cover maps, etc.) for hydrological models.**

[1] Landsat ETM+ = Landsat Enhanced Thematic Mapper; MODIS = Moderate Resolution Imaging Spectroradiometer; ENVISAT/AATSR = Environmental Satellite/Advanced Along-Track Scanning Radiometer

This aim was investigated by considering the set of specific objectives outlined in Section 1.2.3 of Chapter 1.

1.1 To investigate whether the spatial dynamics of *ET* are a major limitation to water availability in the savannah Volta basin and to assess the advantages of satellite-based methods (e.g. [2]SEBAL algorithm) for spatial *ET* modelling.

Two main sources of information were used to assess whether spatial dynamics of *ET* are a major limitation to water availability in the savannah Volta basin: (1) published literature [e.g. HAPEX-Sahel (Goutorbe *et al.,* 1997); GLOWA-Volta (ZEF, 2004) and Gyau-Boakye & Timbulto (2000)]; and (2) analysis of hydrometeorological obtained from local data providers, e.g. Ghana's Meteorology and Hydrology Departments, University Departments, CSIR Research Institutes and the GLOWA-Volta Project (ZEF, 1999). The data extracted from these sources showed that annual river discharges in the savannah Volta basin has declined by about 23-35% since 1970, but the level of rainfall decline is much less (~16%). At the same time, widespread land surface deterioration (i.e. soil and vegetation) has occurred contributing to about $0.5^0$C rise in temperature (Paturel *et al.*, 1997). Given this background, it has been hypothesized that increased evapotranspiration may have accounted for water losses (Gyau-Boakye & Timbulto, 2000; Rosenberg *et al.,* 1990). Looking at the progressive decline of the Volta Lake at the Akosombo dam site (downstream in Ghana) over the last two decades, evaporation losses may well be one of the crucial factors involved.

Although hydrological models are a useful way of predicting evapotranspiration and regional water balance, their implementation in West Africa is often confronted by

[2] SEBAL = Surface Energy Balance for Land algorithm

a scarcity of ground data (Jung, 2006; Schuol & Abaspour, 2006). This is the reason why previous modelling attempts were either unsuccessful or depended on local ground truth data (Paturel *et al.*, 1997; Gyau-Boakye & Timbulto, 2000; Jung, 2006; Schuol & Abbaspour, 2006). Detailed characterisation of vegetation cover and how this controls *ET* processes is a critical issue because the Volta basin covers a very large area and the land cover is extremely heterogeneous. Ten years ago, spatial hydrological modelling was seen as a difficult task because of the scarcity of satellite-based modelling tools. However, given the huge increase in computer power, advances in satellite-based modelling technologies and development of comprehensive analytical tools such as ARC-Hydro GIS, current hydrological research need not be limited to records from sparsely distributed point measurements (Cruise & Miller, 2003). This is where Earth observation based models such as the SEBAL can be very useful. Recent research has shown that it is feasible to model energy and water fluxes using the SEBAL algorithm, which may be parameterized by satellite measurements (Bastiannssen *et al.*, 1998 a&b; Morse *et al.*, 2000; Mekonnen, 2005; Brata *et al.*, 2006). SEBAL has many advantages, hence its adoption here. First, SEBAL has a successful record for energy balance calculation across a wide range of landscapes including West Africa (see Bastiannssen *et al.*, 1998b). Secondly, it has very minimal data inputs and can be parameterized by a range of high-resolution (e.g. ASTER, Landsat) and coarse-resolution (e.g. AVHRR, MODIS, AATSR) satellite data (Parks *et al.*, 1998; Mekonnen, 2005; Jiang & Islam, 2003; Brata *et al.*, 2006). Thirdly, the SEBAL is a public domain algorithm and may be exchanged freely among users. Fourthly, SEBAL is compatible with a wide range of image processing and analytical software including ENVI, ERDAS Imagine, ARC-GIS and MATLAB. Furthermore, SEBAL applies

widely used data formats such as GeoTIFF, which facilitates data manipulation, management and analysis.

1.2 To assess whether the coarse-scale (1 km) MODIS and AATSR sensors are useful sources of spatial data for *ET* modelling in this context.

Recognising the sheer size of the Volta basin (~400,000 $km^2$), its complex heterogeneous savannah landscape (see Figure 2.6) and the need to generate some of the key hydrology-based data through remote sensing, information about recent sensors was reviewed to assess their suitability for regional-scale energy balance studies (e.g. ASTER, Landsat ETM+, MODIS and AATSR). The MODIS Level 1B product was found to possess the following useful characteristics: (1) very well calibrated radiometric data; (2) wide range of spectral channels (36 bands); (3) spectral band passes for precise discrimination of vegetation types; (4) (atmospheric window) thermal bands for land surface temperature mapping; (5) availability of time-series data due to high temporal frequency (1-2 daily global overpass); and (6) freely available research product from the USGS website. The AATSR sensor was found to be useful because: (1) it provides data from both the reflectance and thermal infrared bands; (2) it is supplied to customers as a ready source of brightness temperatures; and (3) the sensor bands and spatial resolution (1 km) are similar to those of MODIS and therefore relevant for comparative studies. The 1 km spatial resolution was seen as a particularly important point, since a single MODIS scene for instance, was sufficient to map energy balance outputs, e.g. land cover, $T_s$, *ET* across the entire study site (5,300 $km^2$), which is unachievable using high-resolution spatial data such as Landsat ETM+ or ASTER.

1.3 To apply the NASA's SRTM DEM for delineation of savannah catchments needed as "substrate" for evapotranspiration (*ET*) and hydrological modelling.

In the absence of high quality digital versions of topographic data in the Volta basin, a DEM produced from SRTM data was used to define the Volta catchment boundary, which hitherto, had been imprecise. Based on *Terrain Pre-processing* modules of the ARC-Hydro software package, all the main Volta tributaries were delineated, including detailed hydrological characteristics like flow direction, drainage points and flow accumulation (Figure 3.2). There were initial problems using the Volta DEM because of mismatch of some of the drainage networks resulting from interpolation of "void pixels" (pixels with no data) originally present in the raw data. However, a new SRTM Level 2 "Water Bodies" product has been developed by NASA to address the issue of "void pixels", which means improvement of the Volta DEM may potentially lead to its application in topographic hydrological models.

1.4 To apply ASTER and Landsat ETM+ data as sources of detailed information for guiding fieldwork and image classification, land cover mapping and validation of spatial estimates of energy and water balance parameters.

Because the spectral variability of land surface targets reduces remarkably at 1 km grid scale and also because of surface heterogeneity, an ASTER image (15 m resolution) and a Landsat ETM+ scene (30 m resolution) acquired on 27$^{th}$ December 2000 and 5$^{th}$ January 2004 respectively, were applied as sources of detailed land surface information and used for different purposes (see Table 7.1). The ASTER scene was used in the field as a source of ground truth information. Specifically, it was used

to locate and guide the selection of sites for the installation of field equipment. It was also used to help locate ground control points, which were subsequently used for classifying the Landsat image. Similarly, the Landsat scene was used to: (1) derive land cover/use classification and evapotranspiration (*ET*) maps and as a complementary source of ground truth information to guide fieldwork; (2) map the wettest and driest pixels in aid of SEBAL-based energy balance modelling; and (3) validate the coarse-resolution (1 km) MODIS and AATSR *ET* models (Figure 7.17).

1.5 To validate the spatial estimates of *ET* using a variety of data sources: (1) published data; (2) scintillometer (eddy correlation) observations; (3) Landsat ETM+ data; and (4) local-scale Penman-Monteith estimates.

The energy and water balance results were evaluated using a variety of methods. The evaluation strategy involved initial validation of net radiation and subsequently, energy balance parameters at the regional and local-scale. Diurnal net radiation determined from the MODIS sensor compared well with radiometer results published by Jegede (1995) over the savannah Osu catchment in Central Nigeria. The same results compared well with scintillometer observations in the Tamale savannah Volta catchment recorded by the GLOWA-Volta Experimental Team. In both cases, diurnal net radiation followed a sinusoidal model with peak radiation around midday at 400 – 450 W $m^{-2}$ (Figure 7.10). On a daily basis, the MODIS instrument slightly under-predicted net radiation by about 40W $m^{-2}$, which is not unreasonable in comparison with published error margins for vegetated catchments.

Similarly, latent heat flux (i.e. *ET*) derived from the net radiation (Figure 5.1) approach was evaluated against GLOWA-Volta ground measurements. In this case

too, there was good agreement between the two measurements ($R^2$ = 0.71), but as expected, MODIS under-predicted regional *ET* by about 22W $m^{-2}$, which is also an acceptable error margin. Following this, both MODIS and AATSR *ET* results were evaluated using high-resolution Landsat ETM+ predictions. Here, the MODIS instrument correlated much better ($R^2$ = 0.71) against its Landsat counterpart than the AATSR sensor ($R^2$ = 0.13) mainly because the MODIS and Landsat have much similar sensor calibration systems. The AATSR sensor was poorly correlated mainly because of its different calibration system. Also, the discrepancies between the Landsat and its coarse-resolution counterparts may be explained by scale-mismatch. Further, predictions from the Penman-Monteith and satellite methods were validated against ground *ET* observations over the Tamale district measured by the GLOWA-Volta team. As expected, the average daily *ET* predicted by the MODIS sensor (2.07 mm $day^{-1}$) more closely followed the Penman-Monteith method (3.90 mm $day^{-1}$) than the AATSR sensor (1.21 mm $day^{-1}$) (see Table 7.10 for details). Variation in the results was explained by differences in modelling techniques as well as sensor calibration systems.

1.6 To demonstrate how spatially derived *ET* data may be verified using sensitivity experiments and subsequently used as inputs to new-generation hydrological models (e.g. the modified Pitman model) for predicting ungauged catchments upstream the Volta Lake.

As a first step, runoff (*Q*) was predicted from savannah catchments using spatial estimates of *ET* and rainfall (*P*) as inputs to an approximated version of the regional water balance model ($Q = P - ET$); several boundary conditions were set, for example, constancy in soil moisture storage and soil evaporation in order to operate this model.

This was followed by analysis of flow sensitivity to declining scenarios of savannah biomass volume. The model predicted that runoff (mm) is absent ($Q$ = 0.0) over 90% of the Volta study area in the dry season, except a few un-vegetated areas in the Tamale district. It also showed that runoff can be strongly dependent on biomass density, which may be estimated using the NDVI. Although the model results closely agreed with measured runoff over the Tamale district, replication of the current study in West Africa may be limited by key factors such as unavailable high quality spatially distributed rainfall estimates, actual biomass data and soil evaporation models.

To illustrate how the above approach may be used for hydrological modelling; previous research in West Africa was first reviewed after which two examples of data integration schemes were proposed. In the first case, a data integration tool was proposed on the basis of satellite and ground-based parameterization of the modified Pitman model (Hughes *et al.,* 2006), which requires few input parameters, that is: (1) satellite-derived DEM, rainfall, *ET* and land-use/cover maps; (2) digital versions of soil and geology maps; and (3) monthly rainfall from ground networks. The expected output is a spatially-derived runoff map. In the second case, a data framework was designed to exclusively assimilate rainfall and *ET* estimates from satellite sensors such as NASA's TRMM and MODIS.

## 9.3 Limitations of the Modelling Approach

This research has been undertaken using two contrasting approaches to derive *ET* estimates: (1) parameterization of the (local-scale) Penman-Monteith equation using ground station meteorological data; and (2) parameterization of the (regional-scale) SEBAL algorithm using satellite observations. To achieve this, a number of key assumptions were made which, to some extent, imposed limitations on the model

outputs. This section discusses some of these limitations including modelling uncertainties and errors.

### 9.3.1 Uncertainties/Errors Associated with Local-scale Energy Balance Modelling

In Chapter 4, the average daily *ET* derived over the Tamale district was 3.90 mm $day^{-1}$ using the Penman-Monteith equation. This result has been used as part of the validation data for both empirical models (e.g. Thornthwaite-Grindley method) and satellite-based predictions. The reason is that the Penman-Monteith method is recognised as one the most accurate methods for deriving *ET* estimates (Allen *et al.*, 1998; FAO, 1998). But the question is whether this is a reasonable conclusion in terms of tropical catchments, where empirical data or environmental coefficients have not been previously derived for the optimization or verification of model outputs. In this context, the Penman-Monteith method could not be applied without applying crop coefficients ($K_c$), even though the method was empirically designed for the prediction of *ET* from single or dual crop/tree stands. The basic assumption in the application of $K_c$ to the Volta catchment was that the area is covered by >90% woodlands. This assumption is quite crude, given that the savannah is a highly complex landscape (Figure 7.14). The $K_c$ method is therefore user-dependent and presents considerable uncertainties. This probably explains why the Penman-Monteith method (3.90 mm $day^{-1}$) overestimated *ET* over the Tamale district compared with the GLOWA-based ground truth data (1.79 mm $day^{-1}$) (see Table 7.10).

### 9.3.2 Uncertainties/Errors Associated with Regional-scale Energy Balance Modelling

Regional and global-scale studies are often characterised by a number of uncertainties (Beven, 2006). In this case, the main uncertainties and error sources are discussed from four perspectives: (1) data errors; (2) application of the SEBAL algorithm; (3) $T_s$ modelling assumptions; and (4) uncertainties in the conceptual hydrological model.

There are a number of compelling studies which show that the MODIS and AATSR sensors are good sources of spatial for energy balance modelling data (Wan & Li, 1997; Wan, 1999; Prata, 2002; Coll *et al.*, 2004; Parks *et al.*, 2005; Sòria *et al.*, 2005; Brata *et al.* 2006). However, derivation of key model parameters from the raw reflectance and radiance data is not always simple and can aggregate errors in the model outputs. For example, calibration of the MODIS L1B data is not straightforward and if not properly executed can introduce errors (Appendices 3.5 & 3.6). Also, AATSR coverage over the Volta basin has data gaps, which even though <10%, somewhat influenced the *ET* predictions (see Figure 7.13b).

The SEBAL algorithm comprises more than 20 computational steps or sub-models (Chapter 6). Some of these steps require decision-making by the user; for example, selection of the dry and wet indicator pixels, determination of prediction algorithms for surface roughness, characteristics of air pressure and selection of ground-based weather data and development of prediction equations for surface to air temperature differences (see Section 5.2.3 of Chapter 5). Although research by Morse *et al.* (2000) has concluded that SEBAL-based predictions are relatively immune to user choice, this cannot be completely ignored. Because of scale differences, identification of the wettest and driest pixels in Landsat TM data (30 m resolution) for

instance, is much easier than MODIS and AATSR. Also, this operation is highly subjective, which makes user experience quite important. A source of error here is execution of spatial correlation techniques to geographically locate "pixels of extreme wetness values" in the MODIS/AATSR imagery from a single Landsat scene.

SEBAL suffers from two major weaknesses: (1) the study area must be a uniform flat terrain; and (2) SEBAL assumes no 24-hour heat carry-over for large water bodies (Morse *et al.*, 2000). Fortunately, the study area is relatively flat and most of the stream widths are much narrower than 100 m, so, the area is not significantly affected by these assumptions. However, the research was affected by the following uncertainties: (1) extrapolation of *ET* models at the time of the satellite overpass to longer periods; and (2) SEBAL's dependence on NDVI as a surrogate for land cover change. The accuracy of SEBAL is potentially limited by extrapolating the *ET* predicted at the time of the satellite overpass to the entire day of the overpass. Further work is needed to understand if the *ET* is constant over a typical day in the Volta basin or if some adjustment is needed to extrapolate the *ET* from the satellite overpass at 10:00 am to the entire day. This may require for example, extensive field-based measurements of soil heat flux or a coupled soil-water balance model in order to accurately extrapolate the satellite data.

Chapter 7 partly addressed the issue of SEBAL's dependence on NDVI for land cover changes. The *ET* models are influenced by this. More work is needed to examine, for instance, the sensitivity of *ET* using other vegetation data such as leaf area index (LAI). It may also be important to examine the seasonal variations in vegetation cover from other test sites. Similarly, the integration of ground-based emissivity may potentially improve $T_s$ modelling compared to empirical emissivity models and derived coefficients (see Equation 5.10).

SEBAL integrates ground air temperature data ($T_a$) in order to predict sensible heat (see Equation 5.14). This is user-dependent and presents another source of uncertainty. The question is whether gridded global temperature data may improve SEBAL predictions compared to ground station data. With the increasing availability of global $T_a$ products (e.g. NOAA's Microwave Sounding Unit-2R (Christy & Spencer, 1995); UK's Hadley Centre HadRT2 data (Parker *et al.*, 1998)), the sensitivity of such data on SEBAL predictions remains to be examined.

Related to the above, the errors observed in Figures 7.13, 7.15, 7.17 may be seen from the dependency of the $T_s$ retrieval algorithm on atmospheric conditions (see Section 5.4). For example, the main influences on top-of-atmosphere measurements in the infrared are water vapour, atmospheric temperature and the surface-air temperature difference. Prata (2002) has shown that variation exists in the $T_s$ algorithm with changing atmospheric water vapour for the ideal tropical atmosphere. For the ideal situation, the gradient of plots between $T_s$ and water vapour should be zero with zero bias, but in reality, this is not the case. This means that the $T_s$ model might yield a diurnal bias at midday when significant variation in water vapour does occur. Thus, some of the inconsistencies in the above results may be found here.

The errors observed in the conceptual hydrological model proposed in Chapter 8 (Tables 2 & 3 and Figure 8.4) are essentially a carry-over from the energy balance modelling approach. For example, the *ET* inputs in Table 8.2 cannot be separated from the aggregated errors from the results displayed in Chapter 7. These include limitations of the SEBAL method and the assumptions which were required to derive $T_s$ (e.g. constancy in surface emissivity, uniformity of atmospheric water vapour, grouping of land cover types, etc.). Similarly, the errors in the biomass-runoff models (Table 8.3 and Figure 8.4) emanate from over-reliance on NDVI as an imperfect substitute for

biomass density. Further, the conceptual model is limited by practical problems such as scarcity of ground station rainfall, soil moisture and evaporation data, spatial interpolation techniques and water balance model assumptions (e.g. constancy in soil moisture storage). These effects will need to be better characterised in subsequent research.

## 9.4 Conclusions

Given the above discussion, the thesis has drawn the following conclusions:

(1) The sheer size of the Volta basin, the sparse coverage of hydrometeorological network stations and the heterogeneity of savannah land cover makes remote sensing a critical source of spatial data for energy and water balance studies.

(2) Although the Penman-Monteith method overestimates *ET* based on ground truth data (1.79 mm $day^{-1}$), it still produces better results (~3.90 mm $day^{-1}$ for the Tamale district) than pan evaporation measurements, which tends to exaggerate actual evaporation by 5.5 – 11.0 mm $day^{-1}$.

(3) Extrapolation of the Penman-Monteith approach to cover the entire Volta basin is not feasible because of wide differences in microclimatic and environmental parameters such as air temperature and wind speed and land cover.

(4) The Grindley (1970) soil moisture balance model is a good method for estimating actual soil moisture and evapotranspiration in the study area; in this case, no difference exists between the Grindley-Thornthwaite and Grindley-Penman-Monteith combination approach when compared with regional water balance data.

(5) Recent medium-resolution (1 km) sensors such as MODIS are a good source of data for measuring regional-scale energy and water fluxes such as *ET*. The

AATSR sensor correlated poorly with a detailed Landsat ETM+ result ($R^2$ = 0.13) because of differences in their sensor calibration. The MODIS sensor performed much better ($R^2$ = 0.71) because of the similarity in sensor calibration with Landsat.

(6) The mean daily *ET* estimates predicted by MODIS (2.07 mm $day^{-1}$) for the Tamale urban catchment is in reasonable agreement with local scintillometer measurements (eddy correlation method) (1.79 mm $day^{-1}$) and estimates from the Penman-Monteith method (3.90 mm $day^{-1}$).

(7) The SEBAL algorithm is potentially useful for assimilating a wide variety of satellite imagery and can be easily driven by MATLAB programming functions to derive energy and water balance parameters. However, a number of important questions remain about the application of the SEBAL scheme, of which iterative solution of the sensible heat equation is the biggest issue.

(7) The satellite-based *ET* model is potentially useful for estimating runoff in the Volta savannah area. In this case, runoff is absent for over 90% of the area in the dry season because of lack of rainfall recharge. As a result, streamflows are largely controlled by groundwater discharge. Estimation of annual runoff using the *ET* model is difficult because of lack of satellite data for the whole year.

(9) The *ET* model can be combined with ground or satellite rainfall data as inputs to new-generation hydrological models (e.g. the modified Pitman model) or for direct rapid assessment of inflows to the Volta Lake.

(10) The above energy and water balance modelling approach may be useful in deriving key data as inputs for hydrological models applicable to West Africa; however, several limitations need to be addressed first. For example: (1) the SEBAL method lacks sufficient validation in West Africa; (2) the SEBAL is

heavily dependent on NDVI as index for biomass volume; (3) the satellite-based approach depends heavily on empirical models, e.g. $T_s$ algorithm, which needs further validation; (4) some uncertainties remain about model inputs and assumptions that relate to derivation of variables such as emissivity and constancy in soil moisture storage; and (5) the conceptual runoff model presented in Chapter 8 has not been validated because of lack of rainfall data.

## 9.5 Future Research Directions

(1) This research has focussed on regional *ET* modelling based on remote sensing methods rather than hydrological modelling. The most critical question is: how can the *ET* model be effectively used for hydrological modelling? This is a challenging and wide-ranging research area which would need to be further pursued using some of the proposals described in Section 8.3 in Chapter 8.

(2) More specifically, the research has shown that both the MODIS and AATSR Level 1 data may potentially be used for operational regional energy and water balance studies; however, their capabilities have been shown to vary considerably because of differences in sensor calibration and variation in the widths of their solar bands. It will be interesting to see, for instance, how the better calibrated AATSR Level 2 compares with the current results.

(3) The *ET* model was derived principally on a daily time scale, but under dry tropical conditions bi-weekly or monthly estimates of *ET* may be more important, for example, the operational management of the Volta Lake. With the release of new 1km Level 3 MODIS products such as the 8-day LST (land surface temperature) (MOD11A2), 16-day VI (vegetation index) (MOD13A2) and 12-month LCD (land cover dynamics) data, it may be reasonable to predict

actual monthly lake evaporation using these new products. A useful approach will be to follow and validate the SEBAL method using aggregated Penman-Monteith and/or Thornthwaite-Grindley (monthly) estimates (see Chapter 4). If reasonable correlations emerge between, say, the remote sensing and Thorthwaite methods, regression equations could then be developed, on which basis the remote sensing tools could be assessed for potential operationalization.

(4) A number of land surface schemes have been developed, such as Two-source Energy Balance, Surface Energy Balance System and Single-source Energy Balance and tested with Landsat TM and AAVHR. It would be useful to cross-correlate these algorithms with MODIS and AATSR data to determine their efficiency; this may lead to operational simplification of the algorithms.

(5) The current research has shown that runoff prediction in the dry "winter" months (November – March) is seriously constrained by lack of rainfall data. Research covering the annual cycle (including wet season) would be important in revealing additional information about regional flow patterns as well as the sensitivity of runoff to changes in land cover. Additionally, more research is needed to monitor flood patterns in the Tamale district.

(6) There is the need to show the extent to which streamflows are controlled by groundwater recharge during the dry season, which may be done through a coupled runoff-groundwater model. This approach could be explored through two key international projects in which I am currently involved: (1) the UNESCO/European Space Agency (ESA) TIGER Project which concerns the application of ENVISAT data products for water resources assessment in the Volta Lake region; and (2) the UNESCO Groundwater Applications of Remote Sensing (GARS) Project which is targeted at coupled runoff-groundwater

modelling in the same area. These projects have recently been discussed at the UNESCO/Integrated Global Water Cycle Observation (IGWCO) conference scheduled for Washington D.C. in March 2007.

(7) New data assimilation tools have been proposed to help drive low-input-data hydrological models such as the modified Pitman model, using satellite rainfall and *ET* estimates as input data. With the successful testing of similar satellite-based methods (e.g. PERSIANN rainfall method) in the southern part of Africa (Hughes *et al.,* 2006), evaluation of the current tools in the Volta Lake basin may be a useful extension of this research.

# REFERENCES

ABDULMUMIN, S. (1988) Crop coefficient and water requirements in the irrigated wheat (*Tritichum aestrium*) in the Nigerian Savannah Zone. *Irrigation Science,* 9 (3):177-186.

ADU, S.V. (1995) Soils of the Bole-Bamboi Area - Northern Region, Ghana. Soil Research Institute (CSIR), *Memoir No.* 14:16-52.

AGRHYMET (1998) Climate change and agro-hydrology in the Sahel (Permanent Interstate Committee for Drought Control in the Sahel (CILSS) Agro-hydro meteorology Centre (AGRHYMET) *Monthly Bulletin, No. M - 08/1998.*

AGYARE, W.A. (2004) Soil characterisation and modelling of spatial distribution of saturated hydraulic conductivity at two sites in the Volta basin of Ghana. *Ecology & Development Series,* No. 17, Cuvillier Verlag, Göttingen. ZEF-University of Bonn, Germany, 194pp.

AGYEPONG, G.T., DUADZE, S.E.K., ANNOR, J., DONYUO, S.S.B., TETTEH, E. & GYEABOUR, A. (1999) Land use and land cover map of Ghana. *Techn. Bulletin #3.* Remote Sensing Applications Unit – University of Ghana, Legon, Accra; 59pp.

ALLEAUME, S., HÉLLY, C., LE ROUX, J., KORONTZI, S, SWAP, R.J., SHUGART, R.R. & JUSTICE, C.O. (2005) Using MODIS to evaluate biomass burning in Southern African savannahs: a case study in Etosha, *International Journal of Remote Sensing,* (26) 19, 4219-4237.

ALLEN, R.G., PEREIRA, L.S., RAES, D. & SMITH, M. (1998) Crop evapotranspiration – Guidelines for computing crop water requirements – *FAO Irrigation Paper No. 56,* UN/FAO, Rome.

ALLEN, R.G. (1996) Assessing integrity of weather data for use in reference evapotranspiration estimation. *Journal of Irrigation & Drainage,* Eng. Division, ASCE 122 (2):97-106.

ALLEN, R.G., SMITH, M., PERRIER, A. & PEREIRA, L.S. (1994) An update of the definition of reference evapotranspiration, *ICID Bulletin* 43 (2):1-34.

ALLEN, R.G., PRUEGER, J. & HILL, R.W. (1992) Evapotranspiration from isolated stands of hydrophytes: Cattail and Bulrush, *Transactions ASAE* 35 (2):1-34.

AJAYI, A.E. (2004) Surface runoff and infiltration processes in the Volta Basin, West Africa: Observation and Modelling. *Ecology and Development Series,* No. 18, 2004. ZEF, University of Bonn, Germany, Cuvillier Verlag Göttingen, 115pp.

AMISIGO, B.A. & VAN DE GIESEN, N. (2005) Using a spatio-temporal dynamic state-space model with the EM algorithm to patch gaps in daily riverflow series, with examples from the Volta Basin, West Africa, *Hydrology and Earth System Sciences Discuss*, 2: 449 – 481.

ANDERSON, M.G. & BATES, P.D. (eds.) (2001) *Model Validation: Perspectives in Hydrological Science,* J. Wiley & Sons, Chichester, England, 461pp.

ANDERSON, M. G. & BURT, T. P. (eds.) (1985) *Hydrological Forecasting.* J. Wiley & Sons Ltd., Chichester, England. 604pp.

ANDRÉ, J.-C., GOUTORBE, J.-P., PERRIER, A., BECKER, F., BESSLEMOULIN, P., BOUGEAULT, P., ANDREINI, M. & VAN DE GIESEN, N. (2001) The

GLOWA-Volta Project – Sustainable Water Use in the Volta Basin. *IHDP Homepage (11/04).*

ASCE (1990) Evapotranspiration and Irrigation Water Requirements: *A Manual American Society of Civil Engineers (ASCE)*, Committee on Irrigation Water Requirements of the Irrigation and Drainage Division of the ASCE, 1990, 332 pp.

ASDAK, C., JARVIS, P.G., VAN GARDENGEN, P. & FRASER, A. (1998) Rainfall interception loss in unlogged and logged forest areas of Central Kalimanta, Indonesia. *J. Hydrology 206: 237-244.*

ASIAMAH, R.D. (2002) Plinthite development in upland agricultural soils in Ghana. In: *Proceedings of the WCCS*, 1448:1-12, August, 2002.

ASRAR, G., FUCHS, M., KANEMASU, E.T. & HATFIELD, J.H. (1984) Estimating absorbed photosynthetic radiation and leaf area index from spectral reflectance in wheat. *Agronomy Journal*, 76: 300-306.

AYIBOTELE, N.B. (1993) Regional hydrology and water resources in the African humid tropics. In: *Hydrology and water management in the humid tropics*, eds. Bonnel, M., Hufschmidt, M.M. & Gladwell, J.S., University Press, Cambridge, p.112-134.

BALME, M., VISCHEL, T., LEBEL, T., PEUGEOT, C. & GALLE, S. (2006) Assessing the water balance in the Sahel: Impact of small scale rainfall variability on runoff. Part 1: Rainfall variability analysis, *Journal of Hydrology,* 331: 336 – 348.

BAILY, B., COLLIER, P., FARRES, P., INKPEN, R. & PEARSON, A. (2003) Comparative assessment of analytical and digital photogrammetric methods in the construction of DEMs of geomorphological forms, *Earth Surface Processes and Landforms,* 28, 307-320.

BASTIAANSSEN W.G.M. (2000) SEBAL-based sensible and latent heat fluxes in the irrigated Gediz Basin, Turkey. *J. Hydrology,* 229 (1&2): 87-100.

BASTIANNSSEN, W.G.M., MENENTI, M., FEDDES, R.A. & HOLTSLAG, A.A.M. (1998) A remote sensing surface energy balance algorithm for land (SEBAL) – Part 1: Formulation. *Journal of Hydrology,* 228: 198-212.

BASTIAANSSEN, W.G.M., PELGRUM, H., WANG, J. MA, J., MORENO, J., ROERINK, G.J. & VAN DER WAL, T. (1998) The Surface Energy Balance Algorithm for Land (SEBAL): Part 2 validation, *Journal of Hydrology,* 212-213: 213-229.

BASTIAANSSEN, W.G.M., PELGRUM, H, MENENTI, M. & FEDDES, R.A. (1996) Estimation of surface resistance and Priestley-Taylor α-parameter at different scales, In: Stewart et al. (1996) (eds.) *Scaling up in hydrology using remote sensing,* J. Wiley & Sons, Chichester, p.255-262.

BASTIANNSSEN, W.G.M. (1995) Regionalization of surface flux densities and moisture indicators in composite terrain: A remote sensing approach under clear skies in Mediterranean climate, *Ph.D. Thesis,* Wageningen University, The Netherlands, 286pp.

BATES, D.A. (1962) Rural water supplies. In: Wills, J.B. (ed.) *Agriculture and land use in Ghana.* Ghana Ministry of Food and Agriculture, pp. 62-76. Oxford University Press, London.

BECKER, F. & LI, Z-L. (1990) Towards a local split-window method over land surfaces, *International Journal of Remote Sensing,* 11:369-394.

BEVEN, K.J. (2006) A manifesto for the equifinality thesis, *J. Hydrology,* 320: 18 – 36.

BEVEN, K. J. (2001) Calibration, Validation and Equifinality in Hydrological Modelling, Anderson, M. G. and Bates, P. D. (eds.), *Model Validation: Perspectives in Hydrological Science,* Wiley, Chichester, 43-55.

BEVEN, K.J. (2001) *Rainfall-runoff modelling – The Primer.* John Wiley & Sons, Chichester, England, 360pp.

BISHT, G., VENTURINI, V., JIANG, L. & ISLAM, S. (2005) Estimation of the net radiation using MODIS data for clear-sky dates. *Remote Sensing of Environment,* 97: 52 – 97.

BLANEY, H.F. & CRIDDLE, W.D. (1950) Determining water requirements in irrigated areas from climatological and irrigation data, *USDA Soil Conservation Service, SCS-TP96,* 44pp.

BOLLE, H. J., ANDRÉ, J. C., ARRUE, J. L., BARTH, H. K., BESSELMOULIN, P., BRASSA, A., DE BRUIN, H., CRUCES, J., ENGMAN, E. T., EVANS, D. L., VAN DE GRIEND, A. KABAT, P., DE SANTA OLLALA M., SHUTTLEWORTH, W. J., STRICKER, J., VAUCLIN, M. & WICKLAND, D. (1993) EFEEDA: European field experiment in a desertification-threatened area. *Annales Geophysicae* 11:173-189.

BOLCH, T. (2004) Using ASTER and SRTM DEMs for studying glaciers and rock-glaciers in Northern Tien Shan. Proc. Part 1 – *Conference on Theoretical and Applied problems of Geography on a Boundary of Centuries*, Almaty, Kazakhstan, June 2004; p.254-258.

BORMANN, H. & DIEKKRUGER, B. (2003) Possibilities and limitations of regional hydrological models applied within an environmental change study in Benin (West Africa), *Physics & Chemistry of the Earth,* 28/33-36: 1323 – 1332.

BOULAIN, N. CAPPALAERE, B., SEGUIS, L., GIGNOUX, J. & PEUGEOT, C. (2006) Hydrologic and land-use impacts on vegetation growth and NPP at the watershed scale in a semi-arid environment, *Regional Environmental Change,* 6:147 – 156.

BRAIMOH, A.K. (2004) Modelling landuse change in the Volta Basin of Ghana. In: *Ecology & Development Series,* 14:1-161 Cuvillier Verlag Göttingen, Germany. ZEF-University of Bonn.

BRATA, N., ISLAM, S., VENTURINI, V, BISHT, G., & JIANG, L. (2006) Estimation and comparison of evapotranspiration from MODIS and AVHRR sensors for clear sky days over the Southern Great Plains, *Remote Sensing of Environment,* 103: 1-15.

BRUNET, Y., BRUTSAERT, W., CARLSON, T., SHUTTLEWORTH, J. & SCHMUGGE, T., TACONET, O., VIDAL-MADJAR, D. & WEILL, A. (1988) HAPEX-MOBILHY: first results from the special observation period. *Ann. Geophys.* 6:477-492.

BURT, T. & SHAHGEDANOVA, M. (1998) An historical record of evaporation losses since 1815 calculated using long-term observations from the Radcliffe Meteorological Station, Oxford, England, *Journal of Hydrology,* 205:101-111.

CARLSON, T. N., PERRY, E. M. & SCHMUGGE, T. J. (1990) Remote estimation of soil moisture availability and fractional vegetation cover for agricultural fields. *Agricultural and Forest Meteorology,* 52: 45 - 69.

CHEMIN, Y. (2003) Evapotranspiration of crops by remote sensing using the energy balance based algorithms, *Technical Report B231/2003*, Asian Institute of Technology, Bangkok, Thailand, 16pp.

CHEN, J-M. & CIHLAR, J. (1996) Retrieving leaf area index of boreal conifer forests using Landsat TM images, *Remote Sensing of Environment,* 57: 153-162.

CHEN, J-M. & ZHANG, R-H. (1989) Studies on the measurements of crop emissivity and sky temperature. *Agricultural and Forest Meteorology,* 49: 23 – 34.

CHEN, T.S. & OHRING, G. (1985) On the relationship between clear-sky planetary and surface albedos: a parameterization for simple energy balance climate models, *Advances in Space Research,* (5) 6:141-144.

CHOUDHURY, B.J. (1991) Potential and limits of vegetation indices for LAI and APAR assessment, *Remote Sensing of Environment,* 35: 161-173.

CHOUDHURY, B. J., IDSO, S. B., and REGINATO, R. J. (1987) Analysis of an empirical model for soil heat flux under a growing wheat crop for estimating evapotranspiration by an infrared-temperature based energy balance equation. *Agricultural and Forest Meteorology* 39: 283 - 297.

CHRISTY, J.R. & SPENCER, R.W. (1995) Assessment of precision in temperatures from the microwave sounding units. *Climate Change,* 30:97-102.

CIHLAR, J., CHEN, J.M. & LI, Z. (1997) Seasonal AVHRR multichannel data sets and products for scaling up biospheric processes, *Journal of Geophysical Research,* 102:29625-29640.

CLOTHIER, B. E., CLAWSON, K. L., PINTER, JR., P. J., MORAN, M. S., REGINATO, R. J., and JACKSON, R. D. (1986) Estimation of soil heat flux from net radiation during the growth of Alfalfa. *Agricultural and Forest Meteorology* 37: 319 - 329.

COHEN, W.B., MAIERSPERGER, T.K., GOWER, S.T. & TURNER, D.P. (2003) An improved strategy for regression of biophysical variables and Landsat ETM+ data, *Remote Sensing of Environment,* 84: 561-571.

COLBY, J. D. & KEATING, P. L. (1998) Land cover classification using Landsat TM imagery in the tropical highlands: the influence of anisotropic reflectance. *International Journal of Remote Sensing* 19 (8): 1479 – 1500.

COLL, C., VALOR, E., CASELLES, V., NICLOS, R., RIVAS, R., SANCHEZ, J.M., & GALVE, J.M. (2004) Evaluation of the ENVISAT-AATSR land surface temperature algorithm with ground measurements in the Valencia test site, *Proceedings of the 2004 ENVISAT & ERS Symposium*, Salzburg, Austria, 6-10 September 2004. (ESA SP-572, April 2005).

COOK, P. G., HATTON, T. J., PIDSLEY, D., HERCZEG, A. L., HELD, A., O'GRADY, A. & EAMUS, D. (1998) Water balance of a tropical woodland ecosystem, Northern Australia: a combination of micro-meteorological, soil physical and groundwater chemical approaches, *Technical Report #67*, 31pp.

CRESWELL, M.P., MORSE, A.P., THOMSOM, M.C. & CONNOR, S.J. (1999) Estimating surface air temperatures, from Meteosat land surface temperatures using an empirical solar zenith angle model, *International Journal of Remote Sensing,* 20:1125-1132.

CRUISE, J. F. & MILLER, R. L. (2003) Hydrologic modelling with remotely sensed databases. In *GIS for Water Resources and Watershed Management* J.G. Lyon (Ed) pp. 189-205.

CURRAN, P. J. & ATKINSON, P. M. (1998) Geostatistics in remote sensing, *Progress in Physical Geography,* 22 (1): 61 – 78.

CURRAN, P.J. (1983) Multispectral remote sensing for the estimation of green leaf area index. *Transactions of Royal Society London*, Ser. A 309:257-270.

DASH, P., GÖTTSCHEM F-M., OLESEN, F-S., & FISCHER, H. (2002) Land surface temperature and emissivity estimation from passive sensor data: Theory and practice, - Current trends, *International Journal of Remote Sensing,* 23:2563-2594.

DAUGHTRY, C. S. T., KUSTAS, W. P., MORAN, M. S., PINTER, JR., P. J., JACKSON, R. D., BROWN, P. W., NICHOLS, W. D., and GAY, L. W. (1990) Spectral estimates of net radiation and soil heat flux. *Remote Sensing of Environment* 32: 111 - 124.

DAVIS, P.A. & TARPLEY, J.D. (1983) Estimation of shelter temperatures from operational satellite sounder data. *Journal of Climatology & Applied Meteorology,* 22: 369-376.

DE BRUIN, H.A.R., NIEVEEN, J.P., DE WEKKER, S.F.I. & HEUSINKVELD, B.G. (1996) Large scale aperture scintillometry over a 4.8 km path for measuring areally-average sensible heat flux: a case study. *Proc. 22nd AMS Symposium on Agriculture and Forest Meteorology*, Feb. 1996, Georgia, Atlanta, USA, p.69-71.

DE BRUIN, H.A.R. (1987) From Penman to Makkink, In: Hooghart & Warmerdam (1987) (Eds.) *Evaporation and weather proceedings and information*, TNO Committee on Hydrological Research, The Hague, The Netherlands, p.5-30.

DENISSON, P.E., ROBERTS, D.A., PETERSON, S.H. & RECHEL, J. (2005) Use of normalised difference water index for monitoring live fuel moisture *International Journal of Remote Sensing* 26 (5): 1035-1042.

DI BELLA, C. M., REBELLA, C. M. & PARUELO, J. M. (2000) Evapotranspiration estimates using NOAA AVHRR imagery in the Pampa region of Argentina. *Int. J. Remote Sensing,* 21 (4): 791 – 797.

DICKINSON, R.E., HENDERSON-SELLERS, A. & P.J. KENNEDY (1993) Biosphere–Atmsophere Transfer Scheme (BATS) Version 1E as coupled to the NCAR Community Climate Model. *NCAR Tech. Note NCAR/TN-387+STR*, 72 pp.

DONOGHUE, D. N. M., WATT, P. J., COX, N. J., DUNFORD, R. W., WILSON, J., STABLES, S. & SMITH, S. (2004) An evaluation of the use of satellite data for monitoring early development of young Sitka spruce plantations. *Forestry*, 77:383-396.

DONOGHUE, D.N.M. (2000) Remote Sensing: sensors and applications. In *Progress in Physical Geography,* 24 (3): 407-414.

DOORENBOS, J. & PRUITT, W.O. (1977) Guidelines for predicting crop water requirements, *FAO Irrigation Drainage Paper* No. 24, UN-FAO, Rome, Italy, 144pp.

DOOGERS, P. (2000) Estimating actual evapotranspiration using a detailed agro-hydrological model, *Journal of Hydrology,* 229:50-58.

DUADZE, S.E.K. (2004) Land use and land cover study of the savannah ecosystem in the Upper West Region (Ghana) using remote sensing In: *Ecology and Development Series* No. 16, 2004; 241pp.

EL MAAYAR, M. & CHEN, J. M. (2006) Spatial scaling of evapotranspiration as affected by heterogeneities in vegetation, topography and soil texture. *Remote Sensing of Environment,* 102: 33 – 51.

ENTEKHABI D. AND EAGLESON P. (1989), Land Surface Hydrology Parameterisation for the atmospheric General Circulation Models Including Subgrid Scale Spatial Variability, *Journal of Climate* 2: 816-831.

ENGMAN, T. (2004) Recent remote sensing advances in hydrology, *J. Hydrological Sciences,* 289: 392-400, IAHS Publ. 289.

FAO (1998) Evapotranspiration: Guidelines for computing crop water requirements – *UN/FAO Irrigation and Drainage Papers No. 56*, Land and Water Division, FAO Press, Rome Italy. 300pp.

FAO (1977) Guidelines for predicting crop water requirements, *Irrigation & Drainage Paper No. 24, UN-FAO*, Land & Water Development Division, Rome, Italy, 144pp.

FAMIGLIETTI J.S. and WOOD E.F. (1995) Effects of Spatial Variability and Scale on Areally Averaged Evapotranspiration. *Water Resources Research,* 31: 699-712.

FRENCH, A. N., JACOB, F., ANDERSON, M. C., KUSTAS, W. P., TIMMERMANSS, W., GIESKE, A., *et al.* (2005) Surface energy fluxes with the Advanced Spaceborne Thermal Emission and Reflection Radiometer (ASTER) at the Iowa 2002 SMACEX site (USA). *Remote Sensing of Environment,* 99: 55 – 65.

FUCHS, M. & TURNER, C. B. (1966) Infrared thermometry of vegetation. *Agron. J.* 58: 579 – 601.

GAMON, J.A., FIELD, C.B., GOULDEN, M.L. & GRIFFEN, K.L. et al. (1995) Relationships between NDVI, canopy structure and photosynthesis in three California vegetation types, *Ecological Applications,* 5(1):28 – 41.

GAN, T.Y. DLAMINI, E.M. & BIFTU, G.F. (1997) Effects of model complexity and structure, data quality and objective functions on hydrological modelling, *Journal of Hydrology,* 182: 81 – 103.

GANGOPADHYAY, P.K., MAATHUIS, B. and van DIJK, P. (2005) ASTER-derived emissivity and coal-fire related surface temperature anomaly: a case study in Wuda, North China, *International Journal of Remote Sensing,* 26 (24): 5555-5571.

GENTINE, P., ENTHEKABI, D., CHEHBOUNI, A., BOULET, G. & DUCHEMIN, B. (2006) Analysis of diurnal evaporative fraction behaviour, *Technical Paper*, MIT Department of Civil and Environmental Engineering, Cambridge, USA, 4pp.

GHANA STATISCAL SERVICE (GSS) (2002) Population and Housing Census of Ghana. *Summary Report of Final Results*. GSS, Ministry Finance & Economic Planning. Medialite Co. Ltd. (2002) (variously paged).

GILLESPIE, A.R., KAHLE, A.B. AND WALKER, R.E. (1986) Colour enhancement of highly correlated images. Decorrelation and HIS contrast stretches. *Remote Sensing of Environment,* 20: 209-235.

GOETZ, S. J. (1997) Multi-sensor analysis of NDVI, surface temperature and biophysical variables at a mixed grassland site. *International Journal of Remote Sensing,* 18 (1): 71 – 94.

GOUTORBE, J. P., DOLMAN, A. J., GASH, J. H. C., KERR, Y. H., LEBEL, T., PRINCE, S. D. & STRICKER, J. N. M. (eds.) (1997) HAPEX-Sahel. Elsevier Science BV – Amsterdam, The Netherlands - Reprinted from *Journal of Hydrology*, 188-189/1-4.

GOUTORBE, J. P., LEBEL, T., TINGA, A., BESSEMOULIN, P., BROUWER, J., DOLMAN, H., GASH, J. H. C., HOEPFFNER, M. KABAT, P., KERR, Y. H., MONTENY, B., PRINCE, S., SÄID, F., SELLERS, P. & WALLACE, J. (1994) HAPEX-Sahel: a large-scale study of land-atmosphere interactions in the semi-arid tropics. *Annales Geophysicae* 12:53-64.

GOWARD, S. N., TURNER, S., DYE, D. G. & LIANG, S. (1994) The University of Maryland improved Global Vegetation Index product. *International Journal of Remote Sensing,* 15: 3365-3395.

GOWARD, S.N. & HUEMMERICH, K.F. (1992) Vegetation canopy PAR absorptance and the normalized difference vegetation index: An assessment using the SAIL model, *Remote Sensing Environment,* 39: 119-140.

GOWARD, S. N., MARKHAM, B., DYE, D. G., DULANEY, W. & YANG, J. (1991) Normalized difference vegetation index measurements from the Advanced Very High resolution Radiometer (AVHRR). *Remote Sensing of Environment,* 35: 257 – 277.

GREEN, A.A. AND CRAIG, M.D. (1985) Analysis of aircraft spectrometer data with logarithmic residuals. *JPL Publications 85-41*, p.111-119.

GRINDLEY, J. (1969) The calculation of actual evapotranspiration and soil moisture deficit over specified catchment areas, *Hydrological Memorandum No. 38*, Meteorological Office.

GYAU-BOAKYE, P. & TIMBULTO, J. W. (2000) The Volta Lake and declining rainfall and streamflows in the Volta river basin. *Environment, Development and Sustainability* 2: 1-10.

HASTENARTH, S. (2000) Interannual and long-term variability of upper-air circulation over the tropical Atlantic and West Africa in boreal summer. *International Journal Climatology* (20) 12:1415-1430.

HALLIWELL, D. and ROUSE, W. R. (1987) Soil heat flux in permafrost: Characteristics and Accuracy of measurement. *Journal of Climatology* 7: 571 – 584.

HAUFFE, H. K. (1989) Site characterisation of the West Ridge Upland Experimental Area (NAES). In: *Nyankpala Agricultural Experimental Station Research Report no. 6, Annual Report, 1987/8, NAES*, p139-154.

HENDERSON-SELLERS, A. & BROWN, V.B. (1992) PILPS: Project for Intercomparison of Land-surface Parameterisation Schemes, *Workshop Report and First Science Plan, IGPO Publication Series No. 5*, Science and Technology Corporation, Hampton, VA, 51pp.

HOOK, S. J., GABELL, A. R., GREEN, A. A. & KEALY, P.S. (1992) A comparison of techniques for extracting emissivity information from thermal infrared data for geologic studies, *Remote Sensing of Environment,* 42:123-135.

HERBECK, G.E. & MEYERS, J.S. (1970) Present day evapotranspiration measurement techniques, *Proc. ASCE*, HY7, 1381-1389.

HUBBARD, J. R. (2000) *Programming with C++*, 2nd Edition, McGraw-Hill Inc., New York, pp.16-45.

HSU, K., GUPTA, H.V., GAO, X., SOROOSHIAN, S. (1999) Estimation of physical variables from multi-channel remotely sensed imagery using a neural network: application to rainfall estimation, *Water Resources Research,* 35 (5), 1605–1618.

HUDAK, A., LEFSKY, M., COHEN, W. and BERTERRETCHE, M. (2002) Integration of Lidar and Landsat ETM+ data for estimating and mapping forest canopy height, *Remote Sensing of Environment* 82, 397-416.

HUETE, A. R. (1989) Soil influence in remotely sensed vegetation spectra. In: *Theory and Applications of Optical Remote Sensing,* ed. G. Asrar, New York, J. Wiley & Sons, pp. 107 – 141.

HUFFMAN, G.J., ADLER, R.F., MORRISSEY, M.M., CURTIS, S., JOYCE, R.J., MCGAVOCK, B., SUSSKIND, J. (2001). Global precipitation at one-degree daily resolution from multi-satellite observations, *Journal of Hydrometeorology*, 2, 36–50.

HUGHES, D.A. (2006) Comparison of satellite rainfall data with observations from gauging station networks, *Journal of Hydrology,* 327: 339 – 410.

HUGHES, D. A., ANDERSSON, L., WILK, J. & SAVENIJE, H. H. G. (2006) Regional calibration of the Pitman model for the Okavango River, *Journal of Hydrology,* 331: 30 – 42.

HUGHES, D.A. (2004) Three decades of hydrological modelling research in South Africa, *South Africa Journal of Science,* 100: 638 – 642.

HUGHES, D.A. (2002) The development of an information modelling system for regional water resources assessments, *Proc. 4th Int. Conf. on FRIEND, IAHS Publ.* No. 274: 43 – 49.

HUMES, K.S., KUSTAS, K.W. & MORAN, M.S. (1994) Use of remote sensing and reference site measurements to estimate instantaneous surface energy balance components over a semiarid rangeland watershed, *Water Resources Research,* (30) 5: 1363-1373.

HUSBAND, N. D. S. & MONTEITH, J. L. (1986) Radiative surface temperature and energy balance of a wheat canopy (1): Comparison of radiative and aerodynamic canopy temperature. *Boundary-Layer Meteorological,* 36: 1 – 17.

IDSO, S. B., AASE, J. K. and JACKSON, R. D. (1975) Net radiation and soil heat flux relations as influenced by soil water content variations. *Boundary-Layer Meteorology* 7: 113 – 122.

IQBAL, M. (1983) *Introduction to solar radiation.* Academic Press, Montreal, Canada, p.1-83.

IRIZARRY-ORTIZ, M. M, WANG, G. L. AND ELTAHIR, E. A. B. (2003) Role of the biosphere in the mid-Holocene climate of West Africa. *Journal of Geophysical Research Atmospheres* 108, doi: 10.1029/2001JD000989.

ISLAM, S., JIANG, L. & ELTAHIR, E. (2003) Satellite based evapotranspiration estimates. *Final project report*: South Florida Water Management District, Sept. 2003.

ITC (1995) Monitoring coal fires in North China: remote sensing and GIS approach, In: *ITC research conference program, abstracts and session reports*: February, 1995, pp. 67-74.

JACOBS, J. M., MYERS, D. A., ANDERSON, M. C. & DIAK, G. R. (2000) GOES surface insolation to estimate wetlands evapotranspiration. *Journal of Hydrology,* 266: 53 – 65.

JACOBSEN, A. & HANSEN, B. U. (1999) Estimation of the soil heat flux/net radiation ratio based on spectra vegetation indexes in high-latitude Arctic areas. *International of Journal of Remote Sensing,* 20, (2): 445 – 461.

JEGEDE, O. O. (1995) Diurnal variations of net radiation at a tropical station – Osu; Nigeria. *Theor. Appl. Climatology,* 58: 161 – 168.

JENSEN, J. R. (1983). Urban/Suburban Land Use Analysis. Chapter 30 in *Manual of Remote Sensing.* Ed. R. N. Colwell, Falls Church, Virginia: American Society of Photogrammetry.

JENSEN, M.E., BURMAN, R.D. & ALLEN, R.G. (ed.) (1990) Evapotranspiration and irrigation water requirements, *ASCE Manuals and reports on Engineering Practices, No. 70,* Am. Soc. Civil Engrs. New York, 360pp.

JENSEN, R.R. and HARDIN, P.J. (2005) Estimating urban leaf area using field measurements and satellite remote sensing data, *Journal of Aboriculture,* 31 (1): 21-27.

JIANG, L. & ISLAM, S. (2003) An intercomparison of regional heat flux estimation using remote sensing data. *International Journal of Remote Sensing,* 24 (11): 2221 – 2236.

JIANG, L. & ISLAM, S. (2001) Estimation of surface evaporation map over Southern Great Plains using remote sensing data. *Water Resources Research,* 3 (2): 329 – 340.

JIMĔNEZ-MUŇOZ, J. C., SOBRINO, J. A., GILLESPIE, A., SABOL, D. & GUSTAFSON, W. T. (2006) Improved land surface emissivity over agricultural areas using ASTER NDVI. *Remote Sensing of Environment,* 103: 474 – 487.

JIMÉNEZ-MUŇOZ, J.C. & SOBRINO, J.A. (2003) A generalized single channel method for retrieving land surface temperature from remote sensing data, *Journal of Geophysical Research,* 108 (D22), 4688, doi:10.1029/2003JD0034800.

JIN, Y. (1990) Emissivities of natural surfaces and surface temperature. *Acta Meteorological Sin.* 4: 106 – 112.

JUNG, G. (2006) Regional climate change and impacts on hydrology in the Volta basin of West Africa, *Unpublished Ph.D. Thesis,* Centre for Development Studies (ZEF) University of Bonn, Germany, 148pp.

JUNK, W.J. (2002) Long-term environmental trends and the future of tropical catchments. *Environmental Conservation,* 29 (4):414-435.

KÄÄB, A. (2002) Monitoring high-mountain terrain deformation from repeated air- and spaceborne optical data: examples using digital aerial imagery and ASTER data, *ISPRS Journal Photogrammetry & Remote Sensing,* 57: 39-52.

KALLURI, S. N. V. & TOWNSEND, J. R. G. (1998) A simple single layer model to estimate transpiration from vegetation using multi-spectral and meteorological data. *International Journal of Remote Sensing,* 19, (6): 1037-1053.

KALMA, J. D. & SIVAPALAN, M. (1995) Scale problems in hydrology: Contributions from the Robertson workshop. In: *Advances in Hydrological Processes* (Scale issues in hydrological modelling) J. Wiley & Sons Ltd., Chichester, UK. p.1-8.

KEALY, P. S. & HOOK, S. J. (1993) Separating temperature and emissivity in thermal infrared multispectral scanner data: Implications for recovering land surface temperatures, *IEEE Transactions on Geosciences and Remote Sensing*, 31 (6):1155-1164.

KESSE, G.O. (1985) *The Geology of Ghana*, 261pp. A.A. Balkema, Rotterdam, The Netherlands.

KIM, Y. & ELTAHIR, E. A. B. (2004) Role of topography in facilitating coexistence of trees and grasses within West African savannahs, *Water Resources Research,* 40 (7): 1445 - 1458, W07505, doi:10.1029/2003, WR02578.

KOLOSKOV, G., MUKHAMEJANOV, KH. & TANTON, T.W. (2007) Monin-Obukhov length as a cornerstone of the SEBAL calculations of evapotranspiration, *Journal of Hydrology,* 335:170 – 179.

KONDO, A. & HIGUCHI, A. (2001) Relationship between satellite-derived spectral brightness and evapotranspiration from a grassland. *Hydrological Processes,* 15: 1761 – 1770.

KUMAR, L., RIETKERK, M., VAN LANGEVELDE, F., VAN DE KOPPEL, J., VAN ANDEL, J., HEARNE, J., DE RIDDER, N., STROOSNIJDER, L., SKIDMORE, A.K AND PRINS, H.T (2002) Relationship between vegetation growth rates at the onset of the wet season and soil type in the Sahel of Burkina Faso: implications for resource utilisation at large scales. *Ecological Modelling,* 149:143-152.

KUNSTMANN H., KRAUSE J. & MAYR S. (2005): Inverse distributed hydrological modelling of alpine catchments; *Hydrology and Earth System Sciences Discussions*; 2: 1–43.

KUSTAS, W. P., MORAN, M. S., HUMES, K. S., STANNARD, D. I., PINTER, P. J., JR., HIPPS, L. E., SWIATEK, E., GOODRICH, D. C (1994) Surface energy balance estimates at local and regional scales using optical remote sensing from an aircraft platform and atmospheric data collected over semiarid rangelands. *Water Resources Research,* 30: 1241-1259.

KUSTAS, W. P., DAUGHTRY, C. S. T. and VAN OEVELEN, P. J. (1993) Analytical treatment of the relationships between soil heat flux/net radiation ratio and vegetation indices. *Remote Sensing of Environment* 46: 319 - 330.

KUSTAS, W. P. and DAUGHTRY, C. S. T. (1990) Estimation of the soil heat flux/net radiation from spectral data. *Agricultural and Forest Meteorology* 49: 205 - 223.

KUSTAS, W.P., MORAN, M.S. JACKSON, R.D., GAY, L.W. DUELL, L.F.W., KUNKEL, K.E. & MATTHIAS, A.D. (1990) Instantaneous and daily values of the surface energy balance over agricultural fields using remote sensing and a reference field in an arid environment. *Remote Sensing of Environment,* 32: 125-141.

KUSTAS, W. P., CHOUDHURY, B. J., MORAN, M. S., REGINATO, R. J., JACKSON, R. D., GAY, L. W., WEAVER, H. L. (1989) Determination of sensible heat flux over sparse canopy using thermal infrared data. *Agricultural and Forest Meteorology* 44: 197 - 216.

LABED, J. & STOLL, M. P. (1991) Spatial variability of land surface emissivity in the thermal infrared band: spectral signature and effective surface temperature. *Remote Sensing of Environment,* 38: 1 - 17.

LACAZE, B., RAUBAL, S. & WINKEL, T. (1994) Identifying spatial patterns of Mediterranean landscapes from geostatistical analysis of remotely-sensed data. *International Journal of Remote Sensing,* 15:2437 – 2450.

LAGOUARDE, J. P. & BRUNET, Y. (1993) A simple model for estimating the daily upward long-wave surface radiation flux from NOAA-AVHRR data. *International Journal of Remote Sensing,* 14 (5): 907 – 925.

LEICA GEOSYSTEMS (2003) *ERDAS Imagine Field Guide*, 7th Edition, Atlanta, Georgia, USA.

LI, K.Y., COE, T. & RAMANKUTTY, N. (2005) Investigation of hydrological variability in West Africa using land surface models, *Journal of Climate,* 18, 3173-3188.

JI, L. & PETERS, J. (2004) A spatial regression procedure for evaluating the relationship between AVHRR-NDVI and climate in the Northern Great Plains, *International Journal of Remote Sensing,* (25) 6, 297-311.

LIPPMANN, S. B., LAJOIE, J. & MOO, B. E. (2005) *C++ Primer*, 4th Edition, Pearson Education, Inc., 885pp.

LIU, C., ZHANG, X. & ZHANG, Y. (2002) Determination of daily evaporation and evapotranspiration of wheat and maize by large-scale weighing lysimeter and micro-lysimeter, *Agricultural & Forest Meteorology,* 111: 109 - 120

LYON, J.G. (ed.) (2003) *GIS for Water Resources and Watershed Management.* Taylor & Francis, London. 266pp.

MA, Y., SU, Z, LI, Z., KOIKE, T. & MENENTI, M. (2002) Determination of regional net radiation and soil heat flux over a heterogeneous landscape of the Tibetan Plateau. *Hydrological Processes,* 16: 2963 – 2971.

MAH, A. (2004) Mapping surface cover types using ASTER data. *Technical Bulletin* 4-2004; Earth Resource Mapping Pty. Ltd, Melbourne, Australia, 11pp.

MAIDMENT, D.R. (ed.) (2002) *Arc-Hydro: GIS for Water Resources* ESRI, California, USA; 203pp.

MANABE, S. (1969) Climate and the ocean circulation - The atmospheric circulation and the hydrology of the Earth's surface. *Monthly Weather Review,* 97 (11): 739-774.

McMANUS, K.B. (2004) Airborne thermography and ground geophysical investigation for detecting shallow ground disturbance under vegetation. Ph.D. thesis, Durham University, UK, 356pp.

MEKONNEN, S.C. (2005) Assessment of catchment water balance using GIS and Remote Sensing: Roxo, Portugal, *MSc. Thesis,* ITC, The Netherlands, 109pp.

METEOROLOGICAL SERVICES DEPARTMENT (2004) *Techn. Report No. 31/2004*, Meteorological Services Department, Ministry of Transport & Communication, Headquarters, Accra, Ghana.

MESSAGER, C., GALLEI, H., BRASSEUR, O., CAPPELEARE, B., PEUGEOT, C., SEGUINS, L, VAUCLIN, M., et al. (In press) Impacts of simulated and observed precipitation forcing on the simulation of water discharge over the Sirba basin, Burkina Faso/Niger, *Climate Dynamics Journal (2006).*

MODIS Characterization Support Team (MCST) (2003) *MODIS LUT Information Guide For Level 1B*, MCST Internal Memorandum # M1036, December 1, 2003. The

latest release is available on-line at http://www.mcst.ssai.biz/mcstweb/L1B/product.html

MONTEITH, J.L. (1981) Evaporation and surface temperature, *Quarterly Journal of Royal Meteorological Society*: 1-27.

MYNENI, R.B. & WILLIAMS, D.L. (1994) On the Relationship between FPAR and NDVI, *Remote Sensing Environment,* 49: 200-211

MORSE, A., TASUMI, M., ALLEN, R.G. & KRAMBER, W.J. (2000) Application of the SEBAL Methodology for Estimating Consumptive Use of Water and Streamflow Depletion in the Bear River Basin of Idaho through Remote Sensing, *Final Project Report:* 2000, The Raytheon Systems Company, Idaho, USA, pp 1-107.

NEMANI, P. R. & RUNNING, S. W. (1989) Estimation of regional surface resistance to evapotranspiration from NDVI and thermal IR AVHRR data. *Journal of Applied Meteorology,* 28: 276 – 284.

NEMANI, P. R., PIERCE, L., RUNNING, S. & GOWARD, S. G. (1993) Developing satellite-derived estimates of surface moisture status. *Journal of Applied Meteorology,* 32: 548 – 557.

NICHOLSON, S.E. & GRIST, J.P. (2001) A conceptual model for understanding rainfall variability in the West African Sahel interannual and interdecadal timescales *International Journal of Climatology,* 21:1733-1757.

NISHADA, K., NEMANI, R. R., RUNNING, S. W. & GLASSY, J. M. (2003) An operational remote sensing algorithm of land evaporation. *Journal of Geophysical Research,* 108 (D9) 4270.

NOUVELLON, Y.P., MORAN, M.S., BRYANT, R.B., NI, W., HEILMAN, P., EMMERICH, B., LOSEEN, D., BÉGUÉ, A., RAMBAL, S. & QI, J. (2000)

Combining a SVAT model with Landsat ETM+ imagery for a 10-year simulation carbon and water budget. *2nd Intl. Conf. Geospatial Information in Agric and Forestry.* 10-12 Jan 2000. Orlando, USA.

OGUNTUNDE, P.G. (2004) Evapotranspiration and complimentary relations in the water balance of the Volta basin: Field measurements and GIS-based regional estimates. In *Ecology and Development Series,* Denich, M. Martius, C. & van de Giesen, N. Eds.: Cuvillier Verlag, Göttingen, pp.103-155.

OLIVER, M.A. (1990) Kriging: "A Method of Interpolation for Geographical Information Systems", *International Journal of Geographic Information Systems*, 4, (4): 313–332.

OKE, T.R. (1977) *Boundary Layer Climates*, 1st Edition, William Clowes & Sons, London, 372pp.

OPOKU-ANKOMAH, Y. & AMISIGO, B. A. (1998) Rainfall and runoff variabilities in the river systems of Ghana. In: *Water Resources Variability in Africa during the XXth Century.* IAHS Pub. No. 252, pp. 307-314.

ORSTOM (1977) The Volta River Basin. *Hydrological Monographs of the Office de la Recherche Scientifique et Technique Outre-Mer (ORSTOM),* Paris, pp. 1-48.

OWE, M. & VAN DE GRIEND, A. A. (1994) Ground-based measurement of surface temperature and thermal emissivity. *Advances in Space Research,* 14 (3): 45 – 48.

PARKER, D.E., GORDON, M., BROWN, S.J. & O'DONNELL, M. (1998) The new monthly gridded global upper-air temperature data sets (HadRT2). *The Hadley Centre, Meteorology Office, UK,* Internal Note No. 84.

PARKS, S., FEDDEMA, J.J & EGBERT, S.L. (2005) MODIS land surface temperature composite data their relationships with climate water budget factors in the Central Great Plains, *International Journal of Remote Sensing,* 26 (6): 1127-1144.

PARODI, G.N. (2002) AVHRR Hydrological Analysis System: *Algorithms and Theory (Version 1.3),* Water Resources Department, ITC, The Netherlands, 31pp.

PATUREL, J. E., SERVAT, E., KOUAMÉ, B., LUBÈS, H., OUEDRAGO, M. AND MASSON, J. M. (1997) Climate variability in humid Africa along the Gulf of Guinea, Part II: An integrated approach. *Journal of Hydrology,* 191:16-32.

PENMAN, H.L. (1948) Natural evaporation from open water, bare soil and grass, *Proc. Roy. Soc.* London, A193, 120-146. (Quoted by Shaw, E.M. (1994) 3rd Ed. Hydrology in Practice, Routledge, England).

PITMAN, W.V. (1973) A mathematical model for generating monthly river flows from meteorological data in South Africa, *Report No. 2/73, Hydrological Research Unit*, University of Witwatersrand, Johannesburg., South Africa, 61pp.

PRATA, F. (2002) Land surface temperature measurement from space: AATSR algorithm – Theoretical basis document, *Technical Report*, CSIRO, Canberra, Australia, 34pp.

PRATA, A. J. (1996) A new long-wave formula for estimating downward clear-sky radiation at the surface. *Quarterly Journal of Royal Meteorological Society*, 122: 1127 – 1151.

PRATA, F. (1994) Land surface temperatures derived from the Advanced Very High Resolution Radiometer and the Along-Track Scanning Radiometer, *J. Geophys. Res.*, 99 (D6) 13,025 – 13, 058.

PRICE, J. C. (1990) Using spatial context in satellite data to infer regional scale evapotranspiration. *IEEE Transactions in Geosciences & Remote Sensing,* 28: 940 – 948.

PRICE, J.C. (1984) Land surface temperature measurements from split window channels of the NOAA-7 Advanced Very High Resolution Radiometer, *Journal of Geophysical Research,* 89 (D5) 7231-7237.

PRIESTLEY, C.H.B. & TAYLOR, R.J. (1972) On the assessment of surface heat flux and evaporation using large scale parameters, *Monthly Weather Review,* 100: 81-92.

PRINCE, S.D., KERR, Y.H., GOUTORBE, T., LEBEL, J-P, TINGA, A., BESSEMOULIN, P., BROUWER, J., DOLMAN, A.J., ENGMAN, E.T., GASH, J.H.C., HOEPFFNER, M., KABAT, P., MONTENY, B., SAID, F., SELLERS, P & WALLACE, J. (1995) Geographical, biological and remote sensing aspects of the Hydrological Atmospheric Pilot Experiment in the Sahel (HAPEX-Sahel) *Remote Sensing of Environment,* 51:215-234.

PRINCE, S. D. (1991) A model of regional primary production of air temperature from remotely sensed surface observations. *Remote Sensing of Environment,* 40: 335 – 346.

QIN, Z., KARNIELI, A. & BERLINER, P. (2001) A mono-window algorithm for retrieving land surface temperature from Landsat TM data and its application to the Israel-Egypt border region, *International Journal of Remote Sensing,* 22:3719-3746.

RAHMAN, H. & DEDIEU, G. (1994) SMAC: a simplified method for the atmospheric correction of satellite measurements in the solar spectrum. *International Journal Remote Sensing* 15 (1): 123-143.

REGGIANI, P., SIVAPALAN, M. & HASSANIZADEH, D.S.M. (2000) Conservation equations governing hill-slope responses: exploring the physical basis of water balance. *Water Resources Research,* 36 (7): 1845-1864.

ROBERTS, J. (2000) The influence of physical and physiological characteristics of vegetation on their hydrological response, *Hydrological Processes,* 14:2885 – 2901.

ROGERS, J.S., ALLEN, L.H. & CALVERT, D.J. (1983) Evapotranspiration for humid regions: developing citrus grove and grass cover, *Transactions ASAE*, 26 (6): 1778-1792.

ROSENBERG, N. J., KIMBALL, B. A., MARTIN, P. AND COOPER, C. F. (1990) From climate and $CO_2$ enrichment to evapotranspiration. In P.E. Waggoner (ed.) *Climate change and U.S. Water Resources.* J. Wiley & Sons, pp. 151-175.

ROUSE, W. R. (1984) Microclimate at Arctic tree line. 3. The effects of regional advection on the surface energy balance of upland tundra. *Water Resources Research,* 20: 74- 78.

SABINS, F. F. (1987) *Remote Sensing: Principles and Interpretation.* 2nd Edition, W. H. Freeman & Co., New York, 449pp.

SALISBURY, J. W. & D'ARIA, D. M. (1992) Emissivity of terrestrial materials in the 8 – 14 μm atmospheric window. *Remote Sens of Environment,* 42: 83 – 106.

SALOMONSON, V. V., BARNES, W. L., XIONG, X., KEMPLER, S. & MASUOKA, E. (2002) An Overview of the Earth Observing System MODIS Instrument and Associated Data Systems Performance, *Proceedings of IGARSS*, 2002.

SAN, B.T. & SÜZEN, M.L. (2005) Digital elevation model (DEM) generation and accuracy assessment from ASTER stereo data *International Journal of Remote Sensing,* 26 (22): 5013-5037.

SCHUOL, J. & ABBASPOUR, K.C. (2006) Calibration and uncertainty issues of a hydrological model (SWAT) applied to West Africa, *Advances in Geosciences,* 9:137 – 146.

SEGUIN, B., COURALT, D. & GUERIF, M. (1994) Surface temperature and evapotranspiration: Application of local scale methods to regional scales using satellite data. *Remote Sensing of Environment,* 49: 287 – 295.

SEGUIN, B. & ITIER, B. (1983) Using midday surface temperature to estimate daily evaporation from satellite thermal IR data. *International Journal Remote Sensing,* 4: 371 - 383.

SELLERS, P., LOS, S., JUSTICE, C., DAZLICH, D., COLLATZ, G., and RANDALL, D. (1996) A revised land surface parameterization (SiB-2) for atmospheric GCM. Part 2: The generation of global fields of terrestrial biophysical parameters from satellite data. *Journal of Climate*, 9: 706-737

SELLERS, P., HALL, F. G., ASRAR, G., STREBEL, D. E., & MURPHY, R. E. (1992) An overview of the First International Satellite Land Surface Climatology Project (ISLSCP) Field Experiment (FIFE). *Journal of Geophysical Research,* 97 D17: 18345-18371

SHAW, E.M. (1994) *Hydrology in Practice.* Chapman & Hall, England (1994); reprinted by Routledge, 2004; 569pp.

SHUTTLEWORTH, W.J., GURNEY, R.J., HSU, A.Y. & ORMSBY, J.P. (1989) FIFE: The variation in energy partition at surface flux sites, In: Rango, A. (1989) (Ed.) *Remote sensing and large scale global processes*, IAHS Press, Wallingford, p. 67-74.

SMITH, R. C. G. & CHOUDHURY, B. J. (1990) Relationship of multispectral satellite data to land surface evaporation from the Australian continent. *International Journal of Remote Sensing,* 11: 2096 – 2088.

SNYDER, R.L., LANINI, B.J., SHAW, D.A. & PRUITT, W.O. (1989) Using reference evapotranspiration and crop coefficients to estimate crop evapotranspiration for trees and vines. *Cooperative Extension*, Univ. California, Berkeley, CA, Leaflet No. 21428, 8pp.

SOBRINO, J.A. & JIMÉNEZ-MUŃOZ, J.C. (2005) Land surface temperature retrieval from thermal infrared data: An assessment in the context of the surface processes and ecosystem changes through response analysis (SPECTRA) mission, *Journal of Geophysical Research,* 110:D16103, doi:1029/2004JD005588.

SOBRINO, J.A., SÒRIA, G. & PRATA, A.J. (2004) Surface temperature retrieval from Along Track Scanning Radiometer-2 data: Algorithms and validation, *Journal of Geophysical Research,* 109, D1101, doi: 10.1029/2003JD004212.

SOBRINO, J. A., LI, Z. –L., SORIA, G. & JIMĔNEZ-MUŃOZ, J. C. (2002) Land surface temperature and emissivity retrieval from remote sensing data. *Recent Research Developments in Geophysics,* 21: 21 - 44.

SOBRINO, J.A., LI, Z-L., STOLL, M.P. & BECKER, F. (1996) Multi-channel and multi-angle algorithms for estimating sea and land surface temperature with ATSR data, *International Journal of Remote Sensing,* 17:2089 – 2114.

SOBRINO, J.A., LI, Z-L., STOLL, M.P. & BECKER, F. (1994) Improvements in the split-window technique for land surface temperature determination, *IEEE Transactions of Geosciences and Remote Sensing,* 32:243-253.

SOBRINO, J. A. & CASSELLES, V. (1991) A methodology for obtaining the crop temperature from NOAA-9 AVHRR data. *Int. J. Remote Sensing,* 12:2461 – 2475.

SÒRIA, G. & SOBRINO, J.A. (2005) AATSR derived land surface temperature from heterogeneous areas, *Proc. ESA's ENVISAT MERIS-AATSR workshop,* Frascati, Italy, 6pp. http://envisat.esa.int.

SOROOSHIAN, S., HSU, K., GAO, X., GUPTA, H.V., IMAM, B., BRAITHWAITE, D. (2000) Evaluation of PERSIANN system satellite-based estimates of tropical rainfall. *Bulletin of the American Meteorological Society,* 81, 2035–2046.

SU, Z. (2002) The Surface Energy Balance System (SEBS) for estimation of turbulent heat fluxes, *Hydrology and Earth Systems Sciences* 6(1): 85-99.

SU, Z., PELGRUM, H. & MENENTI, M. (1999) Aggregation effects of surface heterogeneity in land surface processes. *Hydrology and Earth Systems Sciences,* 3 (4): 549-563.

SUSSKIND, J., PIRAINO, P., ROKKE, L., IREDELL, L., MEHTA, A. (1997) Characteristics of the TOVS pathfinder path A dataset, *Bulletin of the American Meteorological Society,* 78, 1449–1472.

SUTHERLAND, R. A. (1986) Broadband and spectral emissivities (2 -18 μm) of some natural soils and vegetation. *Journal of Atmospheric and Oceanic Technology,* 3: 199 – 202.

SUTHERLAND, R. A. & BARTHOLIC, J. F. (1977) Significance of vegetation in interpreting thermal radiation from a terrestrial surface. *Journal of Applied Meteorology,* 16: 759 – 763.

SÜZEN, M.L. & DOYURAN, V. (2004) A comparison of the GIS based landslide susceptibility assessment methods: multivariate versus bivariate. *Environmental Geology,* 45: 665-679.

TASUMI, M. (2003) Progress in operational estimation of regional evapotranspiration using satellite imagery, *Ph.D. Dissertation,* University of Idaho, Moscow, ID, pp. 145-178.

THORNE, V., COAKLEY, P., GRIMES, D., DUGDALE, G. (2001) Comparison of TAMSAT and CPC rainfall estimates with rainfall, for southern Africa, *International Journal of Remote Sensing,* 22 (10), 1951–1974.

TUCKER, C. J. & SELLERS, P. J. (1986) Satellite remote sensing of primary production. *International Journal of Remote Sensing,* 7: 1395 – 1416.

Van DEURSEN, W.P.A. & KWADIJK, J.C.J. (1994) The impacts of climate change on the water balance of the Ganges-Brahmaputhra and Yangtze Basins, Delft: *Resources Analysis*, 18pp.

Van DE GIESEN, N., KUNSTMAN, H., JUNG, G., LIEBE, J., ANDREINI, M. & VLEK, P. L. G. (2002) The GLOWA-Volta Project: Integrated assessment of feedback mechanisms between climate, landuse and hydrology. In: Beniston, M. (ed.)

Climate Change – Implications for the Hydrological Cycle and for Water Management. *Advances in Global Change Research* 10:151-171.

Van DE GRIEND, A. A. & OWE, M. (1993) On the relationship between thermal emissivity and the normalized difference vegetation index for natural surfaces. *International Journal of Remote Sensing,* 14 (6): 1119 – 1131.

VALOR, E. & CASSELLES, V. (1996) Mapping land surface emissivity from NDVI: application to European, African and South American areas. *Remote Sensing of Environment,* 57: 167 – 184.

VESCOVI, F.D., PARK, S.J. & VLEK, P.L.G. (2002) Detection of human-induced landcover changes in a savannah landscape in Ghana (I) Change detection and quantification. *Technical Report,* Centre for Development Research (ZEF), Bonn, Germany. (http://www.glowa-volta.de/publication/....pdf).

VIAU, A. A. & JANG, J-D. (2005) Thermal moisture stress index based on NOAA-AVHRR/SPOT-VGT in Southern Quebec. In: *Proceedings of the 2nd International VEGETATION User Conference*, Eds. Veroustraete, F, Bartholomé, E. & Verstraeten, W.W., pp. 277 – 282.

VLEK, P. L. G., DENICH, M., MARTIUS, C. & VAN DE GIESEN, N. (2004) *Ecology and Development Series*, Centre for Development Research (ZEF), University of Bonn. Publ. Cuvillier Verlag Göttingen, Germany.

WAN, Z., ZHANG, Y., ZHANG, Q. & LI, Z-L. (2002) Validation of the land surface temperature products retrieved from Terra Moderate Resolution Imaging Spectroradiometer data, *Remote Sensing of Environ.,* 83:163-180.

WAN, Z. (1999) MODIS land surface temperature validation. *The Earth Observer*, 11(3), 29-31.

WAN, Z. & LI, Z-L. (1997) A physics-based algorithm for retrieving land surface emissivity and temperature from EOS/MODIS data, *IEEE Transactions in Geosciences and Remote Sensing,* 35:980 – 996.

WAINWRIGHT, J., PARSONS, A.J. & ABRAHAMS, A.D. (2000) Plot-scale studies of vegetation, overland flow and erosion interactions: case studies from Arizona and New Mexico, *Hydrological Processes,* 14:2921 – 2943.

WANG, G., ELTAHIR, E. A. B & IRIZARRY-ORTIZ, M. M. (2003) Drought Occurrence in West Africa: Role of Vegetation Dynamics – *Journal of Geophysical Research Atmospheres* 108, doi: 11.1029/2001JD000276.

WANG, G. L., ELTAHIR, E. A. B., FOLEY, J. A., POLLARD, D. & LEVIS, S. (2003) Decadal variability of rainfall in the Sahel: Results from the coupled GENESIS-IBIS atmosphere-biosphere model - *Unpublished manuscript.*

WANG, G. L. & ELTAHIR, E. A. B. (2000) Role of ecosystem dynamics in the low-frequency variability of the Sahel rainfall. *Water Resources Research* 36:1013-1021.

WANG, Y. & WOODOCK, C. E. (2004) Evaluation of the MODIS LAI algorithm at a coniferous forest site in Finland. *Remote Sensing of Environment* 91: 114 - 127.

WARD, R.C. & ROBINSON, M. (2000) *Principles of Hydrology*, McGraw-Hill, London & New York, 450pp.

WASHINGTON, R., HARRISON, M., CONWAY, D., BLACK, E. ET AL. (2006) African climate change: Taking the shorter route. *BAMS,* Oct., 1355-1365.

WIEGAND, C.L., RICHARDSON, A.J., ESCOBAR, D.E. & GERBAMANN, A.H. (1991) Vegetation indices in crop assessments, *Remote Sensing of Environment,* 35: 105-119.

WILK, J., KNIVETON, D., ANDERSSON, L., LAYBERRY, R., et al. (2006) Estimating rainfall and water balance over the Okavango River basin for hydrological applications, *Journal of Hydrology,* 331: 18 – 29.

WITTICH, K-P. (1997) Some simple relationships between land surface emissivity, greenness and the plant cover fraction for use in satellite remote sensing. *International Biometeorology,* 41: 58 – 64.

WMO (2003) Twenty-first status of report on implementation of the World Weather Watch (WWW): 40 years of WWW, *WMO Report 957*, 94pp.

WOLSKI, P., SAVENIJE, H.H.G., MURRAY-HUDSON, M. & GUMBRICHT, T. (2006) Modelling of the flooding in the Okavango delta, Botswana, using a hybrid reservoir-GIS model, *Journal of Hydrology,* 331: 58 – 72.

WORLD BANK (1997) *Sub-Saharan Africa: From Crisis to Sustainable Growth*, p.224-5, The World Bank, New York, USA.

WRIGHT, J.L. (1982) New evapotranspiration crop coefficients, *Journal of Irrigation & Drainage,* Div. ASCE, 108:57-74.

XUE, Y. K. & SHUKLA, J. (1993) The influence of land surface properties on Sahel climate, Part I: Desertification. *Journal of Climate* 6: 2232-2245.

YAMAGUCHI, Y., FUJISADA, H., KAHLE, A.B., TSU, H., KATO, M., WATANABE, H., SATO, I. & KUDOH, M. (2001) ASTER instrument performance, operational

status and application to Earth sciences. *IEEE Transactions of Geosciences and Remote Sensing,* 31, 225-238.

ZEF (2004) *Ecology and Development Series: GLOWA-Volta Project, 1999-2005,* eds. Vlek, P.L.G., Denich, M., Martins, C. & van de Giesen, N., Centre for Development Research (ZEF), University of Bonn, Cuvelier Verlag Göttingen, Germany, 138pp.

ZEF (1999) Sustainable Water Use under Changing Landuse, Rainfall Reliability and Water Demands in the Volta basin - *Project Proposal – Centre for Development Research (ZEF)*, University of Bonn, Germany, 89pp.

ZENG, N., NEELIN, J. D., LAU, K. M., & TUCKER, C. J. (1999) Enhancement of interdecadal climate variability in the Sahel by vegetation interaction. *Science* 286: 1537-1540.

ZHANG H., HENDERSON-SELLERS A., PITMAN A.J., MCGREGOR J.L., DESBOROUGH C.E. AND KATZFEY, J. (2001) Limited-area model sensitivity to the complexity of representation of the land surface energy balance *Journal of Climate* 14 (19): 3965-3986.

ZHENG, X., & ELTAHIR, E. A. B. (1997) The response to deforestation and desertification in a model of West African monsoons. *Geophysical Research Letters* 24: 155-158.

ZHENG, X., & ELTAHIR, E. A. B. (1998) The role of vegetation in the dynamics of West African monsoons. *Journal of Climate* 11: 2078-2096.

ZIERL, B. (2001) A water balance model to simulate drought in forested ecosystems and its application to the entire forested area in Switzerland. *Journal of Hydrology 242:115-136.*

ZILLMAN, J. W. (1972) A study of some aspects of the radiation and heat budgets of the southern hemisphere oceans. *Meteorological Study, vol. 26,* Canberra, Australia, 22pp.

**APPENDIX 2.1** ***Summary statistics for 40-year monthly air temperature ($^0$C) in the Volta basin The station IDs are (a) Yendi (b) Bole (c) Tamale (d) Wa and (e) Navrongo***

| (a) | Jan | Feb | Mar | Apr | May | Jun | Jul | Aug | Sep | Oct | Nov | Dec |
|---|---|---|---|---|---|---|---|---|---|---|---|---|
| Minimum | 25.5 | 28.5 | 29.3 | 28.1 | 27.2 | 25.7 | 25.1 | 24.7 | 25.2 | 25.9 | 25.9 | 25.4 |
| Maximum | 29.3 | 31.5 | 32.7 | 32.7 | 30.5 | 27.9 | 27.0 | 26.8 | 27.0 | 28.0 | 29.2 | 28.4 |
| Mean | **27.6** | **29.8** | **30.9** | **30.2** | **28.6** | **26.8** | **25.9** | **25.7** | **26.0** | **27.0** | **27.4** | **26.9** |
| Median | 27.5 | 29.8 | 30.9 | 30.2 | 28.6 | 26.8 | 26.0 | 25.6 | 26.1 | 26.9 | 27.4 | 26.9 |
| Mode | 28.5 | 29.3 | 30.2 | 29.5 | 28.2 | 26.5 | 26.3 | 26.1 | 26.3 | 26.7 | 27.1 | 26.9 |
| Standard deviation | **0.81** | **0.70** | **0.79** | **1.07** | **0.78** | **0.55** | **0.48** | **0.47** | **0.46** | **0.40** | **0.75** | **0.74** |

| (b) | Jan | Feb | Mar | Apr | May | Jun | Jul | Aug | Sep | Oct | Nov | Dec |
|---|---|---|---|---|---|---|---|---|---|---|---|---|
| Minimum | 24.5 | 27.2 | 28.0 | 27.4 | 26.8 | 25.1 | 24.4 | 23.8 | 24.4 | 25.0 | 25.3 | 23.5 |
| Maximum | 28.0 | 30.7 | 31.5 | 30.5 | 30.1 | 27.3 | 26.6 | 25.7 | 26.2 | 29.6 | 27.7 | 26.8 |
| Mean | **26.2** | **28.6** | **29.7** | **29.1** | **28.1** | **26.2** | **25.4** | **25.0** | **25.4** | **26.5** | **26.4** | **25.4** |
| Median | 26.1 | 28.5 | 29.7 | 29.1 | 27.9 | 26.4 | 25.3 | 25.0 | 25.4 | 26.5 | 26.4 | 25.5 |
| Mode | 27.1 | 29.3 | 30.1 | 28.2 | 27.6 | 26.4 | 25.2 | 24.9 | 25.7 | 27.1 | 26.7 | 25.1 |
| Standard deviation | 0.87 | 0.89 | 0.88 | 0.88 | 0.97 | 0.46 | 0.49 | 0.42 | 0.46 | 0.74 | 0.68 | 0.81 |

| (c) | Jan | Feb | Mar | Apr | May | Jun | Jul | Aug | Sep | Oct | Nov | Dec |
|---|---|---|---|---|---|---|---|---|---|---|---|---|
| Minimum | 24.9 | 27.9 | 30.4 | 28.6 | 27.6 | 26.0 | 25.7 | 25.3 | 25.3 | 26.7 | 27.0 | 24.8 |
| Maximum | 29.1 | 31.8 | 33.1 | 33.3 | 30.7 | 28.5 | 27.3 | 27.1 | 27.6 | 29.0 | 30.1 | 28.7 |
| Mean | **27.5** | **30.2** | **31.6** | **30.8** | **29.2** | **27.3** | **26.4** | **26.2** | **26.4** | **27.7** | **28.2** | **27.1** |
| Median | 27.8 | 30.1 | 31.6 | 30.8 | 29.1 | 27.3 | 26.4 | 26.1 | 26.4 | 27.7 | 28.1 | 27.3 |
| Mode | 27.9 | 30.2 | 32.1 | 31.9 | 28.25 | 26.7 | 26.1 | 26.1 | 26.5 | 28.1 | 27.5 | 27.3 |
| Standard deviation | **1.05** | **0.85** | **0.76** | **1.14** | **0.78** | **0.64** | **0.46** | **0.45** | **0.58** | **0.56** | **0.83** | **1.03** |

**APPENDIX 2.1** ***continued (Time-series temperature records, regional Volta basin)***

| (d) | Jan | Feb | Mar | Apr | May | Jun | Jul | Aug | Sep | Oct | Nov | Dec |
|---|---|---|---|---|---|---|---|---|---|---|---|---|
| Minimum | 25.2 | 27.4 | 30.4 | 28.9 | 25.6 | 26.1 | 25.7 | 25.5 | 25.5 | 26.7 | 27.1 | 25.5 |
| Maximum | 30.0 | 31.8 | 33.1 | 33.3 | 30.8 | 28.7 | 27.9 | 27.1 | 27.8 | 29.0 | 29.9 | 28.9 |
| Mean | **28.0** | **30.3** | **31.6** | **31.1** | **29.4** | **27.5** | **26.6** | **26.4** | **26.6** | **27.9** | **28.3** | **27.3** |
| Median | 28.2 | 30.3 | 31.7 | 31.1 | 29.6 | 27.5 | 26.6 | 26.4 | 26.6 | 27.7 | 28.3 | 27.5 |
| Mode | 28.7 | 30 | 32.1 | 31.8 | 29.7 | 27.8 | 26.8 | 26.4 | 26.8 | 27.5 | 28.3 | 27.5 |
| Standard deviation | **1.04** | **0.92** | **0.72** | **1.03** | **0.93** | **0.64** | **0.51** | **0.40** | **0.62** | **0.54** | **0.74** | **0.98** |

| (e) | Jan | Feb | Mar | Apr | May | Jun | Jul | Aug | Sep | Oct | Nov | Dec |
|---|---|---|---|---|---|---|---|---|---|---|---|---|
| Minimum | 25.8 | 28.2 | 30.3 | 30.2 | 28.7 | 27.1 | 26.0 | 25.5 | 25.8 | 27.0 | 26.7 | 25.7 |
| Maximum | 29.3 | 31.7 | 33.9 | 34.1 | 33.1 | 30.1 | 28.3 | 27.3 | 27.9 | 29.4 | 30.3 | 28.7 |
| Mean | **27.5** | **29.9** | **32.1** | **32.3** | **30.6** | **28.3** | **27.0** | **26.4** | **26.8** | **28.2** | **28.2** | **27.2** |
| Median | 27.4 | 29.9 | 32.1 | 32.4 | 30.6 | 28.3 | 27.0 | 26.4 | 26.8 | 28.3 | 28.2 | 27.1 |
| Mode | 26.3 | 30.9 | 31.9 | 31.9 | 30.9 | 27.7 | 26.5 | 26.3 | 26.8 | 28.5 | 27.9 | 27.1 |
| Standard deviation | **0.97** | **0.89** | **0.83** | **0.96** | **0.93** | **0.74** | **0.51** | **0.45** | **0.53** | **0.54** | **0.76** | **0.68** |

**APPENDIX 2.2** ***Summary statistics for 40-year monthly rainfall (mm) in the Volta basin***
***The station IDs are (a) Yendi (b) Bole (c) Tamale (d) Wa and (e) Navrongo***

| (a) | Jan | Feb | Mar | Apr | May | Jun | Jul | Aug | Sep | Oct | Nov | Dec |
|---|---|---|---|---|---|---|---|---|---|---|---|---|
| Minimum | 0.0 | 0.0 | 0.0 | 8.1 | 47.3 | 61.5 | 62.7 | 38.9 | 128.0 | 3.1 | 0.0 | 0.0 |
| Maximum | 45.6 | 55.1 | 212.6 | 134.4 | 273.6 | 331.5 | 348.2 | 453.4 | 566.2 | 270.3 | 68.3 | 106.7 |
| Mean | 3.3 | 6.1 | 52.7 | 78.2 | 133.4 | 171.2 | 185.0 | 228.1 | 252.6 | 106.4 | 8.3 | 7.0 |
| Median | 0.0 | 0.0 | 40.9 | 70.6 | 134.8 | 160.4 | 182.2 | 225.2 | 230.4 | 100.5 | 0.0 | 0.0 |
| Mode | 0.0 | 0.0 | 2.8 | - | - | - | 157.0 | - | - | - | 0.0 | 0.0 |
| St Dev | 10.39 | 12.47 | 51.38 | 33.27 | 54.22 | 58.57 | 63.33 | 89.32 | 86.66 | 58.83 | 15.42 | 20.17 |

| (b) | Jan | Feb | Mar | Apr | May | Jun | Jul | Aug | Sep | Oct | Nov | Dec |
|---|---|---|---|---|---|---|---|---|---|---|---|---|
| Minimum | 0.0 | 0.0 | 0.0 | 40.9 | 42.2 | 55.5 | 53.1 | 65.7 | 95.3 | 15.2 | 0.0 | 0.0 |
| Maximum | 39.1 | 57.1 | 170.9 | 175.8 | 229.4 | 304.7 | 319.3 | 339.0 | 361.0 | 276.9 | 112.3 | 75.7 |
| Mean | 1.8 | 7.0 | 50.6 | 92.4 | 129.2 | 154.5 | 162.7 | 165.4 | 211.6 | 103.5 | 16.5 | 7.4 |
| Median | 0.0 | 2.0 | 41.6 | 84.4 | 133.2 | 139.7 | 156.9 | 156.0 | 205.7 | 88.4 | 7.9 | 0.0 |
| Mode | 0.0 | 0.0 | - | - | - | - | - | - | - | - | 0.0 | 0.0 |
| St Dev | 6.61 | 13.03 | 40.79 | 34.64 | 37.47 | 59.86 | 69.20 | 63.46 | 71.73 | 57.43 | 26.44 | 17.06 |

| (c) | Jan | Feb | Mar | Apr | May | Jun | Jul | Aug | Sep | Oct | Nov | Dec |
|---|---|---|---|---|---|---|---|---|---|---|---|---|
| Minimum | 0.0 | 0.0 | 0.0 | 3.1 | 30.1 | 55.1 | 20.8 | 45.2 | 111.3 | 4.6 | 0.0 | 0.0 |
| Maximum | 60.0 | 91.2 | 145.3 | 239.8 | 351.8 | 314.5 | 365.5 | 401.3 | 495.8 | 243.3 | 90.7 | 33.0 |
| Mean | 3.2 | 9.0 | 46.7 | 81.0 | 122.7 | 155.7 | 154.7 | 200.1 | 226.0 | 88.4 | 10.1 | 2.8 |
| Median | 0.0 | 0.0 | 38.5 | 75.2 | 124.0 | 148.8 | 143.8 | 195.9 | 221.2 | 73.9 | 0.0 | 0.0 |
| Mode | 0.0 | 0.0 | 62 | - | - | - | - | - | - | - | 0.0 | 0.0 |
| St Dev | 10.69 | 16.93 | 35.88 | 52.61 | 53.36 | 66.34 | 69.50 | 84.14 | 76.88 | 58.65 | 19.64 | 6.64 |

**APPENDIX 2.2** ***continued (Time-series rainfall records, regional Volta basin)***

| (d) | Jan | Feb | Mar | Apr | May | Jun | Jul | Aug | Sep | Oct | Nov | Dec |
|---|---|---|---|---|---|---|---|---|---|---|---|---|
| Minimum | 0.0 | 0.0 | 0.0 | 4.2 | 30.4 | 59.3 | 65.8 | 55.8 | 18.8 | 0.0 | 0.0 | 0.0 |
| Maximum | 55.9 | 172.7 | 132.1 | 169.9 | 196.2 | 248.2 | 334.9 | 467.1 | 318.0 | 288.0 | 69.6 | 41.7 |
| Mean | 2.9 | 10.9 | 33.3 | 69.7 | 122.2 | 136.9 | 173.5 | 216.5 | 177.0 | 73.6 | 8.1 | 5.3 |
| Median | 0.0 | 0.7 | 23.1 | 68.5 | 129.2 | 135.9 | 171.2 | 217.8 | 180.1 | 64.1 | 2.7 | 0.0 |
| Mode | 0.0 | 0.0 | 0.0 | - | - | - | - | - | - | - | 0.0 | 0.0 |
| St Dev | 10.03 | 31.72 | 30.89 | 40.73 | 37.44 | 52.85 | 70.86 | 97.12 | 63.99 | 55.71 | 13.23 | 12.02 |

| (e) | Jan | Feb | Mar | Apr | May | Jun | Jul | Aug | Sep | Oct | Nov | Dec |
|---|---|---|---|---|---|---|---|---|---|---|---|---|
| Minimum | 0.0 | 0.0 | 0.0 | 2.6 | 31.8 | 41.9 | 88.4 | 142.4 | 55.7 | 0.7 | 0.0 | 0.0 |
| Maximum | 25.7 | 70.6 | 104.7 | 130.2 | 231.2 | 274.3 | 330.2 | 455.5 | 447.7 | 207.7 | 41.7 | 33.6 |
| Mean | 0.8 | 3.4 | 16.2 | 51.5 | 101.6 | 128.5 | 188.4 | 272.8 | 168.0 | 50.5 | 3.6 | 2.6 |
| Median | 0.0 | 0.0 | 3.6 | 43.0 | 96.2 | 138.2 | 176.8 | 268.7 | 151.8 | 48.5 | 0.0 | 0.0 |
| Mode | 0.0 | 0.0 | 0.0 | - | - | - | - | - | - | - | 0.0 | 0.0 |
| St Dev | 4.11 | 12.03 | 26.16 | 34.29 | 51.73 | 53.40 | 63.70 | 76.54 | 75.34 | 37.98 | 8.83 | 8.23 |

**APPENDIX 3.1** ***Figure 3.2 USGS Windows-based 3-D Visualization Toolbox***

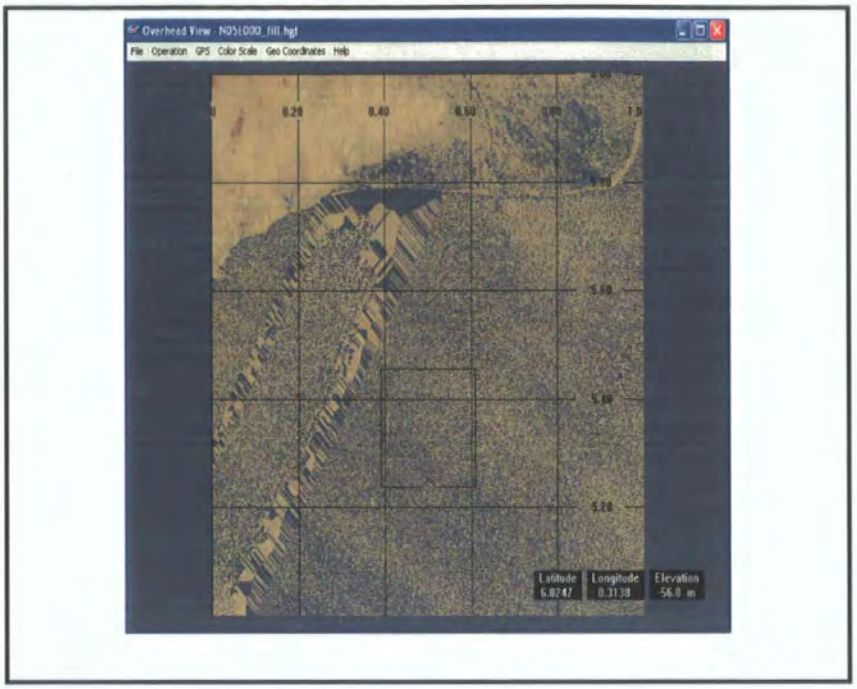


USGS Global Visualisation Viewer, which was used for (1) reading retrieved SRTM tiles (scenes) from the USGS website, (2) converting the raw image files into a GIS format (i.e. GeoTIFF) (3) viewing and reviewing the files, and (4) filling the "void (no data) pixels" before DEM processing using ESRI's ARC-Hydro (GIS) Package. Source: http://glovis.usgs.gov/ImgViewer/Java2ImgViewer.html

## APPENDIX 3.2 *USGS Global Visualization Viewer*

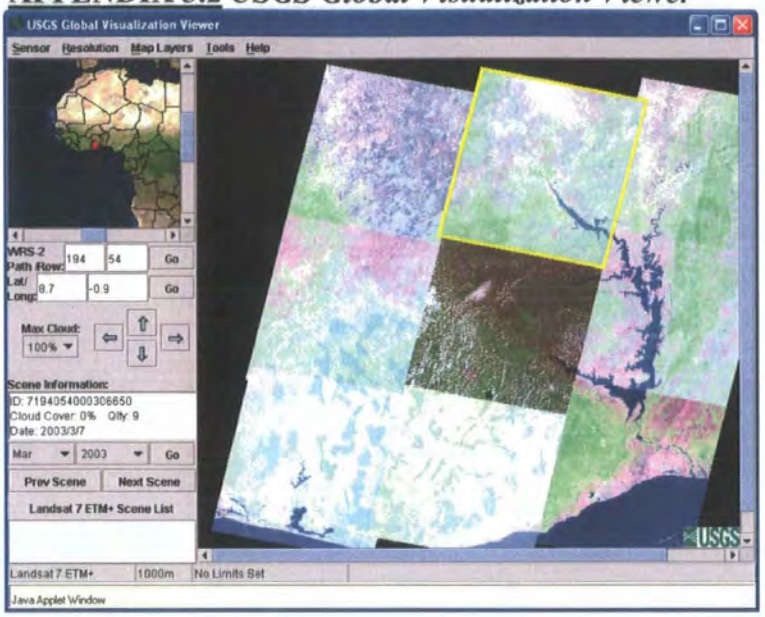


## APPENDIX 3.3 *ESA's BEAM Image Processing Tool*

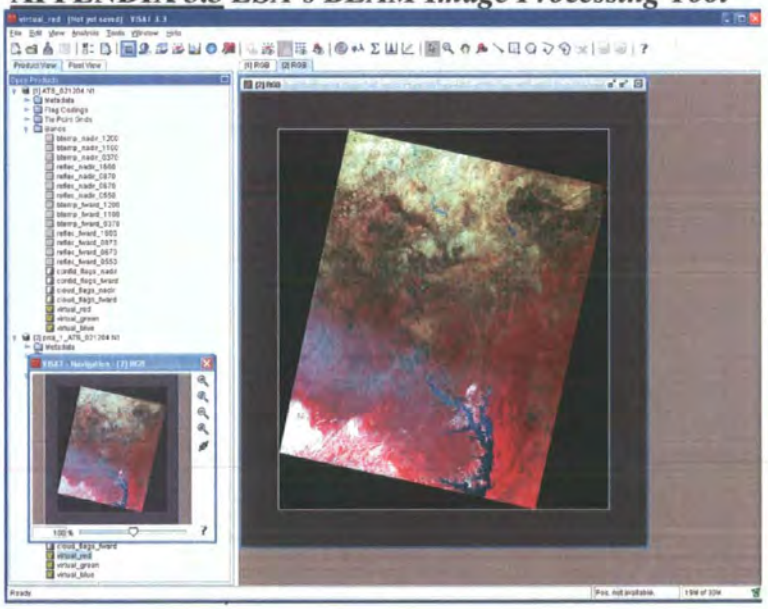

Appendix 3.2 shows an example of a set of Landsat ETM+ files covering the Volta Lake basin and read from the USGS Global Visualization Viewer (GLOVIS). The most important use of the GLOVIS was reprojection of the study to UTM projection and retrieving vital image information.

Appendix 3.3: The BEAM (Basic ERS & Envisat AATSR and MERIS) software has been designed (see http://www.brockmann-consult.de/beam/) to fit a range of operating systems (Windows, UNIX, Linux, etc.). The PC-Windows version used in this research was particularly suited for iterative image processing and exporting data into the widely convertible GeoTIFF format.

## APPENDIX 3.4 *NASA's HDF-EOS to GeoTIFF (HEG) Tool Interface*

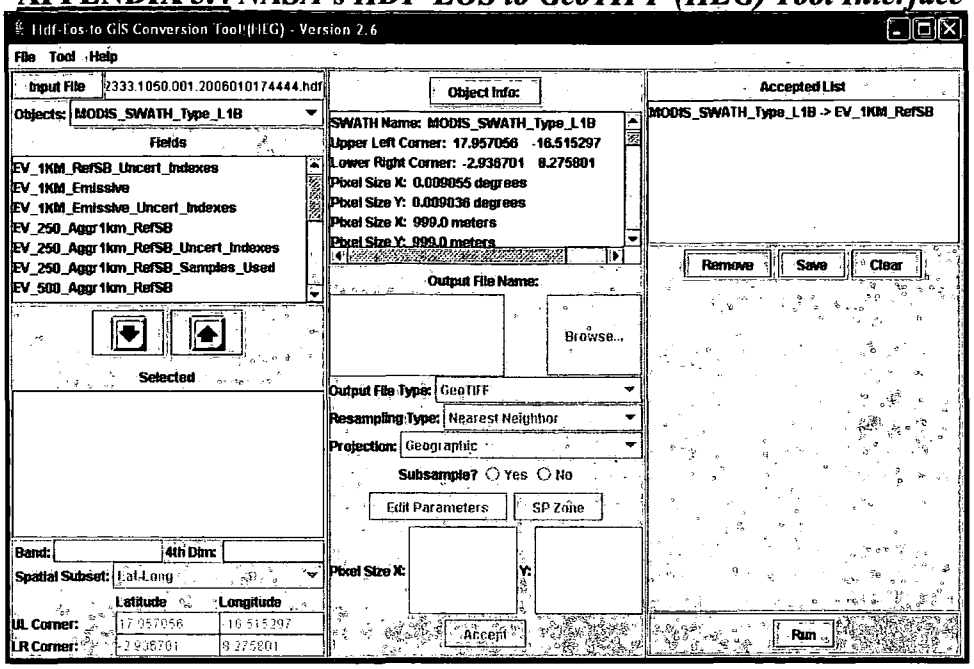


The HDF-EOS to GIS (HEG) Conversion Tool resolves several processing constraints. First, it converts HDF-EOS swath and grid data to HDF-EOS Grid, GeoTIFF or to a generic binary format. Secondly, the tool is used to re-project data from its original format (Integerized Sinusoidal Projection) to standard projections such as UTM. Thirdly, it has functionalities to subset data and to mosaic adjacent granules together. The HEG packages are available for Sun and SGI systems in 'tar' format, and a User's Guide in Microsoft Word is available. The tool runs via Java Version 1.2 or higher. Downloading and installation instructions are available at http://eosweb.larc.nasa.gov/PRODOCS/misr/geotiff_tool.html.

**APPENDIX 3.5** ***MODIS L1B Raw Data Calibration Coefficient – Corrected Counts***

| Date of image acquisition | Band 1 (λ=0.620-0.670μm) | | Band 2 (λ=0.841-0.876μm) | |
|---|---|---|---|---|
| | Corrected count scales | Corrected counts offsets | Corrected count scales | Corrected counts offsets |
| 291102 | 0.126194 | 316.972 | 0.126194 | 316.972 |
| 191202 | 0.126194 | 316.972 | 0.126194 | 316.972 |
| 040103 | 0.126194 | 316.972 | 0.126194 | 316.972 |
| 050203 | 0.126194 | 316.972 | 0.126194 | 316.972 |
| 090203 | 0.126194 | 316.972 | 0.126194 | 316.972 |
| 010204 | 0.126194 | 316.972 | 0.126194 | 316.972 |
| 131104 | 0.126194 | 316.972 | 0.126194 | 316.972 |
| 021204 | 0.126194 | 316.972 | 0.126194 | 316.972 |
| 181204 | 0.126194 | 316.972 | 0.126194 | 316.972 |
| 020105 | 0.126194 | 316.972 | 0.126194 | 316.972 |
| 210105 | 0.126194 | 316.972 | 0.126194 | 316.972 |
| 250105 | 0.126194 | 316.972 | 0.126194 | 316.972 |
| 050205 | 0.126194 | 316.972 | 0.126194 | 316.972 |
| 120205 | 0.126194 | 316.972 | 0.126194 | 316.972 |

| | Band 29 (λ=8.400-8.700μm) | | Band 31 (λ=10.780-11.280μm) | | Band 32 (λ=11.770-12.270μm) | |
|---|---|---|---|---|---|---|
| Image date | Radiance scales | Radiance offsets | Radiance scales | Radiance offsets | Radiance scales | Radiance offsets |
| 291102 | 0.000532487 | 2730.58 | 0.000840022 | 1577.34 | 0.000729698 | 1658.22 |
| 191202 | 0.000532487 | 2730.58 | 0.000840022 | 1577.34 | 0.000729698 | 1658.22 |
| 040103 | 0.000532487 | 2730.58 | 0.000840022 | 1577.34 | 0.000729698 | 1658.22 |
| 050203 | 0.000532487 | 2730.58 | 0.000840022 | 1577.34 | 0.000729698 | 1658.22 |
| 090203 | 0.000532487 | 2730.58 | 0.000840022 | 1577.34 | 0.000729698 | 1658.22 |
| 010204 | 0.000532487 | 2730.58 | 0.000840022 | 1577.34 | 0.000729698 | 1658.22 |
| 131104 | 0.000532487 | 2730.58 | 0.000840022 | 1577.34 | 0.000729698 | 1658.22 |
| 021204 | 0.000532487 | 2730.58 | 0.000840022 | 1577.34 | 0.000729698 | 1658.22 |
| 181204 | 0.000532487 | 2730.58 | 0.000840022 | 1577.34 | 0.000729698 | 1658.22 |
| 020105 | 0.000532487 | 2730.58 | 0.000840022 | 1577.34 | 0.000729698 | 1658.22 |
| 210105 | 0.000532487 | 2730.58 | 0.000840022 | 1577.34 | 0.000729698 | 1658.22 |
| 250105 | 0.000532487 | 2730.58 | 0.000840022 | 1577.34 | 0.000729698 | 1658.22 |
| 050205 | 0.000532487 | 2730.58 | 0.000840022 | 1577.34 | 0.000729698 | 1658.22 |
| 120205 | 0.000532487 | 2730.58 | 0.000840022 | 1577.34 | 0.000729698 | 1658.22 |

**APPENDIX 3.6** ***MODIS Level 1B Image Calibration Coefficients – Scales and Offsets***

***(a) Reflected solar bands***

| Date of image | Band 1 (λ=0.620-0.670μm) | | | Band 2 (λ=0.841-0.876μm) | | |
|---|---|---|---|---|---|---|
| | Reflectance | | Radiance | Reflectance | | Radiance |
| | Scales | Offsets | scales | Scales | Offsets | scales |
| 291102 | 5.15247E-05 | 0.00 | 0.0270699 | 3.19364E-05 | 0.00 | 0.0103649 |
| 191202 | 5.1275E-05 | 0.00 | 0.027067 | 3.17758E-05 | 0.00 | 0.0103619 |
| 040103 | 5.12124E-05 | 0.00 | 0.0270647 | 3.17329E-05 | 0.00 | 0.0103597 |
| 050203 | 5.13241E-05 | 0.00 | 0.0269871 | 3.2088E-05 | 0.00 | 0.0104229 |
| 090203 | 5.11852E-05 | 0.00 | 0.0268847 | 3.21624-05 | 0.00 | 0.0104356 |
| 010204 | 5.05247E-05 | 0.00 | 0.0266074 | 3.18102E-05 | 0.00 | 0.0103484 |
| 131104 | 5.08745E-05 | 0.00 | 0.0265674 | 3.17431E-05 | 0.00 | 0.0102402 |
| 021204 | 5.04319E-05 | 0.00 | 0.0265312 | 3.15164E-05 | 0.00 | 0.0102423 |
| 181204 | 5.02487E-05 | 0.00 | 0.0265361 | 3.14294E-05 | 0.00 | 0.0102532 |
| 020105 | 4.98315E-05 | 0.00 | 0.0263498 | 3.14367E-05 | 0.00 | 0.0102688 |
| 210105 | 4.99124E-05 | 0.00 | 0.026348 | 3.14664E-05 | 0.00 | 0.0102612 |
| 250105 | 4.99524E-05 | 0.00 | 0.0263477 | 3.14871E-05 | 0.00 | 0.0102596 |
| 050205 | 5.01013E-05 | 0.00 | 0.0263467 | 3.15686E-05 | 0.00 | 0.0102551 |
| 120205 | 5.02216E-05 | 0.00 | 0.0263449 | 3.16387E-05 | 0.00 | 0.0102526 |

*Note: The radiance and reflectance offsets have the same values for all reflective solar bands.*

*(b) Thermal emissive bands*

| Date of image | Band 29 (λ=8.400-8.700μm) | | Band 31 (λ=10.780-11.280μm) | | Band 32 (λ=11.770-12.270μm) | |
|---|---|---|---|---|---|---|
| | Radiance | | Radiance | | Radiance | |
| | Scales | Offsets | Scales | Offsets | Scales | Offsets |
| 291102 | 0.000532487 | 2730.58 | 0.000840022 | 1577.34 | 0.000729698 | 1658.22 |
| 191202 | 0.000532487 | 2730.58 | 0.000840022 | 1577.34 | 0.000729698 | 1658.22 |
| 040103 | 0.000532487 | 2730.58 | 0.000840022 | 1577.34 | 0.000729698 | 1658.22 |
| 050203 | 0.000532487 | 2730.58 | 0.000840022 | 1577.34 | 0.000729698 | 1658.22 |
| 090203 | 0.000532487 | 2730.58 | 0.000840022 | 1577.34 | 0.000729698 | 1658.22 |
| 010204 | 0.000532487 | 2730.58 | 0.000840022 | 1577.34 | 0.000729698 | 1658.22 |
| 131104 | 0.000532487 | 2730.58 | 0.000840022 | 1577.34 | 0.000729698 | 1658.22 |
| 021204 | 0.000532487 | 2730.58 | 0.000840022 | 1577.34 | 0.000729698 | 1658.22 |
| 181204 | 0.000532487 | 2730.58 | 0.000840022 | 1577.34 | 0.000729698 | 1658.22 |
| 020105 | 0.000532487 | 2730.58 | 0.000840022 | 1577.34 | 0.000729698 | 1658.22 |
| 210105 | 0.000532487 | 2730.58 | 0.000840022 | 1577.34 | 0.000729698 | 1658.22 |
| 250105 | 0.000532487 | 2730.58 | 0.000840022 | 1577.34 | 0.000729698 | 1658.22 |
| 050205 | 0.000532487 | 2730.58 | 0.000840022 | 1577.34 | 0.000729698 | 1658.22 |
| 120205 | 0.000532487 | 2730.58 | 0.000840022 | 1577.34 | 0.000729698 | 1658.22 |

*Source: MCST (2003) MODIS Level 1B Product User's Guide - MCST Document # PUB-01-U-0202-REV B, MODIS Characterisation Support Team (MCST, NASA), December 2003*

**APPENDIX 3.7** ***Double ring infiltrometer (Complete set)***

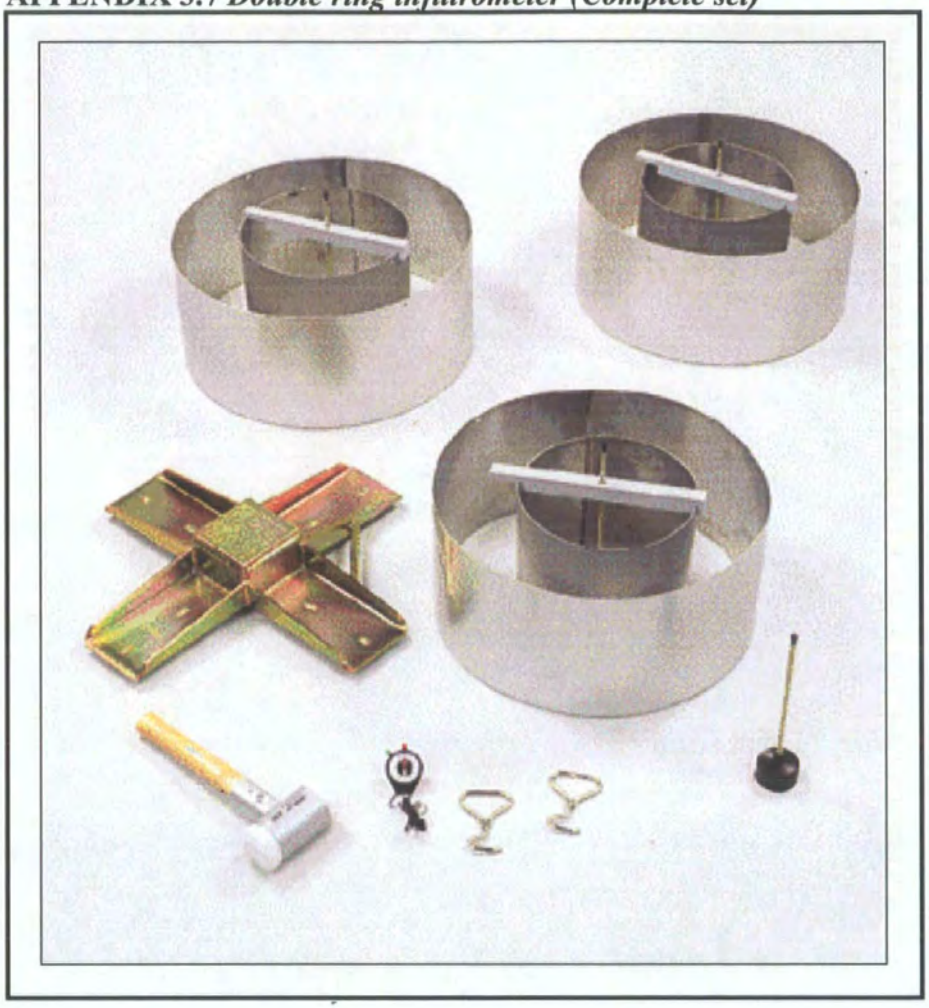

The top figure shows a complete set of the Eijkelkamp double-ring infiltrometer for infiltration measurements in the Volta basin, which will be used for further research. The bottom figure illustrates the measurement procedure.

## APPENDIX 3.8 *Tempcon HOBO-H8 Thermal Data Logger*

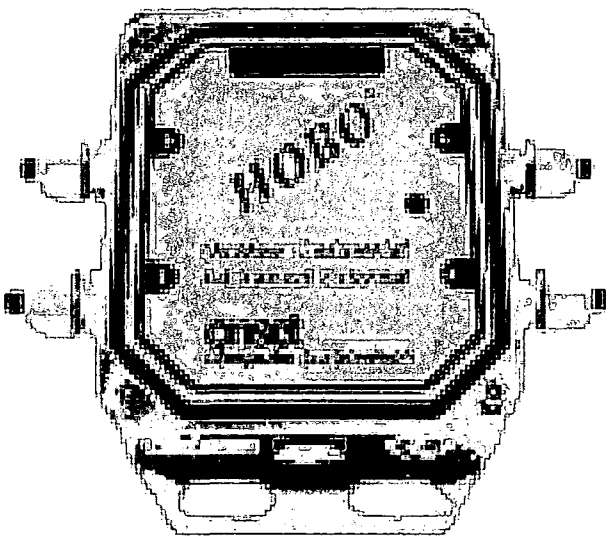

The HOBO H-8 temperature data logger is pocket-size, 4-channel temperature recorder which continuously measures temperature in remote locations. In the field, the channels were first connected to external sensors attached to 1m electric cables. The BoxCar Pro software installed on a laptop computer was used to initialize the logging processed using the BoxCar readout command. The HOBO remained buried in the ground until the sampling period was over. The information was again readout to the computer including 10-minute thermal plots. Further information about the HOBO features, applications and acquisition are detailed at the ONSET Computer Corporation website or suppliers such as MicroDAQ (http://www.microdaq.com/).

**APPENDIX 4.1** ***Sample Meteorological Records from GLOWA-Volta Scintillometer Observations for 2002***

| DOY | Temp (^0C) | RH (%) | Wind speed (m/s) | Soil Heat Flux (W/m^2) | Rainfall (mm) | Pressure (mbar) | Net rad (W/m^2) |
|---|---|---|---|---|---|---|---|
| 1 | 23.47 | 54.20 | 3.28 | 6.94 | 0.00 | 987.98 | 55.41 |
| 2 | 23.39 | 54.26 | 2.84 | 7.74 | 0.00 | 988.73 | 64.47 |
| 3 | 22.88 | 55.16 | 2.64 | 5.00 | 0.00 | 988.84 | 60.08 |
| 4 | 22.63 | 57.89 | 2.33 | 4.38 | 0.00 | 988.24 | 59.17 |
| 5 | 22.24 | 55.21 | 2.76 | 3.72 | 0.00 | 987.41 | 52.61 |
| 6 | 23.02 | 55.06 | 1.58 | 4.06 | 0.00 | 987.11 | 38.82 |
| 7 | 22.93 | 57.78 | 2.11 | 17.59 | 0.00 | 985.99 | 54.08 |
| 14 | 22.18 | 58.45 | 1.81 | 0.48 | 0.00 | 989.54 | 59.26 |
| 15 | 20.51 | 68.33 | 2.54 | 6.28 | 0.00 | 989.08 | 59.69 |
| 16 | 21.64 | 66.31 | 2.94 | 8.63 | 0.00 | 988.32 | 59.52 |
| 17 | 22.35 | 57.90 | 2.66 | 8.44 | 0.00 | 987.73 | 57.40 |
| 18 | 23.10 | 54.67 | 2.68 | 7.78 | 0.00 | 987.31 | 50.04 |
| 19 | 23.64 | 54.34 | 3.00 | 9.95 | 0.00 | 987.54 | 59.46 |
| 20 | 23.71 | 54.86 | 4.04 | 9.65 | 0.00 | 988.66 | 58.62 |
| 21 | 23.87 | 55.01 | 3.71 | 8.06 | 0.00 | 989.33 | 58.95 |
| 22 | 23.68 | 54.35 | 2.51 | 6.49 | 0.00 | 990.11 | 51.69 |
| 23 | 24.02 | 51.61 | 3.02 | 10.55 | 0.00 | 989.80 | 61.41 |
| 24 | 23.75 | 54.80 | 2.81 | 8.15 | 0.00 | 990.30 | 52.82 |
| 25 | 23.76 | 54.76 | 3.13 | 10.24 | 0.00 | 990.55 | 58.84 |
| 26 | 23.32 | 54.28 | 3.39 | 9.25 | 0.00 | 990.40 | 59.29 |
| 27 | 23.14 | 54.75 | 3.91 | 7.99 | 0.00 | 989.81 | 60.19 |
| 28 | 21.97 | 66.47 | 3.57 | 6.64 | 0.00 | 989.85 | 55.20 |
| 29 | 22.37 | 58.18 | 4.01 | 6.97 | 0.00 | 990.06 | 54.94 |
| 30 | 23.14 | 54.69 | 3.63 | 8.39 | 0.00 | 990.56 | 53.56 |
| 31 | 22.68 | 57.97 | 4.36 | 4.38 | 0.00 | 990.49 | 37.47 |
| 32 | 21.62 | 66.58 | 3.56 | 6.19 | 0.00 | 989.26 | 55.46 |
| 33 | 22.58 | 58.02 | 2.72 | 7.28 | 0.00 | 989.71 | 52.85 |
| 34 | 24.07 | 51.60 | 2.41 | 10.08 | 0.00 | 989.46 | 53.91 |
| 35 | 24.32 | 51.49 | 2.69 | 12.48 | 0.00 | 988.54 | 62.32 |
| 36 | 24.16 | 51.52 | 3.45 | 10.21 | 0.00 | 988.21 | 58.37 |
| 37 | 23.72 | 54.76 | 3.21 | 12.09 | 0.00 | 988.19 | 67.93 |
| 38 | 24.22 | 51.49 | 2.69 | 10.17 | 0.00 | 988.11 | 63.04 |
| 39 | 24.60 | 51.33 | 2.97 | 13.15 | 0.00 | 988.18 | 65.88 |
| 40 | 23.90 | 52.09 | 3.48 | 13.41 | 0.00 | 987.58 | 72.34 |
| 41 | 22.89 | 59.32 | 3.51 | 11.76 | 0.00 | 988.28 | 68.76 |
| 42 | 23.21 | 54.78 | 2.99 | 10.64 | 0.00 | 989.14 | 65.73 |
| 43 | 23.24 | 54.72 | 3.59 | 6.19 | 0.00 | 989.91 | 51.61 |
| 44 | 23.66 | 54.76 | 2.81 | 11.59 | 0.00 | 989.26 | 68.07 |
| 45 | 24.68 | 51.26 | 2.56 | 11.54 | 0.00 | 988.99 | 65.46 |
| 46 | 25.31 | 45.78 | 2.39 | 12.35 | 0.00 | 989.02 | 72.91 |
| 47 | 25.94 | 45.23 | 2.18 | 14.30 | 0.00 | 988.54 | 74.94 |
| 48 | 27.05 | 36.16 | 2.23 | 17.27 | 0.00 | 988.61 | 92.23 |
| 49 | 27.30 | 33.20 | 2.53 | 17.46 | 0.00 | 988.09 | 90.48 |
| 50 | 27.32 | 32.98 | 2.97 | 16.55 | 0.00 | 988.05 | 88.35 |
| 51 | 27.44 | 35.76 | 2.40 | 14.60 | 0.00 | 987.81 | 81.35 |
| 52 | 27.07 | 33.08 | 2.12 | 19.60 | 0.00 | 985.92 | 101.61 |
| 53 | 27.83 | 31.20 | 2.11 | 20.56 | 0.00 | 984.49 | 100.95 |
| 54 | 28.34 | 29.00 | 2.55 | 20.00 | 0.00 | 986.07 | 97.48 |
| 55 | 28.53 | 28.97 | 2.63 | 14.10 | 0.00 | 986.36 | 67.78 |
| 56 | 27.94 | 33.11 | 3.03 | 17.85 | 0.00 | 986.44 | 77.84 |

| | | | | | | | |
|---|---|---|---|---|---|---|---|
| 57 | 25.79 | 41.36 | 2.72 | 23.49 | 0.00 | 987.37 | 128.93 |
| 75 | 31.07 | 39.95 | 2.96 | 20.66 | 0.00 | 984.67 | 202.78 |
| 76 | 27.18 | 41.23 | 3.16 | 9.53 | 0.00 | 984.75 | 109.01 |
| 77 | 26.51 | 44.58 | 2.66 | 19.17 | 0.00 | 985.99 | 130.93 |
| 78 | 28.62 | 56.53 | 2.24 | 20.45 | 0.00 | 986.11 | 114.15 |
| 79 | 27.57 | 51.23 | 3.07 | 18.33 | 0.00 | 986.83 | 109.20 |
| 80 | 28.26 | 55.25 | 2.56 | 17.17 | 0.00 | 986.31 | 101.95 |
| 81 | 28.62 | 44.76 | 3.09 | 9.01 | 0.00 | 985.97 | 61.37 |
| 82 | 27.91 | 51.39 | 2.51 | 17.64 | 0.00 | 986.46 | 91.82 |
| 83 | 27.88 | 44.67 | 3.06 | 14.56 | 0.00 | 985.97 | 85.58 |
| 84 | 28.33 | 45.90 | 2.69 | 19.93 | 0.00 | 985.83 | 108.93 |
| 85 | 28.00 | 45.99 | 3.03 | 19.89 | 0.00 | 985.90 | 114.51 |
| 86 | 28.10 | 44.12 | 3.14 | 17.79 | 0.00 | 986.06 | 113.57 |
| 87 | 27.32 | 38.98 | 3.33 | 12.24 | 0.00 | 986.04 | 91.03 |
| 88 | 25.29 | 41.23 | 3.74 | 7.51 | 0.00 | 986.78 | 95.50 |
| 89 | 27.28 | 36.23 | 3.00 | 19.08 | 0.00 | 986.62 | 129.80 |
| 90 | 28.31 | 33.46 | 2.83 | 19.50 | 0.00 | 985.41 | 117.24 |
| 91 | 28.93 | 34.65 | 3.29 | 20.17 | 0.00 | 985.16 | 121.81 |
| 92 | 29.03 | 35.90 | 3.43 | 18.03 | 0.00 | 985.67 | 119.53 |
| 93 | 27.66 | 35.76 | 3.42 | 14.15 | 0.00 | 987.18 | 108.41 |
| 94 | 28.01 | 36.76 | 3.34 | 17.09 | 0.00 | 985.65 | 124.86 |
| 95 | 25.78 | 42.32 | 3.08 | 12.75 | 0.00 | 984.37 | 118.74 |
| 96 | 21.37 | 63.21 | 2.97 | 11.02 | 0.16 | 984.45 | 45.03 |
| 97 | 24.10 | 53.32 | 2.70 | 5.19 | 0.00 | 985.10 | 156.78 |
| 98 | 24.51 | 46.87 | 4.05 | 8.39 | 0.00 | 985.55 | 161.62 |
| 99 | 22.85 | 54.13 | 3.63 | 4.12 | 0.00 | 986.12 | 97.47 |
| 131 | 21.98 | 56.71 | 4.79 | 3.10 | 0.03 | 988.27 | 131.97 |
| 132 | 24.14 | 53.06 | 3.05 | 6.14 | 0.00 | 987.99 | 139.77 |
| 133 | 26.01 | 44.74 | 3.82 | 20.94 | 0.00 | 987.75 | 167.24 |
| 134 | 22.07 | 57.79 | 3.11 | 7.83 | 0.10 | 989.65 | 113.10 |
| 135 | 24.68 | 52.59 | 2.72 | 10.52 | 0.00 | 989.69 | 170.13 |
| 136 | 26.80 | 45.59 | 2.92 | 17.49 | 0.00 | 987.18 | 147.59 |
| 137 | 25.92 | 49.95 | 3.67 | 7.23 | 0.00 | 986.83 | 113.69 |
| 138 | 25.47 | 44.39 | 2.83 | 9.27 | 0.00 | 987.59 | 135.09 |
| 139 | 21.03 | 63.74 | 3.03 | 3.16 | 0.12 | 988.86 | 132.15 |
| 140 | 22.99 | 56.89 | 2.04 | 7.05 | 0.00 | 987.95 | 151.05 |
| 141 | 25.47 | 50.17 | 2.20 | 10.96 | 0.00 | 987.74 | 169.47 |
| 142 | 24.43 | 49.18 | 3.33 | 10.14 | 0.00 | 987.46 | 166.82 |
| 143 | 23.27 | 54.55 | 2.55 | 6.04 | 0.00 | 987.79 | 133.28 |
| 144 | 25.64 | 49.84 | 1.92 | 13.52 | 0.00 | 987.67 | 139.23 |
| 145 | 26.85 | 44.69 | 2.53 | 17.90 | 0.00 | 986.97 | 139.77 |
| 146 | 26.50 | 46.69 | 3.22 | 21.53 | 0.00 | 986.15 | 160.06 |
| 147 | 24.33 | 44.17 | 3.47 | 5.40 | 0.00 | 986.65 | 89.67 |
| 148 | 24.78 | 49.09 | 3.79 | 13.25 | 0.00 | 987.30 | 134.19 |
| 149 | 24.68 | 45.61 | 2.55 | 16.17 | 0.00 | 988.53 | 130.47 |
| 150 | 25.48 | 47.30 | 2.15 | 12.95 | 0.00 | 988.82 | 102.04 |
| 151 | 26.44 | 44.69 | 3.48 | 18.25 | 0.00 | 987.68 | 145.14 |
| 152 | 23.08 | 53.12 | 3.59 | 11.48 | 0.10 | 987.59 | 153.54 |
| 153 | 22.32 | 56.59 | 3.07 | 6.30 | 0.01 | 988.00 | 144.64 |
| 154 | 22.10 | 59.34 | 1.97 | 12.80 | 0.02 | 988.66 | 127.09 |
| 155 | 22.42 | 60.44 | 1.79 | 7.19 | 0.00 | 990.51 | 207.98 |
| 156 | 22.86 | 55.63 | 2.70 | 1.10 | 0.00 | 990.24 | 40.93 |
| 157 | 24.03 | 52.04 | 2.97 | 5.39 | 0.00 | 990.00 | 149.34 |
| 158 | 21.86 | 59.42 | 3.48 | 8.52 | 0.00 | 989.62 | 62.34 |

| | | | | | | | |
|---|---|---|---|---|---|---|---|
| 159 | 21.85 | 57.25 | 2.98 | 4.38 | 0.00 | 990.00 | 110.18 |
| 160 | 21.91 | 57.79 | 2.29 | 0.74 | 0.00 | 990.44 | 101.45 |
| 161 | 21.62 | 59.22 | 2.49 | 1.99 | 0.01 | 990.19 | 100.95 |
| 162 | 23.43 | 51.90 | 2.76 | 6.18 | 0.00 | 990.18 | 150.79 |
| 163 | 23.12 | 51.54 | 3.58 | 8.21 | 0.00 | 989.78 | 125.89 |
| 164 | 22.71 | 52.94 | 2.98 | 7.50 | 0.00 | 989.60 | 128.93 |
| 165 | 22.54 | 58.55 | 2.31 | 1.15 | 0.10 | 990.19 | 86.66 |
| 166 | 20.75 | 66.83 | 2.70 | 16.03 | 0.05 | 991.35 | 135.83 |
| 167 | 23.00 | 58.71 | 2.69 | 8.16 | 0.00 | 990.95 | 164.58 |
| 168 | 23.05 | 57.46 | 2.84 | 4.70 | 0.00 | 991.07 | 149.63 |
| 169 | 21.01 | 66.33 | 3.07 | 12.73 | 0.19 | 992.32 | 99.67 |
| 170 | 21.34 | 65.42 | 2.18 | 7.83 | 0.00 | 992.58 | 131.68 |
| 171 | 22.06 | 64.03 | 2.39 | 6.84 | 0.01 | 992.17 | 140.40 |
| 172 | 20.63 | 67.08 | 2.46 | 12.29 | 0.20 | 991.22 | 88.74 |
| 173 | 22.36 | 61.75 | 2.50 | 0.71 | 0.00 | 991.39 | 172.11 |
| 174 | 23.74 | 57.32 | 2.17 | 1.47 | 0.00 | 991.56 | 155.60 |
| 175 | 22.95 | 59.18 | 2.54 | 6.67 | 0.00 | 991.96 | 145.27 |
| 176 | 23.24 | 58.76 | 2.38 | 3.56 | 0.00 | 990.95 | 121.30 |
| 177 | 19.02 | 71.12 | 2.54 | 5.88 | 0.15 | 991.07 | 19.35 |
| 178 | 20.84 | 66.63 | 2.16 | 4.88 | 0.09 | 990.81 | 151.95 |
| 179 | 20.28 | 67.65 | 1.85 | 12.39 | 0.00 | 991.51 | 98.08 |
| 180 | 21.70 | 64.12 | 1.61 | 4.90 | 0.00 | 991.63 | 112.78 |
| 181 | 22.16 | 58.63 | 2.10 | 13.59 | 0.00 | 990.64 | 114.86 |
| 182 | 20.91 | 63.14 | 3.36 | 5.73 | 0.00 | 991.07 | 119.41 |
| 183 | 21.48 | 62.32 | 2.82 | 0.70 | 0.00 | 990.63 | 131.48 |
| 184 | 21.74 | 62.55 | 2.40 | 0.64 | 0.00 | 991.45 | 129.82 |
| 185 | 22.45 | 59.56 | 2.63 | 0.62 | 0.00 | 991.90 | 148.14 |
| 186 | 21.88 | 62.22 | 2.91 | 0.65 | 0.01 | 990.74 | 105.26 |
| 187 | 17.86 | 74.90 | 2.47 | 2.28 | 0.15 | 989.36 | 104.61 |
| 188 | 17.87 | 72.41 | 3.42 | 8.20 | 0.00 | 988.86 | 53.39 |
| 189 | 20.05 | 66.21 | 2.48 | 7.81 | 0.00 | 990.99 | 111.63 |
| 190 | 21.16 | 64.44 | 2.44 | 3.56 | 0.00 | 991.16 | 151.33 |
| 191 | 21.42 | 63.64 | 2.72 | 5.71 | 0.00 | 988.58 | 119.81 |
| 192 | 18.65 | 71.28 | 3.28 | 7.71 | 0.19 | 988.48 | 92.83 |
| 193 | 19.34 | 67.28 | 2.50 | 5.30 | 0.00 | 989.90 | 165.45 |
| 194 | 20.29 | 68.79 | 2.31 | 8.08 | 0.03 | 991.31 | 79.62 |
| 195 | 21.05 | 66.78 | 2.37 | 3.80 | 0.00 | 991.17 | 141.73 |
| 196 | 20.76 | 66.22 | 2.80 | 7.75 | 0.03 | 989.91 | 161.74 |
| 197 | 18.58 | 72.92 | 2.01 | 2.25 | 0.00 | 990.13 | 80.18 |
| 198 | 20.52 | 66.62 | 2.00 | 6.38 | 0.00 | 991.48 | 118.23 |
| 199 | 19.86 | 70.62 | 1.98 | 10.56 | 0.00 | 991.43 | 36.81 |
| 200 | 21.80 | 63.31 | 2.53 | 0.49 | 0.00 | 991.46 | 174.77 |
| 201 | 18.98 | 72.31 | 2.34 | 12.44 | 0.19 | 991.98 | 71.15 |
| 202 | 19.39 | 69.78 | 2.16 | 9.08 | 0.00 | 992.59 | 91.95 |
| 203 | 20.26 | 67.09 | 2.36 | 7.39 | 0.00 | 992.68 | 100.91 |
| 204 | 20.26 | 67.36 | 2.48 | 9.92 | 0.16 | 990.26 | 142.80 |
| 205 | 20.06 | 68.85 | 2.59 | 7.14 | 0.00 | 990.11 | 148.43 |
| 206 | 23.75 | 56.95 | 1.96 | 7.45 | 0.00 | 988.74 | 115.73 |
| 207 | 20.37 | 69.44 | 2.75 | 9.70 | 0.77 | 988.86 | 110.96 |
| 208 | 18.91 | 74.21 | 1.90 | 5.33 | 0.03 | 989.66 | 41.96 |
| 209 | 20.09 | 67.29 | 1.74 | 4.53 | 0.00 | 989.70 | 99.60 |
| 210 | 18.86 | 70.50 | 2.46 | 5.19 | 0.04 | 989.63 | 54.34 |
| 211 | 20.51 | 66.86 | 2.50 | 5.56 | 0.00 | 990.83 | 142.87 |
| 212 | 21.47 | 64.30 | 1.46 | 2.37 | 0.00 | 990.93 | 127.49 |

| | | | | | | | |
|---|---|---|---|---|---|---|---|
| 213 | 22.15 | 65.56 | 1.96 | 1.02 | 0.00 | 989.12 | 165.20 |
| 214 | 21.00 | 64.18 | 1.74 | 7.81 | 0.00 | 989.62 | 125.75 |
| 215 | 22.78 | 60.59 | 2.08 | 7.69 | 0.16 | 989.62 | 185.78 |
| 216 | 19.14 | 68.25 | 2.08 | 4.33 | 0.00 | 988.81 | 112.18 |
| 217 | 20.85 | 65.84 | 2.40 | 6.79 | 0.00 | 990.51 | 122.45 |
| 218 | 18.47 | 73.15 | 2.97 | 6.08 | 0.10 | 990.60 | 42.95 |
| 219 | 19.19 | 71.56 | 1.74 | 7.47 | 0.00 | 990.69 | 71.33 |
| 220 | 20.37 | 66.43 | 1.68 | 6.46 | 0.00 | 991.44 | 112.45 |
| 221 | 21.25 | 65.56 | 1.96 | 4.48 | 0.00 | 991.00 | 94.66 |
| 222 | 22.02 | 62.67 | 2.12 | 8.55 | 0.11 | 989.93 | 145.79 |
| 223 | 20.75 | 66.77 | 2.26 | 5.70 | 0.01 | 989.23 | 158.11 |
| 224 | 20.71 | 66.68 | 2.60 | 5.49 | 0.00 | 990.17 | 144.50 |
| 225 | 20.37 | 66.64 | 2.11 | 9.58 | 0.00 | 990.91 | 125.99 |
| 226 | 20.90 | 67.22 | 1.65 | 4.28 | 0.00 | 991.81 | 109.01 |
| 227 | 18.65 | 70.86 | 2.29 | 4.37 | 0.09 | 992.06 | 76.52 |
| 228 | 21.02 | 64.80 | 2.00 | 2.37 | 0.00 | 991.61 | 188.94 |
| 229 | 22.03 | 63.41 | 2.01 | 1.58 | 0.00 | 989.93 | 164.51 |
| 230 | 19.12 | 70.50 | 2.09 | 6.18 | 0.15 | 989.45 | 148.01 |
| 278 | 21.32 | 63.56 | 2.26 | 9.79 | 0.01 | 990.19 | 188.94 |
| 279 | 20.95 | 65.65 | 1.58 | 8.01 | 0.00 | 989.59 | 138.63 |
| 280 | 20.85 | 66.34 | 2.11 | 12.43 | 0.00 | 989.79 | 148.85 |
| 281 | 21.27 | 65.28 | 1.60 | 13.95 | 0.00 | 989.71 | 124.67 |
| 282 | 21.60 | 62.26 | 1.74 | 10.94 | 0.00 | 988.94 | 117.45 |
| 283 | 20.89 | 62.59 | 1.66 | 11.92 | 0.00 | 990.57 | 148.04 |
| 284 | 22.44 | 59.33 | 1.42 | 13.32 | 0.00 | 991.22 | 164.72 |
| 285 | 23.29 | 57.39 | 2.40 | 8.12 | 0.06 | 989.49 | 121.87 |
| min | 17.86 | 28.97 | 1.42 | 0.48 | 0.00 | 984.37 | 19.35 |
| max | 31.07 | 74.90 | 4.79 | 23.49 | 0.77 | 992.68 | 207.98 |
| mean | 23.18 | 56.31 | 2.68 | 9.37 | 0.02 | 988.98 | 107.05 |
| std | 2.75 | 10.55 | 0.62 | 5.39 | 0.07 | 1.97 | 40.36 |

**APPENDIX 4.2** ***Extract of FAO Radiation Conversion Tables***

| | |
|---|---|
| equivalent evaporation (mm/day) | 1 mm $day^{-1}$ = 2.45 MJ $m^{-2}$ $day^{-1}$ |
| joule per $cm^2$ per day (J $cm^{-2}$ $day^{-1}$) | 1 J $cm^{-2}$ $day^{-1}$ = 0.01 MJ $m^{-2}$ $day^{-1}$ |
| calorie per $cm^2$ per day (cal $cm^{-2}$ $day^{-1}$) | 1 cal = 4.1868 J = 4.1868 10-6 MJ |
| | 1 cal $cm^{-2}$ $day^{-1}$ = 4.1868 $10^{-2}$ MJ $m^{-2}$ $day^{-1}$ |
| watt per $m^2$ (W $m^{-2}$) | 1 W = 1 J $s^{-1}$ |
| | 1 W $m^{-2}$ = 0.0864 MJ $m^{-2}$ $day^{-1}$ |

Standard unit: mega-joule per square metre and per day (MJ $m^2$ $day^{-1}$) or as equivalent evaporation in mm per day (mm $day^{-1}$) Source: FAO (1998)

## APPENDIX 5.1 *Definition of the Pearson Product-Moment Correlation Coefficient*

In statistics, the Pearson product-moment correlation coefficient ($R$) is a measure of the tendency of two variables $X$ and $Y$ measured on the same object or organism to increase or decrease together. It is defined as the sum of the products of the standard scores of the two measures divided by the degrees of freedom:

$$R = \frac{\sum z_x z_y}{n-1}$$

Note that this formula assumes that the standard deviations on which the Z scores are based are calculated using $n - 1$ in the denominator. The result obtained is equivalent to dividing the covariance between the two variables by the product of their standard deviations. In general the correlation coefficient is one of the two square roots (either positive or negative) of the coefficient of determination ($R^2$), which is the ratio of explained variation to total variation:

$$R^2 = \frac{\sum (Y' - \overline{Y})^2}{\sum (Y - \overline{Y})^2}$$

where $Y$ = a score on a random variable $Y$ $Y'$ = corresponding predicted value of $Y$, given the correlation of $X$ and $Y$ and the value of $X$. $\overline{Y}$ = **sample** mean of $Y$ (i.e., the mean of a finite number of independent observed realizations of $Y$, ***not*** to be confused with the expected value of $Y$)

The correlation coefficient adds a sign to show the direction of the relationship. The formula for the Pearson coefficient conforms to this definition, and applies when the relationship is linear. The coefficient ranges from −1 to 1. A value of 1 shows that a linear equation describes the relationship perfectly and positively, with all data points lying on the same line and with $Y$ increasing with $X$. A score of −1 shows that all data points lie on a single line but that $Y$ increases as $X$ decreases. A value of 0 shows that a linear model is inappropriate – that there is no linear relationship between the variables. The Pearson coefficient is a statistic which estimates the correlation of the two given random variables. The linear equation that best describes the relationship between $X$ and $Y$ can be found by linear regression. This equation can be used to "predict" the value of one measurement from knowledge of the other. That is, for each value of $X$ the equation calculates a value which is the best estimate of the values of $Y$ corresponding the specific value of $X$. We denote this predicted variable by $Y$. Any value of $Y$ can therefore be defined as the sum of $Y'$ and the difference between $Y$ and $Y'$:

$$Y = Y' + (Y - Y')$$

The variance of $Y$ is equal to the sum of the variance of the two components of $Y$:

$$s_y^2 = S_{y'}^2 + s_{y.x}^2$$

Since the coefficient of determination implies that $s_{y.x}^2 = s_y^2(1 - R^2)$ we can derive the identity

$$R^2 = \frac{s_{y'}^2}{s_y^2}$$

The square of $R$ is conventionally used as a measure of the association between $X$ and $Y$. For example, if the coefficient is 0.90, then 81% of the variance of $Y$ can be "accounted for" by changes in $X$ and the linear relationship between $X$ and $Y$.

**APPENDIX 6.1a** ***The SEBAL Code for ERDAS-based Processing of Landsat ETM+ data***

CALCULATION OF RADIATION AND ENERGY BALANCES
RADIANCE (L) PER BAND (DN) BASED ON RADIATION COEFFICIENTS EXTRACTABLE FROM RAW SATELLITE IMAGERY AND HANDBOOKS - UNITS = Wm^-2*ster*micrometre
L1=a+(b-a)*DN/255

EARTH-SUN DISTANCE (D) PER IMAGE SCENE - Readable from LUT Units = AU

RELECTANCE PER BAND (R) based on band-specific Solar Spectral Irradiance (SSI) from LUT and other coefficients including PI, D and SOLAR ANGLE
Rf1=L1*PI*D^2)/(SSI*0.9494)

NORMALISED DIFFERENCE VEGETATION INDEX (NDVI)
NDVI=(Rf2-Rf1)/(Rf2+Rf1)

PLANETARY ALBEDO (Rp) where x1-x5, x7-x8 = SSI constant LUT values; Rf1-Rf5, Rf7-Rf8 = reflectance in bands 1-8
Rp=(x1*Rf1+x2*Rf2+x3*Rf3+x4*Rf4+x5*Rf5+x7*Rf7+x8Rf8)/(x1+x2+x3+x4+x5+x7+x8)

SURFACE ALBEDO (Ro) based on Rp and atmospheric transmissivity constants specific to dry savannah West Africa
Ro=Rp-0.03613/0.75

INSTANTANEOUS ATMOSPHERIC TRANSMISSIVITY (ATR_ins)
ATR_ins=SQRT(Rp-0.03613)/Ro)

BRIGHTNESS TEMPERATURE (BT6) based on Thermal band calibration constants c1 = 666.09 Wm^2*ster*micrometre and c2 = 1282.71 Kelvin
BT6=c2/(ln(c1/L1+1))

THERMAL INFRARED BROADBAND EMISSIVITY (SE) Empirical derivative of NDVI
SE=IF (NDVI<0)0, (NDVI>0) 1.009+0.047*ln(NDVI)

SURFACE TEMPERATURE (Ts) Derivative of BT and SE
Ts=BT*SE^(-0.25)

AIR TEMPERATURE (Ta) Day spatial average from field logger data
Ta=23.43*Ts/Ts

APPARENT EMISSIVITY (Ea) Empirically derived
Ea=0.85*(-ln(0.75))^0.09

INSTANTANEOUS INCOMING LONG WAVE RADIATION (LW_IN_ins)
LW_IN_inst=Ea*0.0000000567*(Ta+273)^4

INSTANTANEOUS OUTGOING LONG WAVE RADIATION (LW_OUT_inst)
LW_OUT_inst=SE*0.0000000567*Ts^4+(1-SE)*LW_IN_ins)

INSTANTANEOUS INCOMING SHORT WAVE RADIATION (SW_IN_ins)
SW_IN_ins=1339.86*ATR_ins

INSTANTANEOUS NET SHORT WAVE RADIATION (SW_NE_ins)
SW_NE_ins=(1-Ro)*SW_IN_ins

INSTANTANEOUS NET RADIATION (Rn_ins)
Rn_ins=SW_NE_ins+LW_IN_ins-LW_OUT_inst

CALCULATING SOIL HEAT FLUX EMPIRICALLY
INSTANTANEOUS SOIL HEAT FLUX (Go_ins)
Go_ins=(Ts-273)*(0.32*1.1*Ro+0.62*(1.1*Ro)^2*(1-
0.98*NDVI^4)*Rn_ins/(100*Ro)

CALCULATION OF ENVIRONMENTAL AND VEGETATION RESISTANCES

SOIL ADJUSTED VEGETATION INDEX (SAVI)
SAVI=IF((1+0.5)*(NIR-R)/(NIR+R+0.5)<0)0, ((1+0.5)*(NIR-R)/(NIR+R+0.5)>0)
(1+0.5)*(NIR-R)/(NIR+R+0.5)

LEAF AREA INDEX (LAI) USE OF FAO EMPIRICAL COEFFICIENTS*/
LAI=IF(SAVI>0.689)6, (-ln(0.689-SAVI)/0.5369)>0) (-ln(0.689-SAVI/0.5369)

ROUGHNESS LENGTH FOR MOMENTUM TRANSPORT (Zom) EMPIRICALLY DETERMINED - FAO
Zom=EXP(-5.809+5.62*SAVI)

ROUGHNESS LENGTH FOR HEAT TRANSPORT (Zoh) FAO EMPIRICAL RELATIONSHIP
Zoh=0.1*Zom

TEMPERATURE DIFFERENCE (Tdel) AIR TEMPERATURE IS SPATIALLY REFERENCED FROM GROUND DATA AND EMPIRICAL FORMULA APPLIED
Tdel=IF(-382.436+1.299*Ts<0)0, (-382.436+1.299*Ts>0) (-382.436+1.299*Ts)

RASTERIZATION OF STABILITY CORRECTION FACTOR FOR MOMENTUM (psim) AND ATMOSPHERIC HEAT TRANSFER (psih)
psim=psih=0*Tdel

DISPLACEMENT HEIGHT (DIS)
DIS=1*(1-((1-EXP(-((20.6*LAI)^0.5)))/((20.6*LAI)^0.5)))

DISPLACEMENT AT BLENDING HEIGHT OR MIXING LAYER (Ubl)
WINDSPEED FROM GROUND DATA AT 2m AND APPROX. MIXING LAYER OF 100m
Ubl=1.9*(ln(100-DIS)-ln(Zom))/ln(2-Zom)-ln(Zom))

FRICTION VELOCITY (Usta) BASED ON BLENDING HEIGHT, VON KARMAN'S CONSTANT (0.41) AND ASSUMED NULL STABILITY*/
Usta=0.41*Ubl/(ln((100-DIS)/Zom)-psih)

ATMOSPHERIC AIR DENSITY (ADD) MODEL EMPIRICALLY DETERMINED
AAD=((99.190-1.59)/Ts*2.87)+(1.59/Ts*4.61)

AERODYNAMIC RESISTANCE (rah)
rah=(ln((2-DIS)/Zoh)-psih)/(0.41*Usta)

CORRECTED SENSIBLE HEAT FLUX (H_ins)
H_ins=1004*ADD*Tdel/rah

CALCULATION OF NET RADIATION (Rn_24) - UNIT OF INTERMEDIATE PARAMETERS = RADIANS

SOLAR DECLINATION (Delta) IS A FUNCTION OF IMAGE DATE IN JULIAN DAYS (JD) READABLE FROM LUT
Delta=0.409SIN(2*PI/365*JD-1.39)

SOLAR ANGLE HOUR (SAh) FOR DIURNAL EXPOSITION - This depends on lat of study area = 9.41 deg North
SAh=ACOS((-TAN(9.41)*TAN(Delta)

SOLAR ANGLE (SA) FUNCTION OF LATITUDE (lat=9.41),SOLAR ANGLE HOUR (SAh) AND SOLAR DECLINATION (Delta) NOTE: UNITS = RADIANS
SA=SAh*SIN(Delta)*SIN(9.41)+COS(Delta)*COS(9.41)*SAh

EXOATMOSPHERIC RADIATION (Kexo_24) FUNCTION OF SOLAR CONSTANT (1367 Wm^-2*micrometre), SOLAR ANGLE, ATR_ins AND EARTH-SUN DIST
Kexo_24=1367*SA/PI*D^2

SOLAR RADIATION AS DAILY AVERAGE (K_24)
K_24=Kexo_24*ATR_ins

NET DAILY RADIATION (Rn_24)
Rn_24=(1-Ro)*(K_24)-110*ATR_ins

CALCULATION OF EVAPOTRANSPIRATION (PET_24) THIS IS RELATED TO Rn_24, LATENT HEAT OF VAPORISATION (Lv) AND DENSITY OF WATER (Dw=1000Kg m^-3)

Lv=(2.501-(0.002361*To))*1000000

PET_24=Rn_24/Lv*1000*8.64*10000000

LAMBDA=(Rn_24-G_ins-H_ins)/(Rn_24-G_ins)

AET_24=PET_24*LAMBDA

**APPENDIX 6.1b** *SEBAL Code for MATLAB-based Processing of MODIS time-series data*

```
main()
%%REFLECTANCE PER BAND
Rf1=Band1*0.000000504319
Rf2=Band2*0.000000315164

%%CORRECTED REFLECTANCE PER BAND
Rfc1=Rf1/0.9494
Rfc2=Rf2/0.9494

%%NORMALISED DIFFERENCE VEGETATION INDEX (NDVI)
NDVI=(Rfc2-Rfc1)/(Rfc2+Rfc1)

%%PLANETARY ALBEDO (Rp)
Rp=if 0.035+(0.545*Rfc1)+(0.32*Rfc2)<0;
        Rp=0;
else
        Rp=0.035+(0.545*Rfc1)+(0.32*Rfc2);
end

%%SURFACE ALBEDO (Ro) based on Rp and atmospheric transmissivity constants
specific to dry savannah West Africa
Ro=Rp-0.03613/0.75

%%INSTANTANEOUS ATMOSPHERIC TRANSMISSIVITY (ATR_ins)
ATR_ins=SQRT(Rp-0.03613)/Ro)

%%RADIANCE FOR THERMAL BANDS (L1)
L31=(Band31-1577.34)*0.000840022*PI
L32=(Band32-1658.22)*0.000729698*PI

BRIGHTNESS TEMPERATURE (BT1) based on Thermal band calibration constants
BT31=1307.3024/(ln(2249.4407/L31+1))
BT32=1198.9568/(ln(1459.5268/L32+1))

%%THERMAL INFRARED BROADBAND EMISSIVITY (SE) Empirical derivative
of NDVI
if NDVI<0.16;
SE=0;
else
SE=1.009+0.047*log(NDVI)

%%SURFACE TEMPERATURE (Ts) Derivative of BT and SE
Ts=0.39*BT31^2+2.34*BT31-0.78*BT31*BT32-1.34*BT32+0.39*BT32^2+0.56

%%AIR TEMPERATURE (Ta) Day spatial average from field logger data
Ta=23.43*Ts/Ts
```

```
%%APPARENT EMISSIVITY (Ea) Empirically derived
Ea=SE/1.3025

%%INSTANTANEOUS INCOMING LONG WAVE RADIATION (LW_IN_ins)
LW_IN_inst=Ea*0.0000000567*(Ta+273)^4

%%INSTANTANEOUS OUTGOING LONG WAVE RADIATION (LW_OUT_inst)
%%LW_OUT_inst=SE*0.0000000567*Ts^4+(1-SE)*LW_IN_ins

%%INSTANTANEOUS INCOMING SHORT WAVE RADIATION (SW_IN_ins)
SW_IN_ins=1339.86*ATR_ins

%%INSTANTANEOUS NET SHORT WAVE RADIATION (SW_NE_ins)
SW_NE_ins=(1-Ro)*SW_IN_ins

%%INSTANTANEOUS NET RADIATION (Rn_ins)
Rn_ins=SW_NE_ins+LW_IN_ins-LW_OUT_inst

%%CALCULATING SOIL HEAT FLUX EMPIRICALLY
%%INSTANTANEOUS SOIL HEAT FLUX (Go_ins)
Go_ins=Rn_ins*((Ts-273.15)/Ro)*(0.0032*1.1*Ro)+(0.0062*1.1*Ro^2)*(1-
0.978*(NDVI^4))

%%CALCULATION OF ENVIRONMENTAL AND VEGETATION RESISTANCES

%%EMPIRICAL ESTIMATION OF LEAF AREA INDEX FROM NDVI
if NDVI>0.61;
LAI=5.6;
else
LAI=5.6*NDVI+1.34;
end

%%OR
LEAF AREA INDEX (LAI) USE OF FAO EMPIRICAL COEFFICIENTS
if SAVI>0.689;
LAI=6.0;
else
LAI=-log(0.689-SAVI/0.5369);
end

%%ROUGHNESS LENGTH FOR MOMENTUM TRANSPORT (Zom)
EMPIRICALLY DETERMINED - FAO
Zom=EXP(-5.809+5.62*SAVI)

%%ROUGHNESS LENGTH FOR HEAT TRANSPORT (Zoh) FAO EMPIRICAL
RELATIONSHIP
Zoh=0.1*Zom

%%TEMPERATURE DIFFERENCE (Tdel) AIR TEMPERATURE IS SPATIALLY
REFERENCED FROM GROUND DATA AND EMPIRICAL FORMULA APPLIED
```

Tdel=IF(-382.436+1.299*Ts<0)0, (-382.436+1.299*Ts>0) (-382.436+1.299*Ts)

%%RASTERIZATION OF STABILITY CORRECTION FACTOR FOR MOMENTUM (psim) AND ATMOSPHERIC HEAT TRANSFER (psih)
psim=psih=0*Tdel

%%DISPLACEMENT HEIGHT (DIS)
DIS=1*(1-((1-EXP(-((20.6*LAI)^0.5)))/((20.6*LAI)^0.5)))

%%DISPLACEMENT AT BLENDING HEIGHT OR MIXING LAYER (Ubl) WINDSPEED FROM GROUND DATA AT 2m AND APPROX. MIXING LAYER OF 100m
Ubl=1.9*(ln(100-DIS)-ln(Zom))/(ln(2-Zom)-ln(Zom))

%%FRICTION VELOCITY (Usta) BASED ON BLENDING HEIGHT, VON KARMAN'S CONSTANT (0.41) AND ASSUMED NULL STABILITY*/
Usta=0.41*Ubl/(ln((100-DIS)/Zom)-psih)

%%ATMOSPHERIC AIR DENSITY (ADD) MODEL EMPIRICALLY DETERMINED
AAD=((99.190-1.59)/Ts*2.87)+(1.59/Ts*4.61)

%%AERODYNAMIC RESISTANCE (rah)
rah=(ln((2-DIS)/Zoh)-psih)/(0.41*Usta)

%%CORRECTED SENSIBLE HEAT FLUX (H_ins)
H_ins=1004*AAD*Tdel/rah

%%CALCULATION OF NET RADIATION (Rn24) UNIT OF INTERMEDIATE PARAMETERS = RADIANS

%%SOLAR DECLINATION (Delta) IS A FUNCTION OF IMAGE DATE IN JULIAN DAYS (JD) READABLE FROM LUT
Delta=0.409*SIN(2*PI/365*JD-1.39)

%%SOLAR ANGLE HOUR (SAh) FOR DIURNAL EXPOSITION - This depends on lat = 9.41 deg North
SAh=ACOS(-TAN(9.41))*TAN(Delta)

%%SOLAR ANGLE (SA) FUNCTION OF LATITUDE (lat=9.41),SOLAR ANGLE HOUR (SAh) AND SOLAR DECLINATION (Delta) NOTE: UNITS = RADIANS*/
SA=SAh*SIN(Delta)*SIN(9.41)+COS(Delta)*COS(9.41)*SAh

EXOATMOSPHERIC RADIATION (Kexo_24) FUNCTION OF SOLAR CONSTANT (1367 Wm^-2*micrometre), SOLAR ANGLE, ATR_ins AND EARTH-SUN DIST (D)
Kexo_24=1367*SA/PI*D^2

%%SOLAR RADIATION AS DAILY AVERAGE (K_24)
K_24=Kexo_24*ATR_ins

```
%%NET DAILY RADIATION (Rn_24)
Rn_24=(1-Ro)*(K_24)-110*ATR_ins

%%CALCULATION OF EVAPOTRANSPIRATION (PET_24) THIS IS RELATED
TO Rn_24 AND EVAPORATIVE FRACTION METHOD

%%PET_ins=(Rn_24-Go_ins-H_ins)

%%Evaporative fraction (EF)
EF=PET_ins/(Rn_24-Go_ins)

%%DAILY PET IS EMPIRICALLY DETERMINED BASED ON
BASTIAANSSEN'S METHOD
PET_24=EF*Rn_24/4.8
```

**APPENDIX 6.1c** *The SEBAL Code for MATLAB-based Processing of AATSR Time-series Data*

```
function [SE, Ts, NDVI, EF, LAI, Rn_24, PET_24, PET_mon, Band4, Band5, Go_ins,
H_ins, Ro]=PETmodel_ats2(data, NDVI2, savi, JD, D)

%% SE=surface emissivity, Ts=surface temp, NDVI=normalised diff veg index,
Rn_24=daily net radiation, PET_ins=instantaneous PET, data=satellite
%% imagery, ConstB1=refl. band1, ConstB2=refl. band2, ConstRF1=corrected, refl.
band1, ConstRF2=corrected refl. band2, PETmodel=gen output model
%% data import
%%DATA FORMAT (*.TIFF)

Band1=data(1:89,:);
Band2=data(90:178,:);
Band3=data(179:267,:);
Band4=data(268:356,:);
Band5=data(357:445,:);
Band6=data(446:534,:);

%%Imported NDVI =(Band2-Band1)/(Band2+Band1);
%e.g. NDVI2 = ndvi_021204;

%%PLANETARY ALBEDO (Rp)
if 0.035+(0.545*Band1)+(0.32*Band2)<0;
   Rp=0;
else
   Rp=0.035+(0.545*Band1)+(0.32*Band2);
end

%%SURFACE ALBEDO (Ro) based on Rp and atmospheric transmissivity constants
specific to dry savannah West Africa
Ro=(Rp-0.03613)./0.75;
```

```
%%INSTANTANEOUS ATMOSPHERIC TRANSMISSIVITY (ATR_ins)
ATR_ins=sqrt((Rp-0.03613)./Ro);

%%Imported BRIGHTNESS TEMPERATURE (Band4=BT11, Band5=BT12; BT
numbers
%%correspond to central wavelengths in micrometres)

%%THERMAL INFRARED BROADBAND EMISSIVITY (SE) Empirical derivative
of NDVI
if NDVI2<0.16;
SE=0;
else
SE=1.009+0.047.*log(NDVI2);
end

%%SURFACE TEMPERATURE (Ts) Derivative of BT and SE
Ts=0.39.*Band4.^2+2.34.*Band4-0.78.*Band4.*Band5-
1.34.*Band5+0.39.*Band5.^2+0.56;

%%AIR TEMPERATURE (Ta) Day spatial average from field logger data
Ta=27.36.*Ts./Ts

%%APPARENT EMISSIVITY (Ea) Empirically derived
Ea=0.85.*(-log(ATR_ins)).^0.09;

%%INSTANTANEOUS INCOMING LONG WAVE RADIATION (LW_IN_ins)
LW_IN_ins=Ea.*0.0000000567.*(Ta+273.15).^4;

%%INSTANTANEOUS OUTGOING LONG WAVE RADIATION (LW_OUT_inst)
LW_OUT_ins=SE.*0.0000000567.*Ts.^4+(1-SE).*LW_IN_ins;

%%INSTANTANEOUS INCOMING SHORT WAVE RADIATION (SW_IN_ins)
SW_IN_ins=1339.86.*ATR_ins;

%%INSTANTANEOUS NET SHORT WAVE RADIATION (SW_NE_ins)
SW_NE_ins=(1-Ro).*SW_IN_ins;

%%INSTANTANEOUS NET RADIATION (Rn_ins)
Rn_ins=SW_NE_ins+LW_IN_ins-LW_OUT_ins;

%%INSTANTANEOUS SOIL HEAT FLUX (Go_ins)
Go_ins=Rn_ins.*((Ts-273.15)./Ro).*(0.0032.*1.1.*Ro)+(0.0062*1.1*Ro.^2).*(1-
0.978*(NDVI2.^4));

%%EMPIRICAL ESTIMATION OF LEAF AREA INDEX (LAI)FROM NDVI
if savi>0.689;
   LAI=6.0;
else
   LAI=-log(0.689-savi)/0.5369;
```

```
end
%%ROUGHNESS LENGTH FOR MOMENTUM TRANSPORT (Zom)
DETERMINED AFTER BY FAO
Zom=exp(-5.809+5.62.*NDVI2);

%%ROUGHNESS LENGTH FOR HEAT TRANSPORT (Zoh) FAO EMPIRICAL
RELATIONSHIP
Zoh=0.1*Zom;

%%TEMPERATURE DIFFERENCE (Tdel) AIR TEMPERATURE IS SPATIALLY
REFERENCED
%%FROM GROUND DATA AND EMPIRICAL FORMULA APPLIED
if (-398.436+1.299*Ts)<0;
   Tdel=0;
else
   Tdel=(-398.436+1.299*Ts);
end

%%DISPLACEMENT HEIGHT (DIS)
DIS=1.*(1-((1-exp(-((20.6.*LAI).^0.5))))./((20.6.*LAI).^0.5)));

%%DISPLACEMENT AT BLENDING HEIGHT OR MIXING LAYER (Ubl)
WINDSPEED FROM
%%GROUND DATA AT 2m AND APPROX. MIXING LAYER OF 100m
Ubl=1.9.*(log(100-DIS)-log(Zom))./(log(2-Zom)-log(Zom));

%%FRICTION VELOCITY (Usta) BASED ON BLENDING HEIGHT, VON
KARMAN'S CONSTANT
%%(0.41) AND ASSUMED NULL STABILITY

%%ITERATED SENSIBLE HEAT FLUX (H_ins)
%%NOTE: ITERATIONS ARE USUALLY LOOPED.  THEY ARE WRITTEN AS
SUCCESSIVE LINES HERE FOR THE CONVENIENCE OF NEW MATLAB
USERS
%%Iteration 1
psim=0.*Tdel;
psih=0.*Tdel;
Usta=0.41*Ubl./(log((100-DIS)./Zom)-psim);
rah=(log((2-DIS)./Zoh)-psih)./(0.41.*Usta);

if 1.12.*1004.16.*Tdel/rah<0;
   H_ins=0;
else
   H_ins=1.12.*1004.16.*Tdel/rah;
end

if H_ins>0;
   len=0;
else
   len=(1.12.*1004.16.*Usta.^3.*Ts)./(0.41.*9.81.*H_ins);
```

```
end
xm=(1-16.*((100-DIS)./len)).^0.25;
xh=(1-16.*((2-DIS)./len)).^0.25;
psim1=2.*log((1+xm)./2)+log((1+xm^2)./2)-2.*atan(xm)+0.5.*pi;
psih1=2.*log((1+xh.^2)./2);

%%Iteration 2
Usta1=0.41*Ubl./(log((100-DIS)./Zom)-psim1);
rah1=(log((2-DIS)./Zoh)-psih1)./(0.41.*Usta1);
if 1.12.*1004.16.*Tdel/rah1<0;
   H_ins1=0;
else
   H_ins1=1.12.*1004.16.*Tdel/rah1;
end

if H_ins1>0;
   len1=0;
else
   len1=(1.12.*1004.16.*Usta1.^3.*Ts)./(0.41.*9.81.*H_ins1);
end
xm1=(1-16.*((100-DIS)./len1)).^0.25;
xh1=(1-16.*((2-DIS)./len1)).^0.25;
psim2=2.*log((1+xm1)./2)+log((1+xm1^2)./2)-2.*atan(xm1)+0.5.*pi;
psih2=2.*log((1+xh1.^2)./2);

%%Iteration 3
Usta2=0.41*Ubl./(log((100-DIS)./Zom)-psim2);
rah2=(log((2-DIS)./Zoh)-psih2)./(0.41.*Usta2);
if 1.12.*1004.16.*Tdel/rah2<0;
   H_ins2=0;
else
   H_ins2=1.12.*1004.16.*Tdel/rah2;
end

if H_ins2>0;
   len2=0;
else
   len2=(1.12.*1004.16.*Usta2.^3.*Ts)./(0.41.*9.81.*H_ins22);
end
xm2=(1-16.*((100-DIS)./len2)).^0.25;
xh2=(1-16.*((2-DIS)./len2)).^0.25;
psim3=2.*log((1+xm2)./2)+log((1+xm2^2)./2)-2.*atan(xm2)+0.5.*pi;
psih3=2.*log((1+xh2.^2)./2);

%%Iteration 4
Usta3=0.41*Ubl./(log((100-DIS)./Zom)-psim3);
rah3=(log((2-DIS)./Zoh)-psih3)./(0.41.*Usta3);
if 1.12.*1004.16.*Tdel/rah3<0;
   H_ins3=0;
else
```

```
   H_ins3=1.12.*1004.16.*Tdel/rah3;
end

if H_ins3>0;
   len3=0;
else
   len3=(1.12.*1004.16.*Usta3.^3.*Ts)./(0.41.*9.81.*H_ins3);
end
xm3=(1-16.*((100-DIS)./len3)).^0.25;
xh3=(1-16.*((2-DIS)./len3)).^0.25;
psim4=2.*log((1+xm3)./2)+log((1+xm3^2)./2)-2.*atan(xm3)+0.5.*pi;
psih4=2.*log((1+xh3.^2)./2);
%%Iteration 5
Usta4=0.41*Ubl./(log((100-DIS)./Zom)-psim4);
rah4=(log((2-DIS)./Zoh)-psih4)./(0.41.*Usta4);
if 1.12.*1004.16.*Tdel/rah4<0;
   H_ins4=0;
else
   H_ins4=1.12.*1004.16.*Tdel/rah4;
end
if H_ins4>0;
   len4=0;
else
   len4=(1.12.*1004.16.*Usta4.^3.*Ts)./(0.41.*9.81.*H_ins4);
end
xm4=(1-16.*((100-DIS)./len4)).^0.25;
xh4=(1-16.*((2-DIS)./len4)).^0.25;
psim5=2.*log((1+xm4)./2)+log((1+xm4^2)./2)-2.*atan(xm4)+0.5.*pi;
psih5=2.*log((1+xh4.^2)./2);

%%Iteration 6
Usta5=0.41*Ubl./(log((100-DIS)./Zom)-psim5);
rah5=(log((2-DIS)./Zoh)-psih5)./(0.41.*Usta5);
if 1.12.*1004.16.*Tdel/rah5<0;
   H_ins5=0;
else
   H_ins5=1.12.*1004.16.*Tdel/rah5;
end

if H_ins5>0;
   len5=0;
else
   len5=(1.12.*1004.16.*Usta5.^3.*Ts)./(0.41.*9.81.*H_ins5);
end
xm5=(1-16.*((100-DIS)./len5)).^0.25;
xh5=(1-16.*((2-DIS)./len5)).^0.25;
psim6=2.*log((1+xm5)./2)+log((1+xm5^2)./2)-2.*atan(xm5)+0.5.*pi;
psih6=2.*log((1+xh5.^2)./2);

%%Iteration 7
```

```
Usta6=0.41*Ubl./(log((100-DIS)./Zom)-psim6);
rah6=(log((2-DIS)./Zoh)-psih6)./(0.41.*Usta6);
if 1.12.*1004.16.*Tdel/rah6<0;
   H_ins6=0;
else
   H_ins6=1.12.*1004.16.*Tdel/rah6;
end

if H_ins6>0;
   len6=0;
else
   len6=(1.12.*1004.16.*Usta6.^3.*Ts)./(0.41.*9.81.*H_ins6);
end
xm6=(1-16.*((100-DIS)./len6)).^0.25;
xh6=(1-16.*((2-DIS)./len6)).^0.25;
psim7=2.*log((1+xm6)./2)+log((1+xm6^2)./2)-2.*atan(xm6)+0.5.*pi;
psih7=2.*log((1+xh6.^2)./2);

%%INSTANTANEOUS LATENT HEAT FLUX (LE_ins)
LE_ins=Rn_ins-Go_ins-H_ins6;

%%EVAPORATION FRACTION (EF)
if LE_ins/(LE_ins+H_ins6)<0;
   EF=0;
else
   EF=LE_ins/(LE_ins+H_ins6);
end

%%CALCULATION OF NET RADIATION (Rn24) UNIT OF INTERMEDIATE
PARAMETERS
%%SOLAR DECLINATION (Delta) IS A FUNCTION OF IMAGE DATE IN
JULIAN DAYS (JD)
%%READABLE FROM LUT
Delta=0.409.*sin(2.*pi.*(JD)./365-1.39);

%%SOLAR ANGLE HOUR (SAh) FOR DIURNAL EXPOSITION - This depends on
lat =
%%9.41 deg North
SAh=acos(-tan(0.162).*tan(Delta));
%%SOLAR ANGLE (SA) FUNCTION OF LATITUDE (lat=9.41),SOLAR ANGLE
HOUR (SAh)
%%AND SOLAR DECLINATION (Delta)
SA=SAh.*sin(Delta).*sin(0.162)+cos(Delta).*cos(0.162).*SAh;

%%EXOATMOSPHERIC RADIATION (Kexo_24) FUNCTION OF SOLAR
CONSTANT
%%(1367 Wm^-2*micrometre), SOLAR ANGLE, ATR_ins AND EARTH-SUN DIST
(D=0.9860)
Kexo_24=1367.*SA./pi.*D.^2;
```

```
%%SOLAR RADIATION AS DAILY AVERAGE (K_24)
K_24=Kexo_24.*ATR_ins;

%%NET DAILY RADIATION (Rn_24)
Rn_24=(1-Ro).*(K_24)-110.*ATR_ins;
if EF.*Rn_24/28.588<0;
   PET_24=0;
else
   PET_24=EF.*Rn_24./28.588;
end

PET_24_ref=1.26.*((1-0.23).*(K_24)-110.*ATR_ins)./28.356;
PET_mon=PET_24_ref.*30;
%%convert outputs to double precision
Ts=double(Ts);
NDVI=double(NDVI2);
Rn_24=double(Rn_24);
PET_mon=double(PET_mon);
PET_24=double(PET_24);
```

**APPENDIX 6.2a** ***Declaration of Variables-by-type designed for future studies, e.g. C++ (MODIS data)***

```
%%GLOBAL VARIABLES AND CONSTANTS

%%Stefan-Boltzmann's constant (S_B)=0.0000000567
%%double S_B
pi=3.142857
double pi

%%Ts coefficients = a = 0.39 b = 2.34 c = -0.78 d = -1.34 e = 0.39 f = 0.56
%%float Ts[0.39,2.34,-0.78,0.39,0.56];

%%LOCAL VARIABLES

%%MODIS bands (Bands1 and 2=reflective bands; bands 31 and 32=thermal bands)
double Band1, Band2, Band31, Band32;
%%Corrected reflectance band1 and band2 (Rfc1, Rfc2)
double Rfc1, Rfc2;
%%Vegetation parameters (NDVI=normalised diff veg index; LAI=leaf area index)
float NDVI, LAI;
%%Albedo (Rp=Planetary albedo; Ro=Surface albedo)
double Rp, Ro;
%%ATR_ins = Instantaneous atmospheric transmissivity
double ATR_ins;
%%Thermal radiances (L3= MODIS band31; L4=MODIS band32)
double L3, L4;
%%Brightness temperature (BT) for MODIS band31 and band32
double BT31, BT32;
```

%%Emissivity (SE = surface emissivity; Ea=Apparent emissivity)
float SE, Ea;
%%Temperature (Ts=surface temperature, Ta=air temperature and Tdel=temp difference)
double (complex) Ts, Ta, Tdel;
%%Instantaneous longwave radiation (LW_IN_ins=Incoming; LW_OUT_ins=Outgoing)
float (complex) LW_IN_ins, LW_OUT_ins;
%%Instantaneous shortwave radiation (SW_IN_ins=Incoming; SW_NE_ins=Net shortwave)
float (complex) SW_IN_ins,SW_NE_ins;
%%Instantaneous radiation fluxes (Rn_ins=net radiation, Go_ins=soil heat, H_ins=sensible heat)
float (complex) Rn_ins, Go_ins, H_ins;
%%Roughness length (Zom=momentum; Zoh=heat)
float Zom, Zoh;
%%Atmospheric stability correction factors (psim=momentum; psimh=heat)
double psim, psih;
%%Displacement and aerodynamic resistance factors (DIS=Displacement height,
%%Ubl=Wind displacement at blending height, Usta=friction velocity, rah=aerodynamic resistance)
float DIS, Ubl, Usta, rah;
%%Atmospheric air density (AAD)
double (complex) AAD;
%%Evaporative fluxes (PET_ins=instantaneous PET, PET_24=daily PET,
%%PET_mon=monthly PET and EF=evaporative fraction)
float (complex) PET_ins, PET_24, PET_mon, EF;
%%Daily net radiation
double Rn_24;

%%Radiation balance parameters (Delta=solar declination, SAh=solar angle hour, SA=solar angle,
%%Kexo=exoatmospheric radiation and K_24=av. daily solar radiation) Angular parameters in radians
double Delta, SAh, SA, Kexo, K_24;

%%DATA
%%Satellite imagery (MODIS)
MODIS radiance (Visible bands 1,2,3)
MODIS radiance (Thermal bands 6,7)
MODIS reflectance (Visible/NIR bands 1,2,3)
NDVI

%%Historical meteorological data and constants
Average wind speed at 2m per second
Displacement wind speed at blending height (100m threshold)

MODIS Julian date (JD) 291102=333, 191202=353, 040103=4, 090203=40, 131104=318, 021204=337, 191204=353, 250105=25

Earth-sun distances (D) JD4/5=0.9832, JD25=0.9836, JD40=0.9878, JD318=0.9892, JD332/3=0.9860, JD351/353=0.9843
COSINE OF SOLAR ZENITH ANGLE (CZA) 291102=0.9672, 191202=0.9665, 040103=0.9494, 090203=0.9526, 131102=0.9619, 181204=0.9665, 250105=0.9501

%%Field data
Air temperature from data logger
Surface temperature from data logger (validation of satellite measurements)

%%MODIS CALIBRATION COEFFICIENTS FOR REFLECTIVE BANDS - LUT
291102 band1=0.0000515247, band2=0.0000319364
191202 band1=0.000051275, band2=0.0000317758
040103 band1=0.0000512124, band2=0.0000317329
090203 band1=0.0000511852, band2=0.0000321624
131104 band1=0.0000508745, band2=0.0000317431
021204 band1=0.0000504319, band2=0.0000315164
181204 band1=0.0000502487, band2=0.0000314294
250105 band1=0.0000499524, band2=0.0000314871

%%MODIS solar declination (delta) values (radians)
%%(calculated from JD using Delta=0.409*sin(2*pi*JD/365-1.39) FAO eqn
291102=-0.3817, 191202=-0.4088, 050103=-0.3963, 090203=-0.2638, 131104=-0.3314, 021204=-0.3909, 181204=-0.4088, 250105=-0.3349

%%MODIS solar angle hour (radians)*/
SAh=acos(-tan(9.41 or 0.164rad)*tan(delta)
291102=1.5043, 191202=1.4991, 050103=1.5015, 090203=1.5261, 131104=1.5138, 021204=1.5025, 181204=1.4990, 250105=1.5132

%%MODIS solar angle (radians)*/
SA=SAh*sin(delta)*sin(0.164)+SAh*cos(delta)*cos(0.164)
291102=1.2858, 191202=1.2525, 040103=1.2719, 090203=1.3886, 131104=1.3205, 021204=1.2771, 181204=1.2597, 250105=1.3288

**<u>APPENDIX 6.2b</u>** ***Declaration of Variables-by-type designed for future studies (AATSR Data)***

| %%GLOBAL VARIABLES AND CONSTANTS*/ | | | TYPE |
|---|---|---|---|
| %%STEFAN-BOLTZMAN'S CONSTANT (S_B)=0.0000000567 | | | |
| double | | | |
| PI | = | 22/7 | double |
| Delta | = | solar declination | double |
| SAh | = | solar angle hour | double |
| SA | = | solar angle | double |
| Kexo | = | exoatmospheric radiation | double |
| K_24 | = | av. daily solar radiation | double |

Ts coefficients = a = 0.39 b = 2.34 c = -0.78 d = -1.34 e = 0.39 f = 0.56 double

%%LOCAL VARIABLES

| | | | |
|---|---|---|---|
| Rf1 | = | reflectance band1 | float |
| Rf2 | = | reflectance band2 | float |

%%MODIS VARIABLE COEFFICIENTS - REFLECTIVE BANDS

| | | | |
|---|---|---|---|
| Rf1 | = | 0.000000504319 | double |
| Rf2 | = | 0.000000315164 | double |
| Rfc1 | = | corrected reflectance band1 | float |
| Rfc2 | = | corrected reflectance band2 | float |
| NDVI | = | normalised diff veg index | float |
| Rp | = | planetary reflectance | float |
| Ro | = | surface albedo | float |
| ATR_ins | = | one-way transmissivity | float |
| L31 | = | radiance - thermal band31 | float |
| L32 | = | radiance - thermal band32 | float |
| BT31 | = | brightness temperature band31 | float |
| BT32 | = | brightness temperature band32 | float |
| SE | = | surface emissivity | float |
| Ts | = | surface temperature | float |
| Ta | = | air temperature | float |
| Ea | = | apparent emissivity | float |
| LW_IN_ins | = | longwave radiation (incoming) | float |
| LW_OUT_ins | = | longwave radiation (outgoing) | float |
| SW_IN_ins | = | shortwave radiation (incoming) | float |
| SW_NE_ins | = | shortwave net radiation | float |
| Rn | = | net radiation | float |
| Go_ins | = | soil heat flux | float |
| SAVI | = | soil adj veg index | float |
| LAI | = | leaf area index | float |
| Zom | = | roughness length (momentum) | float |
| Zoh | = | roughness length (heat) | float |
| Tdel | = | temp difference | float |
| psim=psih | = | stability correction factors | float |
| DIS | = | displacement height | float |
| Ubl | = | displacement at blending height | float |
| Usta | = | friction velocity | float |
| AAD | = | atm air density | float |
| rah | = | aerodynamic resistance | float |
| H_ins | = | corrected sensible heat flux | float |
| Rn_24 | = | net daily radiation | float |
| PET=LE_ins | = | PET or latent heat flux | float |
| Lv | = | latent heat of vaporisation | float |
| LAMBDA | = | evaporative fraction | float |
| AET | = | actual evapotranspiration | float |

%%DATA

%%Satellite imagery (Landsat-7 ETM+, MODIS, AATSR)

Landsat radiance (Visible/NIR bands 1,2,3,4,5,7)
Landsat radiance (Thermal band 6)
MODIS radiance (Visible bands 1,2)
MODIS radiance (Thermal bands 31,32)
AATSR radiance (Visible bands 1,2,3)
AATSR radiance (Thermal bands 6,7)

Landsat reflectance (Visible/NIR bands 1,2,3,4,5,7)
MODIS reflectance (Visible/NIR bands 1,2)
AATSR reflectance (Visible/NIR bands 1,2,3)
NDVI
SAVI
LAI

%%Historical meteorological data and constants
Wind speed
Displacement wind speed at blending height
Roughness length (momentum and heat)
Friction velocity
Air density
Aerodynamic resistance
Stability correction for momentum and heat

AATSR Julian date (JD) 281102=332, 171202=351, 050103=5, 090203=40, 131104=318, 021204=337, 181204=353, 250105=25
Earth-sun distances (D) JD4/5=0.9832, JD25=0.9836, JD40=0.9878, JD318=0.9892, JD332/3=0.9860, JD351/353=0.9843
COSINE OF SOLAR ZENITH ANGLE (CZA) 281102=0.9672, 171202=0.9665, 050103=0.9494, 090203=0.9526, 131102=0.9619, 181204=0.9665, 250105=0.9501

%%Field data
Air temperature from data logger
Surface temperature from data logger

%%AATSR DJD (delta) values (calculated from JD using Delta=0.409*sin(2*pi*JD/365-1.39) FAO eqn
281102=-0.3791, 171202=-0.4083, 050103=-0.3945, 090203=-0.2638, 131104=-0.3314, 021204=-0.3909, 181204=-0.4088, 250105=-0.3349

%%AATSR solar angle hour (radians)
%%SAh=acos(-tan(9.41 or 0.164rad)*tan(delta)
281102=1.5048, 171202=1.4991, 050103=1.5018, 090203=1.5261, 131104=1.5138, 021204=1.5025, 181204=1.4990, 250105=1.5132

%%AATSR solar angle (radians)
%%SA=SAh*sin(delta)*sin(0.164)+SAh*cos(delta)*cos(0.164)
291102=1.2883, 171202=1.2602, 050103=1.2736, 090203=1.3886, 131104=1.3205, 021204=1.2771, 181204=1.2597, 250105=1.3288

## APPENDIX 6.3 *Runoff Estimation Method and MATLAB-GIS Solution for Data Geolocation*

Assuming that soil physical conditions and underlying geology is stable over monthly to annual time periods in the Volta basin (Agyare, 2004; Kesse, 1985), runoff ($Q$) may be estimated on per-pixel basis following the simplified regional water balance equation (Section 3.8) as: $Q = P - ET$; where all the units are in millimetres (mm) and spatial estimates of rainfall ($P$) are derived from interpolation of ground station rainfall data using the inverse distance weighted (IDW) method, and ($ET$) from remotely sensed data (Chapter 5 – 8). In ARC-GIS, the IDW method applies a neighbourhood about the geographic location (map points) of the rainfall stations where a weighted average is taken of their observation values within this neighbourhood. The weights are a decreasing function of distance (d), represented by $w(d) = 1/d^p$ with $p>0$; an inverse power of $p = 2$ was used in this case. Investigation of the co-kriging (i.e. Thiessen polygon) and spline methods proved unsuccessful mainly because of the sparse distribution of ground station networks and their lack of correlation in terms of location distances (Wilk *et al.*, 2006; Oliver, 1990).

Instantaneous $ET$ values were derived from satellite data and integrated over 30 days using the Surface Energy Balance Algorithm for Land (SEBAL) method (Chapter 5) and processed through MATLAB functions (see Chapter 6). One of the most critical data processing issues was the conversion of the MATLAB output format (*.mat) to geo-corrected raster data (*.GeoTiff). As a solution, the following steps were applied:

**Step 1:** The $ET$ product was saved as ASCII file using the MATLAB save command e.g. *save PET_30days_291102.txt PET_30days -ASCII;* (where the first and second parts command are the output and input files, respectively).

**Step 2:** The ASCII (text) file was opened and edited with NOTEPAD using geo-correction information extracted from existing images of the study area as follows: *ncol = 86; nrows = 102; xllcorner = -1.002025; yllcorner = 8.6800843649; cellsize = 0.0090525* and *NODATA_value = -9999.* The output was saved.

**Step 3:** The output in Step 2 was opened in ARC-Info (e.g. Arc:\ w e:\dgg3so\) using the GRID command e.g. *GRID: ET_291102 = asciigrid(PET_30days_291102.txt, float).*

**Step 4:** On the basis of the above simplified water balance equation, spatial estimates of runoff ($Q$) was determined as a difference between rainfall ($P$) and evapotranspiration ($ET$).

# APPENDIX 6.4 *MATLAB Graphical User Interface (GUI) for Data Integration*

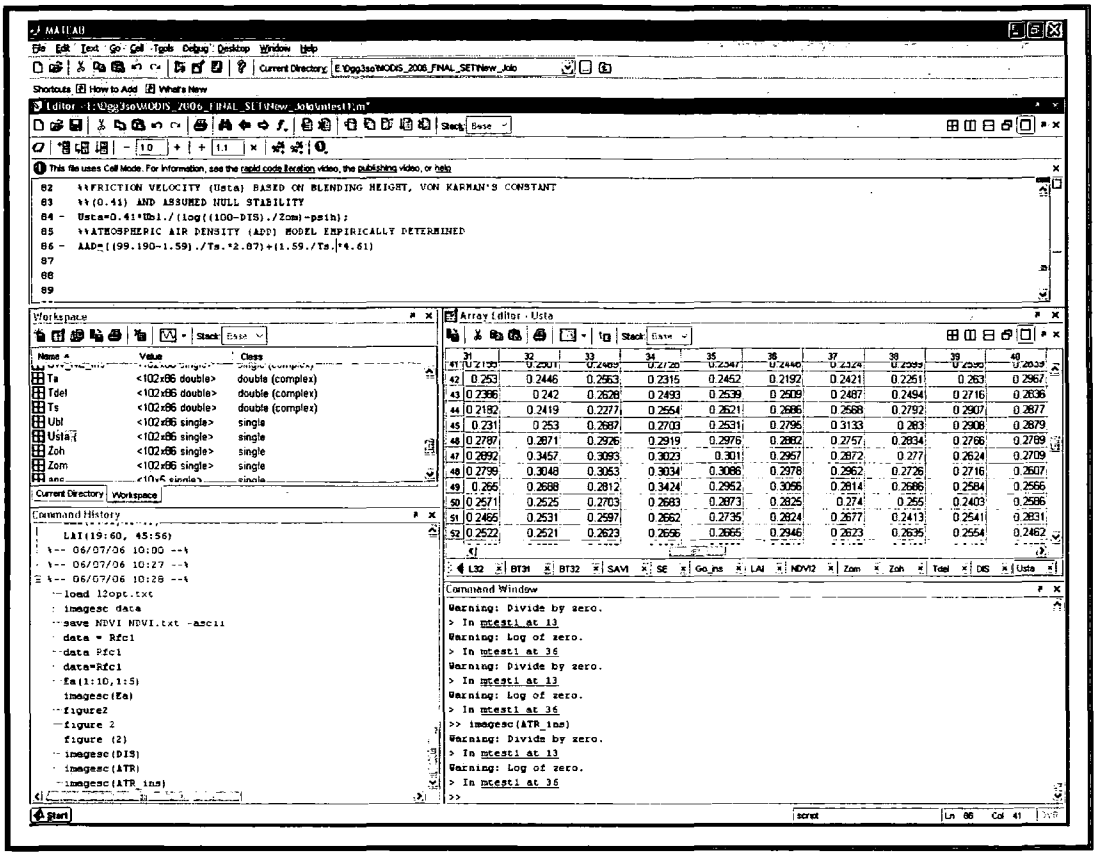

## **APPENDIX 6.5a:** *Examples of MATLAB Plots*

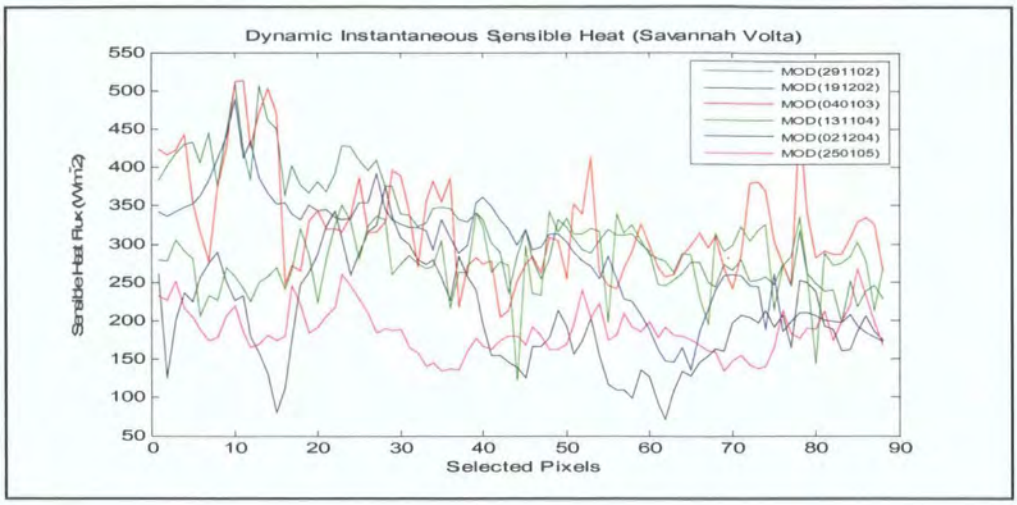


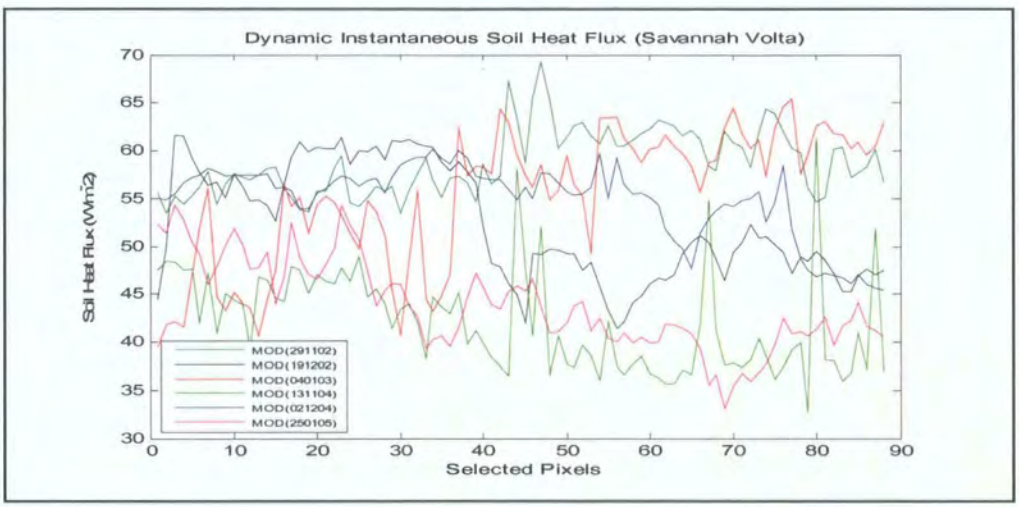


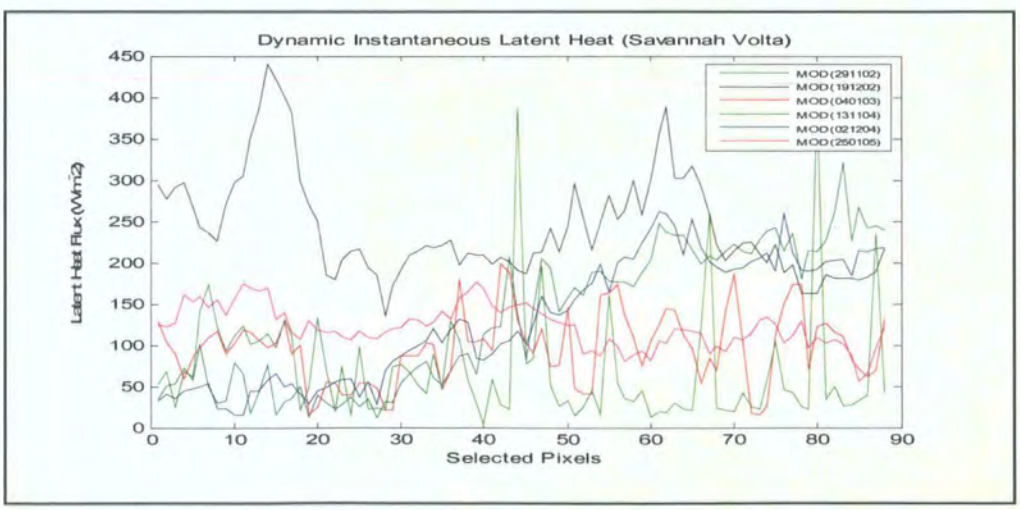

## **APPENDIX 6.5b**: *Examples of MATLAB-derived Maps*